ANALYSIS OF METHODS FOR SOLAR WIND PROPAGATION

FROM LAGRANGIAN POINT L1 TO EARTH

By

Poul F. Jensen

RECOMMENDED:

Advisory Committee Chair

Chair, Department of Physics

APPROVED:

Dean, College of Natural Science and Mathematics

Dean of the Graduate School

29 April 2013

Date

ANALYSIS OF METHODS FOR SOLAR WIND PROPAGATION FROM LAGRANGIAN POINT L1 TO EARTH

A

DISSERTATION

Presented to the Faculty

of the University of Alaska Fairbanks

in Partial Fulfillment of the Requirements

for the Degree of

DOCTOR OF PHILOSOPHY

By

Poul F. Jensen, B.S.

Fairbanks, Alaska

May 2013

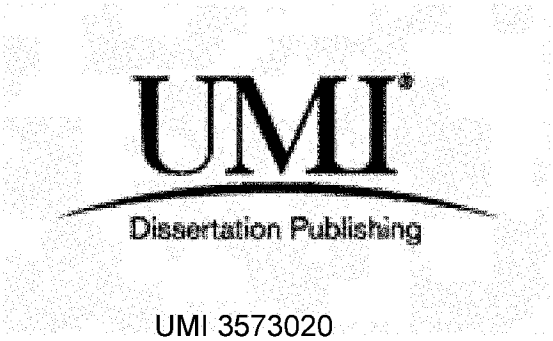

ProQuest LLC
789 East Eisenhower Parkway
P.O. Box 1346
Ann Arbor, MI 48106-1346

Abstract

The Lagrangian point L1 is situated about 1.5 million kilometers sunwards from Earth and provides a unique orbiting point for satellites, placing them constantly upstream in the solar wind, allowing for prediction of solar wind conditions impacting Earth's magnetosphere. Short-term forecasting of geomagnetic activity requires extrapolation of solar wind data from L1 to Earth (typical propagation time around 1 hour), as does any research in interactions between the solar wind and the magnetosphere during intervals when no Earth-orbiting satellites are in the solar wind. To accurately predict propagation delays it is necessary to take the geometry of incoming solar wind structures into account. Estimating the orientation of solar wind structures currently has to be done using single satellite measurements, which will likely remain the case for another decade or more, making it important to optimize single satellite techniques for solar wind propagation. In this study a comprehensive analysis of 8 different single satellite propagation methods was performed, each involving several variable parameters. 4 of these used electric field calculations and had not previously been tested for solar wind propagation. Large amounts of data were propagated from a satellite near L1 to target satellites near Earth for comparison to measured data, using specific test scores to evaluate relative performance between methods and parameter values. Electric field methods worked well for continuous data but did not predict arrival time of discontinuities (abrupt transitions) as accurately as methods based on magnetic field data, one of which delivered the best results on all accounts. This method had also been found to give best results in a previous study, but optimal parameter values were significantly different with the larger data set used here. Propagating 6,926 discontinuities it was found that on average they arrive about 30 seconds later than predicted (about 1% of the propagation time). Barring a systematic error in velocity data or delay calculations the offset suggests an asymmetry in the geometry of solar wind structures. While this idea is physically plausible it was not unambiguously supported by the data.

Table of Contents

Page

Page

List of Figures

Page

Page

Page

List of Tables

List of Appendices

Acknowledgments

This research was supported by the National Science Foundation under grants OPP-0944270 and ATM-0838270. The author thanks the ACE, Wind, IMP-8, and Geotail PIs for use of the magnetometer and plasma data, NASA's Space Physics Data Facility for making the data available and Joe Borovsky, Dan Schechter and Dan Weimer for permission to use copyrighted material.

1 Introduction

"Space weather" is a widely used term referring to processes and conditions in the tenuous medium (plasma) filling out space. Special emphasis is put on the near-Earth environment where interaction between the solar wind (flow of charged particles from the Sun) and Earth's magnetosphere is most important. As is the case for tropospheric weather, gaining the ability to make more accurate and detailed predictions is the main objective for space weather related research. Relative to tropospheric forecasting, space weather forecasting is still in its infancy. Some long-term forecasting is possible based on the solar activity cycle (~11 years), the Sun's rotational period (~4 weeks) and satellite imagery (a few days). However, long-term forecasting lacks information about the orientation of the interplanetary magnetic field (IMF) embedded in the solar wind, which is most important for the magnetospheric response to solar wind input. This information can only be provided by in-situ measurements.

A few Earth-orbiting satellites occasionally enter the solar wind and can provide IMF data vital to magnetospheric research. Another orbiting point for satellites is Lagrangian point L1 situated 1.5 million kilometers sunwards from Earth (about 1% of the distance to the Sun). Satellites stationed here are constantly in the solar wind upstream of the magnetosphere, the transit time from L1 to Earth typically being about an hour. They may then provide data useful both for short-term prediction of geomagnetic activity and for magnetospheric research during intervals when no Earth-orbiting satellites are in the solar wind, but the data must be propagated (extrapolated) from L1 to Earth. The central point in the propagation process is the estimation of phase front normals (PFNs), defining the orientation of solar wind structures. With three or more well-positioned satellites it would be possible to calculate reliable and locally accurate PFN estimates by triangulation. However, there are only two satellites orbiting L1 carrying magnetic field instruments: WIND and the Advanced Composition Explorer (ACE). Only ACE delivers data real time as required for prediction purposes, and WIND's orbit carries it 2-3 times farther away from the Sun-Earth line along which solar wind structures arrive at Earth,

making WIND data less suited for propagation to the magnetosphere most of the time. For these reasons ACE is by far the most frequently used source of magnetic field data from L1, meaning that in practice PFN estimates must be calculated from single satellite data. This produces much less accurate results than triangulation, but there is currently no plan for deploying a multi-spacecraft setup near L1 suitable for triangulation. Barring instrument failure ACE will continue operation until it runs out of fuel in 2024 (see http://www.srl.caltech.edu/ACE/ace_mission.html). The planned successor is another single-satellite mission, the Deep Space Climate Observatory (DSCOVR), due to launch in 2014. This may allow for triangulation calculations between ACE, WIND and DSCOVR in some cases, but the satellites will be too far apart for triangulation on general solar wind data. Hence it is important that single satellite methods for data propagation are analyzed and optimized given that they are expected to prevail for another decade or more.

A few previous studies have tested 4 such methods for propagation of either continuous data or a set of discontinuities (sudden rotations in the IMF). All of them use magnetic field data to derive PFN estimates and involve several variable parameters. The tests consist of propagating a data set from a source to a target satellite and compare propagated to measured data, calculating a test score to define performance. The data set is propagated for a number of values of each of the variable parameters in order to determine what parameter values give the best results. This study used the same approach, but expands significantly on previous work. Much larger data sets were used, spanning over most of a solar cycle and allowing investigation of how results may vary depending on data set. All data was propagated from ACE to a target satellite in the solar wind near the magnetosphere. In addition to the 4 magnetic field based methods 4 corresponding methods using electric field calculations were also tested. This requires deHoffmann-Teller analysis to find a reference frame in which solar wind structures are at rest, and this frame was also tested for data propagation whereas previous studies have only used the plasma rest frame. The parameter space was explored more extensively than done previously, and all methods were tested for propagation of both continuous

data and discrete discontinuities. Finally the best performing methods were tested to see how well discontinuities are handled when propagating continuous data, one particular objective being to investigate the role of data mixing (data points predicted to arrive at the target in a different order than observed at the source), which is perhaps the single biggest issue with single satellite techniques. Altogether, the results from this study give an expanded overview of issues to consider for solar wind propagation and provide a good basis for future studies to further improve propagation techniques.

2 The Solar Wind

Before delving into theory and data analysis for solar wind propagation, it is in order to put the project into perspective with a more general description of the solar wind. Some basic background information is provided to start off, followed by a more detailed explanation of large-scale solar wind structure. A "local" view of the solar wind near Earth shows how the geometry of solar wind structures needs to be assessed in order to make accurate predictions, the techniques for doing so being the subject of this study.

2.1 History

The solar wind is a stream of charged particles (plasma) constantly flowing from the Sun. It consists mostly of electrons and protons mixed with a fraction of heavier elements, mostly Helium ions (He^{2+}). The existence of the solar wind was proposed in various forms since the early 1900s when scientists identified auroras as being caused by particles plunging into the atmosphere. These particles were assumed to come from the Sun, in particular from sunspots, since it had already been established that there is a connection between auroral activity and solar activity. Comet tails provided another clue. Whereas dust tails were known to point away from the Sun due to radiation pressure from sunlight, some comets displayed two distinct tails pointing in slightly different directions (see Figure 2-1). As was proposed, the second tail consists of charged particles (ions) that are accelerated away from the Sun at a higher rate by the solar wind.

Figure 2-1 Comet Hale-Bopp. Example of comet displaying both a white dust tail (bending to the right) and a blue ion tail. Copyright Dan Schechter (1997).

In 1958 E. Parker set up a set of equations governing the steady state of the solar corona. He concluded that the pressure gradient force associated with the pressure drop from the hot corona to interplanetary space is not entirely counterbalanced by solar gravity, implying the presence of a steady radial flow that could explain the above-mentioned observations [*Parker*, 1958] (the force imbalance responsible for acceleration of the solar wind is still debated). Finally, experimental verification followed in the next years with the dawn of the space age and the first satellites exiting Earth's magnetosphere, encountering the solar wind (Soviet satellite Luna 1 being the first in January 1959).

2.2 Basic Properties

Describing the solar wind as a "steady flow" is somewhat misleading. It can be steady for hours, occasionally days during very quiet periods, but generally it is quite variable. At 1 AU (astronomical unit, the distance from the Sun to the Earth) velocities typically range from 300 km/s to 700 km/s, densities from less than 1 particle/cm^3 to a few tens of

particles/cm^3 and the embedded magnetic field from a few to 20 nanotesla (nT = 10^{-9} Tesla) (see Appendix 2 for some data samples and statistics). This variability is inherent to the solar wind even without considering coronal mass ejections (CMEs), which are clouds of ejecta hurled into space by explosions (flares) on the Sun. During the passage of CMEs, densities can reach several hundred particles/cm^3, the magnetic field can reach 50-80 nT and velocities exceed 2000 km/s in extreme cases. Though the speed of the solar wind is highly variable, the direction is close to constant; radially away from the Sun. The Earth's magnetic field is sufficiently strong to dominate over the solar wind magnetic field in a region of space surrounding Earth, creating a "bubble" that deflects the solar wind – the magnetosphere. Likewise, the region of space dominated by the Sun's magnetic field is called the heliosphere. It extends well beyond the planetary orbits and is surrounded by tenuous, interstellar plasma. The solar wind magnetic field inside the heliosphere is commonly referred to as the interplanetary magnetic field (IMF).

Approximate average values for the solar wind parameters observed at 1 AU are listed in Table 2-1 below.

Table 2-1 Average Solar Wind Parameters at 1 AU.

Proton density	6.5 cm^{-3}
He^{2+} density	0.25 cm^{-3}
Electron density	7 cm^{-3}
Flow speed	450 km/s
Magnetic field	$7*10^{-9}$ T

Some observations to put these numbers into perspective:

- At 450 km/s it takes the solar wind 3 days and 20 hours to traverse the distance from the Sun to the Earth (150 million km). For an extreme CME at 2000 km/s the travel time is reduced to a mere 20 hours.

- With V = 450 km/s and Proton/He densities as given in Table 1, the mass flowing through a sphere around the Sun with radius 1 AU (that is, the total mass leaving the Sun) is $1.6*10^9$ kg (1.6 million tons) per second. The mass equivalent of light leaving the Sun amounts to $4.3*10^9$ kg per second. Given that the mass of the Sun is $1.99*10^{30}$ kg it would take over 10,000 billion years for the sunlight and solar wind combined to deplete the Sun entirely at the current rate. In 4.5 billion years (the assumed age of the solar system) the Sun would lose about 0.04% of its mass.
- The density of protons/He^{2+} in Table 1 above corresponds to a mass of 1 gram filling 80 million km^3 or a mass of 13.5 kg filling the volume of the Earth.
- A small bar magnet generates a field strength of ~10 million nT. The strength of Earth's magnetic field at the surface of the Earth is ~50,000 nT. The magnetic field an inch from a wire to, say, a hair drier in use (110V, 1000W), is ~7,000 nT. You would observe 7 nT at a distance of ~250m from this wire (in absence of any other magnetic fields).

2.3 Structure

A key concept in plasma physics is the "frozen-in theorem", stating that plasma under a common range of conditions is tied to the magnetic field. In particular, a plasma parcel can move along the magnetic field lines passing through it, but not across them. Another way to look at this is that if the plasma has a velocity component perpendicular to the magnetic field, it carries the magnetic field along with it. In the solar wind conditions are such that the magnetic field is highly frozen-in. Hence, the structure of the solar wind is in a literal sense tied to the structure of the Sun's magnetic field.

The Sun's magnetic field is dynamic and variable. As a very rough first approximation it can be considered a dipole that reverses direction approximately every 11 years due to internal processes in the Sun, the dipole axis aligning approximately with the Sun's rotational axis. Unlike on Earth, a magnetic dipole reversal on the Sun is a dramatic process that strongly affects conditions on the Sun and throughout the heliosphere. During the reversal when the magnetic field is least organized the Sun has

numerous active regions where local loops of intensified magnetic fields poke through the solar surface. The strong magnetic field inhibits the upwelling of plasma from the Sun's hot interior, the process that is responsible for maintaining the high surface temperature (about 5,800K) of the photosphere (the visible surface of the Sun). The photosphere cools down to 3,500K-4,000K inside the active regions, causing them to appear darker than their surroundings. Some of them are large enough to be observed from Earth by the naked eye as dark spots, sunspots. The earliest record of a sunspot observation dates as far back as 364BC, but not until the early 17^{th} century were sunspots observed and recorded systematically, providing the first reliable record for solar activity and revealing the 11-year activity cycle.

The 11-year activity cycle has two main consequences for solar wind conditions near Earth. One is that the intense magnetic fields in sunspots can build up tension and energy that can be released in sudden explosive events called flares, which are responsible for generating the majority of coronal mass ejections. The other main effect is the occurrence of coronal-hole high-speed streams, fast flows of particles coming from "coronal holes" on the Sun. While coronal holes are always present, they are predominantly located over the Sun's poles during solar minimum when the magnetic field is closest to dipolar and relatively stable. During and after solar maximum large coronal holes often stretch to lower latitudes and across the solar equator. The ecliptic plane (the plane containing Earth's orbit around the Sun) is almost aligned with the Sun's equator (inclination ~7°), and so only coronal holes that extend to low solar latitudes are geoeffective.

The occurrence of coronal holes brings us back to the frozen-in theorem. Coronal holes are regions on the Sun where magnetic field lines are "open" in the sense that they extend far out in the heliosphere (theoretically, magnetic field lines always make closed loops regardless of how far they stretch out). At solar minimum when the solar magnetic field is dominantly dipolar the open field lines are confined to high latitudes around the poles while magnetic field lines at lower latitudes make closed loops. High plasma pressure in the Sun's hot corona is constantly pushing plasma radially away from the Sun. Where the field lines are open the plasma is being pushed along magnetic field lines

and can leave the corona unhindered. However, where magnetic field lines are closed the plasma will be pushed perpendicular to the magnetic field. Because it cannot cross field lines it must carry them along. A closed magnetic loop is similar to a stretched rubber band in the sense that there is a tension force resisting the loop from being expanded. Hence, magnetic tension acts to restrict the flow of plasma out of the corona if it has a component perpendicular to the magnetic field. As a consequence the plasma density is much higher in the corona where it is being held back by a closed magnetic field, and plasma leaving these regions is slowed down significantly compared to that leaving the corona along open field lines. Photos of the Sun taken at ultraviolet wavelengths show the hot plasma (~1,000,000K) in the solar corona while the much cooler photosphere underneath appears dark. Regions with open magnetic field lines are clearly identifiable as dark areas in such photos because of the associated low coronal plasma density, giving rise to the term "coronal holes" (see Figure 2-2).

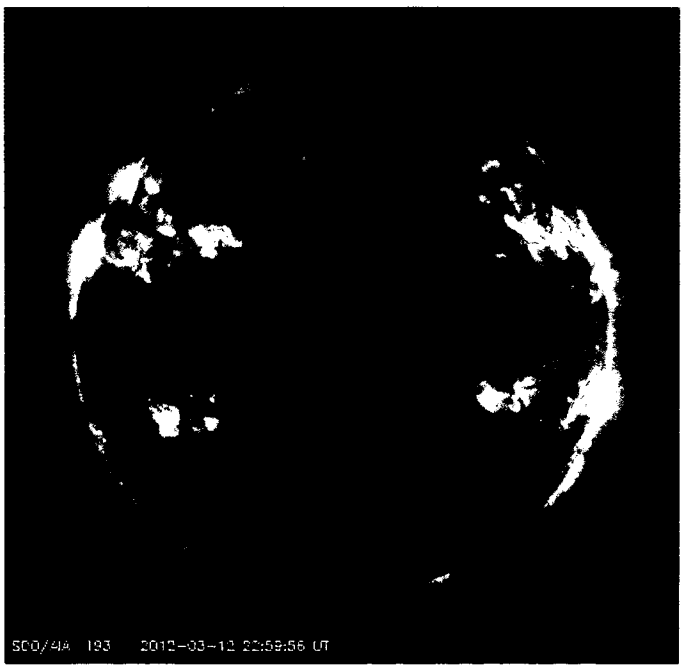

Figure 2-2 Geoeffective Coronal Hole. This image was captured at an extreme ultraviolet wavelength (19.3nm) by the Solar Dynamics Observatory (SDO). Image credit: NASA/SDO (2012).

The Sun's rotation (period ~27 days) also has implications for the structure of the solar wind. Consider a plasma parcel leaving the Sun, carrying magnetic field lines with it. The field lines remain rooted in the source region on the Sun that the plasma originated from (frozen-in theorem again), so as the plasma parcel moves radially away from the Sun, the region that the embedded magnetic field lines connect to rotates away underneath. To help visualize this, think of a (quickly) rotating garden sprinkler. The "strings" of water are twisted into a spiral, and in the same manner solar magnetic field lines are twisted into a spiral pattern named the Parker Spiral after above-mentioned E. Parker. Figure 2-3 is a sketch showing the approximate shape of the Parker Spiral in the ecliptic plane in the inner solar system.

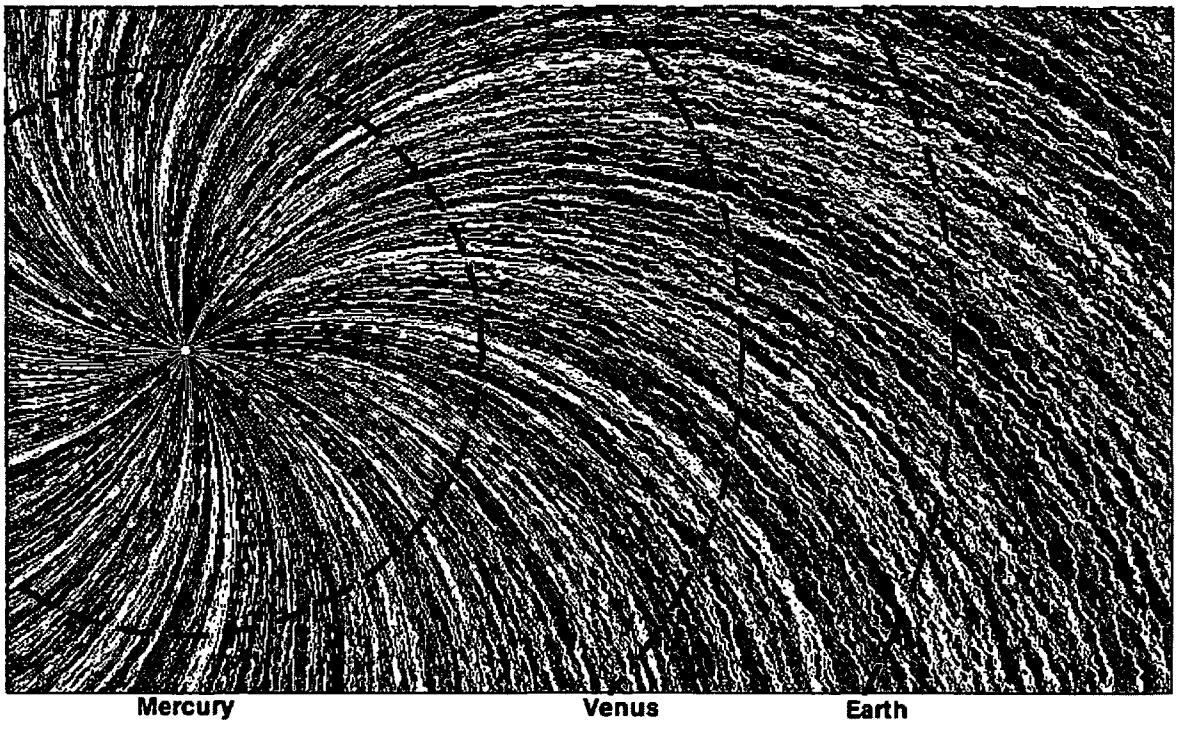

Figure 2-3 Parker Spiral Structure of Solar Wind. Sketch illustrating the spiral structure of magnetic flux tubes along the ecliptic plane in the inner solar system. Inside each flux tube the magnetic field is pointing along the tube, either towards or away from the Sun. Courtesy of Joe Borovsky.

The ACE satellite is situated near Lagrangian point L1 ~1.5 million km upstream of Earth in the solar wind (about 1% of the distance to the Sun) and typically observes intervals of 15 minutes – 2 hours with relatively constant solar wind parameters, separated by sharp transitions of a few seconds to a few minutes (see Appendix B for examples). This corresponds to a flux tube structure of the solar wind with the magnetic field being constant inside flux tubes, pointing towards or away from the Sun along the flux tube. The sharp transitions are then "walls" separating adjacent flux tubes and are commonly referred to as discontinuities. Assuming that the requirements for the frozen-in theorem are strictly satisfied throughout the solar wind, flux tubes observed at Earth can be traced back to separate source regions on the Sun. The size of flux tubes seen by ACE suggests that the source regions are typically the size of granules and supergranules (convection cells on the Sun) [*Borovsky,* 2008]. However, the frozen-in condition may be broken in isolated regions in the solar wind, opening up the possibility that flux tubes may evolve during transit to Earth and are not just "fossils" of magnetic field structures on the Sun. The extent of evolution of solar wind flux tubes is currently a much-debated topic in solar wind research.

Figure 2-4 shows the size and possible structure of solar wind flux tubes convecting by Earth's magnetosphere.

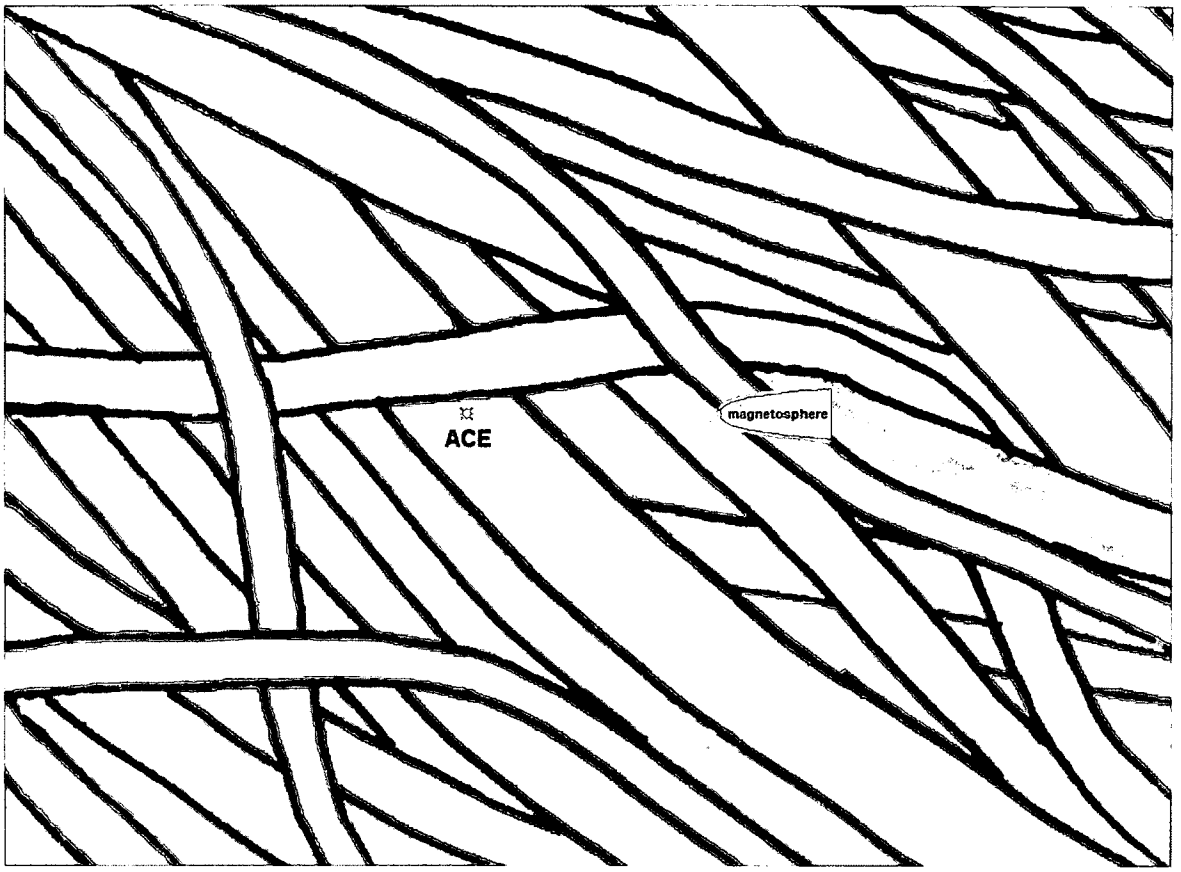

Figure 2-4 Near-Earth Flux Tube Structure. Sketch showing possible structure of solar wind magnetic flux tubes convecting by Earth's magnetosphere. Courtesy of Joe Borovsky.

Because the solar wind velocity is always close to radially away from the Sun, they arrive along the Sun-Earth line. ACE is not positioned exactly on this line, but orbiting around it, which makes it necessary to estimate the orientation of structures observed by ACE in order to calculate accurately the time at which discontinuities arrive at Earth. This is illustrated in Figure 2-5, showing the position of ACE and its average distance from the Sun-Earth line, which is labeled X_{GSE} in reference to the Geocentric Solar Ecliptic (GSE) coordinate system, which will be used throughout this study. This coordinate system has its origin at Earth's center, X- and Y-axes in the ecliptic plane with the X-axis pointing towards the Sun, and the Z-axis towards the north ecliptic pole.

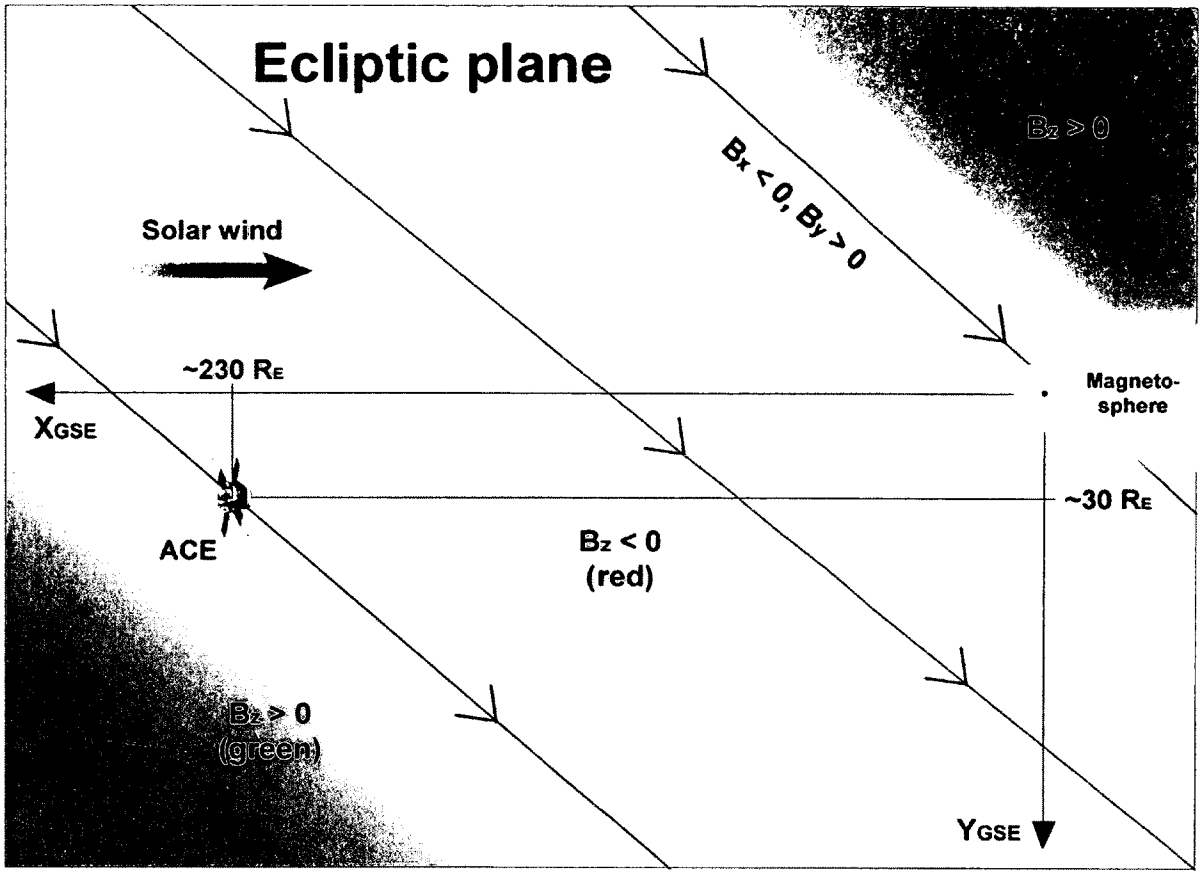

Figure 2-5 ACE Relative to the Magnetosphere. Typical position of ACE in the solar wind. Due to this off-axis position the orientation of phase fronts has to be taken into account in order to accurately calculate arrival times at Earth. The distances and size of Earth and its magnetosphere are to scale. 1 R_E = 6,378 km (Earth's radius).

A flux tube wall is arriving at ACE, but in order to calculate the arrival time at Earth we need to know where it crosses the Sun-Earth line. In order to do so it is assumed for simplicity that phase fronts are flat, infinite planes. The task is then to find an estimate for a normal vector defining the orientation of this plane. This would be a relatively simple job if data from multiple spacecraft were available, but as mentioned previously there is currently no plans for deploying a multi-spacecraft setup suitable for this purpose. Fortunately it is also possible to estimate phase front orientation from single satellite measurements. A number of different methods may be used, and to each can be added endless variations to the details of the calculations. 8 methods are tested in this study, and

the theory behind each and details of their implementation are covered in the next chapter. Whereas they produce less reliable estimates than could be obtained with multiple satellites, they do provide a significant improvement over the previously commonly used "flat delay", which assumes all structures to be aligned with the GSE YZ-plane and convect with the GSE X-component of the plasma bulk velocity.

3 Phase Front Normal Estimation

The central step in calculating propagation delays is to derive estimates for phase front normals (PFNs). In order to do so from single satellite data it is necessary to make some simplifying assumptions. From a quite simple starting point the 8 different PFN estimation methods analyzed in this study are derived, and at the end it is considered what happens when assumptions break down and how to attempt handling this.

3.1 The Rankine-Hugoniot Conditions

Sharp boundaries separating plasma populations with significantly different properties (density, velocity, magnetic field etc.) are commonly observed in space. An ideal approximation to such a boundary is a discontinuity, a separation plane (zero width) across which parameters change abruptly. A discontinuity plane is the prime example of a phase front: A plane along which there is no change. Any change (e.g. in the magnetic field) occurs only in the direction perpendicular to the plane, along the phase front normal. A plasma discontinuity will remain stable (steady state, $\frac{\partial}{\partial t} = 0$) only if the plasma satisfies a set of equilibrium conditions dictating how parameters on one side must relate to those on the other. These are called jump conditions and can be derived from a basic set of MHD (magnetohydrodynamics) equations. For solar wind plasma the conductivity is high and can in practice be considered infinite, which simplifies the MHD equations. This approximation is referred to as ideal MHD. One important consequence of this approximation is that the electric field is given by $\mathbf{E} = -\mathbf{V} \times \mathbf{B}$ where $\mathbf{V}$ is the plasma bulk velocity and $\mathbf{B}$ is the magnetic field. By rewriting the ideal MHD equations assuming steady state and considering a zero-width 1-D discontinuity (1-D: $\frac{\partial}{\partial x} = \frac{\partial}{\partial y} = 0$ when Z-axis is chosen along the discontinuity normal) we obtain the Rankine-Hugoniot conditions; the mathematical form of above-mentioned jump conditions. For the purposes of this study it is sufficient to consider the two simplest of the equations:

$$\mathbf{n}\cdot[\mathbf{B}]=\mathbf{n}\cdot(\mathbf{B}_u-\mathbf{B}_d)=0 \tag{3.1}$$

$$\mathbf{n}\times[\mathbf{V}\times\mathbf{B}]=\mathbf{n}\times(\mathbf{V}_u\times\mathbf{B}_u-\mathbf{V}_d\times\mathbf{B}_d)=0 \tag{3.2}$$

Here **n** is the normal vector perpendicular to the discontinuity plane. Subscripts u and d refer to the two sides of the discontinuity (upstream and downstream). Since the electric field is given by $\mathbf{E}=-\mathbf{V}\times\mathbf{B}$, the two equations state how the magnetic and electric fields may change across the discontinuity. In particular, Equation (3.1) states that the component of **B** parallel to **n** stays constant (only the components perpendicular to **n** may change), and Equation (3.2) states that the components of **E** perpendicular to **n** stay constant (only the component parallel to **n** may change).

The objective is to find the normal vector **n** since this defines the orientation of the discontinuity plane. Consider a discontinuity plane passing by a satellite in the solar wind. Ideally, the satellite would measure constant values of $\mathbf{B}_d$ and $\mathbf{V}_d$ before the passing, then instantly changing to different but constant values $\mathbf{B}_u$ and $\mathbf{V}_u$ after. In the special case that $\mathbf{B}_u$ and $\mathbf{B}_d$ are parallel to the plane, **n** can simply be estimated as:

$$\mathbf{n}=\frac{\mathbf{B}_u\times\mathbf{B}_d}{|\mathbf{B}_u\times\mathbf{B}_d|} \tag{3.3}$$

Verify by substituting this expression into Equation (3.1). Discontinuities that satisfy the condition $\mathbf{B}_u\cdot\mathbf{n}=\mathbf{B}_d\cdot\mathbf{n}=0$ are referred to as tangential. In the flux tube picture of the solar wind this corresponds to magnetic field lines never crossing flux tube walls. Analysis of four-point observations made by the Cluster spacecrafts reveal that almost all discontinuities in the solar wind have a sufficiently small normal component of **B** that they can be classified as tangential or close to tangential [*Knetter et al.*, 2004; *Knetter*, 2005].

Alternatively, the change in the electric field across the discontinuity provides another estimate for **n**:

$$\mathbf{n}=\frac{\mathbf{v}_u\times\mathbf{B}_u-\mathbf{v}_d\times\mathbf{B}_d}{|\mathbf{v}_u\times\mathbf{B}_u-\mathbf{v}_d\times\mathbf{B}_d|} \tag{3.4}$$

Verify by substituting this expression into Equation (3.2).

In reality, **B** and **V** fluctuate continuously because the interior of flux tubes contain small-scale structure due to waves and turbulence, or because each flux tube may contain many smaller flux tubes. Also, transitions are not instantaneous but usually take from a few seconds to a few minutes because flux tubes are separated by transition regions of finite width. In fact, often the magnetic field changes gradually and not in abrupt transitions. Hence it is necessary to generalize above principles to non-ideal conditions with the objective of constructing algorithms to continuously estimate the orientation of phase fronts (that is, calculate **n**) in solar wind data. The following paragraphs describe several propagation methods that can be used on general solar wind data. Each method is dependent on several variable parameters, and the performance varies according to choice of values for these parameters. The set of parameter values that work best will differ from case to case, but given a sufficient amount of data a statistical pattern emerges, showing which values generally work best. Each method will be tested with a range of parameter values by propagating a large amount of ACE data to a target satellite near the magnetosphere (WIND, Geotail or IMP-8).

3.2 Description of Methods

3.2.1 The Cross Product (CP) Method

The first and simplest approach examined is based on calculating the cross product $\mathbf{B}_u \times \mathbf{B}_d$ for each point in the time series. The question is what values to use for the upstream and downstream magnetic fields. Simple time-averages will do the job, but each average could be taken over any number of data points. There is no obvious choice for the number of data points to use for averaging, so this introduces a first variable parameter, which will be denoted N_{box}. Likewise it is not clear how far up- and downstream each average should be centered, making for another variable parameter to be denoted N_{sep}, the number of data points separating the two averages. In principle different N_{box} values could be used upstream/downstream, and each average could be

offset by a different number of data points upstream/downstream, making for four variable parameters instead of two. However, there is little physical motivation for introducing such an asymmetry (except perhaps for special cases such as shocks), and it isn't expected to produce significantly better results. Rather, it will be necessary to limit the number of parameters to keep it computationally manageable to explore the parameter space for an optimum set of values, and there are other, more important parameters to consider. One is a minimum "spreading-angle" between the upstream/downstream magnetic fields, denoted ω. If there is not a significant change between upstream/downstream fields, the direction of the cross product vector may be highly uncertain and the resulting PFN estimate accordingly inaccurate. Hence requiring a minimum spreading-angle may help filter out poor PFNs. Also, the CP method assumes the magnetic field to rotate in a plane parallel to the phase front, perpendicular to the PFN. The component of **B** along the PFN, here taken as an average over a number of points (N_{box}) centered on the point where the PFN is estimated, indicates how well this assumption holds and can be used as another quality check. The maximum normal component to be accepted makes a fourth variable denoted B_n.

In addition to the four CP-specific variable parameters described above, more variables applying to all propagation methods will be added later once the other PFN estimation methods and their associated parameters have been described.

3.2.2 The Electric Field Difference (ED) Method

The other simple option is calculating $\mathbf{V}_u \times \mathbf{B}_u - \mathbf{V}_d \times \mathbf{B}_d$. This can be done in the same way as the cross product method, taking $\mathbf{V}_u$ and $\mathbf{B}_u$ as an average over a number of data points upstream and similarly for $\mathbf{V}_d$ and $\mathbf{B}_d$ downstream. Again this introduces two variable parameters to be tested (neglecting the option of asymmetric parameters for upstream and downstream fields): The number of data points N_{box} to use for averages and the number of data points N_{sep} separating upstream/downstream averages. In addition, it's necessary to consider in which reference frame to take the velocity. Ideally it should be a frame in which the phase front is at rest or more specifically, the frame in which the

magnetic field is time-stationary ($\frac{\partial \mathbf{B}}{\partial t} = \mathbf{0}$). Such an ideal frame doesn't exist in practice, so the best that can be done is to use the frame in which the magnetic field changes as little as possible ($\left|\frac{\partial \mathbf{B}}{\partial t}\right|$ is a minimum). Finding this frame is the objective of deHoffmann-Teller (HT) analysis (see Appendix A). The HT analysis adds two variable parameters: The number of data points N_{HT} used to find the HT frame and a limit for the uncertainty σ_{HT} in the HT frame velocity (for simplicity the expression "HT frame" will be used even though it is only an approximation to this ideal frame). Given that the HT frame is used to calculate the electric field from the cross product $\mathbf{E} = -(\mathbf{V}_{BULK} - \mathbf{V}_{HT}) \times \mathbf{B}$, the value that will be used for σ_{HT} is the maximum standard deviation in the plane perpendicular to **B** (see Appendix A). Quality checks to filter out poorly determined PFNs add another two variable parameters. The ED method builds on the assumption that the tangential components of the electric field remain close to constant, so one quality check parameter will be a minimum ratio r_E between the magnitude of the upstream/downstream electric field difference $|\mathbf{v}_u \times \mathbf{B}_u - \mathbf{v}_d \times \mathbf{B}_d|$ and the standard deviation in the tangential electric field (for N_{box} points around the PFN). The other quality check parameter will be B_n, the maximum component of **B** along the PFN, exactly as for the CP method. This is motivated by observations suggesting that discontinuities in the solar wind are close to tangential [*Knetter et al.*, 2004; *Knetter*, 2005] and analysis results showing that techniques resulting in PFNs close to perpendicular to the mean magnetic field give better results [e.g., *Bargatze et al.*, 2005; *Mailyan et al.*, 2008].

3.2.3 Magnetic Variance Analysis Methods (MVAB, MVAB-0)

Variance analysis is a mathematical method of finding a coordinate system in which changes in a vector field (such as **B**) are most simply described. Specifically it produces an orthogonal coordinate system where two of the axes are along the directions of minimum and maximum variance, respectively. Consider how the magnetic field varies

across a finite-width flux tube wall: Instead of the sudden jump observed for a zero-width discontinuity the magnetic field will gradually rotate from $\mathbf{B}_d$ observed in one (downstream) tube to $\mathbf{B}_u$ observed in the other (upstream). This rotation is caused by a volume current **J** inside the transition region. Assuming this current to be uniform and parallel to the flux tube wall, the normal component B_n is constant throughout the volume while the projection of **B** onto the wall plane gradually rotates as the region is crossed. Consequently, the difference $\Delta\mathbf{B}$ between any two measurements of **B** will be confined to this plane as well. Variance analysis on **B** using a set of measurements from a satellite passing through the flux tube wall at an arbitrary angle will result in a coordinate system with two axes in the tangent plane, corresponding to the directions of maximum and intermediate variance, and one axis perpendicular to the plane in the direction of minimum variance (zero in this ideal case). Hence, the direction of minimum variance provides another estimate for phase front normals.

Given a set of N measurements of **B**, the variance along a direction given by a unit vector **n** is given by

$$\begin{aligned}\sigma_n{}^2 &= \frac{1}{N}\sum_{i=1}^{N}\left(\left(\mathbf{B}_i - \langle\mathbf{B}\rangle\right)\cdot\mathbf{n}\right)^2 = \frac{1}{N}\sum_{i=1}^{N}\left(B_{n,i}{}^2 + \langle B_n\rangle^2 - 2B_{n,i}\langle B_n\rangle\right)\\ &= \langle B_n{}^2\rangle - \langle B_n\rangle^2\end{aligned} \tag{3.5}$$

where angle brackets denote an average over the N measurements. The task is now to find the **n** that minimizes this expression. This is done by differentiating with respect to the components of **n** (e.g. in GSE coordinates), incorporating the constraint $|\mathbf{n}|^2 = 1$ by use of a Lagrange multiplier λ, and setting the derivative equal to zero (which will find all extrema and not only the minimum).

$$\nabla_n\left(\sigma^2 - \lambda\left(|\mathbf{n}|^2 - 1\right)\right) = \nabla_n\left(\frac{1}{N}\sum_{i=1}^{N}\left(\left(\mathbf{B}_i - \langle\mathbf{B}\rangle\right)\cdot\mathbf{n}\right)^2 - \lambda\left(|\mathbf{n}|^2 - 1\right)\right) = \mathbf{0} \tag{3.6}$$

Rewriting the x-component of the equation gives:

(3.7)

$$\frac{\partial}{\partial n_x}\left(\frac{1}{N}\sum_{i=1}^{N}\left(\left(\mathbf{B}_i-\langle\mathbf{B}\rangle\right)\cdot\mathbf{n}\right)^2-\lambda\left(|\mathbf{n}|^2-1\right)\right)=\frac{1}{N}\sum_{i=1}^{N}2\left(\left(\mathbf{B}_i-\langle\mathbf{B}\rangle\right)\cdot\mathbf{n}\right)\left(B_{x,i}-\langle B_x\rangle\right)-2\lambda n_x$$

$$=2\frac{1}{N}\sum_{i=1}^{N}B_{x,i}\left(\left(\mathbf{B}_i-\langle\mathbf{B}\rangle\right)\cdot\mathbf{n}\right)-2\langle B_x\rangle\left(\frac{1}{N}\sum_{i=1}^{N}\mathbf{B}_i-\langle\mathbf{B}\rangle\right)\cdot\mathbf{n}-2\lambda n_x$$

$$=2\frac{1}{N}\sum_{i=1}^{N}B_{x,i}\left(\left(B_{x,i}-\langle B_x\rangle\right)n_x+\left(B_{y,i}-\langle B_y\rangle\right)n_y+\left(B_{z,i}-\langle B_z\rangle\right)n_z\right)-2\lambda n_x$$

$$=2\left(\left(\langle B_x^{\,2}\rangle-\langle B_x\rangle^2\right)n_x+\left(\langle B_xB_y\rangle-\langle B_x\rangle\langle B_y\rangle\right)n_y+\left(\langle B_xB_z\rangle-\langle B_x\rangle\langle B_z\rangle\right)n_z\right)-2\lambda n_x=0$$

After rewriting the other components similarly the resulting set of equations can be written in matrix form:

(3.8)

$$2\left(\begin{bmatrix}\langle B_x^{\,2}\rangle-\langle B_x\rangle^2 & \langle B_xB_y\rangle-\langle B_x\rangle\langle B_y\rangle & \langle B_xB_z\rangle-\langle B_x\rangle\langle B_z\rangle\\ \langle B_xB_y\rangle-\langle B_x\rangle\langle B_y\rangle & \langle B_y^{\,2}\rangle-\langle B_y\rangle^2 & \langle B_yB_z\rangle-\langle B_y\rangle\langle B_z\rangle\\ \langle B_xB_z\rangle-\langle B_x\rangle\langle B_z\rangle & \langle B_yB_z\rangle-\langle B_y\rangle\langle B_z\rangle & \langle B_z^{\,2}\rangle-\langle B_z\rangle^2\end{bmatrix}-\lambda\right)\begin{pmatrix}n_x\\ n_y\\ n_z\end{pmatrix}=\begin{pmatrix}0\\0\\0\end{pmatrix}$$

Rearranging the terms leads to the following equation:

$$\overline{\overline{\mathbf{M}^B}}\,\mathbf{n}=\lambda\mathbf{n} \tag{3.9}$$

where $\overline{\overline{\mathbf{M}^B}}$ is the magnetic variance matrix having elements

$$M^B_{kl}=\langle B_kB_l\rangle-\langle B_k\rangle\langle B_l\rangle \tag{3.10}$$

Equation (3.9) is the eigenvalue equation for $\overline{\overline{\mathbf{M}^B}}$, so the solutions for $\mathbf{n}$ are eigenvectors of $\overline{\overline{\mathbf{M}^B}}$ with associated values of λ given by the eigenvalues. Since $\overline{\overline{\mathbf{M}^B}}$ is symmetric it has three orthogonal eigenvectors ($\mathbf{e}^M{}_1,\mathbf{e}^M{}_2,\mathbf{e}^M{}_3$), and in a coordinate system with the normalized eigenvectors as basis, $\overline{\overline{\mathbf{M}^B}}$ is diagonalized with diagonal terms

$$M^B_{kk}=\lambda_k=\langle B_k^{\,2}\rangle-\langle B_k\rangle^2=\sigma_k^{\,2} \tag{3.11}$$

That is, each eigenvalue is the magnetic variance in the direction of its associated eigenvector. The direction of minimum variance is then given by the eigenvector with the lowest eigenvalue. If the matrix is close to degenerate, the two smallest eigenvalues may come out almost equal, meaning that the variance is almost constant along any normal vector lying in a plane spanned by those eigenvectors, and the direction of minimum variance and hence our PFN estimate is highly uncertain. Physically this means that the plasma volume sampled by the source satellite during the interval used for minimum variance analysis (MVA) is not dominated by a uniform volume current as was assumed. Accordingly, the ratio between the intermediate and minimum eigenvalues provides a quality check that can be used to filter out potentially bad estimates. This ratio and the number of data points used to calculate the variance matrix, denoted r_{ev} and N_{MVA} respectively, are two variables that need to be tested to determine what values give the best results.

PFN estimates are unreliable if the variance matrix is dominated by small-scale structure and/or has a low eigenvalue ratio. In these cases a better estimate can be obtained by constraining the MVA, forcing the PFNs to agree with an assumed large-scale structure. According to the flux tube picture and observed near-tangential properties of solar wind discontinuities [*Knetter et al.*, 2004; *Knetter*, 2005] it is a reasonable assumption that PFNs are perpendicular to the mean magnetic field, $\langle \mathbf{B} \rangle \cdot \mathbf{n} = 0$. This requirement can be satisfied by constraining the MVA to the plane perpendicular to $\langle \mathbf{B} \rangle$, identifying the directions of minimum/maximum magnetic variance within that plane. It's possible to derive the solutions for $\mathbf{n}$ by redoing the math, this time adding a second Lagrange multiplier to implement the constraint $\langle \mathbf{B} \rangle \cdot \mathbf{n} = 0$. However, the same solutions are obtained by solving the eigenvalue equation for a modified variance matrix:

$$\overline{\overline{\mathbf{P}}} \cdot \overline{\overline{\mathbf{M}^B}} \cdot \overline{\overline{\mathbf{P}}} \cdot \mathbf{n} = \lambda \mathbf{n} \tag{3.12}$$

Here $\overline{\overline{\mathbf{P}}}$ is the matrix for projection onto a plane perpendicular to the magnetic field. In terms of a unit vector along $\langle \mathbf{B} \rangle$, $\hat{\mathbf{e}} = \frac{\langle \mathbf{B} \rangle}{|\langle \mathbf{B} \rangle|}$, the elements in the projection matrix are:

$$P_{ij} = \delta_{ij} - e_i e_j, \qquad \delta_{ij} = \begin{cases} 1, i = j \\ 0, i \neq j \end{cases} \qquad \text{(Kronecker Delta)} \tag{3.13}$$

To see why this method gives the correct results, note that the variance in any direction given by a unit vector $\mathbf{n}$ can be written in terms of the variance matrix:

$$\mathbf{n} \cdot \overline{\overline{\mathbf{M}^B}} \cdot \mathbf{n} = \sigma_n^{\,2} \tag{3.14}$$

This can be verified by writing out the expression and comparing to Equation (3.5). Because the projection matrix leaves vectors in the plane perpendicular to $\langle \mathbf{B} \rangle$ unchanged, unit vectors in this plane satisfy:

$$\mathbf{n} \cdot \overline{\overline{\mathbf{P}}} \cdot \overline{\overline{\mathbf{M}^B}} \cdot \overline{\overline{\mathbf{P}}} \cdot \mathbf{n} = \mathbf{n} \cdot \overline{\overline{\mathbf{M}^B}} \cdot \mathbf{n} = \sigma_n^{\,2} \qquad (\langle \mathbf{B} \rangle \cdot \mathbf{n} = 0) \tag{3.15}$$

It then follows that the modified variance matrix $\overline{\overline{\mathbf{P}}} \cdot \overline{\overline{\mathbf{M}^B}} \cdot \overline{\overline{\mathbf{P}}}$ has one eigenvector along $\langle \mathbf{B} \rangle$ with eigenvalue zero and the two other eigenvectors along the directions of minimum/maximum variance in the plane perpendicular to $\langle \mathbf{B} \rangle$, eigenvalues being the variances in the directions of the corresponding eigenvectors. The eigenvector with the lowest, non-zero eigenvalue then serves as the PFN estimate, and the ratio r_{ev} between the two non-zero eigenvalues provides a quality check. The basic MVA method will be referred to as MVAB while the method constrained by $\langle \mathbf{B} \rangle \cdot \mathbf{n} = 0$ will be referred to as MVAB-0.

3.2.4 Electric Variance Analysis Methods (MVAE, MVAE-0)

For the magnetic field the normal component stays constant across an ideal, 1-D discontinuity. For the electric field it is the only component that may change, so just like the direction of minimum magnetic variance can provide a PFN estimate, so can the direction of maximum electric variance. The theory and procedure is exactly the same, only with the electric field substituting the magnetic field and choosing the eigenvector for the maximum eigenvalue, and so there are two variable parameters to consider: Number of data points N_{MVA} used for averaging and the ratio r_{ev} between maximum/intermediate eigenvalues. However, there is one added complication, namely that the electric field depends on the choice of reference frame. Again, the proper reference frame is the rest frame of the phase front, and so the deHoffmann-Teller frame will be employed for this part of the analysis, adding the two variable parameters N_{HT} and σ_{HT}. As is the case for the magnetic field, results could potentially be improved by incorporating the constraint $\langle \mathbf{B} \rangle \cdot \mathbf{n} = 0$, and the basic method will be referred to as MVAE, the constrained method as MVAE-0.

3.2.5 Combination Methods (CPMV-B, CPMV-E)

Comparing results from the MVAB-0 and CP methods, *Weimer and King* [2008] got the idea to combine the two methods as it appeared that a cross-check between the two could reveal questionable PFN estimates. A new algorithm was implemented and tested, and this effort was successful as it gave better test scores for the test data set than either the CP or MVAB-0 methods were able to separately. This algorithm is considered the best currently available, and hence it is obviously of interest to include it in this study. In the work by *Weimer and King* [2008] this new combination method was denoted CPMV. In this study a corresponding combination of the CP and MVAE methods will also be tested, and hence the CP/MVAB-0 method will be denoted CPMV-B while the CP/MVAE variant is denoted CPMV-E. The combination methods compare the PFN estimates from the two "base methods" involved and only use PFNs where they agree to

within a limit angle, which becomes a new variable parameter, here denoted Φ_{diff}. Other variable parameters carry over from each of the CP and MVAB-0/MVAE methods. From the CP method there is the number of data points for boxcar averaging N_{box}, separation between averages N_{sep} and minimum spreading-angle ω. The maximum normal component B_n however is no longer needed as the new parameter Φ_{diff} does a very similar job. As will be shown, MVAE PFNs are close to perpendicular to the magnetic field, and MVAB-0 PFNs have $\langle \mathbf{B} \rangle \cdot \mathbf{n} = 0$ by construction. From the MVAB-0/MVAE methods there is the number of data points used for MVA averaging N_{MVA} and the minimum eigenvalue ratio r_{ev}. Whenever the two methods agree (as defined by Φ_{diff}) an average of the two separate PFN estimates will be calculated and used for propagation.

3.3 Breakdown of Assumptions and Extra Parameters

In the above-described analysis it is assumed that solar wind phase fronts are time-stationary flat planes over the space and time scales considered. While time-stationarity of solar wind structures is a topic of debate it is unlikely to be a significant issue given the relatively short propagation time from ACE to Earth (about an hour). The curvature of flux tube walls, however, is far from negligible. *Borovsky* [2008] found the median flux tube diameter to be ~85 R_E (Earth radii, 1 R_E = 6,378 km), and even though flux tube curvature along the central axis undoubtedly has a much larger characteristic scale it is still expected to be significant in some cases (see Figure 2-4). When the assumptions on which the delay calculations rely break down, the results become inaccurate and often inconsistent. Figure 3-1 shows how the assumed infinite-plane phase front for a PFN estimated at an ACE data point at time t ends up intersecting the phase front for a PFN estimated at some later data point at time $t+\Delta t$.

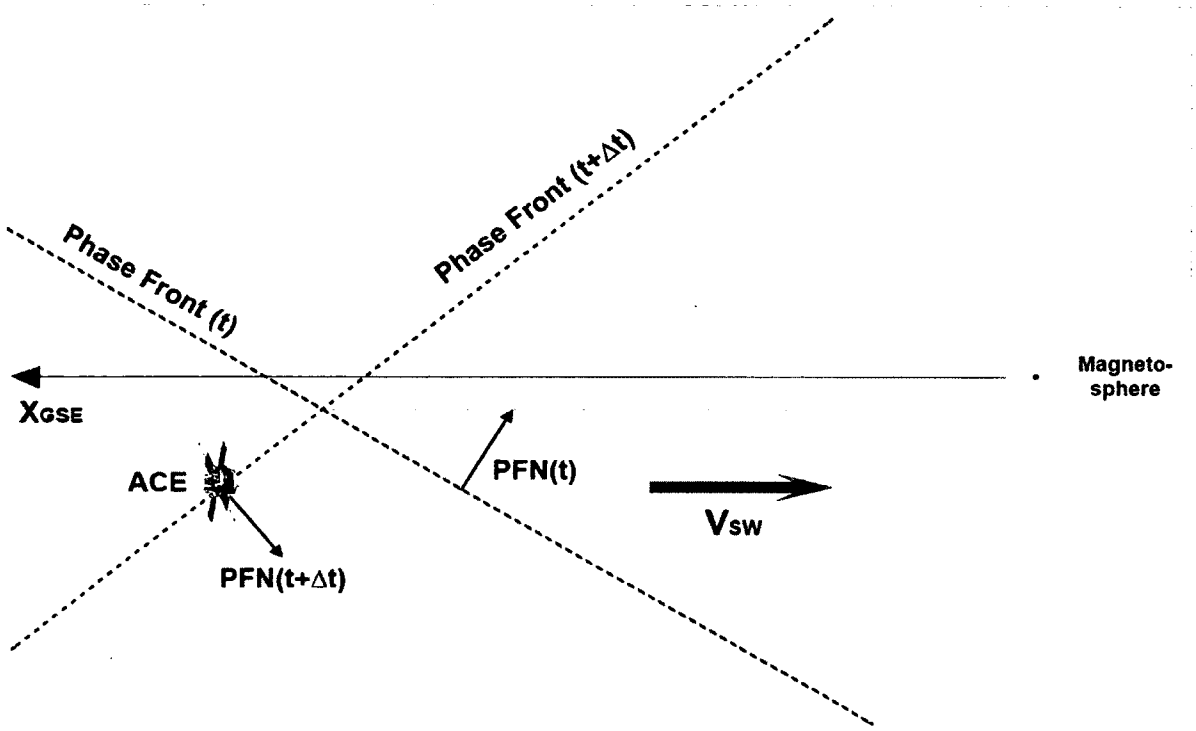

Figure 3-1 Intersecting Phase Fronts. Two PFN estimates are derived from ACE data at times t and t+Δt. Assuming the corresponding phase fronts to be infinite flat planes leads to intersecting phase fronts and reversal of the order in which the data points arrive at a target position anywhere in the shaded area.

When calculating the arrival time at a target location anywhere in the shaded area, the two points will arrive in the reverse order of which they were observed at ACE. As a result, during intervals where PFN directions change relatively suddenly, data points may appear to arrive at a target position in mixed order with values jumping back and forth. To a lesser extent, changes in velocity may contribute to the issue as well. The question is then how to handle this physically implausible mixing of data from different plasma regimes. Three options will be considered: Deleting data points that arrive at the target "early" (that is, before some data points that were measured at ACE at an earlier time), deleting data points that arrive at the target "late" (after some data points that were measured at ACE at a later time) or deleting no data points. In effect this means an extra

variable parameter is added, denoted O_{del} (for "delete option"), applying to all propagation methods regardless of PFN estimation technique.

Another problem arises when PFNs are close to perpendicular to the velocity. Since the velocity is closely aligned with the Sun-Earth line, the delay from ACE to the magnetosphere is roughly given by $\Delta X/V_{SW}$ where ΔX is the distance from the magnetosphere to the phase front along the Sun-Earth line. When the phase front intersects the Sun-Earth line at a shallow angle, the point of intersection becomes highly uncertain for two reasons. First, a small error in the PFN estimate leads to a large error in the point of intersection. Second, the intersection will be a large distance from ACE, increasing the odds that the assumed point of intersection is significantly off due to curvature in the actual phase plane. To avoid data points with highly uncertain delay estimates a cutoff value θ_{lim} for the PFN-velocity angle is employed (details of the implementation will follow later). Like the option for deletion of out-of-sequence data, the PFN-velocity limit angle adds another variable parameter to all propagation methods.

Finally, when propagating the data from the source to the target the usual choice of propagation velocity is the proton bulk velocity. This assumes that magnetic field structures convect passively with the solar wind so that the rest frame in which a structure is stationary is given by the bulk velocity. The observation that almost all discontinuities are near-tangential [*Knetter et al.*, 2004; *Knetter*, 2005] suggests that this is a good approximation, but in principle deHoffmann-Teller analysis should provide a better approximation to the proper rest frame to use for data propagation. Hence, HT analysis can be employed to calculate data propagation velocities for all methods, adding the two variable parameters N_{HT} and σ_{HT}. In the context of data propagation σ_{HT} will refer to the standard deviation in the HT frame velocity along the direction of propagation (see Appendix A). Electric field methods already use HT analysis independently to find a reference frame for calculating **E**, and a subscript will be used as necessary to indicate whether HT frames are used for calculation of **E** ($N_{HT,E}$ and $\sigma_{HT,E}$) or for data propagation ($N_{HT,P}$ and $\sigma_{HT,P}$).

3.4 Summary of Methods and Variable Parameters

8 different methods for PFN estimation have been described along with a number of different variable parameters applicable to each. Table 3-1 and Table 3-2 provide a summary of methods and parameters along with the abbreviations and symbols, which will be used for each of them.

Table 3-1 Propagation Methods and Variable Parameters. The two stars for HT analysis at electric field methods indicate that HT analysis is applicable twice.

	N_{box}	N_{sep}	B_n	ω	r_E	N_{MVA}	r_{ev}	Φ_{diff}	N_{HT}	σ_{HT}	θ_{lim}	O_{del}
CP	*	*	*	*					*	*	*	*
ED	*	*	*		*				**	**	*	*
MVAB						*	*		*	*	*	*
MVAB-0						*	*		*	*	*	*
MVAE						*	*		**	**	*	*
MVAE-0						*	*		**	**	*	*
CPMV-B	*	*		*		*	*	*	*	*	*	*
CPMV-E	*	*		*		*	*	*	**	**	*	*

Table 3-2 Variable Parameters Explained.

N_{box}	# 16-sec data points used for averaging to calculate $\langle \mathbf{B} \rangle$ or $\langle \mathbf{E} \rangle$ values
N_{sep}	# 16-sec data points separating upstream/downstream $\langle \mathbf{B} \rangle$ or $\langle \mathbf{E} \rangle$ values
B_n	Maximum component of $\langle \mathbf{B} \rangle$ along PFN (normalized, $\langle \mathbf{B} \rangle \cdot \mathbf{n} / \lvert \langle \mathbf{B} \rangle \rvert$)
ω	Minimum spreading-angle between up/downstream $\langle \mathbf{B} \rangle$ vectors (degrees)
r_E	Min. ratio: $\lvert \langle \mathbf{E} \rangle_{upstr.} - \langle \mathbf{E} \rangle_{downstr.} \rvert$ /(std. dev. in phase plane component of $\langle \mathbf{E} \rangle$)
N_{MVA}	# 16-sec data points used for averaging in MVA calculations
r_{ev}	Minimum eigenvalue ratio from MVA calculations
Φ_{diff}	Maximum angle between CP and MVAB-0/MVAE PFNs (degrees)
N_{HT}	# 16-sec data points used in deHoffmann-Teller analysis
σ_{HT}	HT frame velocity error estimate (km/s)
θ_{lim}	Maximum angle between PFN and solar wind velocity (degrees)
O_{del}	Option for deletion of out-of-sequence data ("Early", "Late" or "None")

This provides a very broad starting point, much more extensive than it is manageable to explore in detail, but doing so would be a waste of effort anyway. As will be seen some methods give inferior accuracy, and some parameters are less important than others. These methods/parameters will be disregarded as the analysis moves along.

4 Previous Work

As magnetospheric and solar wind plasma measurements became available during the 1960s, techniques to estimate plasma discontinuity normals were developed, both to investigate the structure and dynamics of the magnetopause [*Sonnerup and Cahill*, 1967, 1968] and discontinuities observed in the solar wind [*Siscoe et al.*, 1968; *Burlaga*, 1969]. An increased interest in applying these techniques more generally to structures embedded in the solar wind followed after the launch of the WIND and ACE satellites. Simple propagation delay calculations assuming a fixed orientation of phase planes were associated with considerable inaccuracy [e.g., *Russell et al.*, 1980; *Collier et al.*, 1998], showing that the geometry of solar wind structures needs to be taken into account.

An effort to investigate different methods for PFN estimation was started by D. Weimer [*Weimer et al.*, 2003; *Weimer*, 2004; *Weimer and King*, 2008] who started out testing the MVAB method. His initial results showed a significant improvement when using MVAB PFN estimates as compared to using simple flat delay [*Weimer et al.*, 2003]. Given this success others soon attempted implementing the method, but failed to reproduce the convincing results obtained by Weimer. The source of discrepancy was investigated and found to be a simple error in Weimer's code, resulting in a modified variance matrix [*Weimer,* 2004]. Interestingly the error lead to significantly better results than would have been achieved using the correct variance matrix, and an analysis of the physical implications by *Bargatze et al.* [2005] showed that the modified variance matrix has an eigenvector closely aligned with $\langle \mathbf{B} \rangle$ and with a large, negative eigenvalue. The two other eigenvectors are close to the directions of minimum and maximum variance within the plane perpendicular to the first eigenvector. As a result, the PFNs identified by Weimer's calculations are approximately in the direction of minimum variance perpendicular to the mean magnetic field $\langle \mathbf{B} \rangle$, giving almost identical results to the MVAB-0 method. Due to Weimer's serendipitous results, *Bargatze et al.* [2005] recommended use of modified MVA methods yielding PFNs that are approximately

perpendicular to the mean magnetic field $\langle \mathbf{B} \rangle$, though authors failed to mention that the idea of applying MVA constrained by $\langle \mathbf{B} \rangle \cdot \mathbf{n} = 0$ is not new. *Haaland et al.* [2006] pointed out in a comment that the MVAB-0 method was first used by *Sonnerup and Cahill* [1968] and described in detail by *Sonnerup and Scheible* [1998], leaving little motivation to use the physically incorrect method that Weimer had used by accident.

In his continued work Weimer then adapted the MVAB-0 method instead. Inspired by the work by *Knetter et al.* [2004] he decided to test the cross product method as well, and comparing the results of the two methods led to the idea of combining them to form the CPMV method. For all three methods a range of values were tested for each of the variable parameters involved [*Weimer and King*, 2008], the test score being the mean square error between propagated/measured data values when propagating ACE data to WIND and IMP-8 for 38 days. Table 4-1 shows the combination of parameter values that gave the best results (minimum mean square error) for each of the three methods tested [*Weimer and King*, 2008, Table 1].

Table 4-1 Optimal Parameter Values from Previous Study. These are results from the study by Weimer and King [2008]. Data resolution is 16 sec (15 data points = 4 minutes).

	N_{box}	N_{sep}	B_n	ω	N_{MVA}	r_{ev}	Φ_{diff}	θ_{lim}	O_{del}	Score (nT^2)
MVAB-0	-	-	-	-	25	7.8	-	75°	None	2.624
CP	19	8	0.042	8.8°	-	-	-	75°	None	2.615
CPMV	11	16	-	9.8°	21	1.1	9.9°	75°	None	2.598

The results suggest that about 25 16-sec data points or ~7 minutes of data are needed to calculate the most reliable PFN estimates (CP and CPMV parameter values both require a total of 27 different data points). However, different parameter values may produce the best score if changing some of the details in the calculations or using a different data set. For example, *Weimer and King* [2008] found that without resampling/averaging the

propagated data, the best test score for MVAB-0 was obtained using $N_{MVA} = 77$ (~20.5 minutes) and $r_{ev} = 5.2$. Results were also less consistent and the test score not as good (2.699 nT^2) Also, using a smaller data set (4 days) Weimer obtained the best results for his "modified" MVA method using 105 point averages (28 minutes) and an eigenvalue ratio of 2 [*Weimer et al.*, 2003]. This raises the question of statistical significance and whether the results in Table 4-1 are (approximately) reproducible with other data sets.

Based on the work by Weimer, King and Papitashvili created data sets of 1-minute and 5-minute resolution solar wind data estimated at Earth's bow shock (OMNI 2, accessible online and updated periodically at http://omniweb.gsfc.nasa.gov/) by propagating data from the ACE, WIND, IMP 8 and Geotail spacecrafts (see http://omniweb.gsfc.nasa.gov/html/HROdocum.html). They found that the CPMV method with optimal parameter values as found by *Weimer and King* [2008] resulted in numerous extended data gaps (> 3 hours) during intervals of low solar wind variability. To avoid this problem they implemented their own method for data propagation: Use CP PFN estimate if available, otherwise use MVAB-0 PFN estimate. If neither estimate is available, interpolate between the last and next good PFN estimate available for PFN gaps < 3 hours. For each of the CP and MVAB-0 methods they used the optimal parameters provided by Weimer at the time (before the study by *Weimer and King* [2008]): $(N_{box}, N_{sep}, \omega, B_n, \theta_{lim}) = (17, 28, 13°, 0.035, 73°)$ for the CP method and $(N_{MVA}, r_{ev}, \theta_{lim}) = (77, 5.2, 73°)$ for MVAB-0. The effort to produce the OMNI 2 data sets included a study of factors that may influence the accuracy of data propagation, specifically position of target relative to source, level of variation, solar wind speed and the propagation method used. This was done by propagating ACE data (B_z, the Z-component of the magnetic field) for ~6,000 4-hour intervals during 1998-2000 to WIND's position and correlating with measured data. The results showed a strong dependence on transverse separation (distance in the GSE YZ-plane), but with only a small deterioration for separations < ~40 R_E as is relevant here. Specifically, average correlation coefficients were 0.87 for 0-15 R_E, 0.85 for 15-30 R_E and 0.75 for 30-60 R_E.

No clear deterioration was evident as a function of X-GSE separation. For the bins 0-50 R_E, 50-125 R_E, 125-200 R_E and > 200 R_E the correlation coefficients were 0.78, 0.77, 0.81 and 0.74 respectively. Dependence on variability (standard deviation of B_z) was significant with better results for higher variability. This is expected considering both how correlation coefficients are calculated (subtracting the mean) and the more frequent/reliable PFN estimates available when there are clear rotations in **B** (remember that for spreading-angles < ω the PFN estimate is discarded). There was also a small dependence on solar wind speed (better for lower speeds). Finally, relative to the other factors examined, the dependence on propagation method was insignificant. Between MVAB-0, CP, CPMV and their own combination of CP and MVAB-0 the median correlation coefficient varied between 0.691 and 0.706, the standard deviation of the distribution being ~0.31 (> 5000 bins). This difference may not be as insignificant as it seems, however. Most of the time B_Z is either steady or changing slowly so that the prediction method will have little impact and a small improvement in the overall correlation coefficient may cover over a statistically significant improvement in prediction of arrival times of IMF discontinuities.

Horbury et al. [2001b] used CP and MVAB methods to propagate 268 southward turnings in the IMF from ACE to WIND during an interval where WIND was near Earth (late 1998) and compared them to actual delays determined by visual inspection. This was motivated by their previous finding that solar wind discontinuities appeared to be predominantly tangential [*Horbury et al.,* 2001a] based on PFN estimates found by triangulation using 3 spacecrafts (ACE, WIND and IMP-8), suggesting that the CP method should give good results. This was indeed the case as it predicted 93% of arrival times with an error of less than 10 minutes as opposed to 67% using flat delay and 56% using MVAB. 2 minutes of data centered on the discontinuity was used to derive both CP and MVAB PFN estimates. A similar study by *Mailyan et al.* [2008] compared the accuracy of discontinuity delay estimates for flat delay, CP, MVAB and MVAB-0 using a single set of parameter values (7 minutes of data for MVAB/MVAB-0, 10 16-second data points separated by 7 minutes for CP). By visual inspection they determined the

actual delay times for 198 IMF discontinuities observed by both ACE and a Cluster satellite in front of the bow shock nose (apogee is about 20 R_E). They obtained the best results using the MVAB-0 method for which 65% of the events arrived within +/-5 min of the predicted time with 30% arriving within +/-2 min. There was a significant dependence of Δt on the angle θ between the discontinuity normal and the solar wind velocity with larger Δt for larger θ, a result also found by *Horbury et al.* [2001b].

A topic related to solar wind propagation is that of solar wind structure and evolution. On the relatively short time scale relevant to this study (~1 hour) evolution is unlikely to be a major issue, at least when compared to those of spatial structure and inaccuracy of PFN estimates. However, tied to the discussion of solar wind evolution is the question of the nature of solar wind discontinuities, in particular whether they are rotational or tangential, which is of relevance to data propagation since rotational discontinuities propagate in the plasma rest frame while tangential discontinuities do not. Initial solar wind studies suggested that the majority of discontinuities were rotational [*Smith*, 1973; *Neugebauer et al.*, 1984; *Lepping and Behannon*, 1986; *Söding et al.*, 2001], but they all used MVAB analysis on single spacecraft data to estimate discontinuity normals. Few if any discontinuities could be clearly identified as rotational once the normals were determined by triangulation using multiple spacecraft [*Horbury et al.*, 2001a; *Knetter et al.*, 2004; *Knetter,* 2005]. The latter results are more reliable and suggest that solar wind discontinuities almost always have a small normal component of the magnetic field. The propagation velocity of a rotational discontinuity in the plasma rest frame is proportional to B_n (see Appendix B), and hence even if solar wind discontinuities are rotational their propagation velocities are not expected to deviate much from the plasma bulk velocity.

The study presented here will add several new results to above-mentioned studies. MVA using the electric field has been successfully applied to magnetopause data in the past [*Sonnerup et al.*, 1987, 1990], but it is unknown how well it applies to general solar wind data. Generally, parameter space and options for calculations will also be investigated more thoroughly. All previous work has used the proton bulk velocity for propagating data, but in principle the correct frame to use is an approximated HT frame,

which should follow rotational discontinuities. It will be tested here whether this leads to any improvement in practice. The study will also have a significantly larger statistical basis than previous studies, including data from different parts of the 11-year solar cycle and processing up to about 10 times the data used in the study by *Weimer and King* [2008], 25 and 35 times as many discontinuities as in the studies by *Horbury et al.* [2001b] and *Mailyan et al.* [2008]. Finally, previous studies have analyzed propagation of either general solar wind data or discontinuities in isolation whereas in this study the two will be considered in combination.

5 Data Analysis

This study builds on previous work and as such has borrowed methods and ideas from other studies. However, all code for the analysis has been written from scratch and many ideas for modifications have been tested along the way, some of which have made it into the final code. Furthermore, methods for identifying discontinuities observed at both a source and target satellite were developed specifically for this study. Hence it is necessary to describe the involved algorithms rigorously to help understand the results in detail. First however the goal for the analysis must be clarified by defining how the different propagation methods are going to be compared.

5.1 Test Scores

Previous studies have evaluated the performance of different propagation methods by means of a simple test score calculated from propagated/measured IMF data at a target satellite: The mean square error [*Weimer et al.*, 2003; *Weimer and King*, 2008], the cross correlation function (see http://omniweb.gsfc.nasa.gov/html/HROdocum.html) or the error in predicted arrival times of discontinuities [*Mailyan et al.*, 2008]. The two first apply when propagating a continuum of data while the last is relevant for propagating discontinuities. Both of these are important, but a method and associated parameter values that give the best results for propagating a continuum of data may not be optimal for propagating discontinuities.

Both for the purposes of studying the magnetospheric response to solar wind input as well as for real-time forecasting it would be ideal if continuous data and discontinuities alike were propagated as accurately as possible. Unfortunately, transitions may become ill-defined when propagating a continuum of solar wind data because of mixing of plasma data from the two separate regions around a transition. Figure 5-1 shows an example of this.

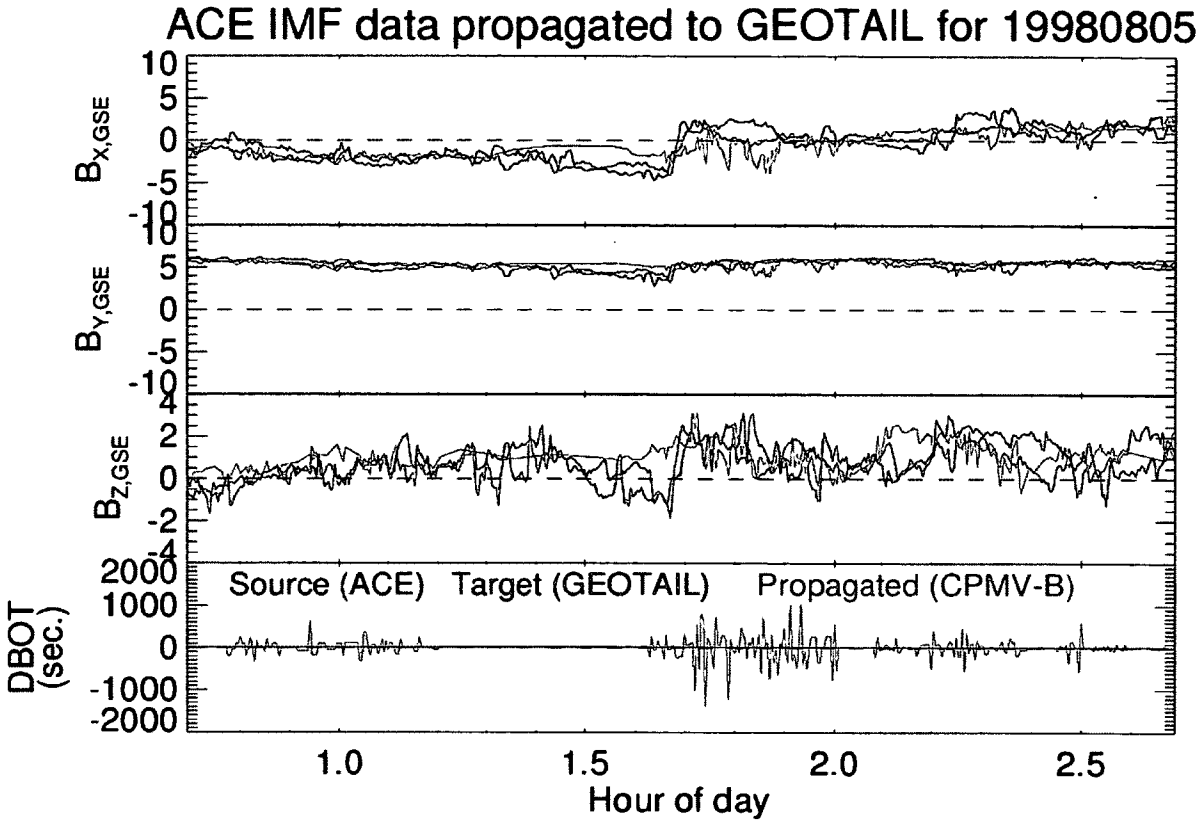

Figure 5-1 Ill-Defined Transition. Geotail IMF data (red) and ACE IMF data shifted by a constant delay (green) and the CPMV-B method (grey) respectively. Negative values of DBOT (duration between observation times) indicate out-of-sequence data.

The first 3 plots show IMF data measured at a target satellite (Geotail, red) along with ACE IMF data shifted by a constant delay (green) and propagated by the CPMV-B method (grey). The bottom plot shows duration between observation times (DBOT) where "observation time" refers to source data before propagation. DBOT would equal the time resolution of the data series if a constant delay was used, but changes when using a variable delay. Negative values of DBOT indicate intervals where out-of-sequence data is occurring. Notice how a distinct IMF transition present in both source and target data at the middle of the interval has been eliminated in the propagated data due to data mixing. It should be noted that the CPMV-B method and parameter values used in this example give close to optimal performance for continuous data

propagation if using the mean square error as a quality measure and testing on a large data set.

Three different options for dealing with out-of-sequence data have been tested in this and previous studies, but none of them are optimal for providing accurate and well-defined delay estimates for discontinuities. Ultimately the goal for research on solar wind propagation would be to develop a method for propagating continuous data as accurately as possible while prohibiting the unphysical mixing of data from different plasma regions. This is a very complicated task and beyond the scope of this project. However, the extent of the problem with data mixing does depend on the propagation method and accompanying parameter values chosen, and so this is an issue to consider when evaluating overall performance.

The performance of propagation methods and associated parameter values will be evaluated and compared in a three-part analysis that considers both propagation of continuous data and discrete events. In Part 1 continuous ACE data will be propagated to a target satellite near the magnetosphere for all intervals where it is providing good solar wind data. In Part 2 discontinuities that can be mutually identified at both ACE and a target satellite near the magnetosphere are propagated in isolation. In Part 3 a continuum of data (2 hours) surrounding each of the discontinuities from Part 2 is propagated. In other words, propagation of continuous data and discrete events will both be investigated separately, but also in combination.

Test scores are needed to define relative performance, and the mean square error will be used for continuous data, denoted by μ_{MSE}. Correlation coefficients were also calculated throughout and could have been used as well, but the results mirror those of μ_{MSE} fairly closely and will not be shown. For discrete events the average difference (absolute value) between predicted and actual arrival times would be the simplest candidate for a test score. However, this is a poor choice in case there is a systematic offset (a tendency for predicted arrival times to be either early or late). Figure 5-2 shows the distribution of arrival time differences (measured minus predicted, denoted Δt_{ROT}) for

a large number of discontinuities propagated from ACE to near-Earth target satellites (the same data set used in the rest of the study, see Section 5.3.3).

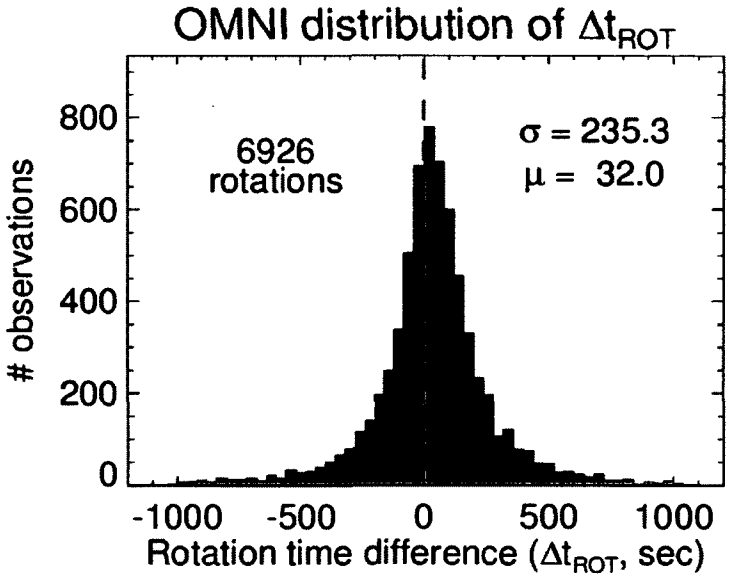

Figure 5-2 OMNI Distribution of Arrival Time Errors. Distribution of arrival time differences Δt_{ROT} for the set of 6,926 IMF discontinuities used in the study (see Section 5.3.3) when using the OMNI method for propagation.

The distribution has an offset from zero, and for as far as this offset is consistent a propagation algorithm may compensate for it simply by subtracting it. What will be used as a test score is the standard deviation of the distribution, denoted $\sigma_{\Delta t}$, as it is a good indicator of how accurate results it is possible to produce for a given method.

Finally, a third test score will be used for indicating how well distinct IMF discontinuities are preserved and matching target satellite data when doing continuous data propagation. The IMF discontinuities used for this study were found by using an automated algorithm (described in detail later) to compare discontinuities identified at ACE and a target satellite, only accepting those with sufficiently high similarity between source/target that they are very likely to represent the same transition observed at both satellites. The same algorithm can then be used to check if the propagated data still contains a discontinuity matching that of the target satellite, given that a match was

present in the original source data. The percentage of discontinuities that remain sufficiently well-defined in the propagated data for the algorithm to accept them as matching the discontinuities in the target satellite data will serve as a third test score. This will be denoted P_{MATCH}, indicating the probability that propagated discontinuities match those observed at the target (according to the fairly strict criteria used here).

5.2 Data Sources

The analysis involves data from 4 different satellites: ACE, WIND, Geotail and IMP-8. All data has been downloaded as CDF files from the Coordinated Data Analysis Web (CDAWeb) (see http://cdaweb.gsfc.nasa.gov/).

5.2.1 ACE

For ACE, data from both the plasma instrument [*McComas et al.*, 1998] and magnetic field instrument [*Smith et al.*, 1998] is used. Magnetic field data has a resolution of 16 seconds while plasma data is 64-second resolution. Plasma data will be interpolated to the 16-second time resolution of the magnetic field data for electric field calculations. The downloaded data (Level 2) is very clean and needs no filtering before using it for the analysis. However, a constant 29.8 km/s has been subtracted from the GSE Y-component of the plasma velocities in order to compensate for the corotational velocity of ACE and must be added back into the data set to obtain the correct velocities for electric field calculations and data propagation. Magnetic field data is available from September 1997 through current, while plasma data coverage starts in February 1998. Since both are required, data analysis runs from the latter date and as close to current as data is available depending on target satellite.

5.2.2 WIND

For WIND, the data used is 3-second resolution data from the magnetic field instrument [*Lepping et al.*, 1995]. Data is resampled (averaged) to 15-second resolution

in order to match the resolution of ACE data (approximately). Coverage runs from 1995 through current, but for this project data use starts in 1998 along with the availability of ACE data and ends in April 2004 when WIND started orbiting L1. Prior to this WIND was orbiting Earth (apogee ~80 R_E) in between making prolonged excursions to ~200 R_E in the +/- Y and X GSE directions. Because the focus of this project is data propagation from ACE to Earth, data was used only from intervals where the ACE-WIND separation was at least 150 R_E in the X GSE direction and at most 60 R_E in the GSE YZ-plane. Furthermore, WIND is required to be outside the bow shock. The WIND magnetometer team has made a list of bow shock crossing identifications available at http://lepmfi.gsfc.nasa.gov/mfi/bow_shock.html. It is not a complete list of all crossings, but rather a list made to identify prolonged solar wind intervals and exclude data of questionable origin, which is the objective here. WIND made a few bow shock crossings since the list was last updated (June 2003). These crossings were identified by visual comparison of WIND and propagated ACE data and conservative estimates added to the list.

An additional issue to consider is foreshock waves. Figure 5-3 Plot a) shows WIND data as the satellite is approaching and eventually crossing the bow shock, and Figure 5-3 Plot b) shows a close-up view of data containing foreshock waves.

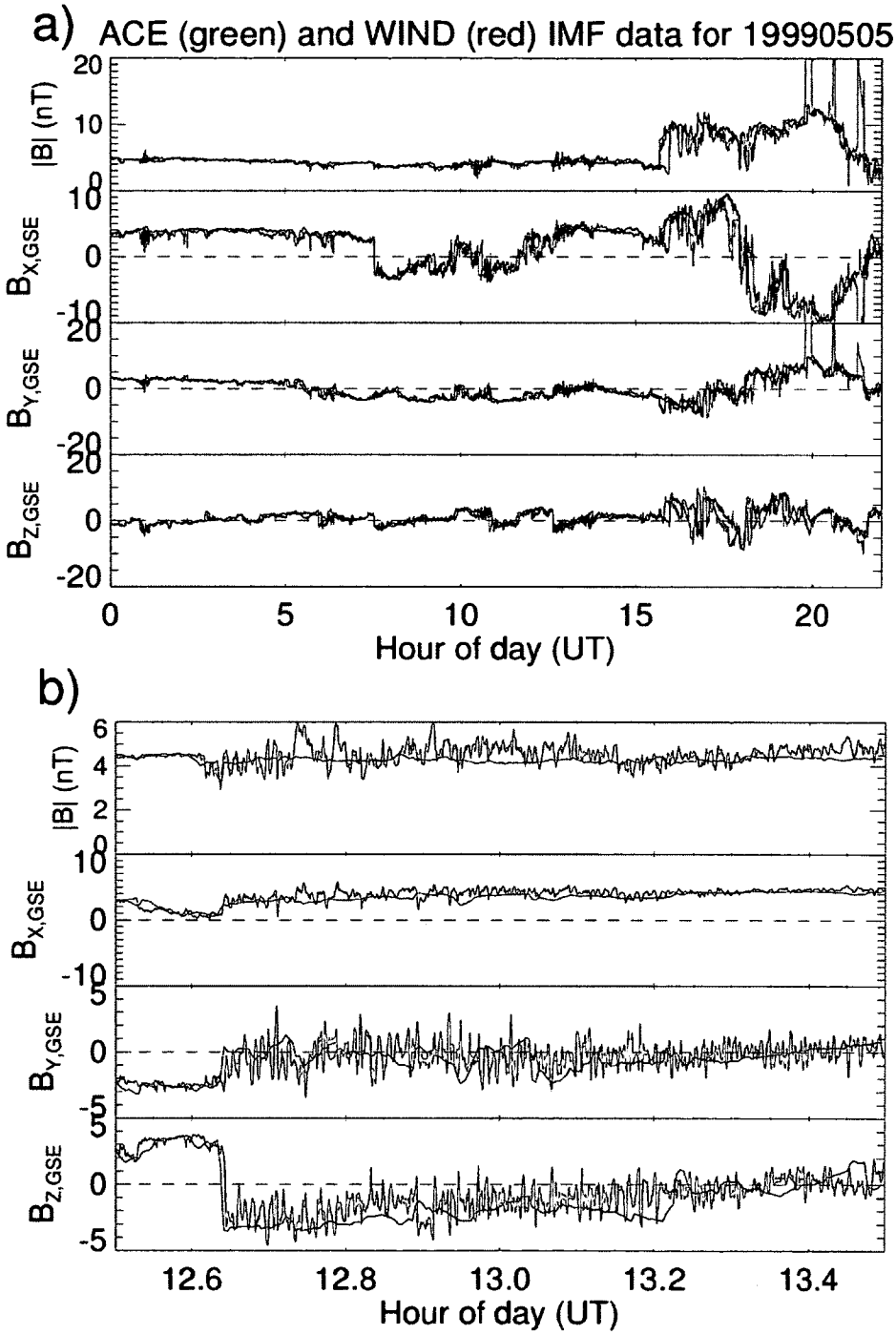

Figure 5-3 WIND Foreshock Wave Example. Sample of WIND IMF data (red) as the satellite approaches the bow shock. Shifted ACE data (green) has been added to the plot for comparison. Grey color indicates WIND data that has been excluded from the study, belonging to an interval contaminated by magnetospheric data.

As can be seen these waves are superimposed on the background IMF, and they typically have periods of ~30 seconds in the spacecraft frame. Mostly the waves do not prevent identification of discontinuities, but they do affect the values of mean square errors. The effect is minimized by smoothing WIND data with a 60 second window before calculating mean square errors. Obviously this also smoothes out other high frequency oscillations in the solar wind, which is also desirable as these are associated with small-scale fluctuations that cannot be propagated accurately over large distances, and eliminating these improves (lowers) mean square errors noticeably.

Finally, WIND data contains spurious data points, which may occasionally affect mean square errors as well. An effective yet relatively simple method for eliminating spurious points is to consider the average difference in magnetic field magnitude $|\mathbf{B}|$ to the two neighboring points:

$$\langle \mathrm{dB} \rangle = \frac{\left| |\mathbf{B}_{i+1}| - |\mathbf{B}_i| \right| + \left| |\mathbf{B}_{i-1}| - |\mathbf{B}_i| \right|}{2} \tag{5.1}$$

When this quantity exceeds a threshold the point is discarded. A suitable threshold value can be determined from looking at the statistical distribution of dB values and was set to 0.4 nT for WIND 3-second data. This removes most spurious data and in particular data values that are significantly off. It also removes some valid data points, especially within foreshock wave data. This is not a problem since most of the resulting data gaps are eliminated when resampling/averaging to 15- or 60-second resolution, and any remaining gaps can be filled in by interpolation.

5.2.3 Geotail

From Geotail, data from the magnetic field instrument [*Kokubun et al.*, 1994] is used. A 3-second resolution data set is available, which was resampled (averaged) to 15-second resolution to compare to ACE data. Data coverage starts in 1992, and Geotail is still operational as of writing. However, here the analysis is limited to

February 1998 - November 2006, from when ACE data becomes available and to the last data accessible via CDAWeb. Newer data is available from elsewhere (Data Archives and Transmission System or DARTS, see http://www.darts.isas.jaxa.jp/spdb/caveats.html) but in a different format. During this interval Geotail was in a geocentric orbit with apogee at ~30 R_E and perigee at ~9 R_E, the apogee moving around the Earth so there are certain seasons where Geotail enters the solar wind regularly. A list of solar wind intervals identified by the OMNI team in preparation of the OMNI 2 data set is available online (see http://nssdcftp.gsfc.nasa.gov/spacecraft_data/geotail/sw_min_merged/00readme) and was used to exclude magnetospheric data. Some errors were identified in this list and corrected manually. The usable solar wind intervals constitute about 30% of Geotail data. They include data with foreshock variability, and as for WIND this issue is solved by smoothing the data with a 60-second running average. Spurious data points are so sparse that filtering is not necessary. However, a systematic shift in the Z-component of the magnetic field has been identified, and a correction was added to some Geotail data sets in 2008. Whereas a corrected data set is not yet available from CDAWeb, daily correction values are available from the Japanese website hosting Geotail data (DARTS, see http://www.darts.isas.jaxa.jp/spdb/caveats.html). These have been added to the data set used for this analysis manually.

5.2.4 IMP-8

Finally, from the IMP-8 satellite data from the magnetic field instrument is used [*Mish and Lepping*, 1976]. The data is 15.34 second resolution, and coverage runs from 1973 to June 2000 when the onboard magnetometer failed. That leaves a relatively short overlap with required ACE data coverage (February 1998 – June 2000) that can be used for this study. During this interval IMP-8 had a geocentric orbit with perigee ranging from 25-32 R_E and apogee in the range 38-44 R_E. The CDF files available for download from CDAWeb contains a region flag specifying intervals where the satellite was in the solar wind (about 60% of the time). Comparison with propagated ACE data confirms that

the flag mostly excludes magnetospheric data effectively (a few intervals where this wasn't the case were removed), though foreshock variability is not excluded. Again smoothing with a 4-point running average (~60 seconds) was applied before calculating mean square errors. Spurious data points are abundant in IMP-8 IMF data and have been eliminated by the same method as for WIND data, calculating <dB> as given by Equation (5.1) and using a threshold value of 0.4 nT.

5.2.5 Available Solar Wind Data

When a target satellite is close to the magnetosphere, the bow shock will often move back and forth across the satellite position, resulting in relatively short intervals of solar wind data interspersed with magnetosheath data. For such intervals the risk of including data with magnetospheric influence may outweigh the benefit of adding these short intervals to the data set, and it was decided to exclude any solar wind data intervals less than 3 hours. Table 5-1 shows the amount of time (hours) that each satellite spent in the solar wind year by year (only near-Earth data for WIND as defined previously).

Table 5-1 Near-Earth Solar Wind Data. Amount of time (hours) each target satellite spent in the near-Earth solar wind. The stars for IMP data indicate that the actual amount of data is significantly less because IMP only provided good data ~75% of the time.

	Geotail	WIND	IMP-8
1998	2,732	1,881	4,744*
1999	2,758	330	5,098*
2000	2,627	0	2,205*
2001	2,639	0	0
2002	2,720	665	0
2003	2,681	225	0
2004	2,599	137	0
2005	2,609	0	0
2006	1,982	0	0
Total	23,347	3,238	12,047*

During the solar wind intervals WIND and Geotail provided good data 99% and 97% of the time, respectively, while the IMP-8 magnetometer had increasingly frequent data gaps up till its failure in June 2000. IMP-8 data coverage for the solar wind intervals used averaged ~75%.

5.3 Discontinuity Algorithms

Identifying discontinuities in the solar wind IMF and matching them up for two satellites can either be done visually or by an automated algorithm. Using an algorithm is the preferred approach for this project because it can search through large amounts of data quickly and is repeatable and objective. On the downside it is impossible to avoid misidentifications, and it ends up being a compromise between minimizing the number of misidentifications and retaining as many valid identifications as possible. Avoiding

misidentifications has been given priority because there is enough data that even with strict requirements it was still possible to find a large number of good identifications.

5.3.1 Identification (Single Satellite)

First, an algorithm is used to identify IMF discontinuities for individual satellites. The steps are:

Algorithm A Discontinuity Identification

A1) For each data point consider the 1-, 5- and 30-minute average IMF on both sides. The before/after average values are separated by 2, 6 and 31 minutes respectively (non-overlapping with a 1-minute gap between them).

A2) Calculate the rotation angle between before/after IMF vectors for each of the three averaging intervals.

A3) Check if all angles exceed a threshold value (30 degrees used).

A4) Check if the sum of rotation angles (1, 5, 30 minutes) is at a maximum within a 15-minute window.

A5) Check if there is an interval of "steady" IMF (which means no other rotations satisfying above criteria) for an interval of 30 minutes either before or after the discontinuity (but not necessarily both).

The last condition serves to filter out less distinct rotations. It also reduces the potential for mismatches when comparing discontinuities from two satellites to find matching pairs, which is the next task.

5.3.2 Comparison Between Satellites

Having used Algorithm A to identify suitable IMF discontinuities in data from a source and target satellite, the algorithm for identifying matching discontinuity pairs proceeds as follows:

Algorithm B Discontinuity Matching

B1) For each discontinuity at the source satellite (ACE) consider the discontinuities found at the target satellite within a 3-hour window (one hour before, two hours after) as candidates for a match.

B2) For each candidate consider the 1/5/30-minute IMF averages before/after used in Algorithm A. These are required to agree between source/target discontinuities to within some angle. The thresholds used were 45 degrees for 1- and 5-minute averages, 30 degrees for the 30-minute average.

B3) If the IMF magnitude around a discontinuity (the mean of before/after 5-minute averages) at the target satellite is more than 1.5 times the magnitude at the source satellite the discontinuity is discarded.

B4) If one and only one match is found within the window, this is accepted as a valid match – subject to one last check:

B5) If the delay between the matching source/target discontinuity pair differs from the "best match delay" (see description below) by more than 5 minutes, the match is rejected as invalid.

Inevitably, this algorithm will miss a lot of matching discontinuities (representing the same flux tube wall), mostly because they do not meet the requirements due to differences in the IMF observed at the source and target satellite locations, or because there are two or more similar discontinuities within a 3 hour window. The requirements are relatively strict in order to avoid misidentifications. In Step B5, the potential match is checked by comparing the delay to a "best match delay". This is a variable delay found by a procedure that attempts to line up the source and target satellite data series to maximize the cross correlation coefficients. The procedure was introduced by *Weimer et al.* [2002] (though they minimized the mean square error instead and referred to it as "measured delay") and mostly matches up IMF structures quite accurately, providing an independent estimate of the propagation delay for each discontinuity.

5.3.3 Data Sample and Results

To illustrate how the IMF discontinuity algorithms work, Figure 5-4 shows 8 hours of ACE and Geotail IMF data with all discontinuities identified by Algorithm A indicated with vertical lines.

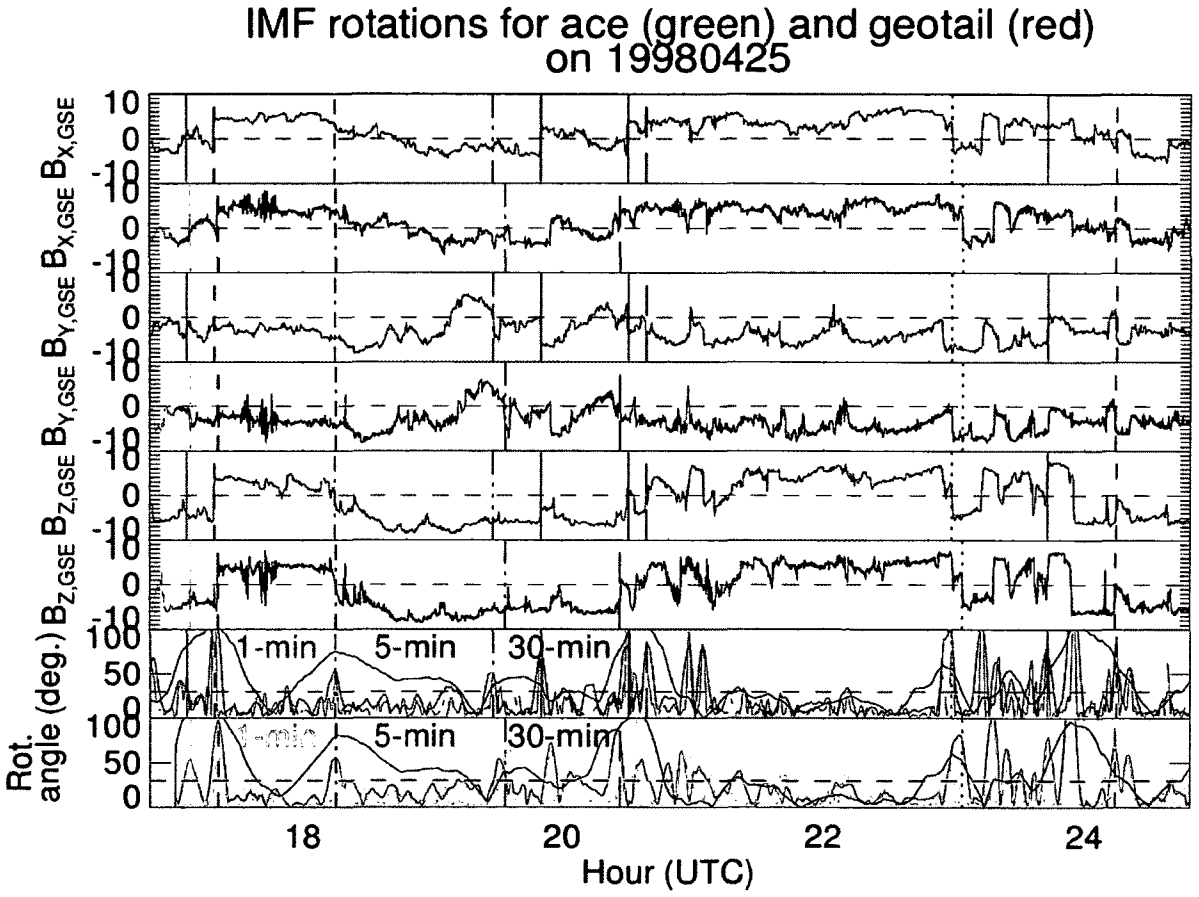

Figure 5-4 Discontinuity Identification Example. 8 hours of Geotail and shifted ACE IMF data with discontinuities identified by Steps A1-A5 indicated by vertical lines. Discontinuities that were found to match in Steps B1-B4 are plotted with a darker color and different line styles. The bottom two plots show the angle between upstream/downstream IMF for 1-, 5- and 30-minute intervals (see Step A1).

Discontinuities that were found to match by Steps B1-B4 have been plotted with a darker color and different line styles for each pair of discontinuities. Geotail data was shifted by

a constant delay (the average delay for matching discontinuities) to make visual comparison easier. The two bottom plots show the angle between before/after IMF for the 1-, 5- and 30-minute averages (Step A1) used in the algorithm with the threshold angle of 30 degrees indicated. This helps explain why some clearly visible discontinuities were bypassed (keeping Steps A4 and A5 in mind). Overall, Algorithm A does a decent job of identifying flux tube boundaries, and visual inspection verifies that the discontinuities matched up by Steps B1-B4 do indeed correspond to the same flux tube boundaries - with one exception. The discontinuity pair occurring around 20.30 UTC appears to be a mismatch. The correct match for the Geotail discontinuity was actually identified in ACE data, but slight differences in the IMF profile (see X-component in particular) caused the wrong discontinuity to be accepted, illustrating why strict requirements are needed to avoid mismatches.

Figure 5-5 shows the same data as Figure 5-4, but this time the delay added to the ACE data is the "best match delay", which is used in Step B5 to identify and reject mismatches.

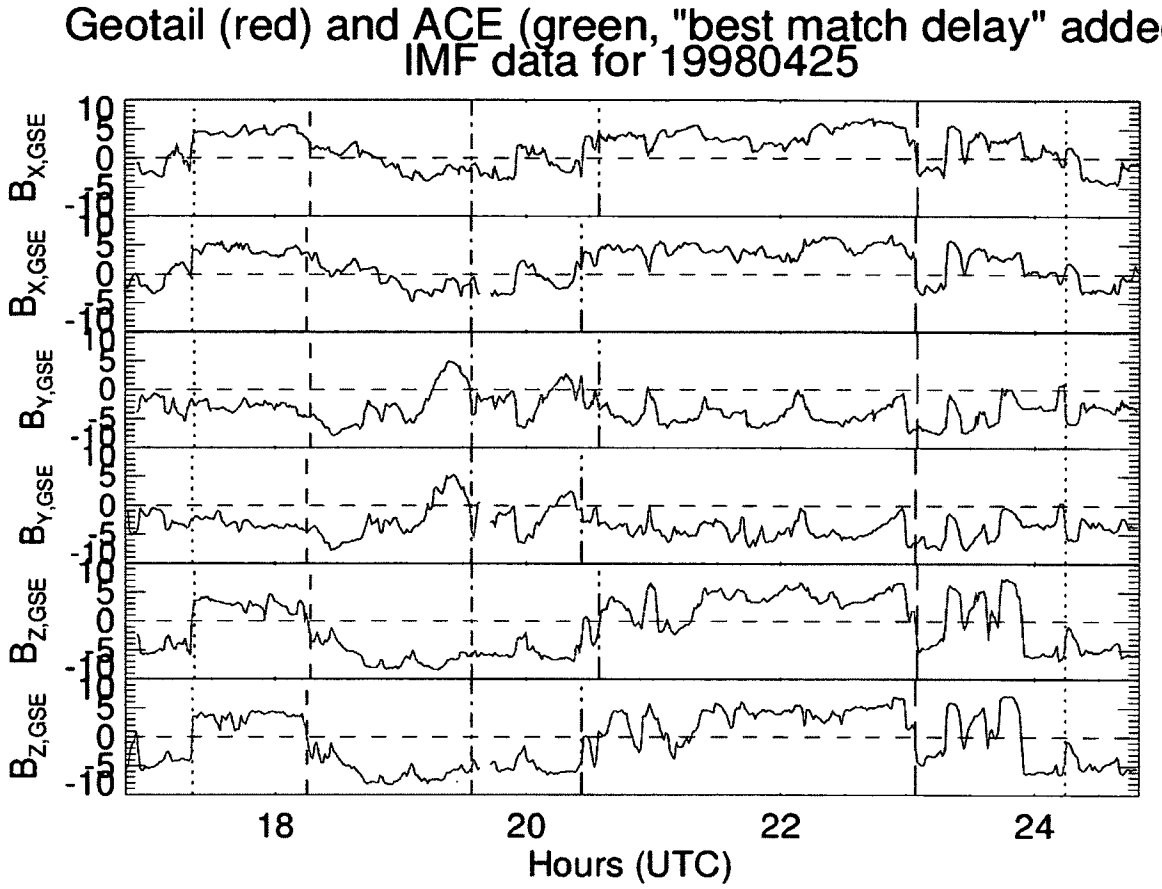

Figure 5-5 Discontinuity Match Check. Geotail and ACE data for same interval as in Figure 5-4, but with ACE data shifted by the maximum correlation delay used in Step B5 to verify matching discontinuities identified by Steps B1-B4. One discontinuity pair (red) was rejected as a mismatch.

Out of the 6 discontinuities 5 were found to agree within less than a minute while the mismatched discontinuity was rejected with a deviation of 7.7 minutes. A visual check of more than 200 discontinuities revealed only a single case where a questionable match passed the best match delay test in Step B5, verifying that Algorithm B provides reliable results on a statistical basis.

Table 5-2 summarizes the results of using above set of algorithms with WIND, IMP-8 and Geotail as target satellites (qualifying solar wind data only), ACE as the source satellite.

Table 5-2 Discontinuity Data Set. Summary of results obtained with the discontinuity identification and comparison algorithms.

	# discontinuities (A1-A5)	# matches (B1-B4)	# verified matches (B5)
Geotail	13,707	5,135	4,453
WIND	4,101	1,451	1,202
IMP-8	5,465	1,795	1,271
Total	23,273	8,381	6,926

For each satellite the set of matching discontinuities verified in Step B5 will be used for the further analysis. The large number of discontinuities identified by Algorithm A that did not have a match in ACE data according to Steps B1-B4 may seem concerning. However, this is mostly a matter of small differences causing different discontinuities to be identified at each satellite and the fairly strict requirements on what constitutes a match.

5.4 Data Propagation Algorithms

Solar wind data is propagated from ACE to a target satellite near the magnetosphere in two different ways: Propagation of discrete events (IMF discontinuities) and propagation of continuous data. Given a method of PFN estimation and a set of parameter values to use, the process of data propagation can be described as a series of steps in either case.

5.4.1 Continuous Propagation

Starting with propagation of continuous data there are quite a few details to consider, and accordingly the algorithm that was used in the end is somewhat complicated. The steps are:

Algorithm C Continuous Propagation

C1) For each ACE data point a PFN estimate is calculated using the given method.

C2) Discard all PFN estimates that do not satisfy the set of relevant conditions (eigenvalue ratio, spreading-angle etc.) except, don't apply PFN-velocity limit angle yet (Step C5).

C3) Fill in PFN gaps created by Step C2 by linear interpolation.

C4) Fill gaps < 30 minutes in ACE IMF and bulk velocity data by linear interpolation.

C5) Calculate the angle between the PFN and bulk velocity for each data point. Discard PFN estimates where this angle exceeds the limit angle.

C6) Fill in PFN gaps created by Step C5 by linear interpolation. This will often reintroduce PFNs with an angle to the bulk velocity exceeding the limit angle.

C7) If applicable, calculate HT frame velocities for propagation. For data points where the uncertainty in the HT velocity exceeds the given threshold σ_{HT}, the HT velocity estimates are discarded. Fill gaps of < 30 minutes by linear interpolation.

C8) Calculate for each data point the propagation time from source to target satellite

$$t_{prop} = \frac{\mathbf{n} \cdot \Delta\mathbf{R}}{\mathbf{n} \cdot \mathbf{V}}$$

where $\mathbf{n}$ is the PFN estimate (unit vector), $\Delta\mathbf{R} = \mathbf{R}_{target}-\mathbf{R}_{source}$ is the separation vector from the source to the target satellite and $\mathbf{V}$ is the propagation velocity. For data points with PFN-velocity angle above the limit angle θ_{lim}, the denominator is replaced by $|\mathbf{v}|\cdot\cos(\theta_{lim})$, rounding the PFN-velocity angle down to the limit angle.

C9) If applicable, remove out-of-sequence data (either "early" or "late" arriving data).

C10) Resample the remaining data points in the propagated data series to match the measured data series from the target satellite. Linear interpolation is used to cover gaps < 30 minutes and averaging is used when several source data points arrive within an interval of a single target data point.

Obviously, the procedure outlined above is just one out of many possible options. It is based on the procedures used in previous work [*Weimer et al.*, 2003; *Weimer and King*, 2008], but with the addition of using a HT frame for data propagation (Step C7) and interpolating PFN gaps caused by too high PFN-velocity angle (Step C6). Many different variations to the procedure were tested for a few different propagation methods and corresponding parameter sets, and the variations resulted in practically identical or worse results when compared to above procedure, with one exception. It is possible to improve some test scores by discarding data points with PFN-velocity angle above the limit angle instead of interpolating PFNs (Step C6) and rounding down the angles (Step C8). This has been done in previous studies, but unfortunately it occasionally causes significant gaps in propagated data, something it's a priority to avoid – both because data gaps are obviously undesirable, but also because it complicates interpretation of results when the propagated data sets differ too much (the extent and position of data gaps differ depending on propagation method and parameter values). It is however worth noting that for some studies it may be better to avoid intervals with high PFN-velocity angles entirely since the propagated IMF is associated with higher uncertainty.

It should be noted that the interpolation of PFNs in Steps C3 and C6 is done by interpolating latitude and longitude angles. The geometrically correct approach would be for interpolated PFNs to follow a great circle between the start/end PFNs. However, not only is interpolating latitude and longitude simpler to implement, more importantly it also helps avoid high latitudes (think of intercontinental flights) and thereby high PFN-velocity angles. A subtle point is that bulk velocities are used to calculate the PFN-velocity angle even when HT frame velocities are used for propagation. This is because HT frame velocities tend to have a larger component along the average magnetic field $\langle \mathbf{B} \rangle$ (see Appendix B). Since most propagation methods require PFNs to be close to

perpendicular to $\langle \mathbf{B} \rangle$, the result is that the PFN to HT velocity angle is larger while the calculated delay is hardly affected. The larger PFN-velocity angle would cause more data points to be discarded when using HT frame velocities, corresponding to applying a lower limit angle. Hence the PFN to bulk velocity angle is always used for consistency. Tests also showed this to improve test scores slightly.

5.4.2 Discrete Propagation (Discontinuities)

In contrast to the case of continuous data propagation, the procedure for propagating discrete events was kept extremely simple:

Algorithm D Discrete Propagation

D1) For a given method and set of parameter values calculate a PFN estimate **n** for one data point at the center of the discontinuity to define the direction of propagation.

D2) Calculate the HT frame velocity for the center point if HT velocities are used for propagation.

D3) Calculate the propagation time from source to target satellite for the discontinuity as

$$t_{prop} = \frac{\mathbf{n} \cdot \Delta\mathbf{R}}{\mathbf{n} \cdot \mathbf{V}}$$

where $\Delta\mathbf{R} = \mathbf{R}_{target} - \mathbf{R}_{source}$ is the separation vector from the source to the target satellite and **V** is the propagation velocity.

The PFN estimate at the center point is used regardless of eigenvalue ratio, PFN-velocity angle etc., so none of the PFN filtering parameters apply to this part of the analysis. There are frequently small gaps in ACE velocity data that are patched by linear interpolation as necessary to make sure that a PFN and velocity estimate can be obtained for all PFN estimation methods and propagation velocities tested.

5.5 Test Score Calculation Algorithms

Finally, algorithms are needed for comparison of propagated and measured data to derive the test scores. There is an algorithm for each of the three different parts of the study: Continuous propagation of general solar wind data, discrete propagation of discontinuities and continuous propagation around the same discontinuities.

5.5.1 Continuous Data (General)

For continuous propagation of general solar wind data only one test score is considered, the mean square error. The algorithm for obtaining this proceeds as follows:

Algorithm E Test Score, Continuous/General

E1) For each target satellite solar wind interval ACE data is propagated starting 2 hours before and ending coincident with the target solar wind interval using Algorithm C.

E2) Smooth both the resampled propagated data series and the measured data series by a 4-point running average (4 points ~ 1 minute).

E3) For each solar wind interval calculate the mean square error between the smoothed propagated/measured data series:

$$\mu_{MSE,INT} = \frac{\sum_{j=1}^{3}\sum_{i=1}^{N_{INT}}\left(B_{(PROP.),i,j} - B_{(MEAS.),i,j}\right)^2}{3N_{INT}}$$

The index i counts over the data points in the series while index j counts over the three GSE X/Y/Z-components. Note that N_{INT} refers to the number of contributing data points in one interval (not the number of intervals) and is used in the final step below.

E4) Calculate the test score μ_{MSE} as a weighted average over all propagated intervals:

$$\mu_{MSE} = \frac{\sum_{i=1}^{M} N_{INT,i}\,\mu_{MSE,INT,i}}{\sum_{i=1}^{M} N_{INT,i}}$$

where M is the number of intervals and N_{INT} is the number of contributing data points for each interval from the previous step.

5.5.2 Discrete Discontinuities

For discrete propagation of discontinuities the only test score considered is $\sigma_{\Delta t}$, the standard deviation in the distribution of predicted minus actual arrival times. The steps in the calculation are:

Algorithm F Test Score, Discrete/Discontinuities

F1) Propagate all IMF discontinuities with an identified match at a target satellite (Algorithm B) from the source (ACE) to the target satellite using Algorithm D.

F2) For each discontinuity calculate the difference between predicted and actual arrival time:

$$\Delta t_{rot} = t_{rot,measured} - t_{rot,propagated}$$

F3) Filter out the 4% of the discontinuities with the highest differences Δt_{rot}.

F4) Calculate the test score $\sigma_{\Delta t}$ as the standard deviation of the distribution of Δt_{rot} for the remaining 96% of the discontinuities:

$$\sigma_{\Delta t} = \sqrt{\frac{\sum_{i=1}^{N} \left(\Delta t_{rot,i} - \mu_{\Delta t}\right)^2}{N-1}}$$

where $\mu_{\Delta t}$ is the mean of the contributing Δt_{rot} values:

$$\mu_{\Delta t} = \frac{\sum_{i=1}^{N} \Delta t_{rot,i}}{N}$$

The standard deviation gives consistent results for distributions that are close to Gaussian given a sufficient number of observations. The distribution of Δt_{rot} is far from Gaussian and has very long tails with numerous observations far outside the bulk of the distribution. These observations have an unreasonably large impact on both the standard deviation and the mean, which is highly undesirable. The quality parameter $\sigma_{\Delta t}$ should reflect how a given method and associated parameter values performs for the majority of observations rather than the outliers. Hence Step F3 was implemented to eliminate the tails, ensuring consistent results. In practice it cuts out observations with Δt_{rot} values that deviate more than about 4-5 standard deviations from the mean. The remaining distribution is still not close to Gaussian. The standard deviation may still function as a reliable indicator for the spread of the observations, but it should be kept in mind that it doesn't translate to the probabilities known from Gaussian distributions with which it is typically associated.

5.5.3 Continuous Data (Discontinuities)

For the analysis of continuous data propagation around discontinuities all three test scores come into play and the associated algorithm inherits elements of Algorithm E and Algorithm F described above to derive μ_{MSE} and $\sigma_{\Delta t}$.

Algorithm G Test Scores, Continuous/Discontinuities

G1) For each IMF discontinuity found by Algorithm B propagate 4 hours of ACE data, from 3 hours before to 1 hour after the event is observed at the target satellite, using Algorithm C. If less than 10 propagated data points fall within the 2-hour interval surrounding the target discontinuity the procedure is interrupted here and no results calculated for that combination of parameter values.

G2) The 4 first Steps A1-A4 in the IMF discontinuity identification algorithm is used to identify discontinuities in the 2-hour interval of propagated data from the source satellite.

G3) For each discontinuity identified, the 1/5/30-minute IMF averages before/after are compared to the corresponding averages for the target discontinuity. All averages must agree to within a threshold (45 degrees for 1- and 5-minute averages, 30 degrees for the 30-minute average) for a match to be accepted.

G4) If one or more discontinuities are found to match the target event, the time difference Δt_{rot} to the closest (in time) source discontinuity is recorded (with Δt_{rot} as defined in F2).

G5) Sort all discontinuities according to how often a match was found in Step G4 (each event is propagated a large number of times with different combinations of parameter values) and filter out the 20% of events with the lowest match occurrence. Then use Steps F3-F4 to calculate $\sigma_{\Delta t}$ for the remaining 80% of events. (Note: Filtering 20% of events is for this step only; Steps G6-G7 use 100% of events.)

G6) Calculate P_{MATCH} as the percentage of observations with a successful match in propagated data:

$$P_{MATCH} = \frac{N_{\Delta t}}{N_{ROT}} \cdot 100$$

where $N_{\Delta t}$ is the number of successful Δt_{rot} observations (G4) and N_{ROT} is the total number of intervals propagated.

G7) Calculate μ_{MSE} for the 2-hour intervals surrounding the target discontinuities (including those where no match was found in Step G4) using Steps E2-E4.

There was some trial and error involved in finding a good method for calculating $\sigma_{\Delta t}$. Difficulty arises because it varies significantly across parameter space which and how many events were found to have a match in Step G4. Using all available matching events for each parameter combination would result in comparing different data sets. Not only may that lead to inconsistent results, but events with a high "failure rate" also have a higher average uncertainty associated with the predicted arrival time, introducing a bias with higher P_{MATCH} leading to higher $\sigma_{\Delta t}$. Mostly it is the same events that fail to match in

Step G4, and it is possible to find a subset of events that have a match for all parameter combinations tested. Using this subset would eliminate above-mentioned inconsistency and bias issues, but has other drawbacks. One problem is the question of statistical significance because the subset represents a small minority of events (typically < 20%) selected by a non-random process. Another is practical: The size of the subset depends on what parts of parameter space is analyzed, being reduced as the volume and/or the number of parameter combinations tested increases. The chosen approach of filtering out the 20% of events with the lowest match rate is a compromise. It retains a large number of events while significantly reducing the difference between data sets used at different points in parameter space. However, as will be seen there are cases where a significant bias is still present and must be taken into account when interpreting $\sigma_{\Delta t}$ results.

6 Results

Main results from the three different parts of the analysis are presented in the following sections. Parts 1 and 2 will contain some explanation and interpretation of results, but some questions will be left unanswered until addressed in Part 3. Comparing the three different test scores adds some information that is helpful to explain the distributions in Part 1 and 2. Two other topics that are deferred to separate sections later are statistical significance and a comparison to results from a previous study [*Weimer and King*, 2008].

6.1 Part 1: Continuous Propagation of General Data

This part of the analysis in principle has the biggest data set to consider, consisting of almost all solar wind data from each of the three target satellites – in the case of WIND restricted to intervals where it is near Earth. Table 5-1 lists the amount of data available from each satellite year by year. All methods and parameters listed in Table 3-1 are tested, using Algorithm C for data propagation and Algorithm E for computing the mean square error μ_{MSE}. It is not computationally manageable to explore all the methods and parameters presented in Table 3-1 in detail for this large data set. Thankfully this is not necessary either. Test runs used only the (relatively) small WIND data set. This is mostly sufficient, and a later section on statistical significance will examine the validity of results. Furthermore, for each method parameter space can be greatly reduced after some initial analysis.

Generally, the approach for each method is to start with a very roughly spaced grid in parameter space, covering a wide range of values to make sure that the volume giving the best results is inside the grid. Ideally a number of values would be picked for each parameter and all combinations of parameter values tested. However, the smallest parameter space to be covered (MVAB and MVAB-0) has 6 dimensions. Even with just 5 values per parameter (except 3 for O_{del}) this adds up to $5^5*3 = 9{,}375$ combinations for each of which a data set needs to be propagated. Given the number of test runs needed

and the processing power available it is in practice necessary to restrict most runs to about 1,000 combinations of parameter values. This corresponds to 3-4 values per parameter ($3^6 = 729$), which is hardly adequate when a wide range of values needs to be covered. To be able to test more values the rigorous approach of testing all combinations must be abandoned. A simple workaround was used: Split the parameter values into two sets and test all combinations within each set, but not across the sets. This is not a compromise without issues, but with carefully chosen parameter values it will suffice for the purpose of providing a rough overview across parameter space. The results from the initial test runs can then be used to justify a much-needed reduction of parameter space, allowing for a finer grid in subsequent test runs.

To help put the results in perspective, Table 6-1 lists the corresponding μ_{MSE} values obtained when using the simple flat delay (PFNs along the negative GSE X-axis) and using a "best match delay" algorithm that attempts to match up source/target data using a variable delay so as to maximize correlation coefficients (same as used in Algorithm B).

Table 6-1 Reference Mean Square Errors. Mean square errors for the three data sets when using classic "flat delay" and "best match delay" respectively.

		Mean Square Error (μ_{MSE})			
		B_X	B_Y	B_Z	Mean
Geotail	"Flat Delay"	3.411	3.723	4.830	3.988
	"Best Match"	2.208	2.259	2.581	2.349
WIND	"Flat Delay"	3.455	3.830	5.061	4.115
	"Best Match"	2.024	2.213	2.517	2.251
IMP-8	"Flat Delay"	3.818	4.015	4.778	4.204
	"Best Match"	2.511	2.459	2.496	2.489

It should be noted that even though μ_{MSE} is the only indicator of relative performance that will be presented, correlation coefficients and coverage of propagated data were also

monitored throughout the analysis. Results for correlation coefficients are very similar and have been left out for simplicity. Monitoring of propagated data coverage resulted in numerous adjustments to the data propagation algorithms and PFN estimation methods so as to handle gaps efficiently and minimize gaps in propagated data. Importantly this also minimizes differences between the propagated data sets (in terms of location and extent of gaps) that each method and parameter value combination produces. Such differences easily become a problem because filters are designed to remove data associated with higher uncertainty. If gaps caused by filtering were not properly interpolated, using stricter filtering could produce better results simply by means of leaving out data, introducing a bias that would complicate interpretation. In the end there appeared to be no such bias left in the results, except in cases where extreme combinations of parameter values inevitably result in significantly reduced coverage. Such parameter combinations are not suitable for general data propagation and are filtered out by applying a minimum requirement for propagated data coverage (98%).

6.1.1 MVAB-0

Starting with the MVAB-0 method, Table 6-2 lists the two sets of values chosen for an initial test run. For each combination of parameter values in each set Algorithm C was used to propagate ACE IMF data to match the WIND data set (3,238 hours) and mean square errors were calculated using Algorithm E.

Table 6-2 MVAB-0 Initial Parameter Values. The 2 sets of parameter values used for initial test of MVAB-0 method.

Parameter	Value Set 1	Value Set 2
# MVA points (N_{MVA})	3, 13, 51, 201	7, 25, 101
Min. eigenvalue ratio (r_{ev})	1, 4, 16	1, 2, 8, 32
# HT averaging points ($N_{HT,P}$)	0 (bulk), 3, 7, 25, 101	0 (bulk), 3, 13, 51, 201
Uncertainty in $\mathbf{V}_{HT}$ ($\sigma_{HT,P}$)	1, 4, 16, ∞	2, 8, 32, ∞
PFN-velocity limit angle (0_{lim})	65, 75, 85	70, 80
Remove option (O_{del})	"Early", "Late", "None"	"Early", "Late", "None"

There is no simple way to display the test scores across the multi-dimensional parameter space since a single plot can only show results as a function of 2 variable parameters. Using Plot a) in Figure 6-1 as an example the two parameters considered are N_{MVA} and r_{ev}. For each combination of values (N_{MVA}, r_{ev}) the data set has been propagated many times, one for each combination of values of the other four parameters. Plot a) then shows the best test score (minimum μ_{MSE}) obtained for each (N_{MVA}, r_{ev}) combination.

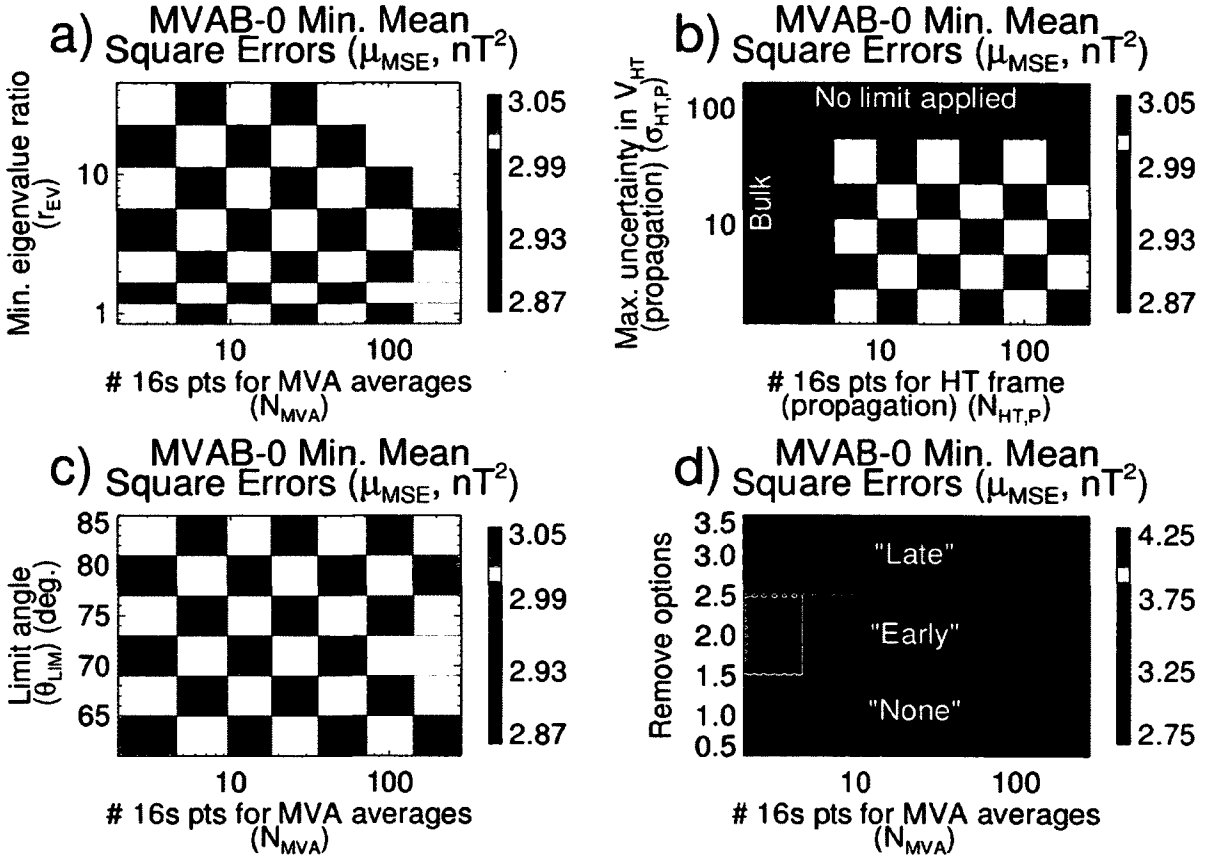

Figure 6-1 Part 1 MVAB-0 Initial Results. Minimum values of μ_{MSE} when using the parameter values listed in Table 6-2 and comparing propagated ACE data to the WIND solar wind data set. Plot a) shows results obtained as a function of N_{MVA} and r_{ev}, in Plot b) as a function of $N_{HT,P}$ and $\sigma_{HT,P}$, in Plot c) as a function of N_{MVA} and θ_{lim} and in Plot d) as a function of N_{MVA} and O_{del}.

While these plots aren't pretty they represent well the very rough overview the initial test runs give. The white slots represent combinations that were not tested, except for the two missing data points in Plot a). Generally, using a higher number of data points for MVA result in lower eigenvalue ratios, so the combination of using high N_{MVA} and high r_{ev} result in extended intervals where no PFN estimates are accepted, causing significant gaps in propagated data coverage. Accordingly all results for those combinations were filtered out due to the minimum coverage requirement.

A first thing to note is that the color scales were kept the same in Plots a) - c) but changed in Plot d), which shows that either method for removing out-of-sequence data

consistently gives significantly higher mean square errors than removing no out-of-sequence data, regardless of values used for other parameters. This behavior is consistent for other methods as well and allows for reducing parameter space by a factor of 3. The results are so unambiguously in favor of removing no out-of-sequence data that there is no need to keep testing the two other options. One obvious problem with the "early"/"late" options is that a few spurious data points with propagation delay estimates that are significantly off will cause a much larger amount of good data to simply be erased. It was attempted to mitigate this problem by applying a filter to remove such data points and reduce the amount of data erased by the "early"/"late" filter options. Specifically, for each data point the 20 closest data points in both the source and the propagated data series were considered. If these two sets had less than 5 points in common the point was considered isolated, potentially spurious, and was filtered out from the propagated series. While this modification helped μ_{MSE} and $\sigma_{\Delta t}$ scores some for the "early"/"late" options they remained worse than when doing no filtering, and so this approach was abandoned.

Plots a) – c) reveal the relative importance of the remaining 5 parameters. The number of MVA averaging points N_{MVA}, the minimum eigenvalue ratio r_{ev} and the limit angle θ_{lim} all have a clear impact on test scores while the choice of $N_{HT,P}$ for HT propagation velocities is less important and the HT uncertainty limit $\sigma_{HT,P}$ hardly matters at all. Based on these results the parameter space was further reduced for subsequent test runs by choosing a single value for $N_{HT,P}$ and not applying $\sigma_{HT,P}$, effectively leaving a much more manageable 3-dimensional parameter space. The parameters $N_{HT,P}$ and $\sigma_{HT,P}$ will be revisited to examine closer what effect they do have, small as it is.

Figure 6-2 shows results as a function of (N_{MVA}, r_{ev}) and (N_{MVA}, θ_{lim}) using ($N_{HT,P}$, $\sigma_{HT,P}$, O_{del}) = (3, ∞, "none").

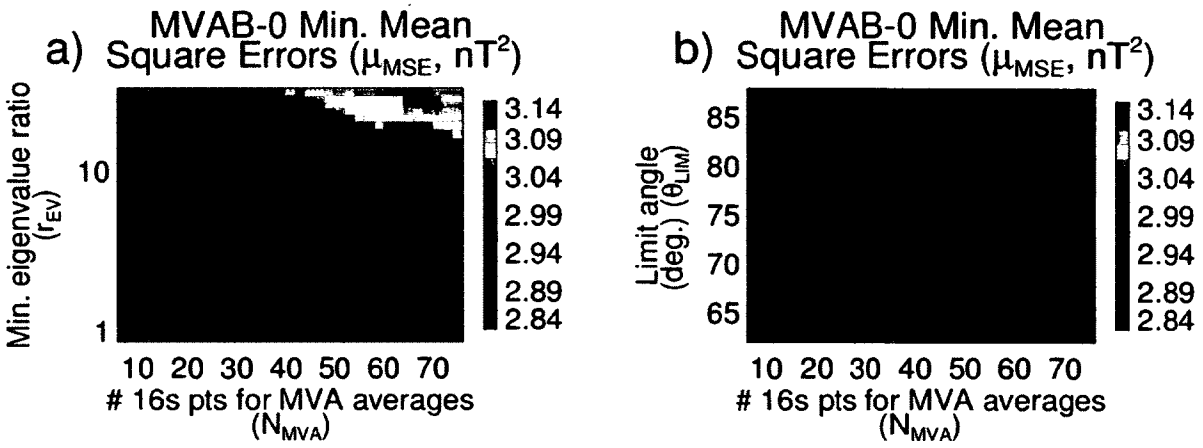

Figure 6-2 Part 1 MVAB-0 Detailed Results. Minimum values of μ_{MSE} as a function of (N_{MVA}, r_{ev}) (a) and (N_{MVA}, θ_{lim}) (b) when comparing propagated ACE data to the WIND solar wind data set.

The lowest mean square error was found to be 2.862 nT^2 at parameter values (N_{MVA}, r_{ev}, θ_{lim}) = (31, 5, 79°). There is a range of values for the parameters that give similar results, and given the "noise" in these plots the particular values that came out on top in this test should be considered specific to this data set. However, qualitatively the distribution of μ_{MSE} should be quite similar for other sufficiently large data sets (see Section 6.6 on statistical significance).

Returning to $N_{HT,P}$ and $\sigma_{HT,P}$, Figure 6-3 shows the distribution of μ_{MSE} as a function of these two variables when using the parameter values (N_{MVA}, r_{ev}, θ_{lim}) = (31, 5, 79°) that were found to give best results in above test run.

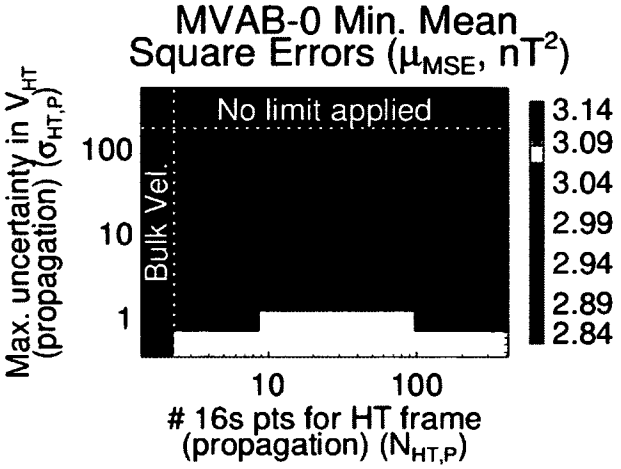

Figure 6-3 Part 1 MVAB-0 HT Results. Minimum values of μ_{MSE} obtained as a function of $N_{HT,P}$ and $\sigma_{HT,P}$ when using (N_{MVA}, r_{ev}, θ_{lim}) = (31, 5, 79°) and comparing propagated ACE data to the WIND solar wind data set.

Note that the color scale is kept the same as in Figure 6-2. The white area at the bottom represents combinations where too much data was filtered out, causing gaps in propagated data and hence failing to meet the minimum coverage requirement. Lowest μ_{MSE} is obtained with either bulk velocities or $N_{HT,P} = 3$, the latter being marginally better. The advantage (if any) gained by applying $\sigma_{HT,P}$ is insignificant. Tests like this have been done for other methods and parameter values, and the results have certain common features. Best results are obtained with either bulk velocities, $N_{HT,P} = 3$ or $N_{HT,P} > 100$ with little variation as $N_{HT,P}$ is increased beyond 100, and there is little or no advantage to applying $\sigma_{HT,P}$. As a consequence the parameter $\sigma_{HT,P}$ will be dropped from further consideration, and it is only necessary to test 3 different propagation velocities (bulk, $N_{HT,P} = 3$ and $N_{HT,P} = 101$). While the dependence on $N_{HT,P}$ is statistically significant, the difference between best/worst $N_{HT,P}$ is about the same magnitude as the random variations in Figure 13 resulting from varying (N_{MVA}, r_{ev}, θ_{lim}) slightly. In Appendix B HT velocity data samples are shown, illustrating why using HT frames and the particular choice of $N_{HT,P}$ has little effect. While HT velocities may deviate significantly from bulk velocities, HT frames move close to parallel to the magnetic field in the plasma rest frame. Since the MVAB-0 method produces PFNs perpendicular to

$\langle \mathbf{B} \rangle$ by design, the velocity component along PFNs is close to the same for bulk and HT frame velocities. The uncertainty in $\mathbf{V}_{HT}$ is generally small and also mainly along the magnetic field (see Appendix B), and it is then no surprise that applying the parameter $\sigma_{HT,P}$ is practically useless.

6.1.2 MVAB

Previous studies have shown that there are considerable problems using the MVAB method to estimate PFNs for solar wind propagation [*Weimer*, 2004; *Knetter,* 2005]. Nevertheless the method was tested for completeness and to put the poor results into perspective. The MVAB method has the same 6 parameters as the MVAB-0 method, and in a similar manner an initial test run showed that 3 of the parameters can be eliminated by choosing ($N_{HT,P}$, σ_{HT}, O_{del}) = (3, ∞, "none"), leaving only 3 parameters to investigate. However, for these the results come out very different. Figure 6-4 shows results as a function of (N_{MVA}, r_{ev}) and (N_{MVA}, θ_{lim}), respectively.

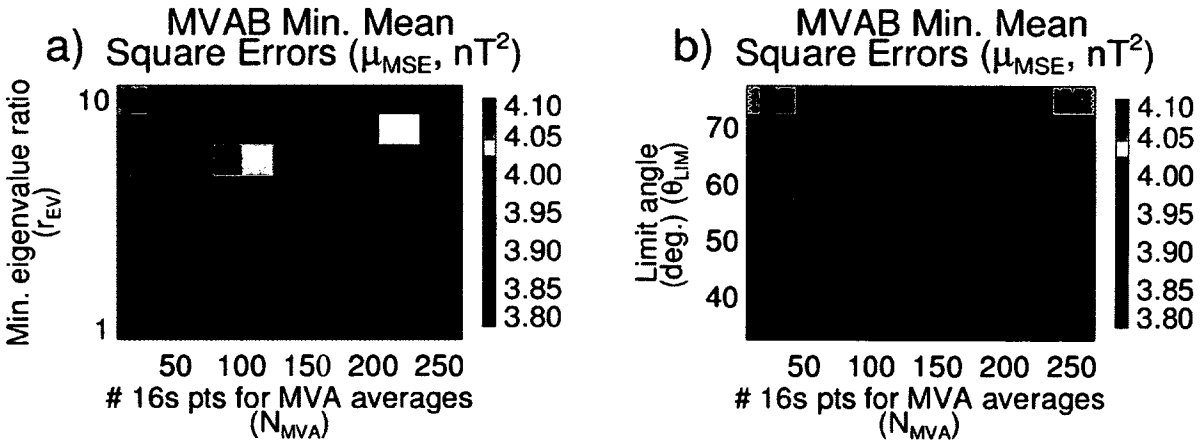

Figure 6-4 Part 1 MVAB Results. Minimum values of μ_{MSE} obtained as a function of (N_{MVA}, r_{ev}) (a) and (N_{MVA}, θ_{lim}) (b) when comparing propagated ACE data to the WIND solar wind data set.

The MVAB method works best with high N_{MVA} (70-110), low eigenvalue ratio (< 2) and a much lower limit angle (45°-55°). The results are considerably worse than for MVAB-0 with a minimum mean square error of 3.817 nT^2 found at (N_{MVA}, r_{ev}, θ_{lim}) = (91, 1.3, 52°) (from a separate, higher resolution test run than that shown in Figure 6-4). This is not much better than using simple flat delay and the very low limit angle suggests that the method produces poor PFN estimates that are better filtered out (interpolated) a lot of the time.

Figure 6-5 shows the distribution of PFN estimates produced by the MVAB method for a whole year (1999).

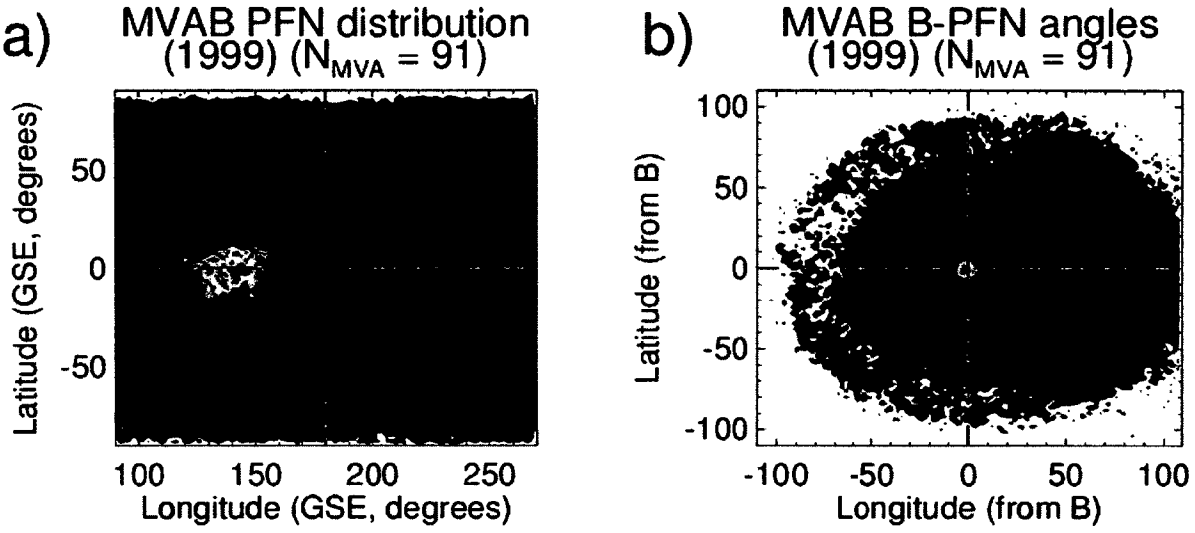

Figure 6-5 Part 1 MVAB PFN Distribution. Distribution of directions of MVAB PFN estimates relative to the negative X_{GSE}-axis (a) and relative to the magnetic field (b).

Plot a) uses a spherical coordinate system converted from GSE coordinates, showing the half of the sphere pointing away from the Sun. The PFNs produced are concentrated around the Parker Spiral direction (compare this to Figure B-1 in Appendix B showing the distribution of B in the same format), suggesting that they are close to parallel to **B**. Plot b) confirms this, showing PFN directions relative to **B**. In this and similar plots to follow, **B** refers to the measured value at the single data point where the PFN is

estimated. The distance from the origin is the angle between PFNs and **B** so that PFNs perpendicular to **B** are located on a circle of radius 90 centered at the origin, and the X- and Y-axes are aligned with a local GSE longitude-latitude grid as seen from **B**. **B**-vectors pointing towards the Sun were reversed since the same was done for PFNs, which are defined to point away from the Sun. PFNs are highly concentrated in the direction of **B** with a small density enhancement close to perpendicular to **B**.

This explains the poor performance and points to an issue that has been neglected. The focus of this project is large-scale solar wind structures, but the small-scale structure still plays an important role, as it is the dominant source of fluctuations inside flux tubes and hence governing for what PFN estimates the different methods will produce a lot of the time. Remembering that PFNs are in the direction of minimum variance in **B**, Plot b) in Figure 6-5 shows that small-scale fluctuations in **B** are strongly dominated by perturbations perpendicular to **B**, a property of shear Alfvén waves (see Appendix B). Indeed, if this is what they are the MVAB method is actually highly successful finding accurate PFN estimates, but they would apply to the phase fronts of Alfvén waves travelling along the magnetic field and not the large-scale phase fronts that are relevant for propagation over long distances. The MVAB method is simply the wrong tool for the job. The small population of PFNs that are close to perpendicular to **B** presumably represent large-scale structures, leaving open the possibility that we may see a different distribution and better performance when doing discrete propagation of IMF discontinuities.

6.1.3 MVAE

Continuing with the MVAE method there are now 8 variable parameters to deal with, 6 of them being the same as for MVAB/MVAB-0 and the two extra being the HT frame parameters associated with finding a reference frame for the electric field. As argued previously 2 parameters can be disregarded: O_{del} (removing no out-of-sequence data gives better results) and $\sigma_{HT,P}$ (applying this limit has little or no benefit). Again bulk velocities or $N_{HT,P} = 3$ works best for propagation. Furthermore, initial test runs show that

using only 3 data points to find a HT reference frame for the electric field ($N_{HT,E} = 3$) and applying no uncertainty limit $\sigma_{HT,E}$ unambiguously gives the best results. Thanks to this it is once again possible to focus analysis on the three parameters N_{MVA}, r_{ev} and θ_{lim}, and Figure 6-6 summarizes the results of a test run using a range of values for each of these variables.

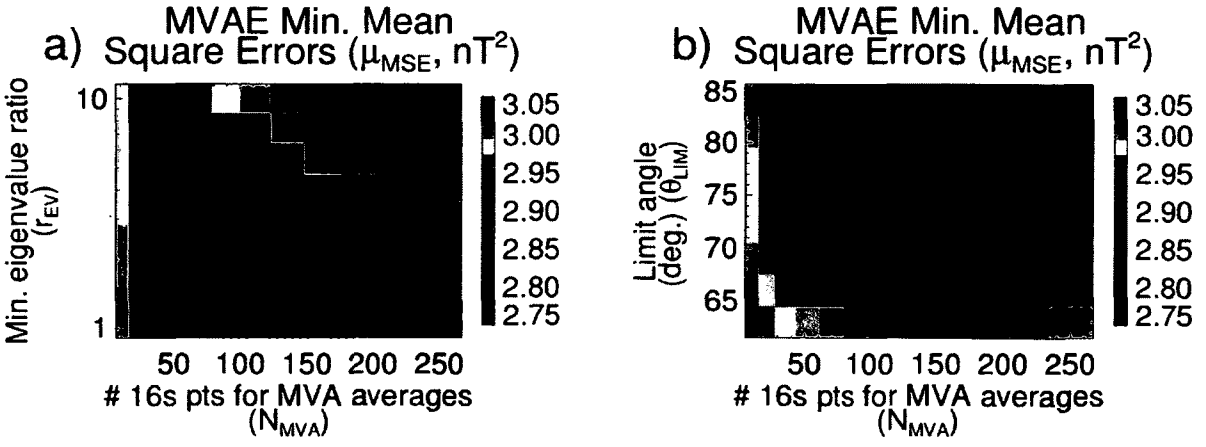

Figure 6-6 Part 1 MVAE Results. Minimum values of μ_{MSE} obtained as a function of (N_{MVA}, r_{ev}) (a) and (N_{MVA}, θ_{lim}) (b) when comparing propagated ACE data to the WIND solar wind data set.

The MVAE method works best using a high number of data points (100-200) for the MVA, a low minimum eigenvalue ratio (< 2) and a limit angle close to 80°. A higher resolution test run found a minimum μ_{MSE} of 2.775 nT^2 at (N_{MVA}, r_{ev}, θ_{lim}) = (127, 1.3, 79°) and using bulk velocities for propagation. Using these parameter values, Figure 6-7 shows how results depend on the HT parameters ($N_{HT,E}$, $\sigma_{HT,E}$) for the electric field reference frame, justifying the choice of reducing parameter space by testing only for ($N_{HT,E}$, $\sigma_{HT,E}$) = (3, ∞).

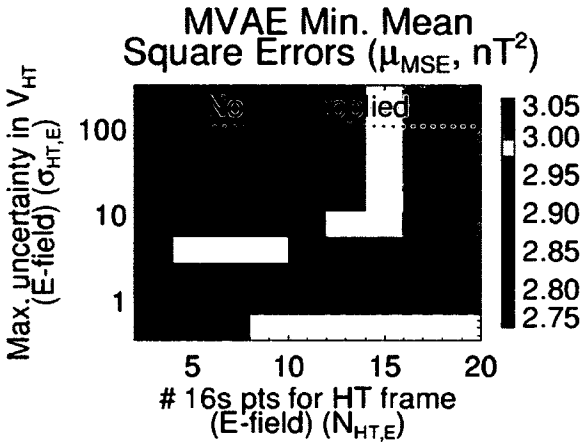

Figure 6-7 Part 1 MVAE HT Results. Minimum values of μ_{MSE} obtained as a function of $N_{HT,E}$ and $\sigma_{HT,E}$ when comparing propagated ACE data to the WIND solar wind data set, using (N_{MVA}, r_{ev}, θ_{lim}) = (127, 1.3, 79°).

The MVAE method clearly does not suffer from the same issues the MVAB method does and even gives slightly better test scores than MVAB-0. Figure 6-8 shows the distribution of PFNs produced by the MVAE method for a year's worth of data (1999) in the same format as Figure 6-5.

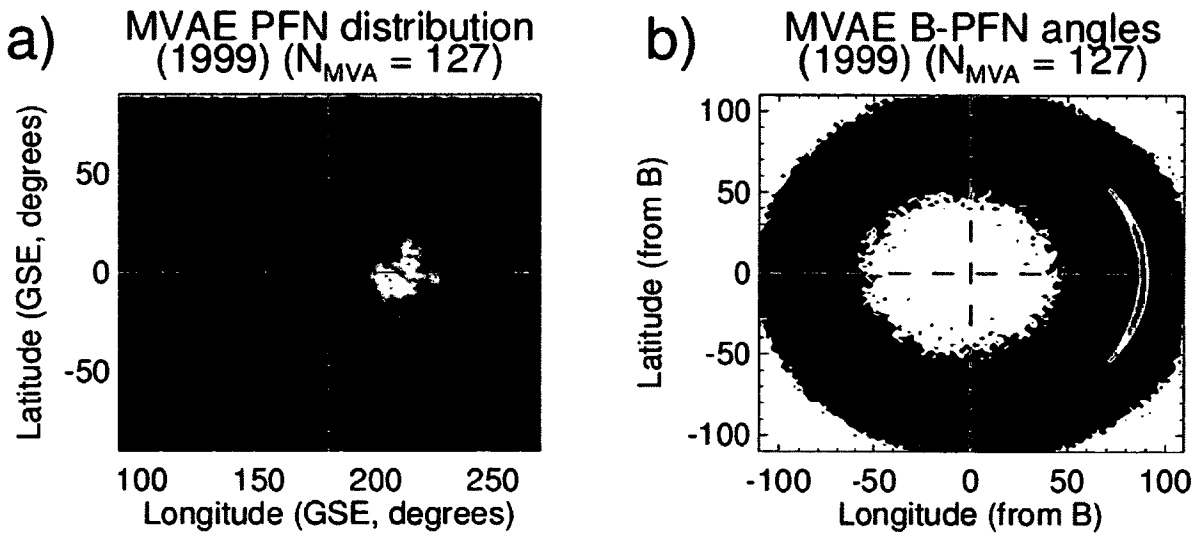

Figure 6-8 Part 1 MVAE PFN Distribution. Distribution of directions of MVAE PFN estimates relative to the negative X_{GSE}-axis (a) and relative to the magnetic field (b).

By default PFNs are quite close to perpendicular to **B** (~82% within 80-10θ degrees), making them good proxies for large-scale phase fronts in the solar wind. To understand why this is the case, consider the velocity and magnetic field as a superposition of large, constant background components $\mathbf{V}_0$ and $\mathbf{B}_0$ and small, time-variable perturbation quantities $\delta\mathbf{V}(t)$ and $\delta\mathbf{B}(t)$. Then derive the time-dependent component of the electric field:

$$\begin{aligned} &\mathbf{E} = -\left(\mathbf{V}_0 + \delta\mathbf{V}(t)\right)\times\left(\mathbf{B}_0 + \delta\mathbf{B}(t)\right) \\ &\Rightarrow \delta\mathbf{E}(t) = -\delta\mathbf{V}\times\mathbf{B}_0 - \mathbf{V}_0\times\delta\mathbf{B} - \delta\mathbf{V}\times\delta\mathbf{B} \end{aligned} \tag{6.1}$$

The variable component $\delta\mathbf{E}$ is dominated by the two terms involving the background components $\mathbf{B}_0$ and $\mathbf{V}_0$. Not only are $\delta\mathbf{V}$ and $\delta\mathbf{B}$ assumed to be small, they also tend to be proportional (see Appendix B), which further minimizes their cross product. On the other hand they tend to be perpendicular to $\mathbf{V}_0$ and $\mathbf{B}_0$, which are necessarily close to proportional because the reference frame is a HT frame that minimizes the electric field. Hence $\delta\mathbf{E}$ lies close to a plane perpendicular to $\mathbf{B}_0$, and the direction of maximum variance will likewise be close to this plane.

6.1.4 MVAE-0

Given that the MVAE method already produces PFNs close to perpendicular to the magnetic field, the added requirement $\langle\mathbf{B}\rangle\cdot\mathbf{n} = 0$ is not expected to change much. Indeed, initial tests show that parameter space can be reduced in the same way, leaving only the 4 variable parameters N_{MVA}, r_{ev}, θ_{lim} and $N_{HT,P}$ with only two options to test for $N_{HT,P}$: Using bulk velocities or $N_{HT,P} = 3$ for propagation. For these variables the picture is also much the same as the distribution of results in Figure 6-9 shows.

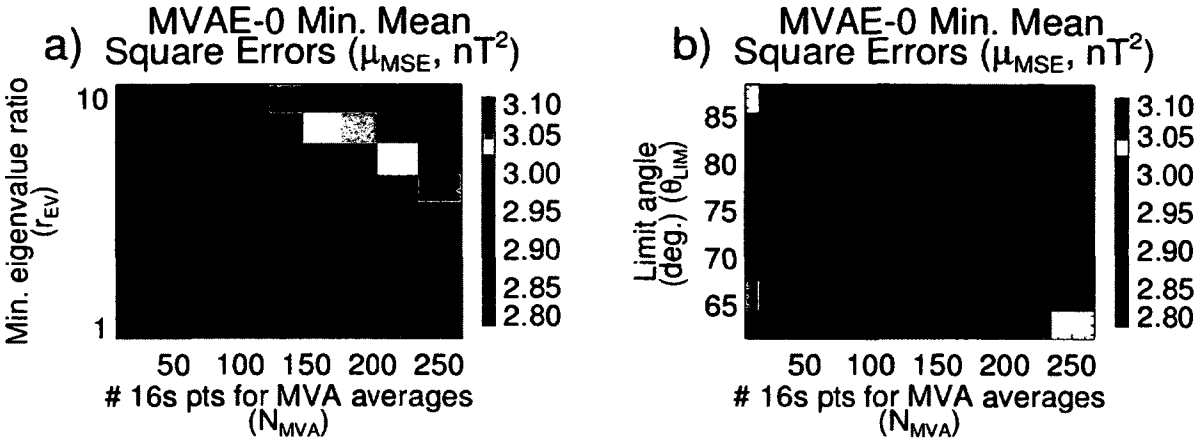

Figure 6-9 Part 1 MVAE-0 Results. Minimum values of μ_{MSE} obtained as a function of (N_{MVA}, r_{ev}) (a) and (N_{MVA}, θ_{lim}) (b) when comparing propagated ACE data to the WIND solar wind data set.

A higher resolution test run found a lowest mean square error of 2.826 nT^2 at (N_{MVA}, r_{ev}, θ_{lim}) = (125, 1.2, 79°) and using bulk velocities for propagation, putting it between MVAE and MVAB-0 in terms of the test score. The simple assumption that PFNs are perpendicular to the mean magnetic field is a very good approximation most of the time, and enforcing it can make even a "wrong tool" like the MVAB method produce good results. However, best results are obtained when allowing some deviation from this requirement, and the MVAE/MVAE-0 results presented here provide an example of that.

All in all, the results for the 4 different MVA methods motivated the decision to introduce the CPMV-E method. As previously mentioned the CPMV-B method has given superior test results in previous studies, and given that the MVAE method gives better test scores than MVAB-0 on the larger data set used in this study it is then an obvious next step to combine the CP and MVAE methods to see if that may improve on the results obtained with the CPMV-B method.

6.1.5 CP

The CP method has 8 variable parameters, 2 of which (O_{del}, $\sigma_{HT,P}$) can be disregarded as for other methods. The choice of propagation velocities is also relatively unimportant,

and bulk velocities can be used as a starting point for simplicity, temporarily eliminating the parameter $N_{HT,P}$. However, for the remaining 5 parameters the distribution of results is significantly more complicated. Figure 6-10 shows test scores from the first test runs covering an extensive volume of parameter space with low resolution.

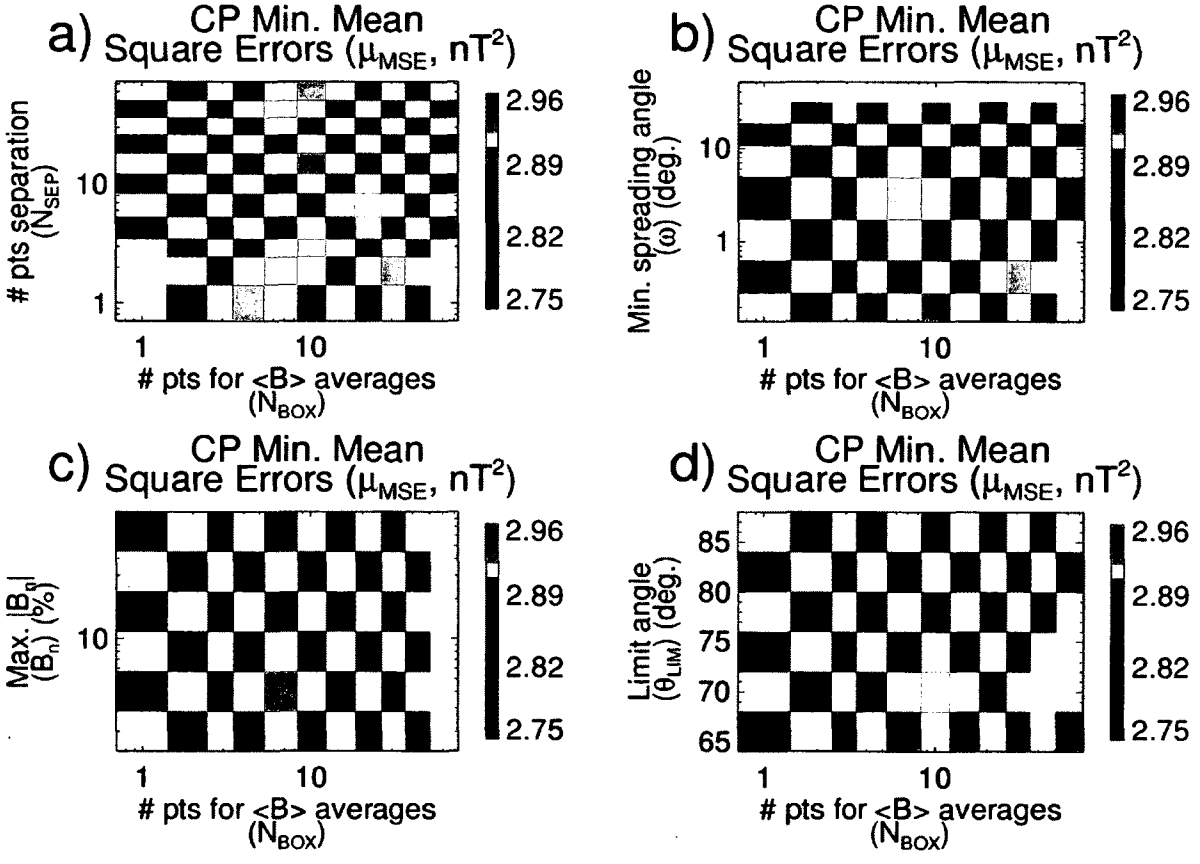

Figure 6-10 Part 1 CP Initial Results. Minimum values of μ_{MSE} (a) when comparing propagated ACE data to the WIND solar wind data set. Results are shown as a function of parameter pairs (N_{box}, N_{sep}) (a), (N_{box}, ω) (b), (N_{box}, B_n) (c) and (N_{box}, θ_{lim}) (d).

The distribution has two distinct minima. One is $N_{box} = 1$, high N_{sep}, high ω and high B_n and the other is $N_{box} \sim 25$, $N_{sep} = 1$ and $\omega \sim 1°$ (relatively independent of B_n). Both minima occur with a limit angle in the upper 70s. Better resolution test runs of these two areas revealed that the better scores are obtained with $N_{box} = 1$ (as Figure 6-10 suggests),

and

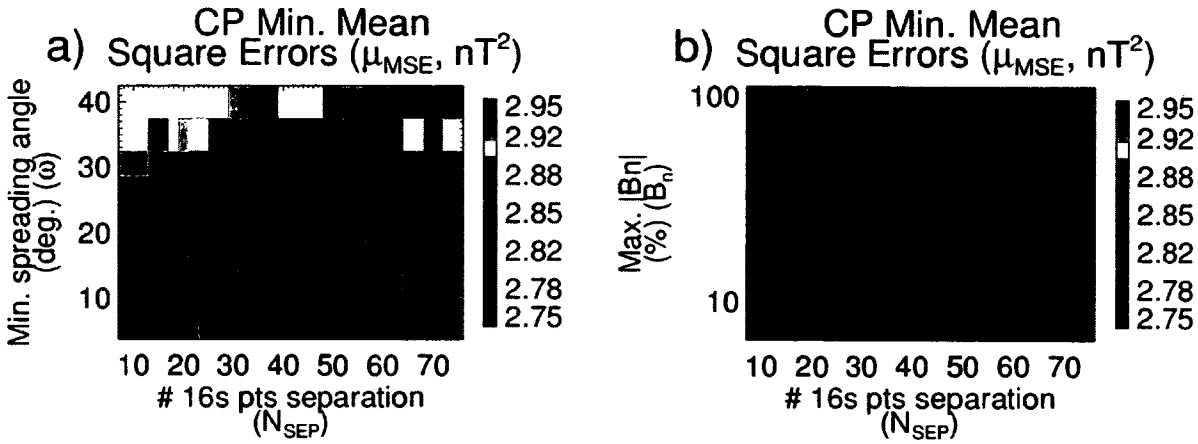

Figure 6-11 shows results when using $\theta_{lim} = 78°$.

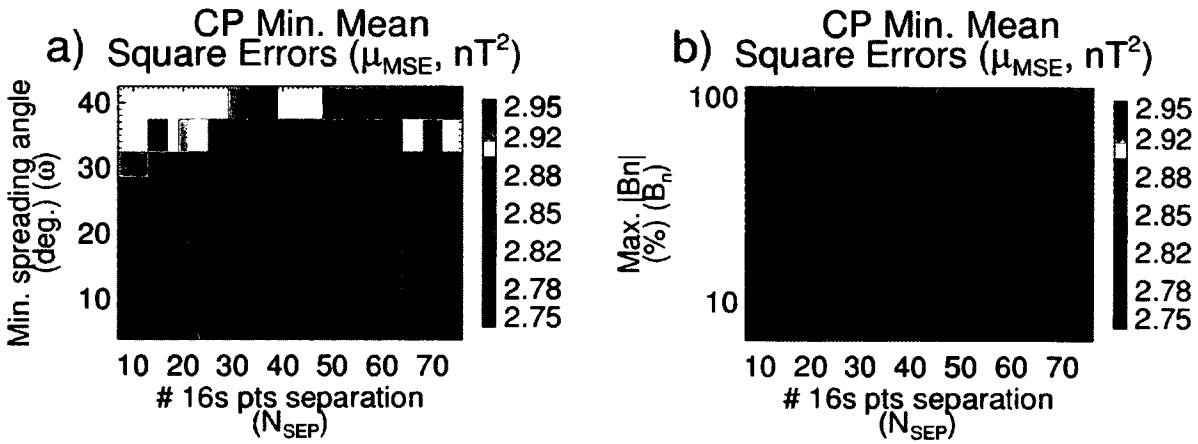

Figure 6-11 Part 1 CP Detailed Results. Minimum values of μ_{MSE} obtained as a function of (N_{sep}, ω) (a) and (N_{sep}, B_n) (b) when using (N_{box}, $N_{HT,P}$, θ_{lim}) = (1, bulk, 78°) and comparing propagated ACE data to the WIND solar wind data set.

After testing other limit angles and HT velocities for propagation the best test score found was $\mu_{MSE} = 2.770$ nT^2 at (N_{box}, N_{sep}, ω, B_n, $N_{HT,P}$, θ_{lim}) = (1, 22, 14°, 20%, 101, 79°), but except for $N_{box} = 1$ there is a range of values for each parameter for which the minimum could just as well have occurred.

The distribution of PFNs produced by the CP method is similar to that shown for the MVAE method (Figure 6-8) though PFNs stay closer to perpendicular to **B**. PFNs are perpendicular to upstream/downstream quantities $\mathbf{B}_u$ and $\mathbf{B}_d$, which also makes them quite close to perpendicular to the center value **B** most of the time.

6.1.6 ED

The ED method as a starting point has no less than 10 variable parameters. Deleting no out-of-sequence data (O_{del} = "none") and omitting $\sigma_{HT,P}$ eliminates 2 of them, and the parameter $N_{HT,P}$ can also be ignored initially, using bulk velocities while uncovering dependence on other parameters. It also turns out that best results are unambiguously obtained when using $(N_{HT,E}, \sigma_{HT,E}) = (3, \infty)$ just as it was the case for the other electric field methods (MVAE, MVAE-0). This leaves a parameter space very similar to that of the CP method with the minimum spreading-angle ω having been replaced by the minimum ratio r_E (see Table 3-1 and Table 3-2). Figure 6-12 shows test results using a sparse grid covering a large volume of the remaining 5-dimensional parameter space.

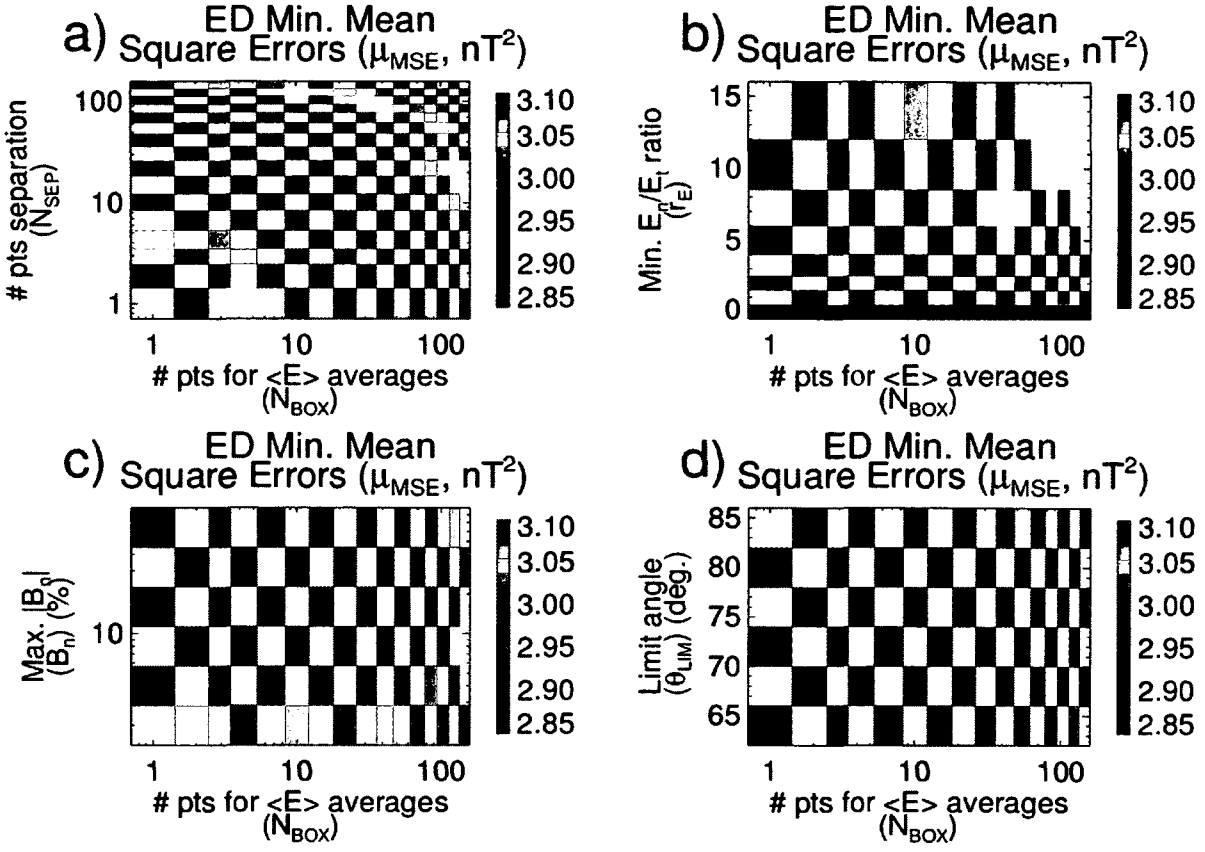

Figure 6-12 Part 1 ED Initial Results. Minimum values of μ_{MSE} (a) when comparing propagated ACE data to the WIND solar wind data set. Results are shown as a function of parameter pairs (N_{box}, N_{sep}) (a), (N_{box}, r_E) (b), (N_{box}, B_n) (c) and (N_{box}, θ_{lim}) (d).

Similar to the CP method, the ED method has 2 different minima for the μ_{MSE} distribution, one with low N_{box} and high N_{sep} and vice versa for the other. Further test runs confirmed that best scores are obtained with $N_{sep} = 1$, and Figure 6-13 shows results for a test run with (N_{sep}, $N_{HT,P}$, B_n) = (1, bulk, 30%) and a higher resolution grid for N_{box}, r_E and θ_{lim}.

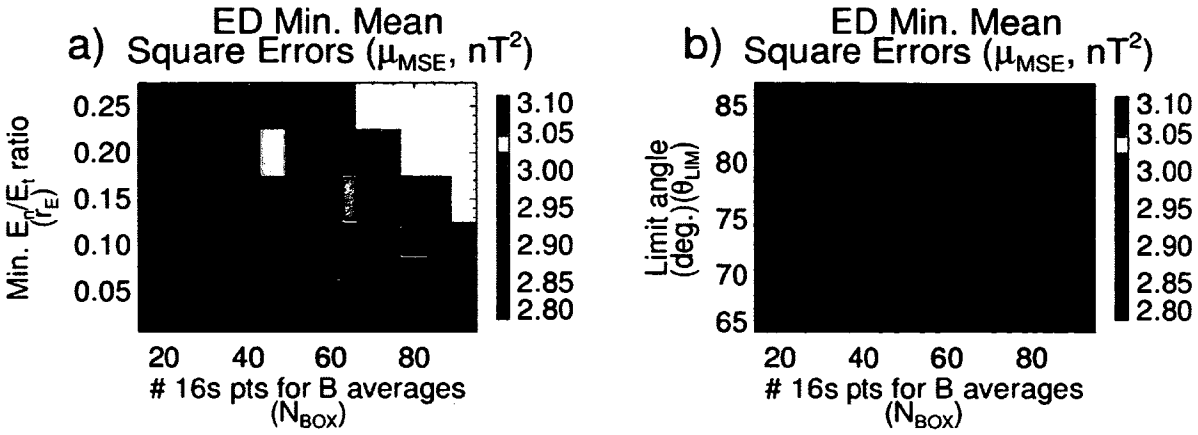

Figure 6-13 Part 1 ED Detailed Results. Minimum values of μ_{MSE} obtained as a function of (N_{box}, r_E) (a) and (N_{box}, θ_{lim}) (b) when using (N_{sep}, B_n, $N_{HT,P}$) = (1, 30%, bulk) and comparing propagated ACE data to the WIND solar wind data set.

A minimum μ_{MSE} of 2.841 nT^2 was found at (N_{box}, r_E, θ_{lim}) = (62, 0.025, 77°), similar to the best score obtained with MVAB-0 (2.862 nT^2). The ED PFN distribution for N_{sep} = 1 and high N_{box} is qualitatively very similar to that of the MVAE method (Figure 6-8) except more spread out. The upstream/downstream $\langle \mathbf{E} \rangle$ vectors are perpendicular to upstream/downstream $\langle \mathbf{B} \rangle$ and almost identical for N_{sep} = 1 and high N_{box}. The difference vector will then be close to perpendicular to **B** and have small magnitude, which explains why such a low value of r_E is required too.

6.1.7 CPMV-B

The CPMV-B method also has 10 variable parameters, several of which can be eliminated readily. As usual only one option for O_{del} and $\sigma_{HT,P}$ needs to be considered, and for $N_{HT,P}$ the best results were obtained using a high value ($N_{HT,P}$ = 101 will be used). Fortunately it turns out that the CP parameters N_{box} and N_{sep} can be eliminated too because μ_{MSE} decreases monotonously as both are lowered all the way to the lowest values. N_{box} = 1 and N_{sep} = 2 will be used. With such small separation between the $\langle \mathbf{B} \rangle$ vectors for the cross product, spreading-angles are mostly close to zero and the minimum

spreading-angle ω must likewise be very low. In fact there is no significant benefit from applying this filter at all, allowing elimination of another variable. For N_{MVA} a high value works best, and correspondingly a low minimum eigenvalue ratio must be used. Again, r_{ev} may actually be omitted altogether as it doesn't improve results significantly applying it. This leaves only 3 variables for which a range of values needs to be tested: N_{MVA}, Φ_{diff} (max. angle between CP/MVAB-0 PFNs) and θ_{lim}. Figure 6-14 shows results of a test run for these 3 parameters.

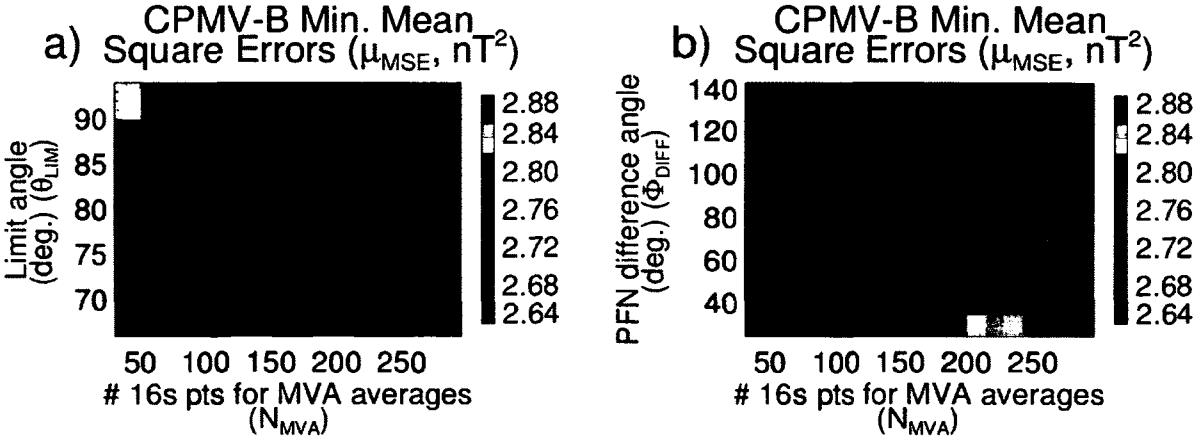

Figure 6-14 Part 1 CPMV-B Results. Minimum values of μ_{MSE} obtained as a function of (N_{MVA}, θ_{lim}) (a) and (N_{MVA}, Φ_{diff}) (b) when using (N_{box}, N_{sep}, r_{ev}, ω, $N_{HT,P}$) = (1, 2, 1, 0, 101) and comparing propagated ACE data to the WIND solar wind data set.

A test run with a finer grid found a minimum of $\mu_{MSE} = 2.664$ nT^2 to be located at (N_{MVA}, Φ_{diff}, θ_{lim}) = (85, 80°, 80°), a significant improvement over any of the individual methods.

Figure 6-15 shows the distributions of PFNs produced by the CPMV method.

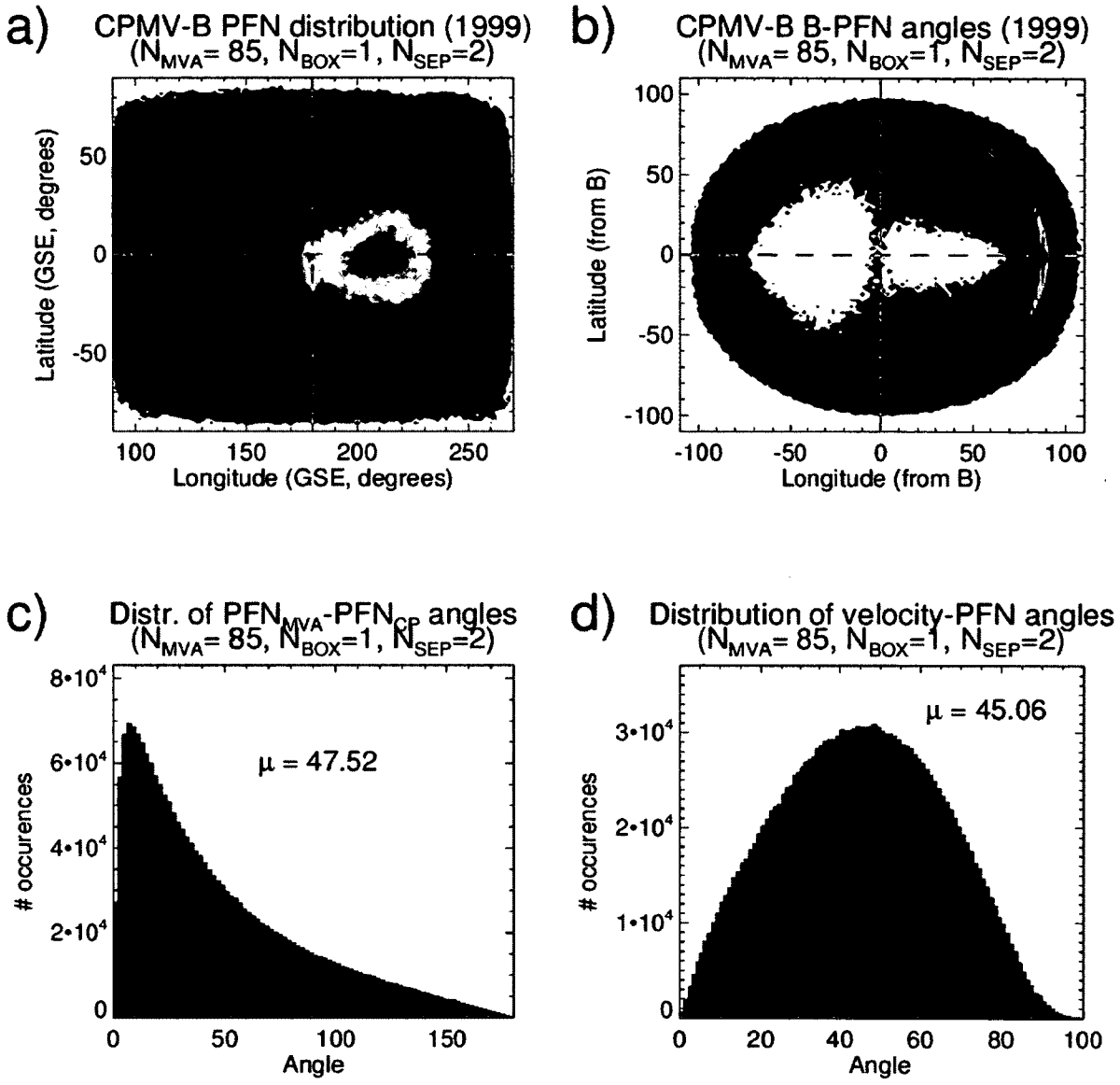

Figure 6-15 Part 1 CPMV-B PFN Distributions. Distributions of PFNs relative to the negative X_{GSE}-axis (a) and relative to the mean magnetic field (b) obtained when using the CPMV method with N_{box} =1, N_{sep} = 2 and N_{MVA} = 85 on all ACE data from one year (1999). Plot c) shows the distribution of CP/MVAB-0 difference angles and Plot d) the distribution of velocity-PFN angles.

PFNs are concentrated in a ring perpendicular to **B** but with higher density inside the circle than the individual methods. The distribution has significantly lower density outside of ±40° latitude and 150°-250° longitude than either the CP or MVAB-0

methods. This is a consequence of the process of merging CP and MVAB-0 PFNs, which lessens the probability of getting PFNs with outlying latitudes or longitudes significantly. Furthermore, instead of adding the two PFN vectors and normalizing (mathematically correct averaging), the PFN merging is done by taking the average latitude and longitude, a deliberate choice that also contributes significantly to avoiding PFNs with high latitudes. Also shown are the distributions of CP/MVAB-0 difference angles and velocity-PFN angles. As can be seen the PFNs produced by the MVAB-0 and CP methods differ significantly, not unexpected given that CP uses only 2 data points as opposed to 85 for MVAB-0. This explains why a high Φ_{diff} is required.

6.1.8 CPMV-E

Finally, the CPMV-E method has 12 variable parameters: The same 10 as CPMV-B and in addition the HT frame parameters $N_{HT,E}$ and $\sigma_{HT,E}$ associated with finding a HT reference frame for the electric field. For the 10 parameters shared with CPMV-B the distribution of test scores is almost identical (in terms of where the best results are found), allowing for elimination of 7 variables by using the constant values (N_{box}, N_{sep}, r_{ev}, ω, $N_{HT,P}$, $\sigma_{HT,P}$, O_{del}) = (1, 2, 1, 0, 101, ∞, "none"). For the two additional HT frame parameters best results are obtained with ($N_{HT,E}$, $\sigma_{HT,E}$) = (3, "none") as it was the case for the MVAE method, and so it is once again only necessary to test a range of values for the three parameters N_{MVA}, Φ_{diff} and θ_{lim}. Figure 6-16 shows the results. Note that the color scale is the same as in Figure 6-14 with the corresponding results for CPMV-B.

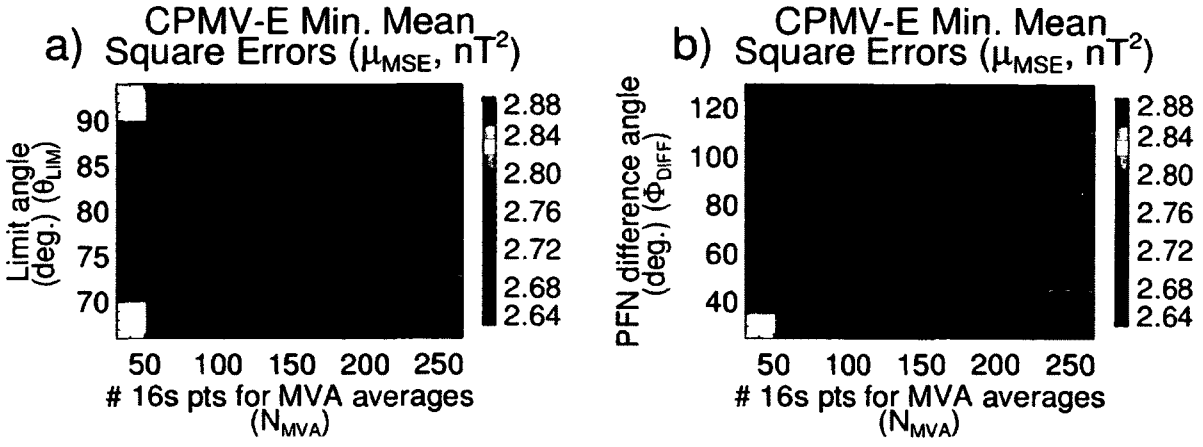

Figure 6-16 Part 1 CPMV-E Results. Minimum values of μ_{MSE} obtained as a function of (N_{MVA}, θ_{lim}) (a) and (N_{MVA}, Φ_{diff}) (b) when using (N_{box}, N_{sep}, r_{ev}, ω, $N_{HT,P}$) = (1, 2, 1, 0, 101) and comparing propagated ACE data to the WIND solar wind data set.

The best test score of $\mu_{MSE} = 2.671$ nT^2 was found at (N_{MVA}, Φ_{diff}, θ_{lim}) = (111, 62°, 78°), almost but not quite matching the best score for CPMV-B.

6.2 Part 2: Discrete Propagation of Discontinuities

In this part of the analysis the IMF discontinuities identified by Algorithm A and Algorithm B and listed in Table 5-2 are propagated from ACE to the respective target satellites using Algorithm D. Only one test score applies: The standard deviation $\sigma_{\Delta t}$ of the Δt_{rot} distribution where Δt_{rot} is the difference between propagated and measured arrival times. This is calculated using Algorithm F. All methods listed in Table 3-1 are tested for completeness, but because PFN estimation and data propagation was kept extremely simple (limited to a single data point) none of the parameters used to filter PFNs or propagated data apply. With much less data to propagate and a significantly reduced parameter space for each method the computational burden is reduced sufficiently that the whole data set can be propagated for all methods. Specifically, all results shown are obtained by propagating all discontinuities for all 3 target satellites (6,926 discontinuities in total), filtering out the 4% with the highest errors in propagation

delays and calculating the standard deviation of the remaining distribution (6,649 discontinuities) as described by Algorithm F. To provide a reference for the results, Figure 6-17 shows the distribution of $\Delta t_{rot} = t_{rot,measured} - t_{rot,propagated}$ when propagating the data set using simple flat delay (a) and when using the "best match delay" (b).

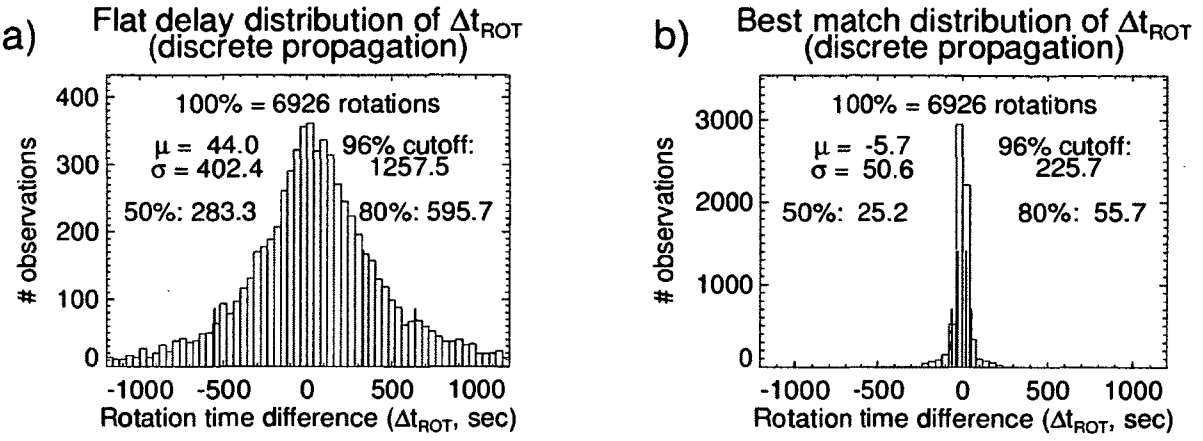

Figure 6-17 Reference Distributions of Arrival Time Errors. Distribution of Δt_{rot} when using simple flat delay (a) and when using "best match delay" (b).

Using flat delay gave a standard deviation of 402 seconds with 96% of observations being less than 1257 seconds (~21 minutes) from the mean value, which is 44 seconds. That is, on average discontinuities are measured 44 seconds later at the target satellite than predicted from flat delay. The somewhat artificial results in Plot b) gives an impression of the uncertainty inherent to the data and automated algorithms used. The algorithms manage to "define" the discontinuity time fairly accurately. In spite of differences in source and target data, 84% of discontinuities are found to match within 1 minute. This shows that the contribution to $\sigma_{\Delta t}$ that can be attributed to the use of automated algorithms is small.

6.2.1 MVAB-0

For the MVAB-0 method the simplified data propagation process only depends on 2 variable parameters: The number of data points used for MVA averages (N_{MVA}) and the number of data points used to find a HT frame for propagation (if any) ($N_{HT,P}$). The distribution of $\sigma_{\Delta t}$ as a function of these two parameters is shown in Figure 6-18, Plot a).

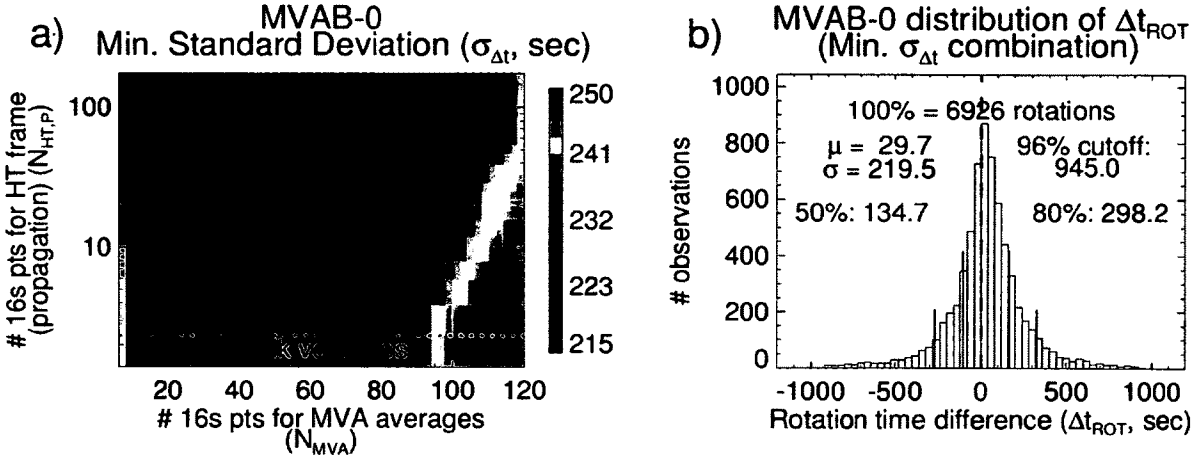

Figure 6-18 Part 2 MVAB-0 Results. Distribution of $\sigma_{\Delta t}$ for the MVAB-0 method as a function of N_{MVA} and $N_{HT,P}$ (a) and histogram for Δt_{rot} for the parameter value combination with the lowest $\sigma_{\Delta t}$ (b).

A minimum of $\sigma_{\Delta t} = 219.5$ seconds was obtained at (N_{MVA}, $N_{HT,P}$) = (43, 167), but results are very similar for $30 < N_{MVA} < 50$ and $N_{HT,P} > 50$. It is tempting to compare results to those obtained for continuous data propagation in the previous section, but because those results are affected by filtering not applied here they are not directly comparable. There is however one noteworthy difference, namely that in the case of discrete propagation of IMF discontinuities there is a clear advantage to using a HT frame for propagation with better results for high $N_{HT,P}$. The study by *Knetter* [2005] found that most discontinuities could be either rotational or tangential, but none could unambiguously be identified as rotational. The increased accuracy in propagation delays when using a HT frame rather than bulk velocities suggests that part of the discontinuities that cannot be reliably

identified as either tangential or rotational are actually rotational with a small but finite velocity in the plasma rest frame.

Plot b) shows the distribution of Δt_{rot} for the parameter value combination that gave the lowest standard deviation $\sigma_{\Delta t}$. Like for flat delay the mean is shifted from zero with discontinuities being measured later than predicted though the gap is reduced to 30 seconds.

6.2.2 MVAB

The MVAB and MVAB-0 methods have the same variable parameters, here N_{MVA} and $N_{HT,P}$. Figure 6-19 shows the distribution of $\sigma_{\Delta t}$ for these two variables along with the Δt_{rot} distribution with the lowest $\sigma_{\Delta t}$.

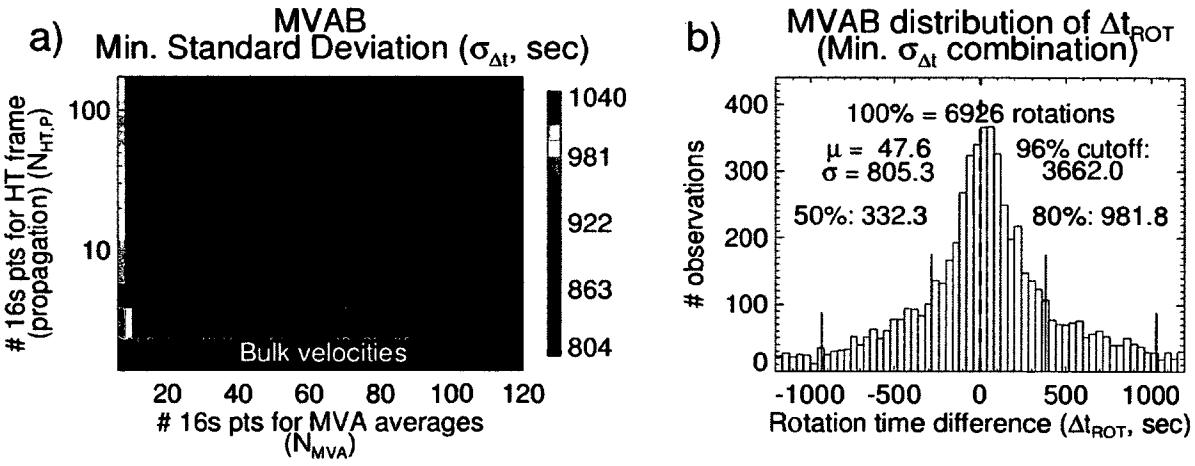

Figure 6-19 Part 2 MVAB Results. Distribution of $\sigma_{\Delta t}$ for the MVAB method as a function of N_{MVA} and $N_{HT,P}$ (a) and histogram for Δt_{rot} for the parameter value combination with the lowest $\sigma_{\Delta t}$ (b).

As was the case for continuous data propagation the MVAB method delivers much worse results than MVAB-0, but for discrete propagation the test scores are even significantly worse than when using a simple flat delay, the best score being $\sigma_{\Delta t}$ = 805 seconds compared to 402 seconds for flat delay. This may seem somewhat surprising given that

the poor performance in the case of continuous propagation appeared related to PFNs pointing along the magnetic field most of the time due to small-scale alfvenic fluctuations. For distinct IMF discontinuities the MVAB method would be expected to be less influenced by small-scale structure and hence identify PFNs for large-scale structures more often. In spite of what the test scores suggest, Figure 6-20 shows that this is indeed the case (compare to Figure 6-5 with corresponding plots for continuous propagation).

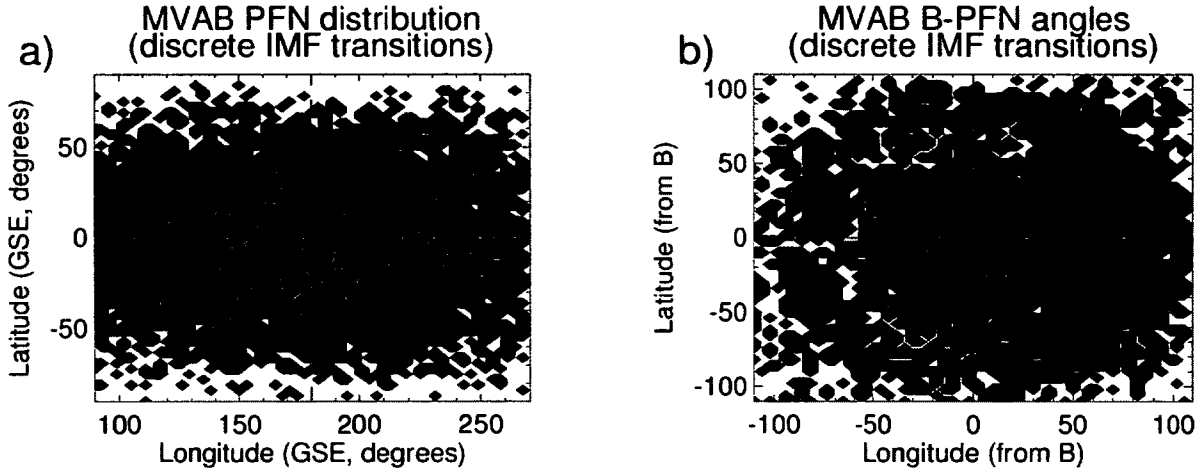

Figure 6-20 Part 2 MVAB PFN Distribution. Distribution of directions of MVAB PFN estimates relative to the negative X_{GSE}-axis (a) and relative to the magnetic field (b) for discrete propagation of 6,926 IMF discontinuities.

Plot a) shows that PFNs are no longer concentrated along the Parker Spiral direction. Plot b) shows that there's still a density peak in the direction of **B**, but the distribution is clearly more spread out and with a larger percentage along a ring perpendicular to **B**. While this improvement does bring the MVAB method closer to other methods in terms of producing PFNs suitable for large-scale propagation, it remains the least accurate by a large margin, and the test score $\sigma_{\Delta t}$ for discrete propagation is much more sensitive to the problem than the continuous test score μ_{MSE}. There are several reasons why the effect on μ_{MSE} is less dramatic. During intervals with almost constant IMF (e.g. the interior of flux tubes) the higher uncertainty has little or no impact for most of the data points, filtering

helps eliminate bad PFNs and the effect of extreme outliers is somewhat mitigated by the smoothing of propagated data before calculating μ_{MSE}.

6.2.3 MVAE

The MVAE method shares the parameters N_{MVA} and $N_{HT,P}$ from the MVAB/MVAB-0 methods and additionally has the two parameters $N_{HT,E}$ and $\sigma_{HT,E}$ that both apply to discrete propagation, making a total of 4 variable parameters. However, an initial test run showed that there is no advantage to applying the uncertainty limit for HT frame velocities, just as it was the case for continuous propagation, so $\sigma_{HT,E}$ was dropped from further consideration. Also, the lowest standard deviations were obtained using high values (> 100) of both N_{MVA} and $N_{HT,E}$, so the main test run focused on high (N_{MVA}, $N_{HT,E}$) and used a range of values for $N_{HT,P}$. Results are shown in Figure 6-21 as a function of (N_{MVA}, $N_{HT,E}$).

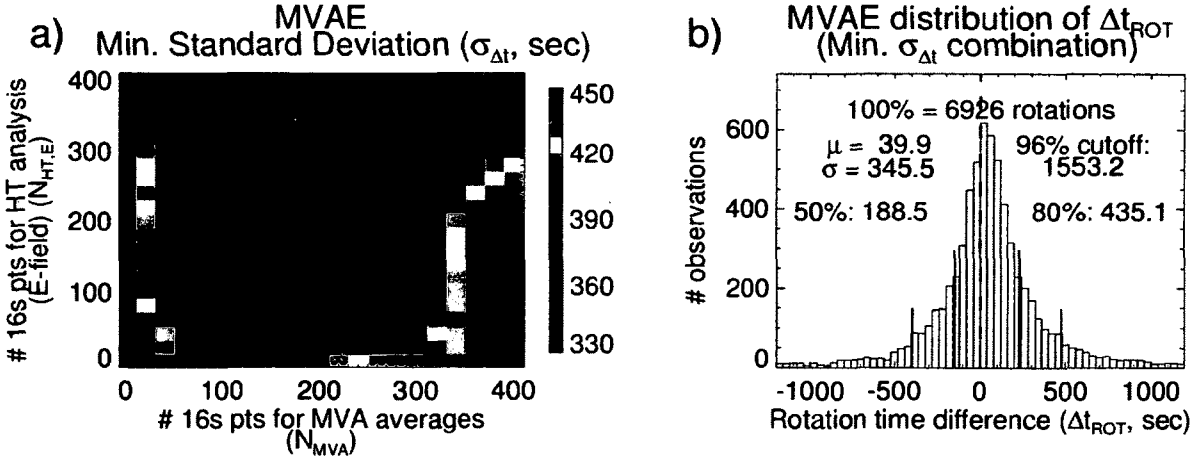

Figure 6-21 Part 2 MVAE Results. Distribution of $\sigma_{\Delta t}$ for the MVAE method as a function of N_{MVA} and $N_{HT,E}$ (a) and histogram for Δt_{rot} for the parameter value combination with the lowest $\sigma_{\Delta t}$ (b).

The dependence on $N_{HT,P}$ is not shown but is similar to that for MVAB-0 (or MVAE-0, see next section) with best results for $N_{HT,P} > \sim 50$. The minimum standard deviation found was $\sigma_{\Delta t} = 345.5$ seconds, considerably higher than for MVAB-0.

In contrast, for continuous data propagation the MVAE method produced better test scores than MVAB-0. Figure 6-8 showed that MVAE PFNs are predominantly quite close to perpendicular to the magnetic field. This was explained by small-scale perturbations in **V** and **B** being the dominant source of variability in **E** most of the time. The discrete data analysis is restricted to a minority of PFNs where a large change in **V** and **B** occurs due to the passage of a large-scale structure, and accordingly the PFN distribution might be different. However, as Figure 6-22 shows PFNs mostly remain close to perpendicular to **B** although there is a larger spread in observations.

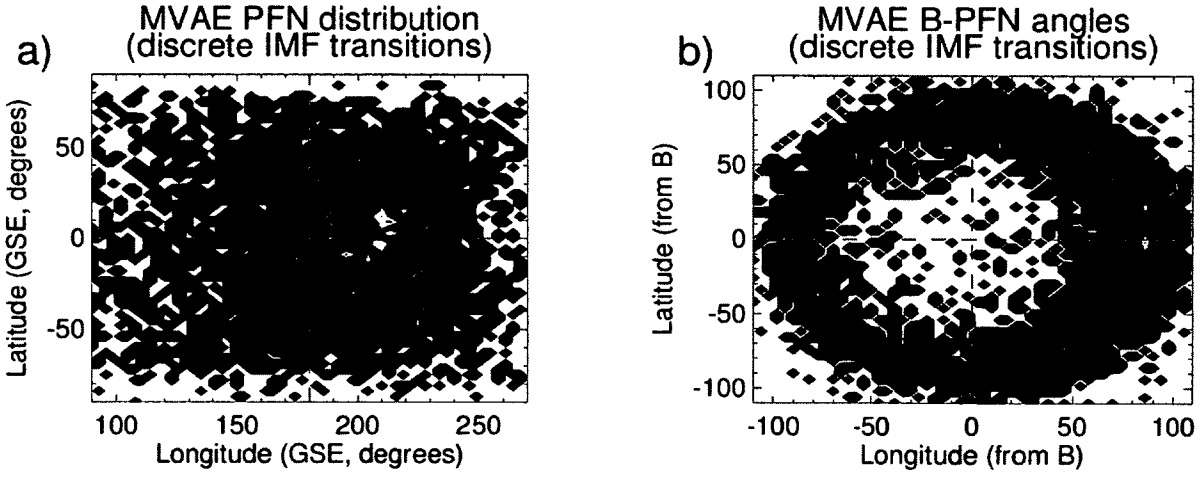

Figure 6-22 Part 2 MVAE PFN Distribution. Distribution of directions of MVAE PFN estimates relative to the negative X_{GSE}-axis (a) and relative to the magnetic field (b) for discrete propagation of 6,926 IMF discontinuities.

To explain this, again consider the time-variable component of the electric field:

$$\delta\mathbf{E}(t) = -\delta\mathbf{V}(t)\times\mathbf{B}_0 - \mathbf{V}_0\times\delta\mathbf{B}(t) - \delta\mathbf{V}(t)\times\delta\mathbf{B}(t) \qquad (6.2)$$

In this case $\mathbf{B}_0$ and $\mathbf{V}_0$ refer to the measured values at the center point where the PFN is evaluated ($\mathbf{V}_0$ is relative to the HT reference frame), $\delta\mathbf{V}(t) = \mathbf{V}(t)-\mathbf{V}_0$ and $\delta\mathbf{B}(t) = \mathbf{B}(t)-\mathbf{B}_0$ where $\mathbf{V}(t)$ and $\mathbf{B}(t)$ are the velocity/IMF series measured by ACE. $\mathbf{V}_0$ and $\mathbf{B}_0$ are close to parallel because $\mathbf{E}_0 = -\mathbf{V}_0\times\mathbf{B}_0 \approx \mathbf{0}$ in the HT frame, and observations show that changes in the magnetic field and velocity across discontinuities tend to be close to proportional (see Appendix B) so the term $\delta\mathbf{V}(t)\times\delta\mathbf{B}(t)$ is relatively small. $\delta\mathbf{E}(t)$ is then dominated by a sum of two terms that are close to perpendicular to $\mathbf{B}_0$, explaining why the direction of maximum variance in $\mathbf{E}$ remains close to perpendicular to $\mathbf{B}$ for discontinuities as well.

6.2.4 MVAE-0

The MVAE-0 method has the same variable parameters as the MVAE method. Again the HT frame uncertainty limit $\sigma_{HT,E}$ had negligible effect and was dropped. For both MVAE and MVAE-0 it was also the case that either a very low or a very high value for $N_{HT,P}$ gave better results, but whereas for MVAE a very high value gave minimum standard deviations, for MVAE-0 the best results were obtained with $N_{HT,E} = 3$. Figure 34 shows results as a function of the two remaining parameters (N_{MVA}, $N_{HT,P}$).

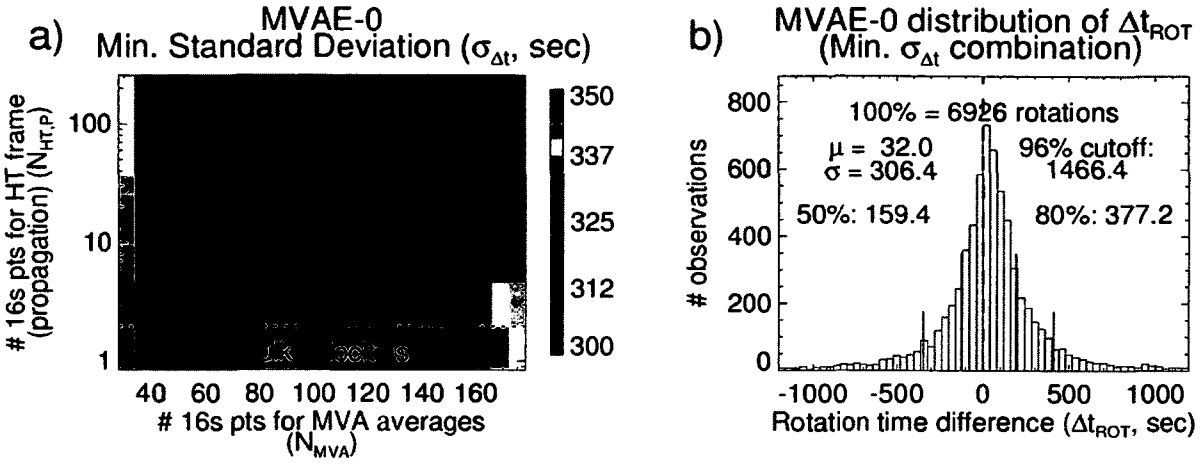

Figure 6-23 Part 2 MVAE-0 Results. Distribution of $\sigma_{\Delta t}$ for the MVAE-0 method as a function of N_{MVA} and $N_{HT,P}$ and histogram for Δt_{rot} for the parameter value combination with the lowest $\sigma_{\Delta t}$ (b).

Applying the requirement $\langle \mathbf{B} \rangle \cdot \mathbf{n} = 0$ does improve results compared to the unrestricted MVAE method, lowering the minimum $\sigma_{\Delta t}$ to 306.4 seconds. This however remains significantly higher than for the MVAB-0 method.

6.2.5 CP

For discrete propagation the CP method has only 3 applicable variable parameters: N_{box}, N_{sep} and $N_{HT,P}$. The dependence on $N_{HT,P}$ is the same as for previous methods with better results for higher $N_{HT,P}$, and Figure 6-24 shows the distribution of $\sigma_{\Delta t}$ for the remaining two parameters N_{box} and N_{sep}.

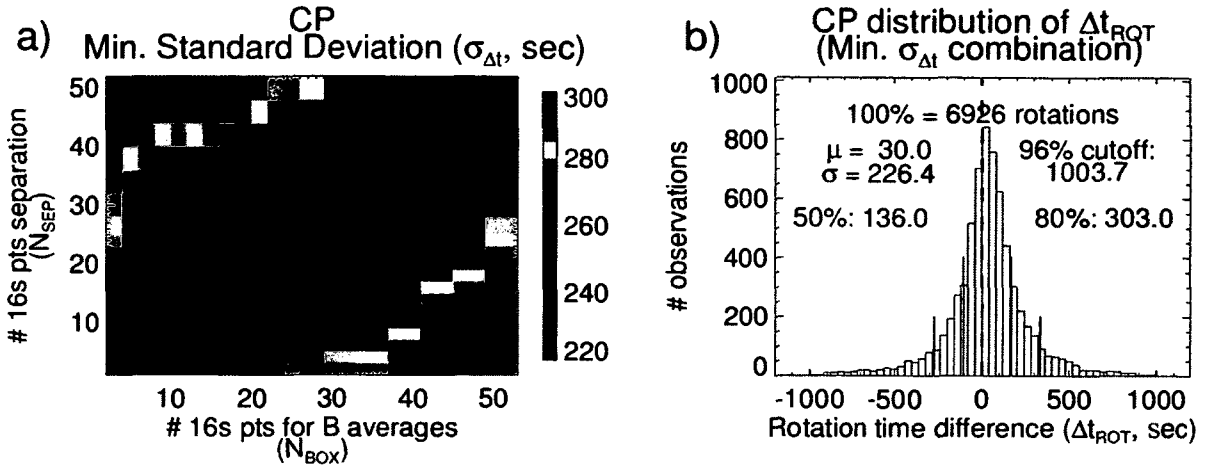

Figure 6-24 Part 2 CP Results. Distribution of $\sigma_{\Delta t}$ for the CP method as a function of N_{box} and N_{sep} (a) and histogram for Δt_{rot} for the parameter value combination with the lowest $\sigma_{\Delta t}$ (b).

A minimum standard deviation of 226.4 seconds was found at $(N_{box}, N_{sep}, N_{HT,P}) = (11, 8, 121)$, pretty close to the score for MVAB-0. Results remain close to optimal with $N_{box} \approx N_{sep}$, values in the range ~ 7 – 25 and $N_{HT,P} > 50$.

6.2.6 ED

The ED method has 5 variable parameters applicable to discrete propagation: N_{box}, N_{sep}, $N_{HT,E}$, $\sigma_{HT,E}$, and $N_{HT,P}$. Again $\sigma_{HT,E}$ has little or no effect and can be dropped from consideration. Initial tests showed that $N_{HT,E} = 3$ unambiguously gave the best results, and for $N_{HT,P}$ the pattern from previous methods repeats with best results for high values. Figure 6-25 shows results as a function of the two remaining parameters N_{box} and N_{sep} using $N_{HT,P} = 101$.

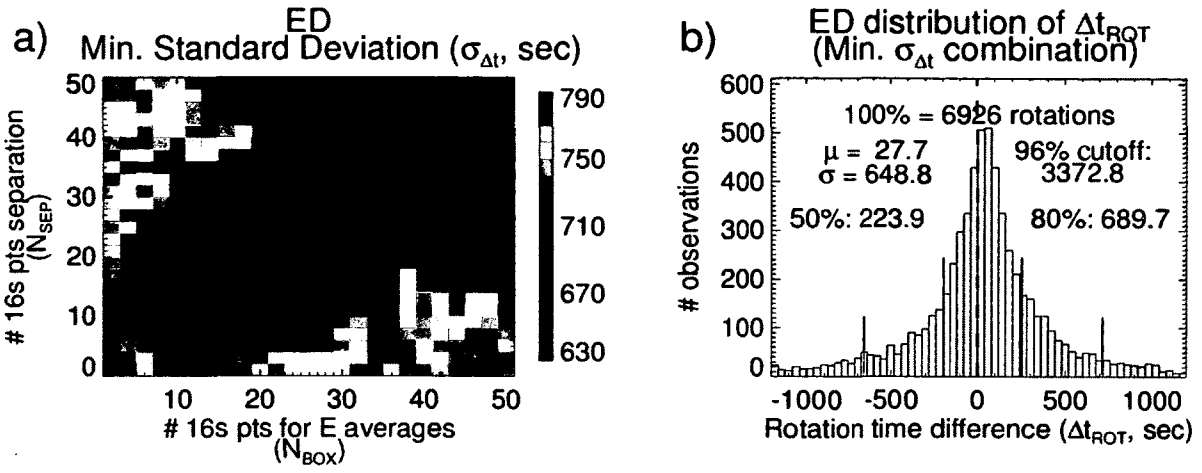

Figure 6-25 Part 2 ED Results. Distribution of $\sigma_{\Delta t}$ for the ED method as a function of N_{box} and N_{sep} (a) and histogram for Δt_{rot} for the parameter value combination with the lowest $\sigma_{\Delta t}$ (b).

The minimum value of $\sigma_{\Delta t}$ = 648.8 seconds was found at (N_{box}, N_{sep}) = (22, 25), significantly worse than for simple flat delay ($\sigma_{\Delta t}$ = 402.4 seconds). This is perhaps somewhat surprising given that it was able to give test scores similar to MVAB-0 for continuous propagation. The ED method also exhibits the biggest change in PFN distribution from continuous to discrete propagation. When propagating discrete discontinuities there is a much smaller density close to perpendicular to **B,** which at least partly explains the relatively poor test scores.

The remarkable symmetry in Figure 6-25 Plot a) turns out to be no coincidence. In fact, checking the calculations reveal that switching N_{box} and N_{sep} gives the exact same PFNs. The symmetry is broken slightly in Figure 6-25 because one parameter must be odd when the other is even, and for continuous propagation it was obscured due to the application of the minimum ratio r_E (see Table 3-2), which introduces a stronger asymmetry to the results.

6.2.7 CPMV-B

The CPMV-B method has 4 variable parameters for discrete propagation: N_{MVA}, N_{box}, N_{sep} and $N_{HT,P}$. Better results are obtained with high $N_{HT,P}$. Figure 6-26 shows results for a test run with $N_{HT,P} = 101$.

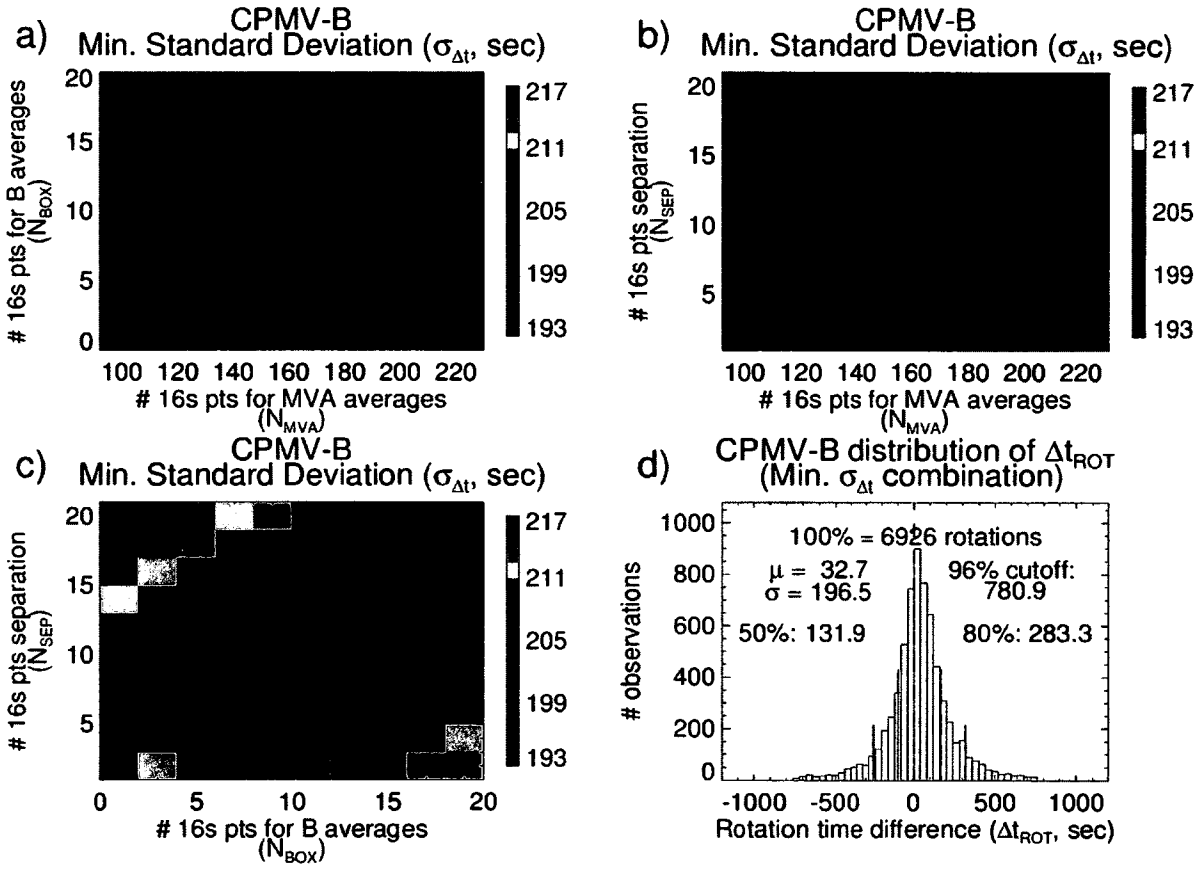

Figure 6-26 Part 2 CPMV-B Results. Distribution of $\sigma_{\Delta t}$ for the CPMV-B method as a function of (N_{MVA}, N_{box}) (a), (N_{MVA}, N_{sep}) (b), (N_{box}, N_{sep}) (c) and histogram for Δt_{rot} for the parameter value combination with the lowest $\sigma_{\Delta t}$ (d).

The minimum $\sigma_{\Delta t} = 196.5$ seconds occurs at (N_{MVA}, N_{box}, N_{sep}) = (133, 7, 4), again a significant improvement over any of the individual methods.

6.2.8 CPMV-E

For the CPMV-E method there are 5 variable parameters applicable to discrete propagation: N_{box}, N_{sep}, $N_{HT,E}$, $\sigma_{HT,E}$, and $N_{HT,P}$. As usual $\sigma_{HT,E}$ has little or no effect and can be dropped from consideration. Initial tests showed that $N_{HT,E} = 3$ unambiguously gives the best results along a high value for $N_{HT,P}$ (101 will be used). This leaves the same parameter space as for CPMV-B, and the distribution of results is quite similar. They are shown as a function of (N_{box}, N_{sep}) in Figure 6-27 while the dependence on N_{MVA} has been omitted.

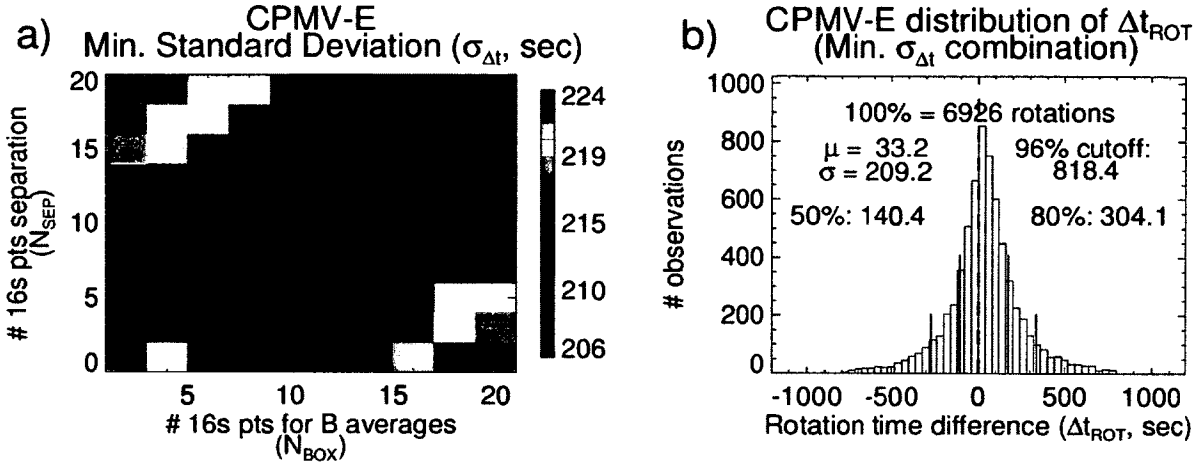

Figure 6-27 Part 2 CPMV-E Results. Distribution of $\sigma_{\Delta t}$ for the CPMV-E method as a function of N_{box} and N_{sep} (a) and histogram for Δt_{rot} for the parameter value combination with the lowest $\sigma_{\Delta t}$ (b).

The minimum of $\sigma_{\Delta t} = 209.2$ seconds is at (N_{MVA}, N_{box}, N_{sep}) = (153, 11, 8). Not quite as good as the score for CPMV-B, yet still an improvement over any of the individual methods.

6.3 Summary of Results, Parts 1 and 2

Table 6-3, Table 6-4 and Table 6-5 give an overview showing the best test scores and corresponding parameter values for each method in Part 1 (general continuous propagation, μ_{MSE}) and Part 2 (discrete propagation of discontinuities, $\sigma_{\Delta t}$) of the analysis. Some trivial results were omitted from the tables: The delete option O_{del} was left out as removing no out-of-sequence data consistently gave the best results, and $\sigma_{HT,P}$ and $\sigma_{HT,E}$ were omitted because they were mostly not applied (did not affect results).

Table 6-3 Parts 1 and 2: MVA Results. Best results (μ_{MSE} from Part 1 and $\sigma_{\Delta t}$ from Part 2) for MVA methods and the corresponding combinations of parameter values. Results for continuous propagation were obtained from the WIND data set (3,238 hours), and for discrete propagation all available discontinuities from WIND, IMP and Geotail (6,926 discontinuities) were used.

		N_{MVA}	r_{ev}	$N_{HT,P}$	$N_{HT,E}$	θ_{lim}
MVAB	$\mu_{MSE} = 3.817$	91	1.3	3	-	52°
	$\sigma_{\Delta t} = 805.3$	99	-	Bulk	-	-
MVAB-0	$\mu_{MSE} = 2.862$	31	5	3	-	79°
	$\sigma_{\Delta t} = 219.5$	43	-	167	-	-
MVAE	$\mu_{MSE} = 2.775$	127	1.3	Bulk	3	79°
	$\sigma_{\Delta t} = 345.5$	221	-	241	381	-
MVAE-0	$\mu_{MSE} = 2.826$	125	1.2	Bulk	3	79°
	$\sigma_{\Delta t} = 306.4$	67	-	183	3	-

Table 6-4 Parts 1 and 2: CP/ED Results. Best results for CP and ED methods and the corresponding combinations of parameter values, obtained using the WIND data set (3,238 hours) for continuous propagation and 6,926 IMF discontinuities (WIND, IMP, Geotail) for discrete propagation.

		N_{box}	N_{sep}	B_n	ω	r_E	$N_{HT,P}$	$N_{HT,E}$	θ_{lim}
CP	$\mu_{MSE} = 2.770$	1	22	20%	14°	-	101	-	79°
	$\sigma_{\Delta t} = 226.4$	11	8	-	-	-	121	-	-
ED	$\mu_{MSE} = 2.841$	62	1	30%	-	0.025	Bulk	3	77°
	$\sigma_{\Delta t} = 648.8$	22	25	-	-	-	101	3	-

Table 6-5 Parts 1 and 2: CPMV/OMNI Results. Best results for the CPMV-B and CPMV-E methods with corresponding parameter values. Also listed are the results for the alternative CPMV method and parameter values used for establishing the OMNI database. CPMV-B and CPMV-E results were obtained using the WIND data set (3,238 hours) for continuous propagation and 6,926 IMF discontinuities (WIND, IMP, Geotail) for discrete propagation.

		N_{box}	N_{sep}	ω	B_n	N_{MVA}	r_{ev}	Φ_{diff}	$N_{HT,P}$	$N_{HT,E}$	θ_{lim}
CPMV-B	$\mu_{MSE} = 2.664$	1	2	0°	-	85	1	80°	101	-	80°
	$\sigma_{\Delta t} = 196.5$	7	4	-	-	133	-	-	101	-	-
CPMV-E	$\mu_{MSE} = 2.671$	1	2	0°	-	111	1	62°	101	3	78°
	$\sigma_{\Delta t} = 209.2$	11	8	-	-	153	-	-	101	-	-
OMNI	$\mu_{MSE} = 2.947$	17	28	13°	3.5%	77	5.2	-	Bulk	-	73°
	$\sigma_{\Delta t} = 235.3$	17	28	-	-	77	-	-	Bulk	-	-

6.4 Part 3: Continuous Propagation of Discontinuities

The third part of the analysis uses the same set of IMF discontinuities that was used for discrete propagation, identified by Algorithm A and Algorithm B and listed in Table 5-2. For each transition a 2-hour interval centered on the transition is propagated from ACE to the target satellite using Algorithm C, and the test scores $\sigma_{\Delta t}$, μ_{MSE} and P_{MATCH} are then calculated using Algorithm G. In summary, Part 3 considers the accuracy of arrival times for discontinuities ($\sigma_{\Delta t}$), continuous data accuracy (μ_{MSE}) and preservation of distinct discontinuities (P_{MATCH}) collectively. The test score P_{MATCH} is indicative of the extent to which out-of-sequence data renders discontinuities in source data unrecognizable in the propagated data. Visual inspection verified that when an IMF discontinuity fails to match the target after propagation, data mixing is most often at fault (about 3 out of 4 cases). In most of the remainder of cases the data was "stretched" without mixing taking place, causing one of the rotation angles (1/5/30 minutes) to dip below the threshold so no discontinuity was identified by Algorithm A.

Considering several test scores requires a different approach. It turns out that the volume in parameter space giving near-optimal results differs between test scores. This is particularly true between μ_{MSE} and P_{MATCH}, and it limits the ability to reduce parameter space. It is implausible to do high-resolution test runs to resolve distributions in detail, and instead the priority will be to give a more qualitative overview. While it's necessary to retain a larger volume of parameter space for each method there's little reason to test every method at this point. The MVAB and ED methods produced relatively poor results in Parts 1 and 2 and will therefore be omitted. So will MVAE-0 and CPMV-E because the results for these two methods are very similar to those of MVAE and CPMV-B, and the differences would be largely negligible given the less detailed approach in this section. There are then 4 methods to go through results for: MVAB-0, MVAE, CP and CPMV-B. A side benefit of neglecting poor performing methods is that the range of test scores decreases sufficiently to keep the same color scales on plots for all methods, making results easier to compare.

It is important to keep in mind that each plot only presents a cross section of multi-dimensional parameter space. Within that cross section good results for one test score may appear to overlap with good results for another even though they are separated in one of the dimensions not shown. Hence it is necessary to check plots for all parameters to assess properly to which extent volumes of good test scores actually overlap.

6.4.1 MVAB-0

Part 3 of the analysis is sufficiently different from either of Parts 1 and 2 that it was decided to test all 6 variable parameters for MVAB-0 (N_{MVA}, r_{ev}, $N_{HT,P}$, $\sigma_{HT,P}$, θ_{lim} and O_{del}) as a starting point. Figure 6-28 shows results from a test run where a range of values for all parameters was used, though results are only shown as a function of ($N_{HT,P}$, $\sigma_{HT,P}$) and (N_{MVA}, O_{del}) respectively.

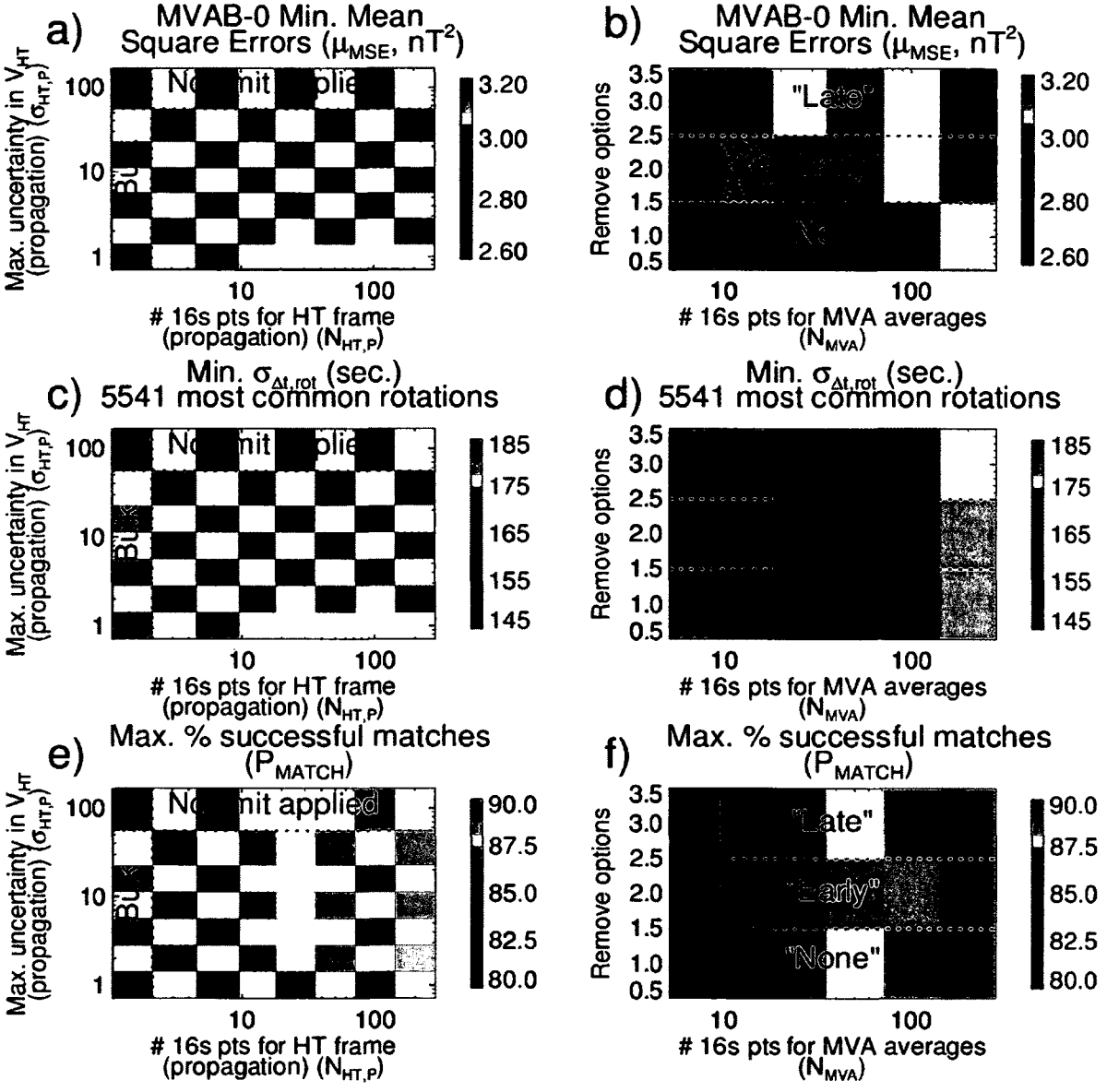

Figure 6-28 Part 3 MVAB-0 Initial Results. Distribution of test scores μ_{MSE} (a-b), $\sigma_{\Delta t}$ (c-d) and P_{MATCH} (e-f) as a function of parameters ($N_{HT,P}$, $\sigma_{HT,P}$) (a, c, e) and (N_{MVA}, O_{del}) (b, d, f) for the MVAB-0 method.

Plots a) - b) are in agreement with results from Part 1 of the analysis: $N_{HT,P}$ and $\sigma_{HT,P}$ have relatively little influence on the test score μ_{MSE} (compare to Figure 6-1) and removing no out-of-sequence data gives significantly better results. Using a HT frame improves $\sigma_{\Delta t}$ with 3-4 seconds while applying $\sigma_{HT,P}$ makes little or no difference.

Corresponding results for the case of discrete propagation were shown in Figure 6-18 Plot a) and likewise showed an improvement of a few seconds when using a HT frame, though with significantly higher $\sigma_{\Delta t}$ overall. That plot included all discontinuities whereas here 20% are filtered out, specifically the 20% where a matching discontinuity most often cannot be identified in propagated data. If replicating Figure 6-18 Plot a) but with the exact same 20% of discontinuities filtered out the result is an almost identical distribution with $\sigma_{\Delta t}$ lowered a few seconds uniformly across the plot, e.g. the minimum is lowered from 219.5 to 215.6 seconds. Hence, for the majority of discontinuities tested a significantly more accurate arrival time estimate is obtained when using continuous rather than discrete propagation. Conversely, if only considering the 20% of discontinuities that were filtered out, discrete propagation gives $\sigma_{\Delta t} \sim 275$ seconds while continuous propagation gives $\sigma_{\Delta t} \sim 300$ seconds with more than half of the discontinuities missing because no match was identified. This shows that for a minority of cases where data mixing is a problem, discrete propagation is a better option for estimating arrival time of discontinuities.

Moving on, the one thing to take away from Plot d) is that removing "early" or "late" out-of-sequence data results in higher $\sigma_{\Delta t}$ relative to doing no filtering. Plot e) reveals that there is a pronounced advantage to using a HT frame with a high number of data points for propagation when it comes to data mixing. A look at Figure B-5 in Appendix B explains why. Doing so smoothes out high frequency velocity fluctuations and, more importantly, it also smoothes out sudden jumps in the plasma velocity at IMF discontinuities. Such velocity jumps are inevitably responsible for some mixing of data from separate flux tubes in propagated data. This advantage is independent of propagation method and other parameter values used, and as a consequence $N_{HT,P} = 101$ will be used for the remainder of Part 3. Once again there's little or no advantage to applying $\sigma_{HT,P}$, and this parameter will also be dropped from here on. Finally, Plot f) shows that data mixing is not the only factor affecting the test score P_{MATCH}. Removing "late" or "early" data points ensures zero data mixing, yet these two options do not increase odds that propagated discontinuities match those measured at the target. Data

mixing may significantly alter the profile of propagated IMF transitions, but so may removal of data, and the very crude options tested here provide no overall improvement on this account. The firm conclusion is that they are not viable options for solving the problem with out-of-sequence data, and they will be disregarded for the rest of Part 3.

Having eliminated 3 variable parameters it was possible to use a somewhat refined grid to test the remaining 3 MVAB-0 parameters, and results are shown in Figure 6-29. The volume in parameter space that gives near-optimal results is similar and overlapping for μ_{MSE} and $\sigma_{\Delta t}$, each of which is separate from that of P_{MATCH}.

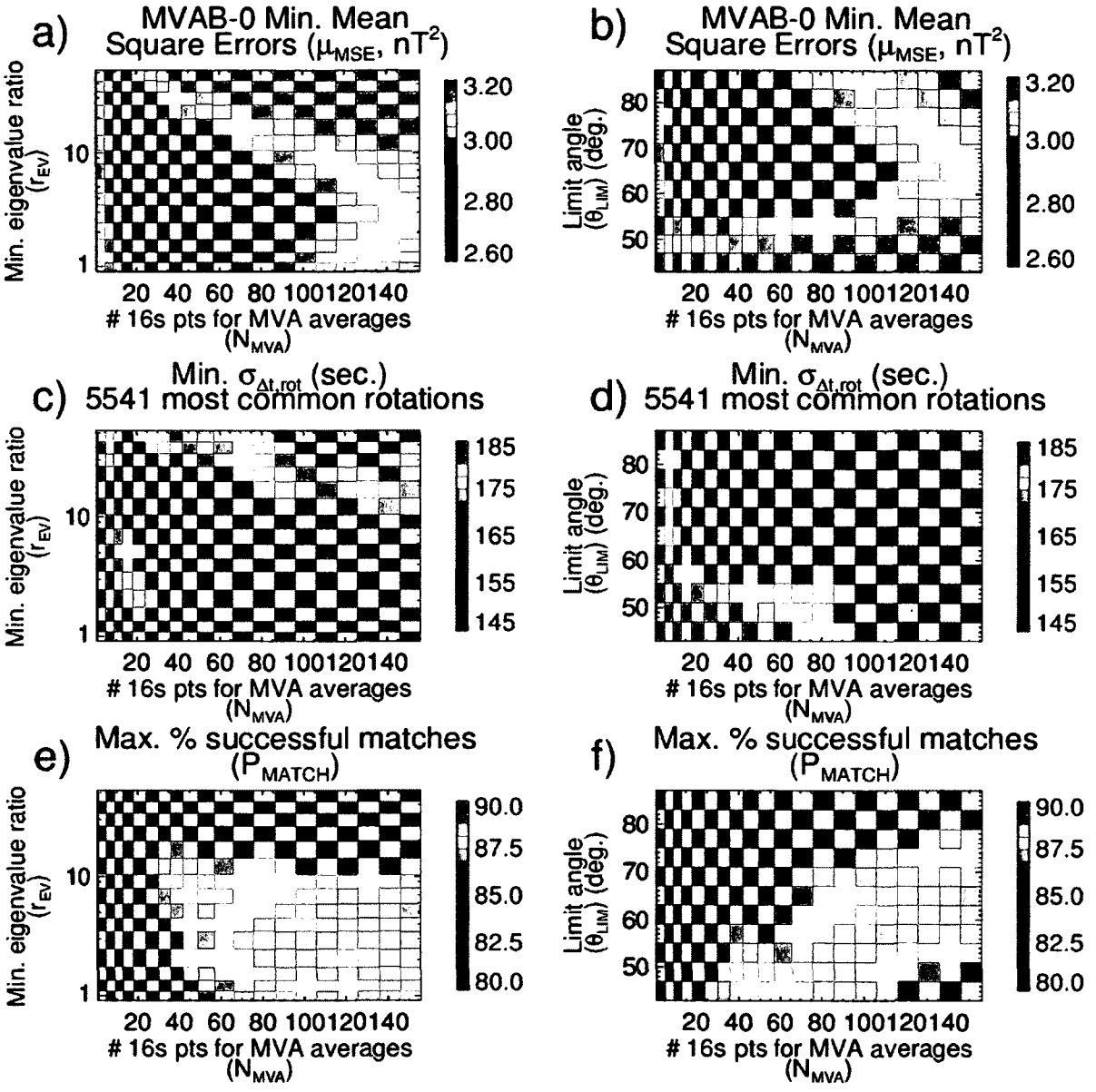

Figure 6-29 Part 3 MVAB-0 Detailed Results. Distribution of test scores μ_{MSE} (a-b), $\sigma_{\Delta t}$ (c-d) and P_{MATCH} (e-f) as a function of parameters (N_{MVA}, r_{ev}) (a, c, e) and (N_{MVA}, θ_{lim}) (b, d, f) for the MVAB-0 method.

Caution is needed when considering the $\sigma_{\Delta t}$ distribution. As mentioned when describing Algorithm G for calculating $\sigma_{\Delta t}$ there is a bias because the data set differs from point to point according to which discontinuities are successfully matched, and discontinuities that tend to "fail" matching the target after propagation are associated with

higher average uncertainty in the arrival time. Most of the additional discontinuities that are included where P_{MATCH} is high are prone to data mixing, an indicator that the assumptions made for delay calculations are violated. Hence it is necessary to look at $\sigma_{\Delta t}$ and P_{MATCH} distributions in tandem. Consider the dependence on the limit angle as an example (Plots d) and f)). Best $\sigma_{\Delta t}$ scores are obtained with $\theta_{lim} = 85°$, the maximum tested. Propagation time for data with this high of a PFN-velocity angle is highly uncertain, either very short (possibly negative) or very long, which leads to mixing with previous or later data and consequent failure of the discontinuity matching algorithm. Lowering the limit angle filters out PFNs for such data, but they are replaced by interpolation and PFN-velocity angles exceeding the limit angle after interpolation are rounded down. The data is still propagated, only with a lower PFN-velocity angle enforced. Data mixing is reduced and the source IMF profile is better preserved. The source profile included a match for the target discontinuity, so P_{MATCH} may increase (depending on N_{MVA}) all the way down to 45° or lower. However, when actual PFN-velocity angles in the solar wind exceed the limit angle, calculated delay estimates are off. Lowering the limit angle increases both the amount of data affected and how much delay estimates are off. Choosing a limit angle is a compromise between avoiding data mixing and retaining accuracy in delay estimates. Returning to the bias in $\sigma_{\Delta t}$, Table 6-6 gives 2 examples to illustrate the effect.

Table 6-6 Data Bias Example. 2 examples illustrating how $\sigma_{\Delta t}$ is affected by data set variations between points in parameter space. The first example compares 2 points separated by θ_{lim}, the second compares 2 points separated by N_{MVA}.

Parameter values	Unique		Common		Total	
	# rot.	$\sigma_{\Delta t}$	# rot.	$\sigma_{\Delta t}$	# rot.	$\sigma_{\Delta t}$
$N_{MVA} = 61$, $r_{ev} = 4$, $\theta_{lim} = \mathbf{69°}$	303	237.53	4783	148.54	5086	155.39
$N_{MVA} = 61$, $r_{ev} = 4$, $\theta_{lim} = \mathbf{85°}$	77	259.24	4783	149.60	4860	151.92
$\mathbf{N_{MVA} = 45}$, $r_{ev} = 4$, $\theta_{lim} = 69°$	173	269.01	4844	151.37	5017	156.86
$\mathbf{N_{MVA} = 101}$, $r_{ev} = 4$, $\theta_{lim} = 69°$	337	227.84	4844	152.91	5181	158.84

The first example compares 2 points in parameter space separated only by limit angle, splitting the set of matching discontinuities into a subset unique to each point and a subset common to both. For the common subset containing the vast majority of discontinuities, $\sigma_{\Delta t}$ is slightly lower for $\theta_{lim} = 69°$ than $\theta_{lim} = 85°$. However, the subset of unique discontinuities is significantly larger for $\theta_{lim} = 69°$ and is associated with somewhat higher $\sigma_{\Delta t}$. This pushes the total $\sigma_{\Delta t}$ for $\theta_{lim} = 69°$ a few seconds beyond that for $\theta_{lim} = 85°$. In conclusion, the minimum of $\sigma_{\Delta t}$ for $\theta_{lim} = 85°$ (Figure 6-29 Plot d)) is a bias artifact. Note however that the bias only accounts for a few seconds difference. The other example compares 2 points in parameter space separated by N_{MVA} and was included to show that the relation between P_{MATCH} and $\sigma_{\Delta t}$ is more complex than the example with limit angles suggests. The unique subset of discontinuities is larger for high N_{MVA}, but is associated with a higher $\sigma_{\Delta t}$ for low N_{MVA}. In effect the unique subsets contribute about equally to the total $\sigma_{\Delta t}$.

The distributions for μ_{MSE} are quite similar to those found for general data propagation (Part 1, Figure 6-2) except that a lower limit angle works better. As will be seen in the section on statistical significance the optimal limit angle for the WIND data set used in Part 1 is higher than for the larger Geotail data set, which may explain most if not all of the difference. Best μ_{MSE} scores are generally obtained with rather low N_{MVA},

outside the range that gives lowest $\sigma_{\Delta t}$ (compare Plots b) and d) in Figure 6-29 closely). Likewise, note that using high $N_{HT,P}$ doesn't give lower mean square errors in spite of improving $\sigma_{\Delta t}$ (Figure 6-29 Plots a) and c)). More accurate discontinuity arrival times surely help reduce mean square errors, but something else has a larger impact on μ_{MSE}: Data mixing. Comparing to the P_{MATCH} distributions supports the suggestion that data mixing helps lower mean square errors, and in Appendix C it is explained and shown in some detail how data mixing affects μ_{MSE}.

6.4.2 MVAE

With 3 variable parameters eliminated ($N_{HT,P}$, $\sigma_{HT,P}$ and O_{del}) the MVAE method has 5 variables left to consider (N_{MVA}, r_{ev}, $N_{HT,E}$, $\sigma_{HT,E}$ and θ_{lim}). Of these, $\sigma_{HT,E}$ has a negligible impact on results and can also be disregarded. Figure 6-30 shows distributions of test scores as functions of the remaining 4 parameters.

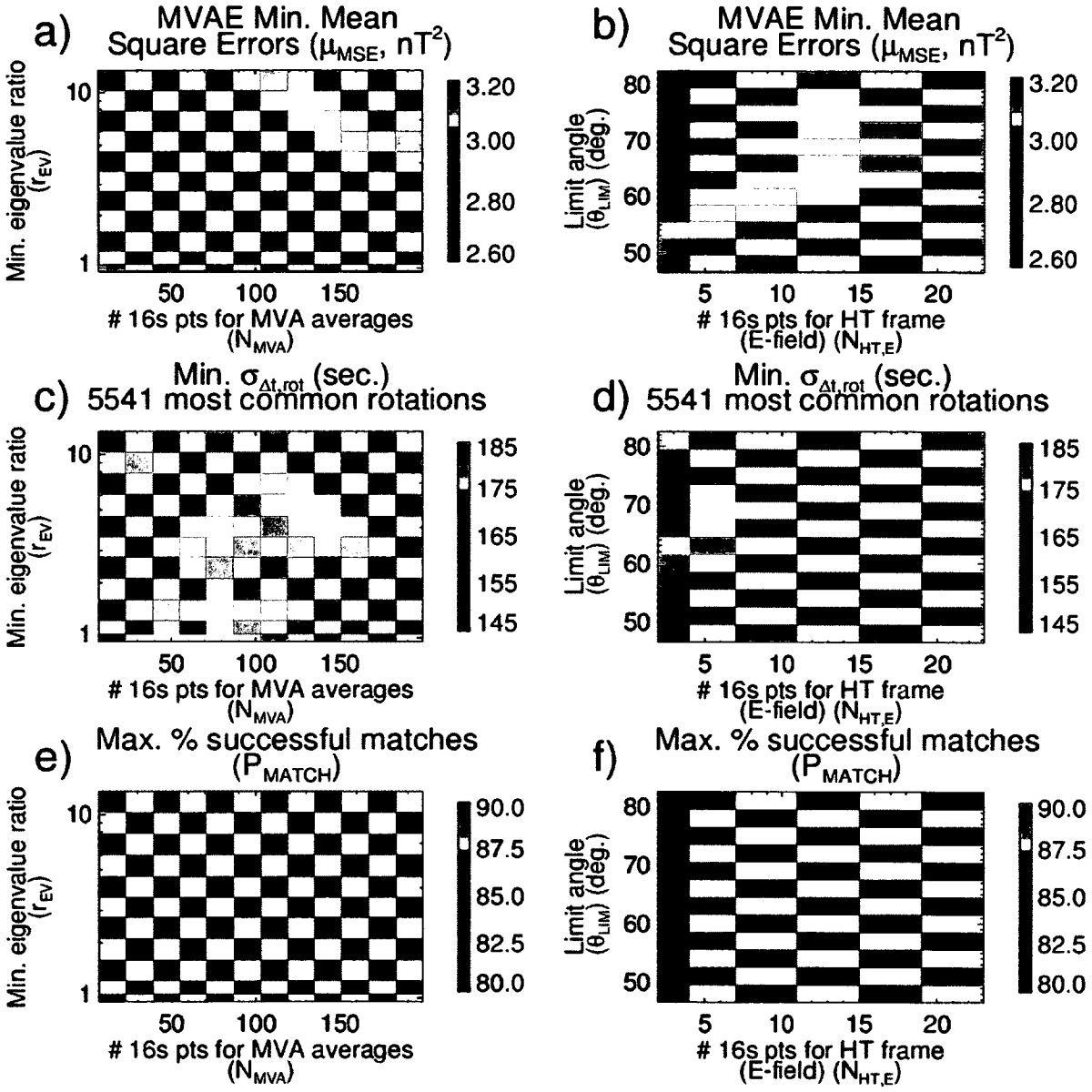

Figure 6-30 Part 3 MVAE Results. Distribution of test scores μ_{MSE} (a-b), $\sigma_{\Delta t}$ (c-d) and P_{MATCH} (e-f) as a function of parameters (N_{MVA}, r_{ev}) (a, c, e) and ($N_{HT,E}$, θ_{lim}) (b, d, f) for the MVAE method.

Compared to continuous/general propagation (Part 1, Figure 6-6 and Figure 6-7) the minimum for μ_{MSE} occurs for lower N_{MVA} (50-125 versus 100-175) and lower θ_{lim} (66°-72° versus 72°-81°) but still with low r_{ev} (~2 or less) and $N_{HT,E} = 3$. The shift to lower N_{MVA} likely has to do with higher variability in the discontinuity-centered data set. One

cause of higher variability is that long quiet intervals are excluded, and another is a higher ratio of coronal-hole high-speed stream data during years after solar maximum (see Section 6.6 on statistical significance). When IMF variability is high, actual changes in PFN direction may not be resolved properly with an averaging interval of 30 minutes or more. The parameter values giving lowest $\sigma_{\Delta t}$ mostly coincide with those giving low μ_{MSE}, in particular $N_{HT,E} = 3$. In contrast, best P_{MATCH} scores are obtained with $N_{HT,E} > 5$ and $\theta_{lim} < 60°$, completely separate from the volume that gives best results for the two other test scores. This lends the question whether $\sigma_{\Delta t}$ is influenced by a bias as discussed in the previous section, but that is not the case – overall, accuracy just gets worse for increasing $N_{HT,E}$. Comparing to MVAB-0 results (Figure 6-29) the minimum μ_{MSE} values are about even, but MVAB-0 produces significantly better scores for $\sigma_{\Delta t}$ and P_{MATCH}. The MVAE method overall produces less accurate PFN estimates around discontinuities and also causes more data mixing, particularly for parameter values that give low $\sigma_{\Delta t}$ and μ_{MSE}. The higher level of data mixing coinciding with the minimum in $\sigma_{\Delta t}$ likely explains why μ_{MSE} scores remain low. When considering the test scores collectively the MVAB-0 method is capable of producing somewhat better results than MVAE.

6.4.3 CP

For the CP method 5 variables are relevant to consider at this point: N_{box}, N_{sep}, B_n, ω and θ_{lim}. As Figure 6-31 and Figure 6-32 show, test scores have a non-trivial dependence on all of these.

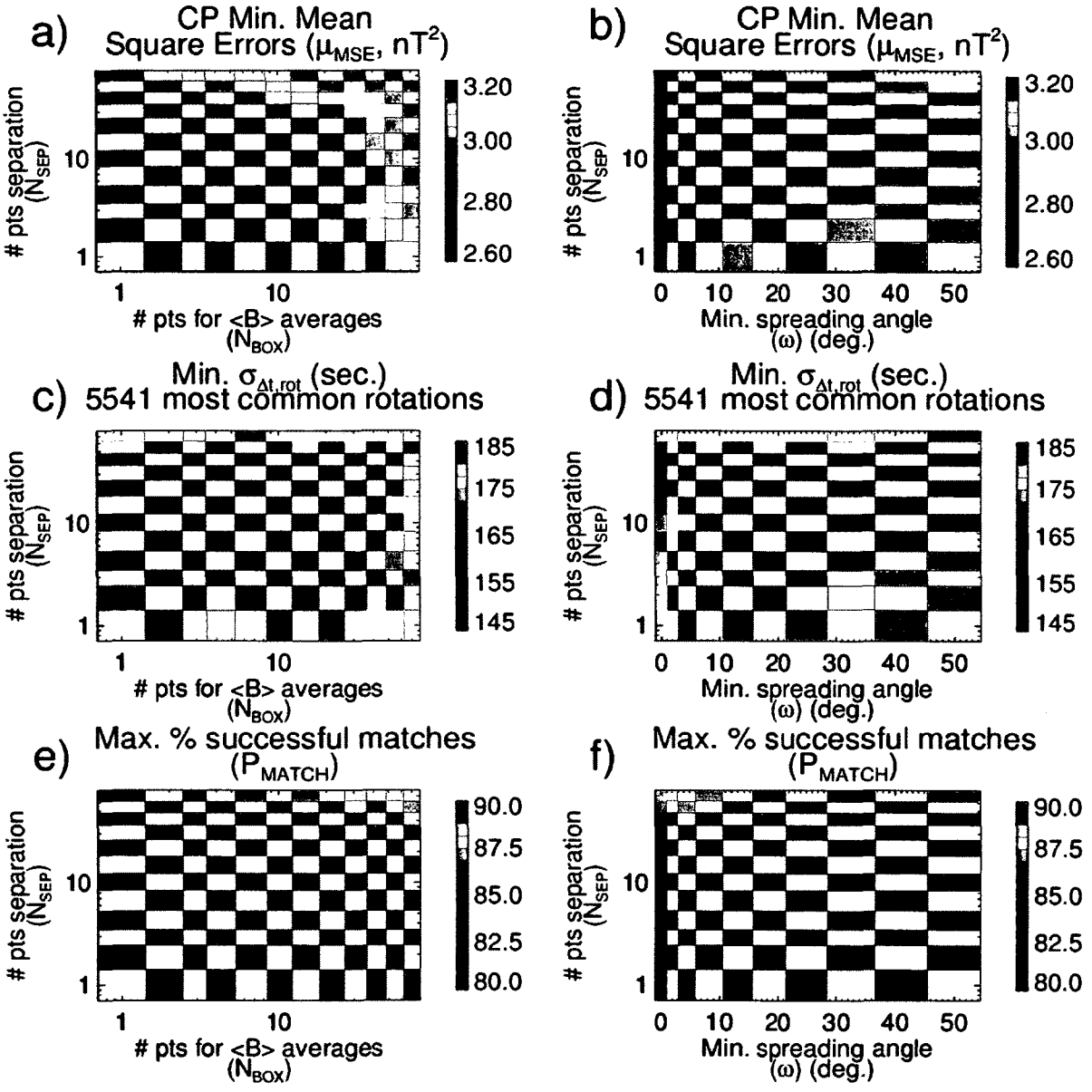

Figure 6-31 Part 3 CP Results 1. Distribution of test scores μ_{MSE} (a-b), $\sigma_{\Delta t}$ (c-d) and P_{MATCH} (e-f) as a function of parameters (N_{box}, N_{sep}) (a, c, e) and (ω, N_{sep}) (b, d, f) for the CP method.

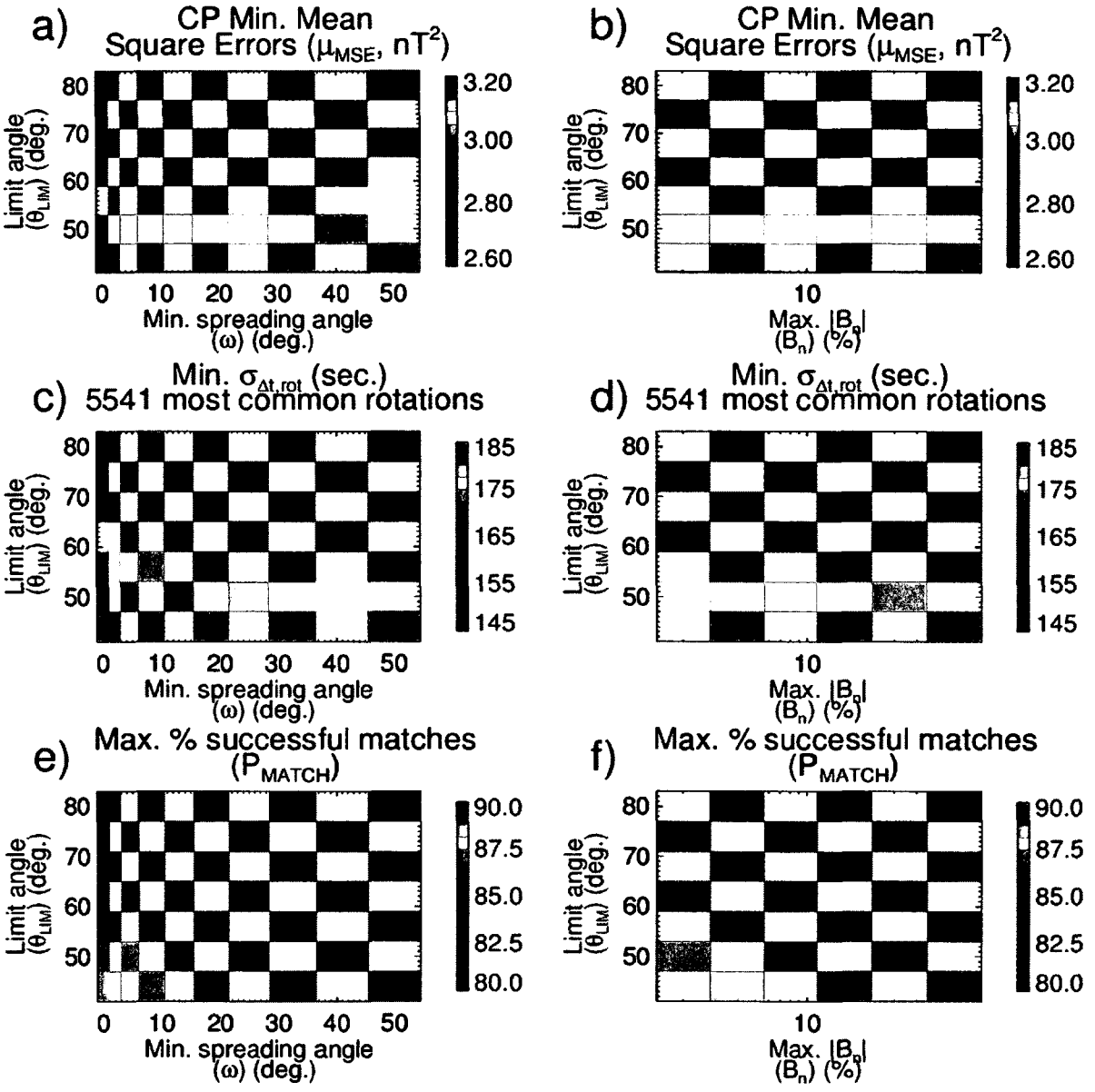

Figure 6-32 Part 3 CP Results 2. Distribution of test scores μ_{MSE} (a-b), $\sigma_{\Delta t}$ (c-d) and P_{MATCH} (e-f) as a function of parameters (ω, θ_{lim}) (a, c, e) and (B_n, θ_{lim}) (b, d, f) for the CP method.

Near-optimal μ_{MSE} is confined to a specific range of parameter values: N_{box} = 1 or 2, N_{sep} between 10 and 25, ω between 15 and 35, $\theta_{lim} \approx 65°$-$75°$ and $B_n > 10$. This is mostly similar to results for continuous/general propagation (Part 1, Figure 6-10 and Figure 6-11) except for lower N_{sep} and θ_{lim}. Good $\sigma_{\Delta t}$ scores spread out over a wider range of

parameter values, overlapping with good μ_{MSE} scores, while best scores for P_{MATCH} are again obtained with parameter values that are non-optimal for μ_{MSE} and $\sigma_{\Delta t}$. Comparing to the MVAB-0 and MVAE methods, the CP method can produce slightly lower μ_{MSE} than either while the best $\sigma_{\Delta t}$ and P_{MATCH} scores fall in between. If looking for a good compromise between low μ_{MSE} and maintaining low data mixing MVAB-0 is still the better option.

6.4.4 CPMV-B

Having eliminated 3 variables still leaves 7 variable parameters to consider for the CPMV-B method: N_{MVA}, r_{ev}, N_{box}, N_{sep}, ω, Φ_{diff} and θ_{lim}. Thankfully, using high N_{MVA} and low r_{ev} gives near-optimal results for all 3 test scores, allowing to pick just one value for each (N_{MVA} = 141 and r_{ev} = 1.5 have been used) in order to reduce parameter space to a more manageable 5 dimensions. Figure 6-33 and Figure 6-34 show the results.

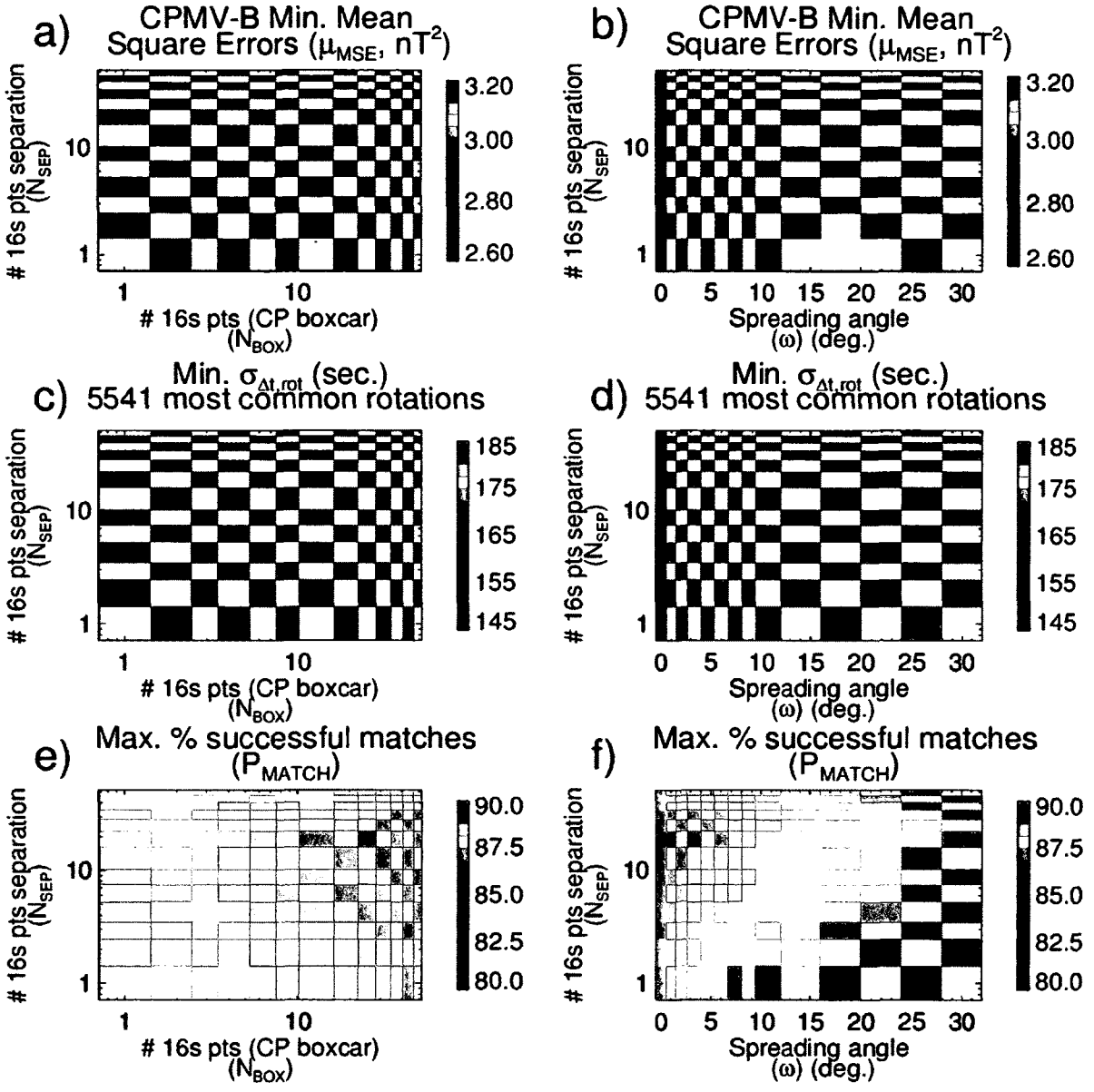

Figure 6-33 Part 3 CPMV-B Results 1. Distribution of test scores μ_{MSE} (a-b), $\sigma_{\Delta t}$ (c-d) and P_{MATCH} (e-f) as a function of parameters (N_{box}, N_{sep}) (a, c, e) and (ω, N_{sep}) (b, d, f) for the CPMV-B method.

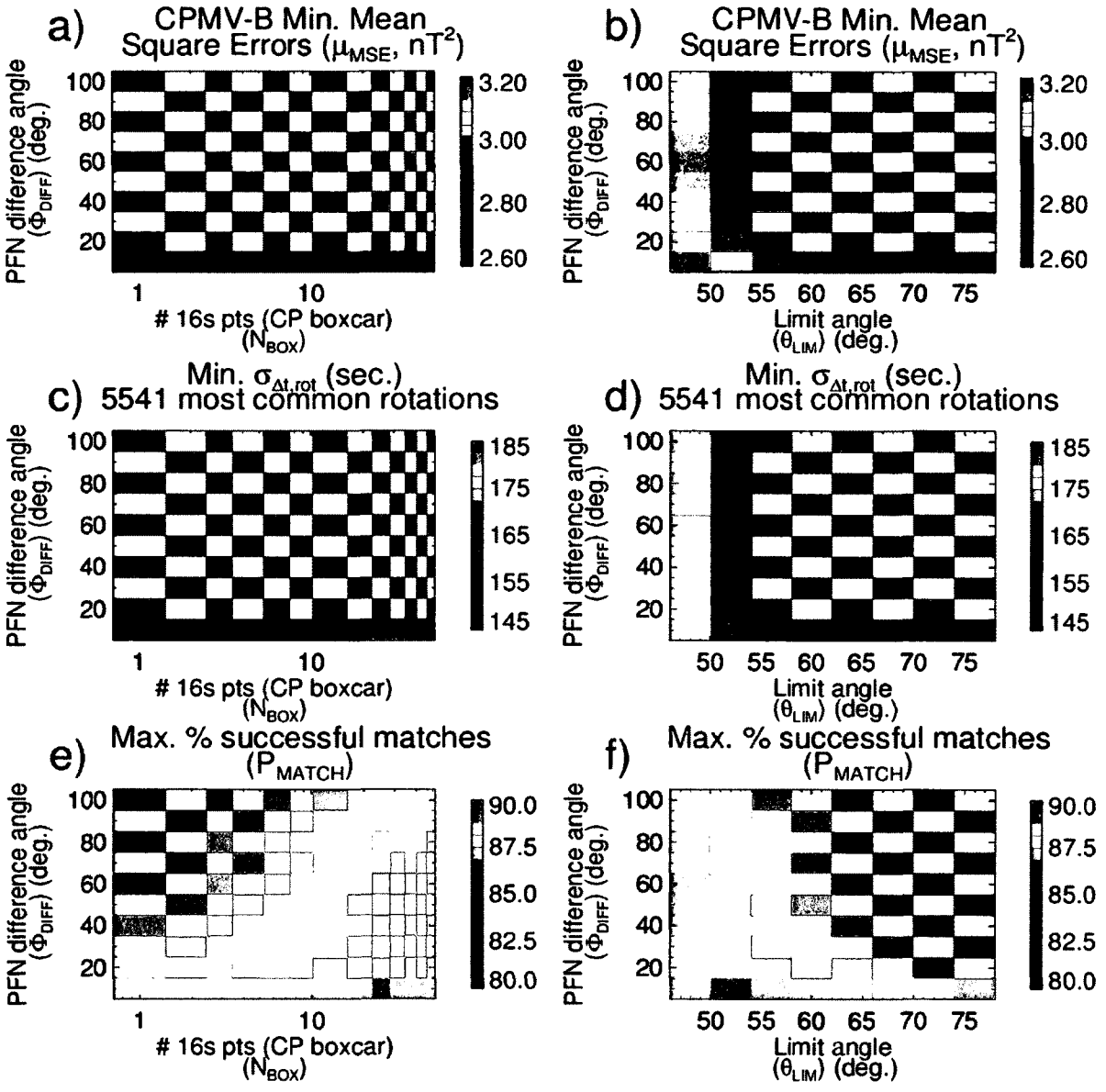

Figure 6-34 Part 3 CPMV-B Results 2. Distribution of test scores μ_{MSE} (a-b), $\sigma_{\Delta t}$ (c-d) and P_{MATCH} (e-f) as a function of parameters (N_{box}, Φ_{diff}) (a, c, e) and (θ_{lim}, Φ_{diff}) (b, d, f) for the CPMV-B method.

The lowest mean square errors are obtained using low N_{box} and N_{sep}, a low minimum spreading-angle and allowing a high MVAB-0/CP difference angle. The only noticeable difference from the results for general data propagation is that μ_{MSE} doesn't deteriorate as much for limit angles < 70° (Part 1 Figure 6-14). In contrast, the best scores for P_{MATCH}

are obtained for medium or high N_{box} and N_{sep}, low maximum PFN difference angle Φ_{diff} and a low limit angle θ_{lim}. For these four parameters the range of values that give best results for P_{MATCH} and μ_{MSE} are largely complements of each other. The volume that gives good results for $\sigma_{\Delta t}$ is mostly coincident with that which gives good μ_{MSE} but more expansive. In Figure 6-33 it appears to overlap a volume with high P_{MATCH}. However, Plots b), d) and f) in Figure 6-34 show that the overlap of good $\sigma_{\Delta t}$ and P_{MATCH} is limited to the lowest value of Φ_{diff} tested (10°), which produces significantly higher mean square errors. Still, for the volume of parameter space that has good μ_{MSE} and $\sigma_{\Delta t}$ the P_{MATCH} scores are as good as they were for MVAB-0 and better than CP and MVAE, and so the CPMV-B method stands out as giving best results without any drawbacks.

A main reason the CPMV-B method was not used for building the OMNI database was the use of parameter values that caused frequent gaps of > 3 hours with no PFN estimates available. According to the results presented here the CPMV-B method actually works best with very sparse filtering and hence no such extended gaps.

6.5 Comparison to Previous Work

A lot of computer code and many revisions of the code have been involved in producing the results presented. The code has been written in Interactive Data Language (IDL). Errors are inevitable, and for an extensive project like this there is always a possibility that errors can have gone unnoticed. However, the code has gone through a lot of scrutiny and in the end produced results that were consistent and explainable, occasionally in spite of differing from prior expectations. This leaves hope that any errors left are peripheral and have a negligible impact on results. One way to partially check the IDL code used in this study is to revise it so as to process the same data set used by *Weimer and King* [2008] to see if it reproduces their results (approximately – there is rich potential for differences in code implementation). For this purpose Algorithm C for data propagation needs to be modified in order to mimic the algorithm used in that study. Data points with a PFN-velocity angle above the limit angle are discarded altogether (rather

than removing and then interpolating such PFNs), and propagated and target data are not smoothed by a 4-point running average.

Figure 1 from *Weimer and King* [2008] is a plot of the distribution of mean square errors for MVAB-0 as a function of N_{MVA} and r_{ev}. This is shown in Figure 6-35 Plot b) alongside corresponding results generated with the code used in this study.

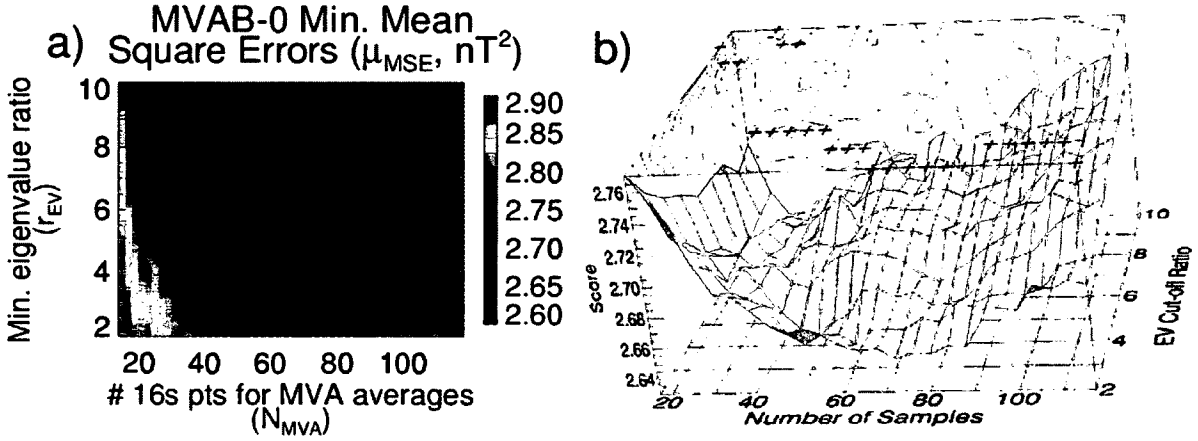

Figure 6-35 Comparison to Previous Study. MVAB-0 results as a function of (N_{MVA}, r_{ev}) (a) compared to Figure 1 from Weimer and King [2008] (b). Same data set was used for both plots (38 days, 1998-1999, WIND and IMP-8).

Due to the different plot styles it is difficult to compare the distributions in much detail, but there is significant disagreement. In particular, the distribution in Plot b) has lowest mean square errors for $N_{MVA} < 40$ with a minimum of 2.624 nT^2 at (N_{MVA}, r_{ev}) = (25, 7.8). This is outside the area that gives near-optimal mean square errors according to the code used in this study, which produces a minimum score of 2.604 nT^2 at (N_{MVA}, r_{ev}) = (51, 7.1).

Weimer and King [2008] also tested the CP and CPMV-B methods. For CP a minimum mean square error of 2.615 nT^2 was found at (N_{box}, N_{sep}, B_n, ω) = (19, 8, 4.2%, 8.8°), and for CPMV-B the minimum of 2.598 nT^2 was found at (N_{MVA}, r_{ev}, N_{box}, N_{sep}, ω, Φ_{diff}) = (21, 1.1, 11, 16, 9.8°, 9.9°), both with a PFN-velocity limit angle of 75°. For these specific parameter value combinations the IDL code

used in this study produced mean square errors of 2.761 nT^2 (CP) and 2.735 nT^2 (CPMV-B), but this is significantly away from the volume that produces near-optimal results. For CP a minimum of 2.670 nT^2 was found at (N_{box}, N_{sep}, B_n, ω) = (10, 27, 4%, 21°) while for CPMV-B a minimum of 2.553 nT^2 was found at
(N_{MVA}, r_{ev}, N_{box}, N_{sep}, ω, Φ_{diff}) = (107, 2.0, 1, 2, 6.0°, 26°).

In conclusion, an unknown but significant difference in code implementation remains, and it would require a detailed comparison of the two sets of code used to find it. Either set could be free of errors, but unfortunately comparing the results does not provide a convincing argument that this is likely the case.

6.6 Statistical Significance

An important question that remains to be answered about the results presented is that of statistical significance. Are the data sets used sufficiently large that the results are not just specific to this study? For example, in Part 1 the WIND data set was used, but about 2/3 of that data comes from a span of little more than a year (1998-1999, see Table 5-1). Would distributions look different for the IMP or Geotail data sets, and is there a significant dependence on phase of the solar cycle?

Figure 6-2 Plot a) showed the distribution of minimum μ_{MSE} as a function of (N_{MVA}, r_{ev}) for the WIND data set. Those same results have been plotted in Figure 6-36 Plot a) for comparison with corresponding distributions for the IMP and Geotail data sets.

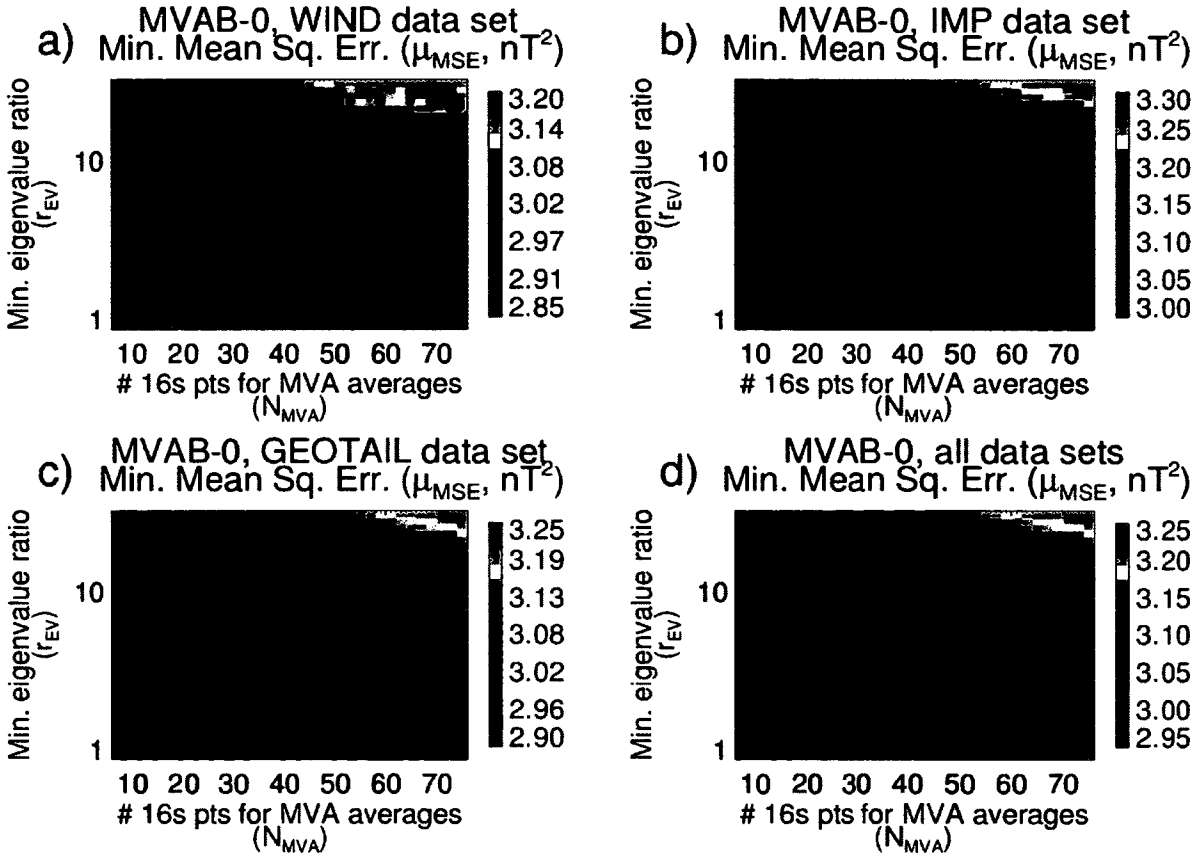

Figure 6-36 Variation by Satellite Data Set. Minimum values of μ_{MSE} for the MVAB-0 method as a function of (N_{MVA}, r_{ev}) when comparing propagated ACE data to the WIND (a), IMP (b) and Geotail (c) data sets. Plot d) shows results for all three data sets combined.

The distributions are mostly similar, yet there are some differences. Most noteworthy is that Geotail has near-optimal results all the way down to $N_{MVA} = 3$. Given that the Geotail data set is the only one stretching most of a solar cycle (almost 9 years) fairly evenly this suggests that the results may shift systematically as a solar cycle progresses.

Figure 6-37 shows how the distribution changes as a function of time.

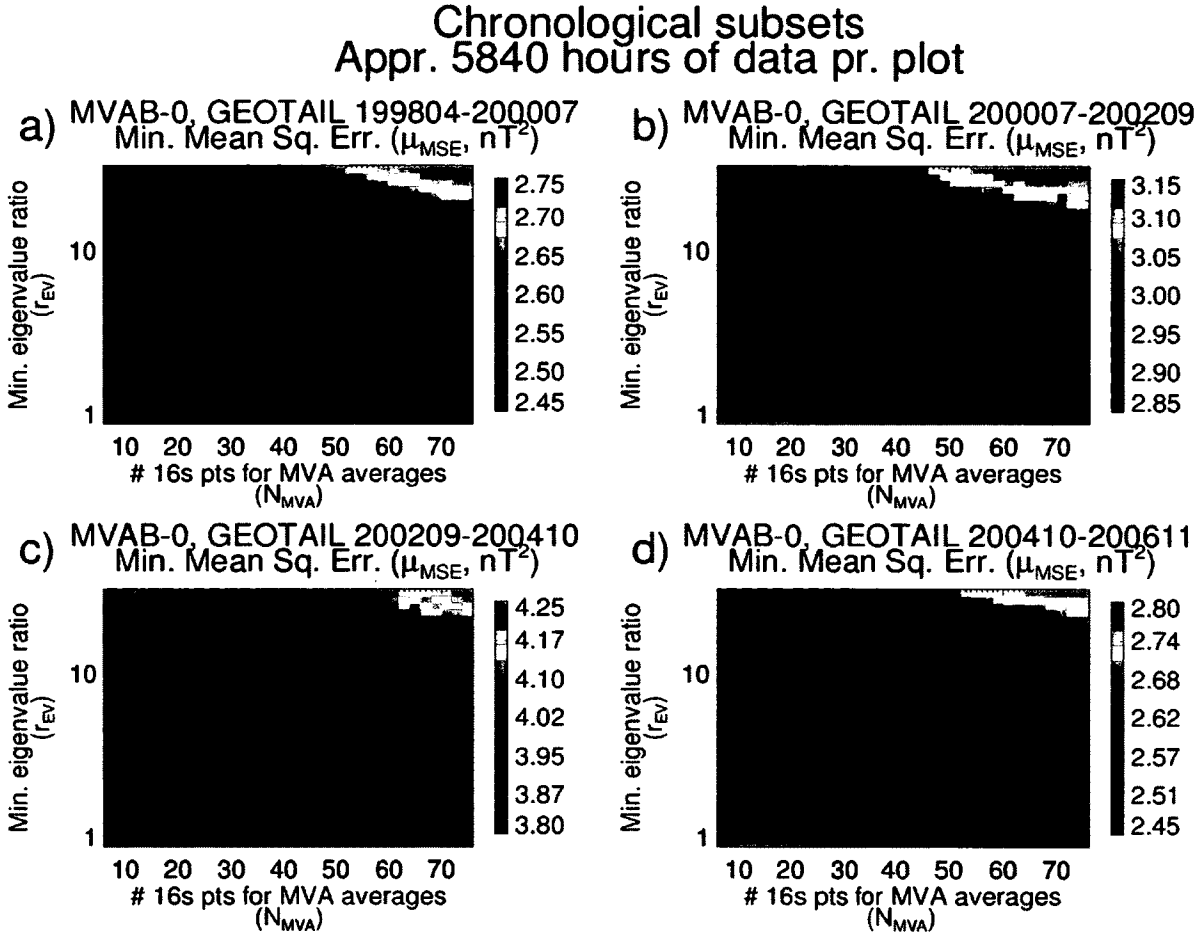

Figure 6-37 MVAB-0 Variation for Chronological Subsets 1. Minimum values of μ_{MSE} for the MVAB-0 method as a function of (N_{MVA}, r_{ev}) when comparing propagated ACE data to 4 chronologically ordered subsets of the Geotail data set.

The Geotail data set was split in 4 chronologically ordered subsets each of which spans a little more than 2 years. The first subset (Plot a)) covers April 1998 – July 2000 from which most of both the WIND and IMP data sets come, and the distribution is indeed quite similar to the corresponding ones for WIND and IMP (Figure 6-36 Plots a) and b)). However, during the years after solar maximum a lower value for N_{MVA} works better. Plot c) shows that $N_{MVA} = 3$ works best over extended periods of time, coincident with significantly higher mean square errors overall. It appears that during 2002-2004 there was a higher fraction of data with high variability where data mixing is effective in lowering mean square errors.

Two distinct features characterize the solar wind during the years following a solar maximum. One is a relatively high occurrence of coronal mass ejections. Even though CME ejecta still constitute a small minority of the data, the stronger magnetic field means very large mean square errors where source and target data disagrees, and so these intervals may carry enough weight that data mixing here can make an impact at the statistical level. The other feature is a high occurrence of large coronal holes extending down across the solar equator and associated higher percentage of data inside coronal-hole high-speed streams in the ecliptic plane. Inside high-speed streams the IMF is much more variable on short time scales as Figure 6-38 shows.

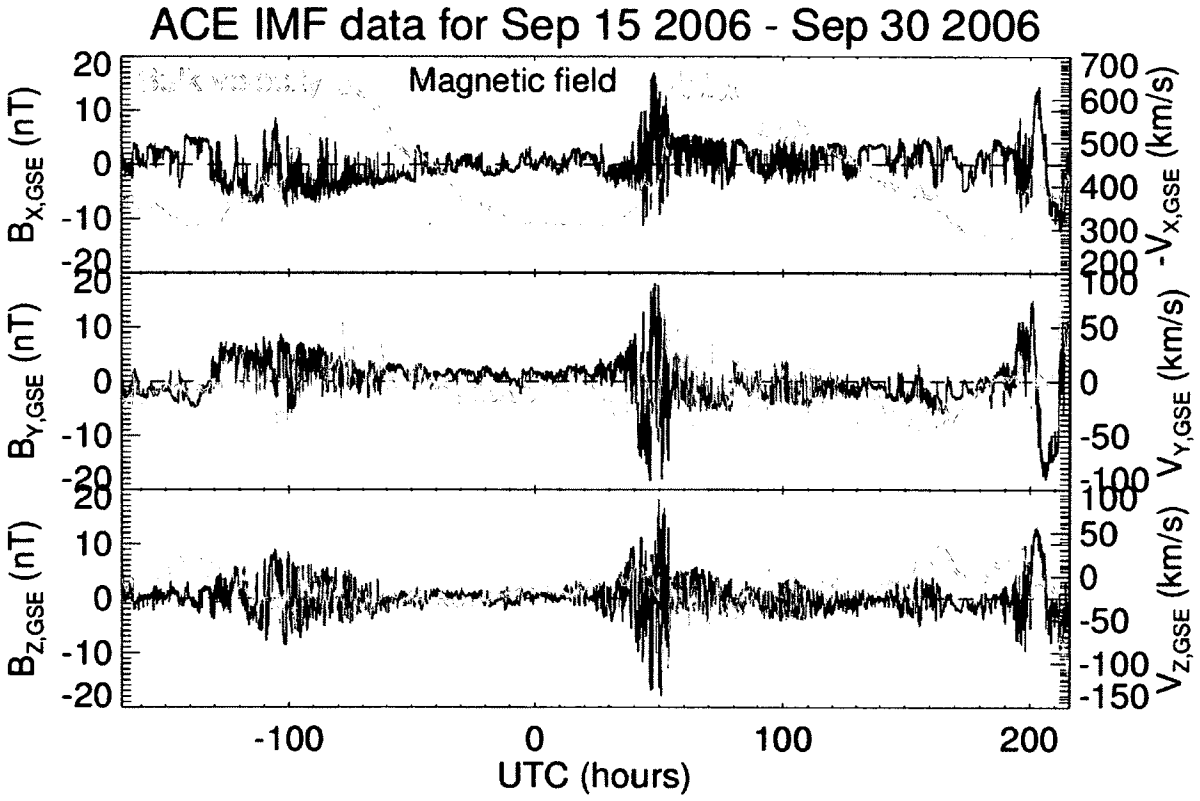

Figure 6-38 Coronal-Hole High-Speed Streams. 15 days of solar wind data with a mix of quiet intervals and coronal-hole high-speed streams. Notice the much higher IMF variability during high-speed streams.

With higher variability propagated data points with inaccurate PFN estimates are much more likely to deviate considerably from target data, causing higher mean square errors that may however be reduced through data mixing.

The optimal limit angle in terms of μ_{MSE} also appears to change systematically with phase of the solar cycle as Figure 6-39 shows.

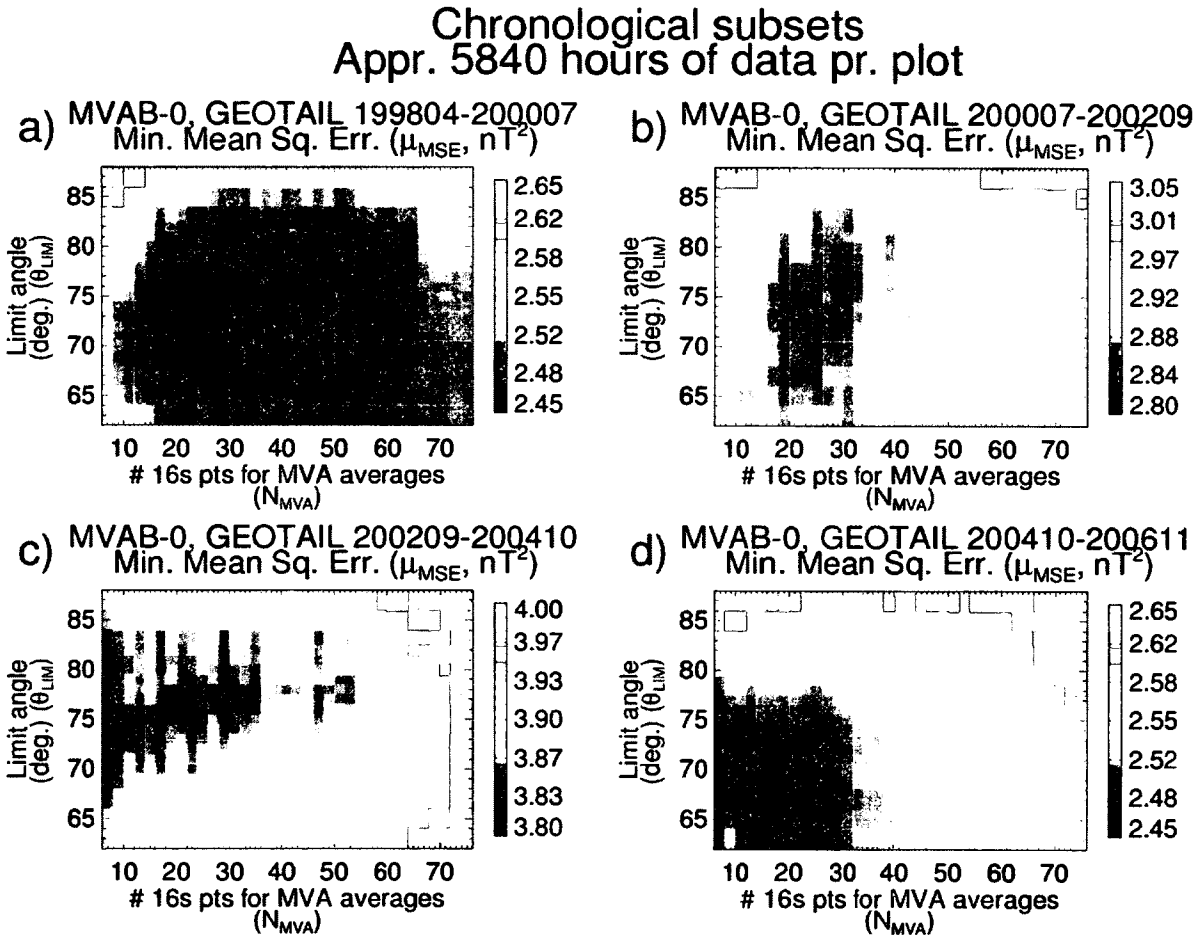

Figure 6-39 MVAB-0 Variation for Chronological Subsets 2. Minimum values of μ_{MSE} for the MVAB-0 method as a function of (N_{MVA}, θ_{lim}) when comparing propagated ACE data to 4 chronologically ordered subsets of the Geotail data set.

The range of angles giving best results was generally highest (~70°-83°) during 2002-2004 and lowest (~63°-75°) during the quieter 2004-2006. This could be because

the Parker Spiral stretches out during fast streams, giving higher average PFN-velocity angles. However, while this makes sense, caution with interpretation is needed as Figure 6-40 shows.

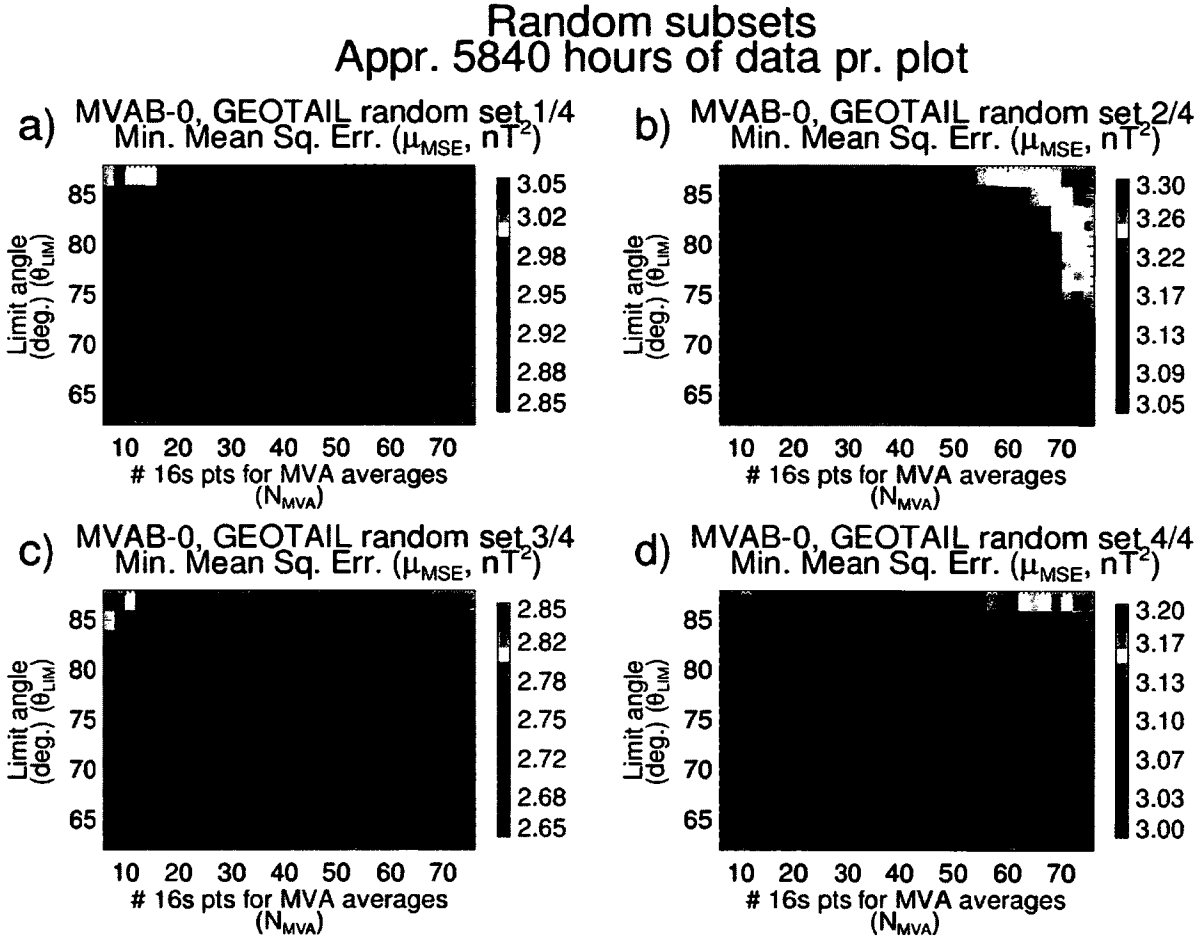

Figure 6-40 MVAB-0 Variation for Random Subsets. Minimum values of μ_{MSE} for the MVAB-0 method as a function of (N_{MVA}, θ_{lim}) when comparing propagated ACE data to 4 random subsets of the Geotail data set.

Here the Geotail data set was split in 4 parts each of which were spread evenly across the 9-year interval from which data was used, but otherwise being random samples of solar wind data. Distributions are more similar than for chronologically ordered subsets, yet it would appear that even with ~6,000 hours of data there may still be significant

sample variation. Note how Plot b) stands out, in particular the artificial looking steps in μ_{MSE} at $N_{MVA} = 35$ and $N_{MVA} = 45$. These steps were also present in Figure 6-39 Plot b) for the simple reason that they were caused by one single 70-hour interval of Geotail data with very high mean square error (minimum $\mu_{MSE} \sim 15$) due to extended intervals where ACE/Geotail were seeing different flux tubes. When this is the case a small change in a parameter value may make a big difference. It is clearly undesirable that a small amount of data where the assumptions for delay calculations are violated can carry so much weight, a point to consider in future studies. Note however that the minimum in any one of the plots occurs in an area with near-optimal results in any of the others, which is not the case in the chronologically ordered subsets. In that sense the distributions for WIND data shown in Figure 6-2 agree nicely with the large Geotail data set, suggesting that parameter values found to be optimal for the WIND data set are indeed close to optimal for solar wind data in general (in terms of the mean square error).

Given that the CPMV-B method produced superior results it is of interest to check what results look like for the large Geotail data set and in particular whether there is significant variation with phase of the solar cycle. Trivial results can be assumed to apply generally (e.g. μ_{MSE} decreasing monotonously with N_{box} and N_{sep}), but the optimal values of N_{MVA}, θ_{lim} and Φ_{diff} could vary some. Figure 6-41 shows the distribution of μ_{MSE} as a function of (θ_{lim}, Φ_{diff}) for chronologically ordered Geotail subsets.

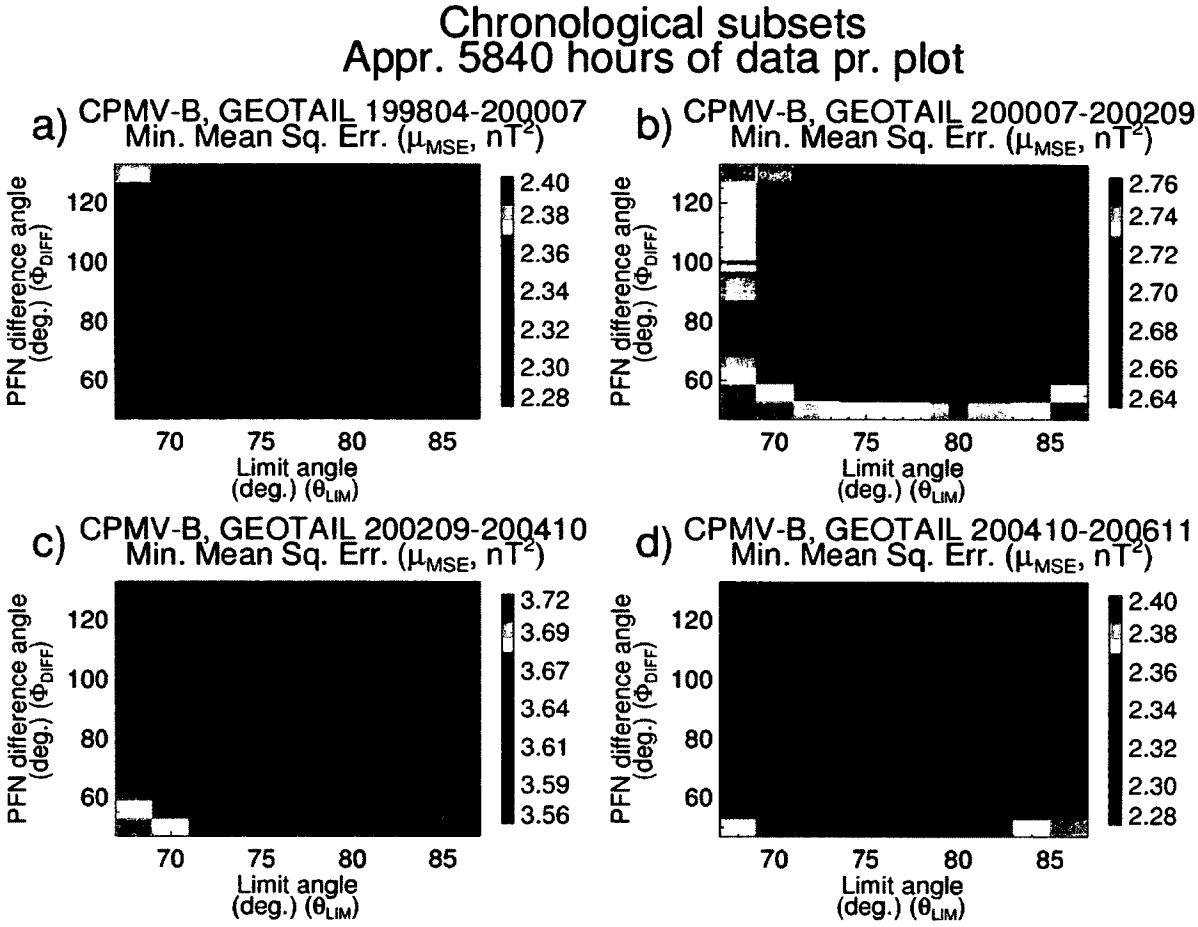

Figure 6-41 CPMV-B Variation for Chronological Subsets. Minimum values of μ_{MSE} for the CPMV-B method as a function of (θ_{lim}, Φ_{diff}) when comparing propagated ACE data to 4 chronologically ordered subsets of the Geotail data set.

The distribution does indeed shift significantly, but with an overlap in near-optimal results around $\theta_{lim} = 80°$ and $\Phi_{diff} = 100°$. With the WIND data set best results occurred around (θ_{lim}, Φ_{diff}) = (80°, 80°) (Figure 6-14) and with N_{MVA} from ~70 and up, which is in fine agreement with the Geotail data set.

For the case of discrete propagation there is less potential for dependence on solar cycle, and the definition of the test score $\sigma_{\Delta t}$ eliminates potential for isolated observations to have influence at the statistical level. The different distributions shown in Part 2 generally vary little when split into subsets with one exception. There is some change in

how results depend on N_{MVA} for the methods employing this parameter, particularly for CPMV-B. The variation with solar cycle is shown in Figure 6-42.

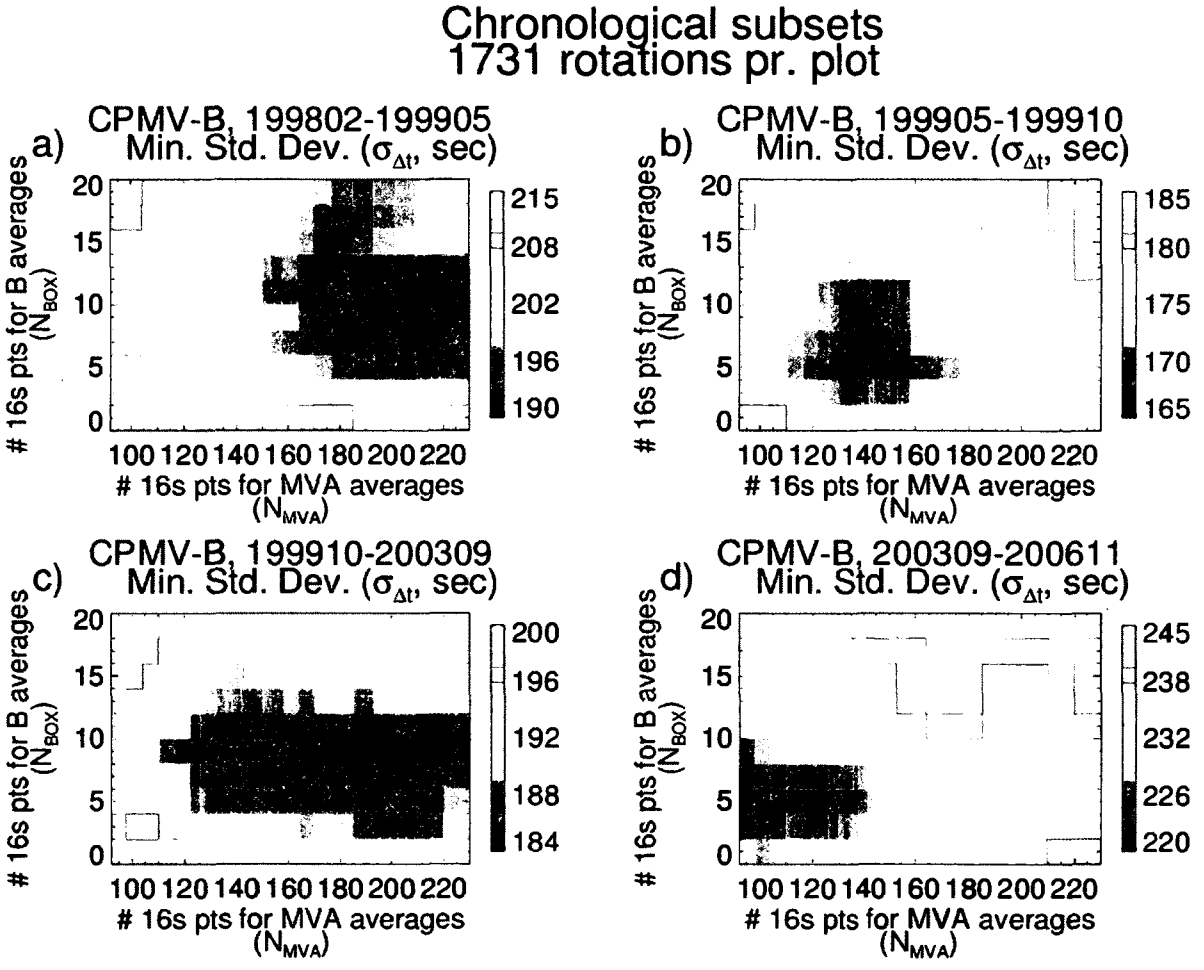

Figure 6-42 Variation for Discontinuity Subsets. Minimum values of $\sigma_{\Delta t}$ for the CPMV-B method as a function of (N_{MVA}, N_{box}) when dividing the full discontinuity data set into 4 chronologically ordered subsets.

Given that the data sets used in Part 1 and Part 2 of the study generally produce statistically significant results this is also expected for the data set used in Part 3. Indeed there is little change between subsets, except that $\sigma_{\Delta t}$ consistently degrades for high limit angles (from ~75°) for the last of 4 chronologically ordered subsets (09/2003 – 11/2006).

7 Discussion

8 different methods for propagating solar wind data from ACE to the magnetosphere have been tested. These can be divided into 3 groups: Magnetic field base methods (MVAB, MVAB-0 and CP), electric field base methods (MVAE, MVAE-0 and ED) that are parallels to their magnetic field counterparts, and then two combination methods (CPMV-B and CPMV-E). All methods were tested for 3 different applications: Continuous propagation of general solar wind data (Part 1), discrete propagation of IMF discontinuities (Part 2) and continuous propagation of IMF discontinuities (Part 3).

7.1 Summary and Interpretation

Figure 7-1 shows a graphical summary of the results from Part 1 and Part 2 listed in Table 6-3, Table 6-4 and Table 6-5 and with results for flat delay, "best match delay" (see notes for Algorithm B) and the CPMV variant used to produce the OMNI database added for comparison.

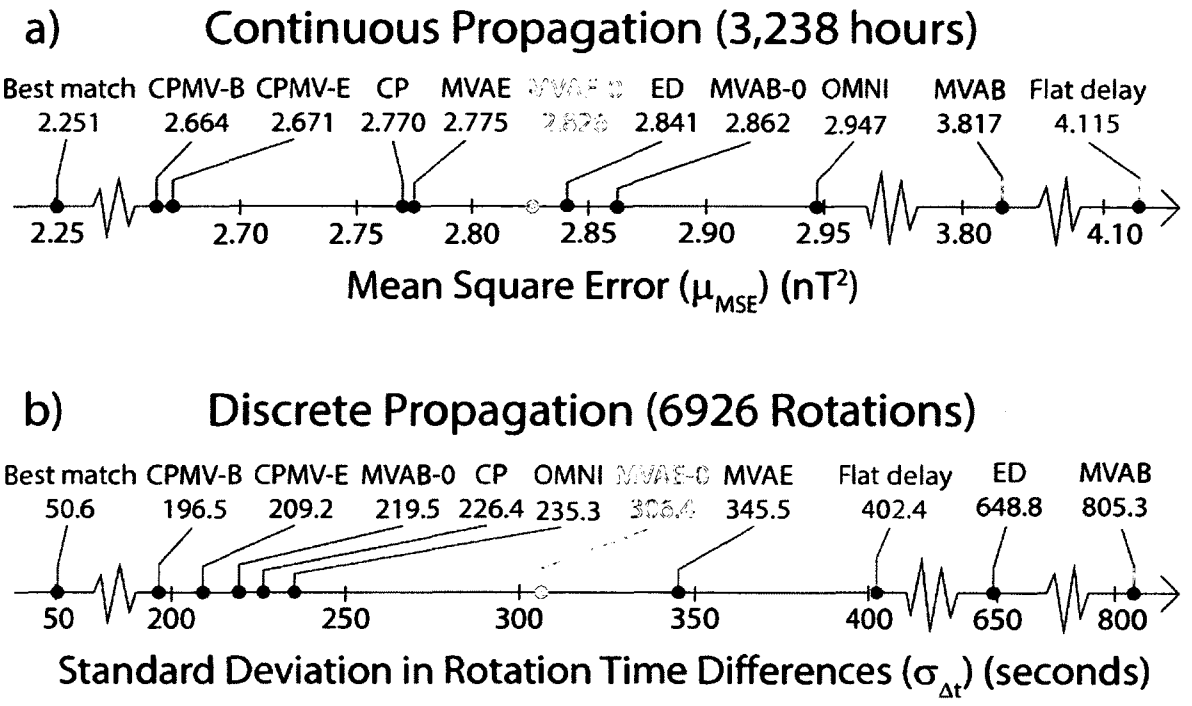

Figure 7-1 Graphical Overview of Results. Best test scores (μ_{MSE} and $\sigma_{\Delta t}$) listed in Table 6-3, Table 6-4 and Table 6-5 and with results for "best match delay", flat delay and OMNI CPMV delay added.

The CPMV-B method gave superior results for both continuous and discrete propagation followed by the alternative combination method CPMV-E. CP and MVAB-0 methods also produced good results in both cases while the electric field methods MVAE, MVAE-0 and ED did well for continuous propagation but produced mediocre results for discontinuities. For either application the MVAB method gave the worst results. For comparison the OMNI CPMV variant performed well for discrete propagation but did not produce quite as low mean square errors for continuous data.

The more qualitative overview in Part 3 confirmed the same relative performance between methods established in Parts 1 and 2 as described above. Furthermore it showed that a majority of discontinuities can be predicted with significantly better accuracy when propagating a surrounding continuum of data as opposed to a single data point (~25% reduction in standard deviation for a distribution containing 80% of the discontinuities). For the remaining minority the IMF profile is commonly altered by data mixing when

doing continuous propagation, making it difficult to impossible to estimate an arrival time accurately. In these cases discrete propagation gives better results on average. It was also shown that the lowest mean square errors were obtained with parameter values that cause a high level of data mixing, having the side effect of altering IMF profiles and increasing the percentage of discontinuities that could not be identified in propagated data. However, this pattern does not repeat when comparing the different methods tested. The CPMV-B method convincingly gives both the lowest mean square errors and best timing accuracy for discontinuities and at the same time maintains a high rate of discontinuities identifiable in propagated data.

In setting up the different methods and their variable parameters the focus was on the large-scale structure of the solar wind. Interaction between the solar wind and the magnetosphere is dominated by large-scale structures, and small-scale structures cannot be extrapolated accurately over large distances anyway. However, most of the time (inside flux tubes) solar wind fluctuations are dominated by small-scale structure, which may then determine the orientation of PFN estimates. This poses a challenge because these structures have characteristics of Alfvén waves propagating along flux tubes, roughly perpendicular to the orientation of the large-scale structures that the methods are aimed for. The underlying theory from which all the propagation methods were derived is that of plasma discontinuities, more specifically the Rankine-Hugoniot jump conditions. The response to waves wasn't taken into account, and so the study in part turned into an empirical investigation of how they affect PFN estimates for each method.

The MVAB method turns out to be effective for determining the orientation of wave phase fronts. Unfortunately that means it produces PFNs that are mostly parallel to $\langle \mathbf{B} \rangle$ and do not agree with the large-scale solar wind structure, making it a poor tool for propagating solar wind data. Imposing the requirement $\langle \mathbf{B} \rangle \cdot \mathbf{n} = 0$ effectively fixes the issue, and accordingly the MVAB-0 variant produces much better results. Electric field perturbations associated with waves are perpendicular to **B**, leading the MVAE method to produce normals that are also perpendicular to $\langle \mathbf{B} \rangle$ and hence generally good PFN

estimates. Adding the requirement $\langle \mathbf{B} \rangle \cdot \mathbf{n} = 0$ changes little, and the MVAE and MVAE-0 methods overall produce very similar results. Inside flux tubes perturbations to $\langle \mathbf{B} \rangle$ are generally small compared to $\langle \mathbf{B} \rangle$ itself and therefore the CP method is relatively unaffected, producing PFNs that agree with large-scale structures. The ED method is not similarly insensitive to small-scale structure, but given the right parameter values it will also produce PFN estimates roughly perpendicular to **B** regardless and is capable of performing well for continuous solar wind propagation.

Small-scale structure has less influence when propagating discontinuities, yet the poor MVAB results show that waves propagating along **B** are still significant. The MVAE/MVAE-0 methods still give decent results (better than flat delay) but do not compare well to MVAB-0 or CP. PFNs remain close to perpendicular to **B**, but with more deviation compared to both the continuous case and to CP/MVAB-0. The poor results of the ED method illustrate that the Rankine-Hugoniot jump condition for the electric field is not accurate, and so the decent results of MVAE/MVAE-0 would seem to be caused by the influence of waves. It also helps that discontinuities tend to obey an alfvenic relationship (see Equation (B.3) in Appendix B and comments about the time variable part of the electric field in Part 1, MVAE). Some vector algebra shows that the alfvenic property also makes the ED method produce PFN estimates close to perpendicular to the magnetic field. It is also worth noting that conflicting assumptions were made in the process of setting up the electric field methods. On one hand they are based on a Rankine-Hugoniot jump condition for changes in the electric field across ideal discontinuities. On the other hand, HT analysis on an ideal discontinuity would find a perfect frame with zero electric field on both sides of the discontinuity, leaving the electric field methods unable to find a PFN estimate.

A first for this study is the use of HT velocities for data propagation. For continuous propagation (Part 1) it led to slightly lower mean square errors for some methods. However, although statistically significant the improvements were practically negligible. Part 2 revealed a more noticeable improvement in accuracy of predicted arrival times for discontinuities (a few percent drop in the standard deviation) when using HT frames

calculated from a high number of data points. Perhaps the most significant advantage to using a HT frame (high $N_{HT,P}$) was uncovered in Part 3: It helps prevent out-of-sequence data, in particular mixing of data from adjacent flux tubes around discontinuities. Figure 7-2 shows a data sample illustrating how using HT velocities with high $N_{HT,P}$ (here 101) prevents most of the data mixing that sudden variations in bulk velocities cause when using these for propagation.

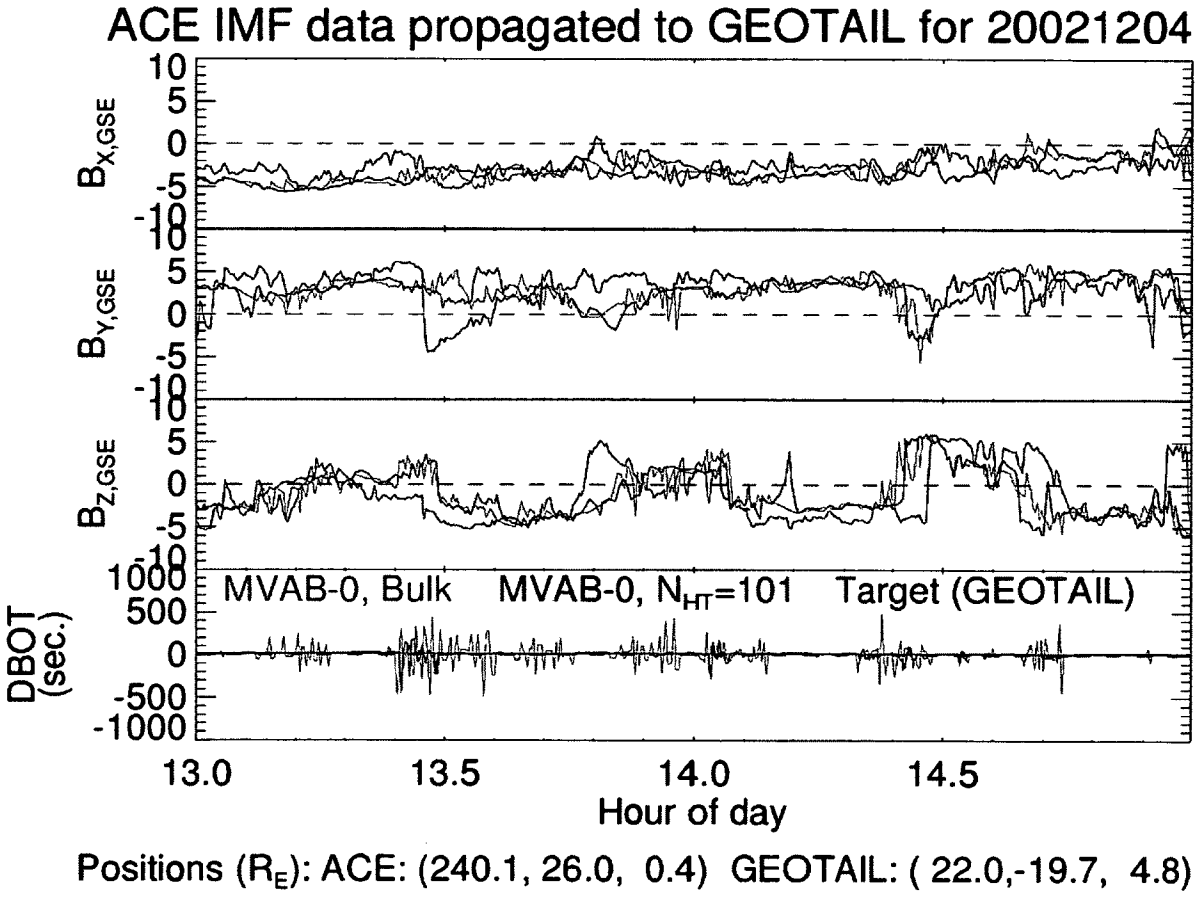

Figure 7-2 HT Data Mixing Reduction. 2 hours of ACE IMF data propagated to Geotail using MVAB-0 with (N_{MVA}, r_{ev}, θ_{lim}) = (101, 5, 70°) and using bulk (grey) and HT velocities (green, $N_{HT,P}$ = 101) for propagation. Also plotted is measured Geotail data (red). Bottom plot shows duration between observation times (DBOT) with negative values corresponding to out-of-sequence data.

Negative values of DBOT (duration between observation times) in the bottom plot represent out-of-sequence data. Figure B-5 in Appendix B shows bulk and HT velocities for the day that this interval was taken from. The MVAB-0 parameter values used were chosen so as to minimize data mixing due to varying PFN directions in order to expose data mixing caused by velocity variations. Generally, the methods and parameter values found to give near-optimal test scores for μ_{MSE} and $\sigma_{\Delta t}$ are associated with significantly higher variability in PFN directions, which then becomes the dominant source of data mixing (e.g. compare to Figure 5-1). Using bulk velocities (or low $N_{HT,P}$) still contributes and can occasionally cause ill-defined transitions on its own as seen around 14:25UT in Figure 7-2. In summary, using HT velocities for propagation (high $N_{HT,P}$) manages to decrease data mixing while maintaining practically identical mean square errors and improving accuracy for predicted discontinuity delays slightly (both discrete and continuous propagation). An interesting side note is that the more accurate delay estimates for IMF discontinuities when using HT velocities suggests that there is a population of rotational discontinuities with small but finite propagation velocities in the plasma rest frame, a question that previous studies have left unanswered [e.g., *Knetter,* 2005].

Results also reveal that on average discontinuities arrive at the target about 30 seconds later than predicted. This corresponds to an error of about 1% in either velocity or distance. Adding this shift when doing continuous propagation also improves mean square errors slightly. For example, the best score for CPMV-B is lowered from $\mu_{MSE} = 2.664\ nT^2$ to $\mu_{MSE} = 2.652\ nT^2$ when a constant 30 seconds is added to the calculated propagation delays.

Starting with velocity, one possible explanation for the offset would be a systematic error in ACE data. King and Papitashvili did a cross-spacecraft comparison between ACE and WIND plasma velocity data (16360 hours, 1998-2004) (see http://omniweb.gsfc.nasa.gov/html/HROdocum.html). Flow speeds agreed to within 1% or less with WIND speeds generally exceeding those of ACE, so if anything this would suggest ACE velocities being slightly low. A flow angle bias could also make the

difference. Good PFN distributions are centered around +45° azimuth relative to the velocity with no elevation angle offset. Hence an azimuth bias would most likely be required, and the ACE-WIND cross-comparison showed a ~0.2° azimuth difference, but with WIND being higher, corresponding to ACE velocities having a lower PFN-directed component. Hence, comparison to WIND data does not suggest that ACE data produces too high propagation velocities. To explain the 30-second offset as a result of velocity error both ACE and WIND would have to be subject to a similar and unknown systematic error.

A second possible explanation would be if the solar wind decelerates during the travel time from L1 to Earth, but assuming a constant average deceleration the solar wind would have to slow down by about 2% over this relatively short distance, which is in disagreement with both models (*McGregor et al.* [2011]) and observations (e.g. above-mentioned WIND-ACE comparison). A third candidate for an explanation would be deceleration of the solar wind in the foreshock region (where flux tubes intersect the bow shock). A statistical study by *Fu et al.* [2009] shows that solar wind velocity drops are mostly limited to within ~10 R_E from the bow shock in a region where the angle between the IMF and bow shock normal is less than ~60°. On average solar wind speeds here are lowered by 1-2% (though with a large spread in observations, reductions up to ~10% are observed). Hence the deceleration would only influence the data over a relatively short distance and only for part of the observations, making it unlikely to be responsible for a shift in discontinuity arrival time of the magnitude observed. This is supported by looking at the shift as a function of where the target satellite was located at the time of observation. Figure 7-3 shows how the shift varies depending on where discontinuities were observed.

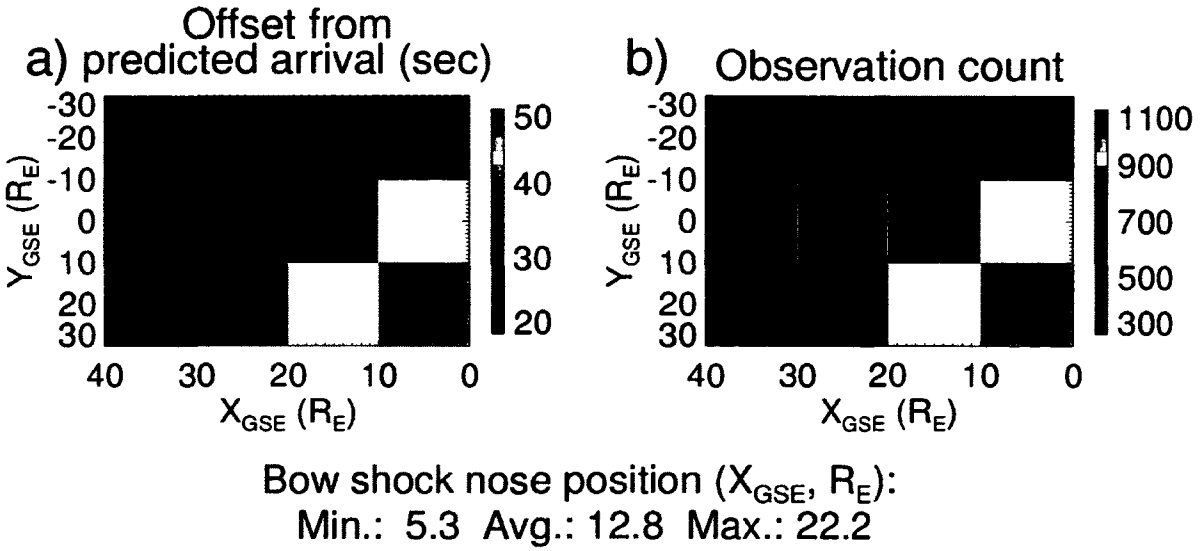

Figure 7-3 Arrival Offset vs. Target Position. Shift of average discontinuity arrival time from predicted (a) and number of discontinuities observed (b) as a function of target satellite position.

The average bow shock nose location is at about X_{GSE} = 13 R_E, and the dominant IMF direction (Parker Spiral) is across the plot from upper left to lower right. This means that the foreshock deceleration region would mostly be restricted to $X_{GSE} < \sim 10$ R_E on the dusk side of Earth (positive Y_{GSE}) but extend to $X_{GSE} < \sim 20$ R_E on the dawn side. Shifts vary somewhat randomly with position, if anything being higher on the dusk side, but not dipping below ~25 seconds anywhere.

Next the option of distance error is considered. For average solar wind speeds the 30 seconds corresponds to a distance error of ~2 R_E in the X_{GSE} direction or a ~1.5 R_E error along the dominant PFN direction (perpendicular to Parker Spiral in ecliptic plane). Satellite positions are known to within meters, so an error of this magnitude must be explained by failure of the assumption that phase fronts are infinite planes. In particular, the offset may be an indication that phase fronts are predominantly bending towards the Sun so that tangent planes are most often ahead of the actual phase front. Considering the flux tube image of the solar wind there are two different types of curvature to consider: Along a flux tube and along the circumference of a flux tube. The latter is expected to have significantly shorter scale and therefore seems more likely to be responsible for the

discrepancy. If the flux tubes had circular or elliptical cross sections, the "front" and "back" sides of the flux tubes would be oppositely curved and there would be no bias in the delay errors. However, generally flux tubes must have a somewhat different shape since circular/elliptical cross sections would not fill out space, and it makes sense that they would on average have an asymmetry that cause most phase fronts to curve towards the Sun. Figure 7-4 illustrates a scenario where almost all phase fronts curve towards the Sun.

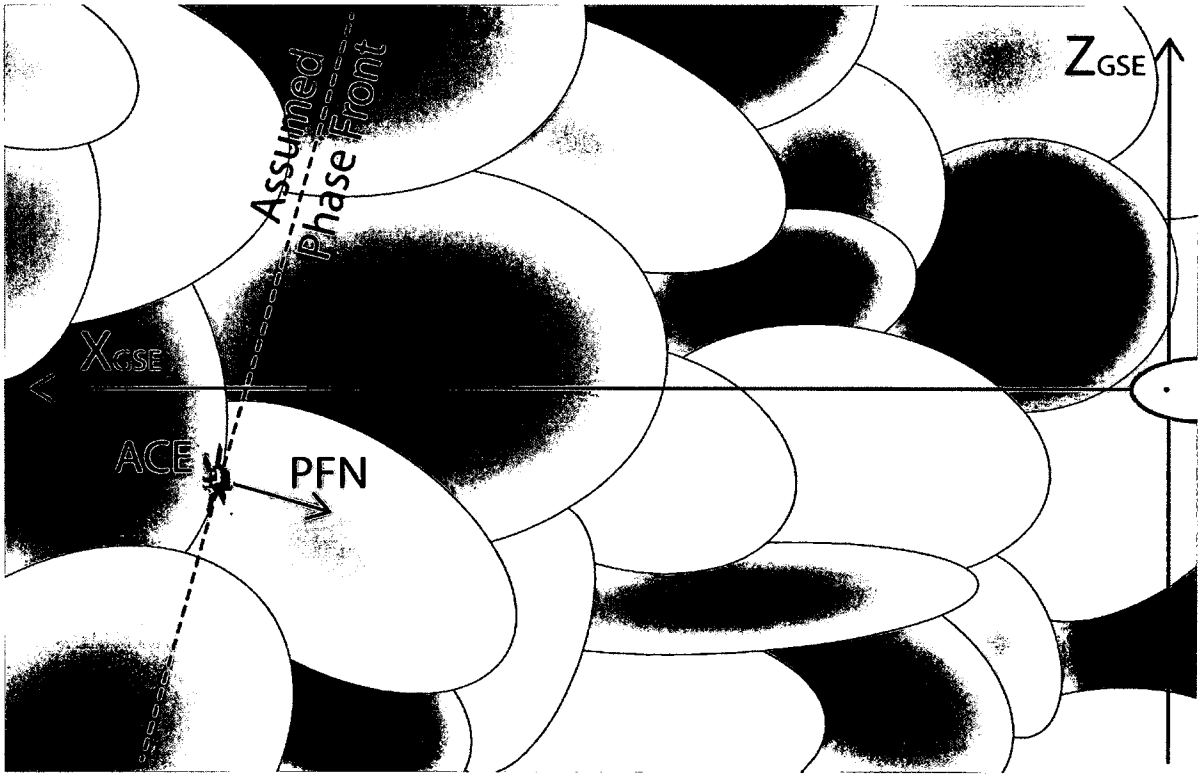

Figure 7-4 Sunward Curving Phase Fronts. This sketch illustrates the possibility of solar wind flux tube geometry with a dominance of phase fronts curving towards the Sun. Note how the assumed phase front observed at ACE is ahead of the actual phase front, which will therefore arrive later than predicted.

Note how the phase front arriving at ACE is farther away from Earth than the infinite plane assumed in the calculations, causing predicted arrival to be too early. Figure 7-4

exaggerates the point of sunward curving phase fronts as it is more likely that a large percentage of phase fronts would be expected to curve away from the Sun even if sunward curvature is dominant. A possible physical explanation for such an asymmetry could be that upstream flux tubes have expanded incrementally less than their downstream neighbors and therefore have a slightly higher interior plasma pressure, which could over time cause the separating walls to "bulge" and expand into the volume of downstream flux tubes. Another way to consider this is that upstream flux tubes are being pushed against downstream tubes due to the Sun's rotation. There are also options for asymmetry in curvature along flux tubes with a majority of flux tubes bending towards the Sun. The Parker Spiral structure is one such example, but the spiral curvature is negligible on the scale considered here. Some flux tubes could still be "closed" as they arrive at Earth, bending through the heliospheric current sheet and returning to the Sun. However, significant curvature would be restricted to a volume close to the current sheet, which ACE crosses only occasionally. Curvature along flux tubes would only be expected to be responsible for a small systematic error, significantly less than observed.

If ACE were sitting exactly on the Sun-Earth line, phase front geometry would hardly affect predicted arrival times. It is the transverse separation (distance in the GSE YZ-plane) between ACE and Earth that causes a significant error when the geometry is not accounted for correctly. Likewise, a distance error due to phase front curvature should grow monotonously as the transverse distance between ACE and the target satellite increases. If the 30-second offset is indeed due to a distance error caused by curvature effects it is then expected that the offset has a pronounced dependence on transverse source-target separation. Table 7-1 shows how the error varies when the discontinuities are split into 5 equally large subsets (1,384 observations each) sorted according to transverse source-target separation. The position change of the GSE coordinate system during transit due to Earth's orbital motion around the sun was taken into account when calculating transverse separations.

Table 7-1 Offset Dependence on Transverse Separation. The set of 6,926 discontinuities was split into 5 equally large subsets, sorted according to transverse separation between ACE and the target satellite, and standard deviation and offset was calculated for each.

ACE-target separation in GSE YZ-plane (R_E)			Standard deviation	Offset
Min.	Median	Max.	(seconds)	(seconds)
0.73	11.67	16.71	135.84	31.45
16.71	20.61	24.21	145.99	30.22
24.21	27.70	32.49	165.74	37.55
32.49	38.64	46.57	217.34	35.77
46.57	58.62	98.91	330.36	22.91

The standard deviation is a measure of prediction error due to geometric effects. Specifically the main error sources are inaccurate PFN estimates and curvature of phase fronts, both causing the assumed flat phase front plane to be off. Consistent with this, the standard deviations in Table 7-1 show a pronounced and unambiguous dependence on transverse separation. However, the offset shows no such dependence, calling into question the hypothesis that the offset is caused by curvature effects.

Propagation of data from ACE to Earth may serve one of two purposes: Real-time forecasting or studies of past data. The OMNI database is commonly used for the latter, and the results from this study suggest it is based on a non-optimal propagation method (see Figure 7-1). Specifically, propagation for OMNI was done using a combination of the CP and MVAB-0 methods devised by King and Papitashvili (see http://omniweb.gsfc.nasa.gov/html/HROdocum.html) with parameter values that were found during the research done by *Weimer and King* [2008] but different from the values published in their final article. A main reason they implemented an alternative to the CPMV-B method was to avoid extended gaps with no good PFN estimates available, but these gaps were a result of the parameter values used and can be avoided with values found to be near-optimal in this study. Before considering updating the OMNI database more research would be required though. The significant differences between the results

presented in this study and those found by *Weimer and King* [2008] suggest a need for validation. More important improvements to the single satellite propagation techniques are also possible and will be discussed in the following section. For real-time forecasting the results in this study may serve as a guide, but actual implementation is a matter of priority. It's desirable to use only a short interval of data for PFN estimation, but also to avoid data mixing and of course to have the propagated data be accurate. A compromise will have to be made to strike a balance between these objectives.

7.2 Suggestions for Future Research

Propagation of solar wind data from ACE to the magnetosphere has some inherent problems that cannot be solved. One is the compromise between out-of-sequence data and detrimental filtering, and another is the difference in IMF structures arriving at ACE and Earth respectively. However, there is still potential for improving the relatively simple propagation techniques tested in this study.

The problem with out-of-sequence data is an inescapable consequence of having inadequate data available for the task, and while intervals with data mixing in propagated data are undesirable they illustrate well the uncertainty associated with the single satellite propagation technique. More specifically it is intervals of extended data mixing (significant overlap between data from two different flux tubes) that are of particular concern. It's clear that a method for estimating which data is more likely to be "correct" (closer to actual target data) when extended mixing occurs must be more sophisticated than the "early"/"late" options tested here. A statistical study could be done on cases of extended data mixing, looking at properties of involved flux tubes (e.g. orientation relative to plasma velocity, size, "late"/"early" etc.) and their separatrix, comparing the distributions for "observed" and "erased" flux tubes. This might allow adding a weight to flux tubes according to the probability that they will be observed when extended data mixing occurs.

Handling of data mixing should be part of a wider effort to indicate reliability of propagated data. There are prolonged intervals of time where propagated ACE data

correlates rather poorly with that at a near-Earth target satellite as opposed to other intervals where the correlation is near perfect. Apart from cases of extended data mixing it is not possible to tell the quality/accuracy of propagated data without such an indicator. Again, a statistical study of the properties of solar wind data with good versus poor correlation with target data could help establish a reliability indicator (positions of source/target satellite should clearly be taken into account as well). One particular idea is to investigate the structure of the solar wind "flux tube spaghetti". It may be possible to estimate the curvature of flux tube walls in the plane perpendicular to the tube axis given the IMF direction inside, duration of ACE passage and possibly the orientation of PFNs at the surrounding flux tube walls. Perhaps this information could be used to identify cases where flux tubes seen by ACE may not impact the magnetosphere. An example is shown in Figure 7-5 where ACE passes through the top of a circular flux tube aligned with the Parker Spiral, a case where it may be predicted that the flux tube will miss the magnetosphere (if PFN estimates at flux tube walls are accurate).

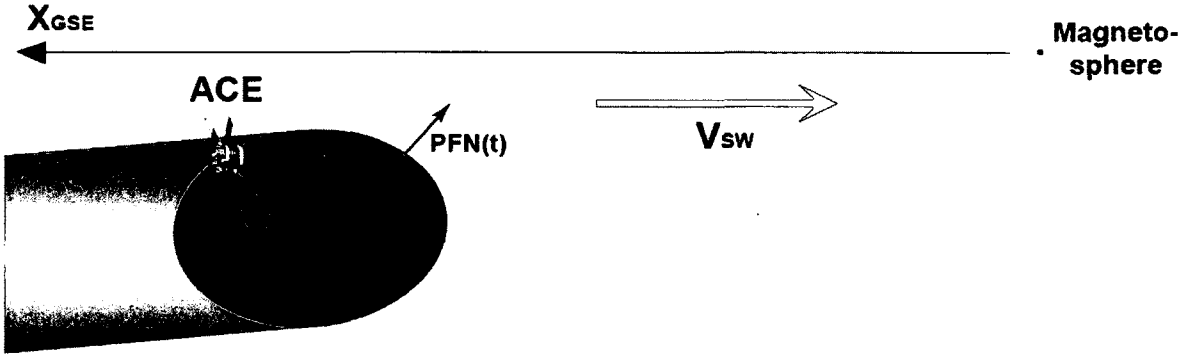

Figure 7-5 Flux Tube Missing Earth. A flux tube seen by ACE doesn't impact the magnetosphere. The flux tube axis (given by the interior magnetic field direction) and the PFNs at the flux tube walls may indicate when this is likely to happen.

Of course, as argued previously flux tubes generally need to deviate from circular shape to fill out space, which is why the actual geometry needs to be assessed. This could be done in part by statistical studies of flux tubes observed by multiple satellites varying

distances apart. An estimate for single satellite PFN accuracy is also needed, and a study of Cluster data could facilitate that, comparing single satellite PFN estimates in between satellites and to those derived from triangulation (similar to the analysis by *Knetter* [2005] for MVAB, but for a good PFN estimation method like CPMV-B instead). Another way to investigate possible flux tube structure would be through MHD simulations [e.g., *Greco et al.*, 2008], comparing results to actual solar wind observations.

Using WIND and ACE data in combination may be particularly useful for investigating geometry of flux tubes near L1. Comparing data from both these monitors may also be directly used to assess the reliability of data propagated from either, something that could become valuable for short-term prediction assuming both ACE and DSCOVR will be delivering data real-time from 2015. It is also desirable to have error estimates on the arrival time of specific transitions. For this purpose it would be useful to examine how the error depends on different properties of transitions, such as the variables that are used to (attempt to) filter out poor PFN estimates. A quick check of the set of IMF discontinuities used in this study reveals that when using the most accurate method (CPMV-B) and parameter values there is no significant dependence on eigenvalue ratio, spreading-angle or the normal component of **B** while there is a clear tendency for increasing errors as the PFN-velocity angle is increased beyond ~60° (see Figure 7-6).

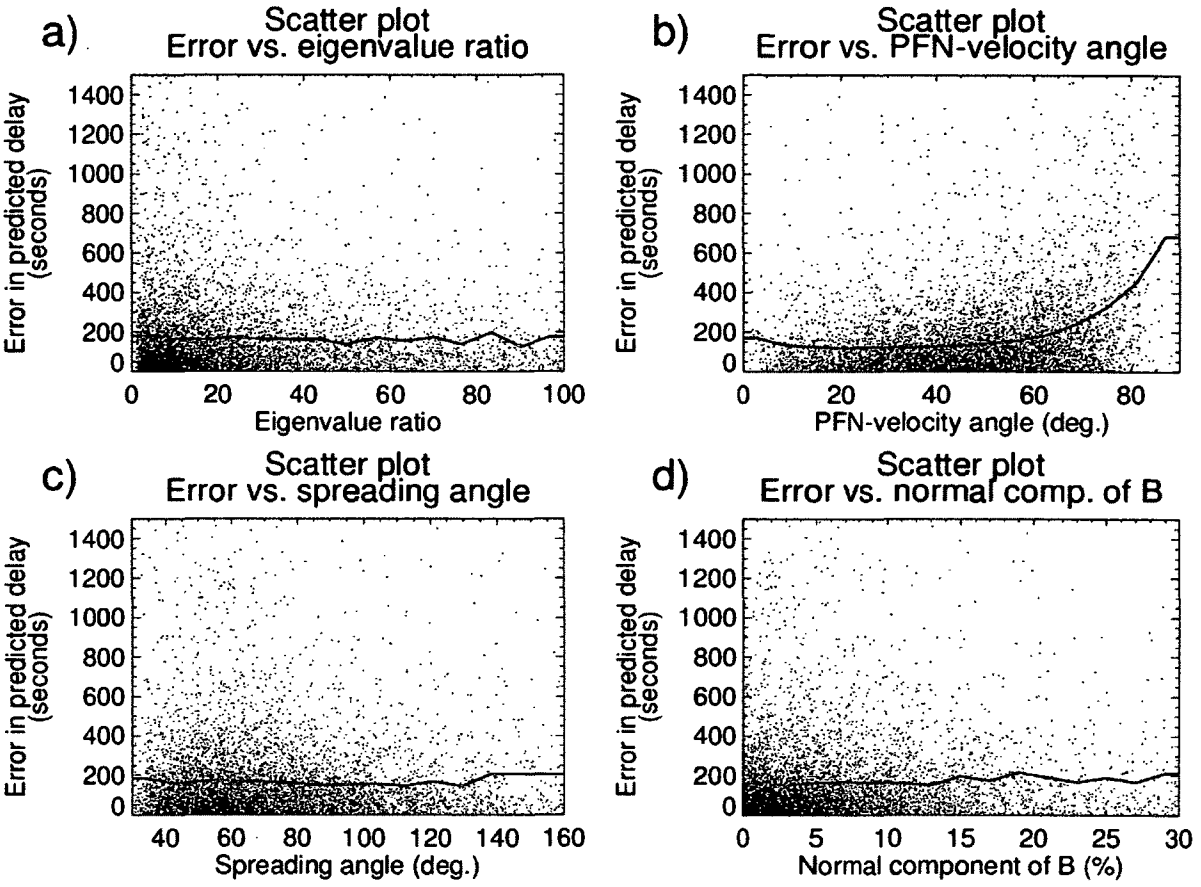

Figure 7-6 Arrival Error Dependencies. Distribution of timing errors when propagating a single data point for the IMF discontinuities listed in Table 5-2 using the CPMV-B method, shown as a function of eigenvalue ratio (a), PFN-velocity angle (b), spreading-angle (c) and normal component of ***B*** *(d). The red line indicates the average value of errors in bins along X-axis.*

Above results are for discrete propagation of a single data point at each discontinuity, and a future study should do a similar check for continuous propagation, which was shown in this study to improve accuracy of predicted arrival times for most discontinuities.

Future studies should take small-scale structure into account. It is determining for what PFN estimates are produced by the different methods in the interior of flux tubes, and it also has a significant impact on test scores derived from comparing propagated and measured data series, such as the mean square error used in this and other studies. Filtering out small-scale structure both from source data (ACE) and measured target

satellite data may improve the quality of propagated data, and it would also make test scores better indicators for how accurately large-scale structures are propagated. Of course, solar wind data cannot be cleanly divided into small- and large-scale structure, and it will be a challenge designing a filter that makes a good compromise between effectively eliminating small-scale structure while preserving essential large-scale structure.

Another step forward would be to divide solar wind data into different subsets to be tested separately. To be practically useful the sorting criteria should be made quantitative so they can be implemented in an automated algorithm, but they may be designed to identify qualitative types of solar wind data such as different phases of coronal-hole high-speed streams, coronal mass ejecta etc. The objective is to devise a method for adjusting parameter values according to the characteristics of observed data - for example, changing the number of data points used for PFN estimation according to the length/time scale of observed solar wind structures. Differentiating solar wind data could lead to a substantial improvement in propagation results compared to the one-size-fits-all approach that has been used so far.

It should be considered carefully what to use as a test score for indicating relative performance. As shown in this study the mean square error has issues to be aware of. One is that it favors data mixing (Appendix C) and another is that unreasonably large weight is given to some short intervals (see notes for Figure 6-40). Both would be mitigated by using the mean error rather than the mean *square* error. However, using the mean error instead means that more weight is given to small-scale structure during quiet intervals, which is undesirable. Filtering data to get rid of some small-scale structure as suggested above would mitigate this problem.

Finally, it should be tested whether adding an offset to calculated propagation delays improves results, as was the case in this study. If so some investigation should be done to identify the source of this offset.

7.3 Findings in Brief

The main points to take away from this study are:

1) The CPMV-B method is currently the most accurate for propagation of both continuous solar wind data and discontinuities. However, this study found the parameter values that give optimal results to be significantly different from those found in the study where the method was devised [*Weimer and King*, 2008].
2) Electric field methods give decent results for propagation of continuous data, but they are inferior to methods using the magnetic field for propagation of discontinuities.
3) Using HT velocities for propagation gives a small improvement in results while reducing mixing of data from adjacent flux tubes.
4) Best results were obtained when adding a constant offset of about 30 seconds to propagation delays. A tempting explanation would be asymmetric flux tube geometry, but examination of data did not verify this hypothesis.
5) Results from this study can be used to improve the OMNI database, which is based on a propagation method that produces somewhat worse test scores in comparison.
6) There is still potential for significant improvement of solar wind propagation based on single satellite observations, and more studies ought to be done before an eventual update of the OMNI database.

8 Conclusion

The initial motivation for this study was to test the option of using the electric field for single satellite propagation given that previously tested methods only use the magnetic field. Also, with more data and processing power available it was possible to both use significantly larger data sets and test each method in greater detail, allowing to evaluate to which extent the results of previous studies were dependent on the smaller data sets used. It was found that existing magnetic field methods overall perform better than similar methods using the electric field. Results were largely in agreement with previous studies, though some dependency on data set was observed. New optimal parameter values were derived for the best performing method, and these new values make it better suited for practical application. Currently, most scientists in need of solar wind data for magnetospheric research obtain it from a precompiled database with data that has already been propagated to Earth's bow shock. This database was (and is) compiled using a non-optimal method, which has the advantage of producing few/small gaps in propagated data. With the new parameter values found in this study the best performing method shares this property and could be implemented. However, updating the database would be a major undertaking, and the potential for other and more significant improvements should be investigated first.

The broad extent of this study also makes it a good reference point for future studies, pointing to what needs investigation for further improvement and issues to consider. The two major issues with current single satellite methods is that estimates of how structures are oriented are associated with considerable uncertainty, and they have significant curvature, which is completely unaccounted for. Both could be helped with better knowledge of the geometry of solar wind structures, calling for statistical studies using multi-satellite observations to assess curvature of structures. In this study it was found that structures arrive 30 seconds later than predicted on average, indicating a systematic error, which could be due to an asymmetry in the geometry of structures. Currently the

methods are also used on a "one-size-fits-all" basis. Given how variable the solar wind is methods should be developed to adapt according to the type of solar wind data observed.

In order to optimize methods for solar wind propagation it is needed to define measures for performance. A quantity that was used in this and previous studies is the mean square error between propagated and measured magnetic fields, but it became clear that it favors data mixing (data points arriving in mixed order), which is somewhat detrimental as it can make sharp transitions unidentifiable in propagated data. This further illustrated a need to differentiate methods according to the type of data.

While there is potential for significantly improving single satellite methods for solar wind propagation they have some inherent limitations that cannot be helped. There are times when a source satellite near L1 and a target near the magnetosphere observe completely different structures. The best that can be done is to attempt identifying when this may happen, which again calls for an investigation of solar wind structure geometry. Optimizing methods for accuracy is only relevant when the source satellite sees what actually arrives, and developing an indicator of the reliability of propagated data is perhaps the most important objective for future studies.

References

Bargatze, L. F., R. L. McPherron, J. Minamora and D. Weimer (2005), A new interpretation of Weimer et al.'s solar wind propagation delay technique, *J. Geophys. Res., 110*, A07105, doi:10.1029/2004JA010902.

Borovsky, J. E. (2008), Flux tube texture of the solar wind: Strands of the magnetic carpet at 1 AU?, *J. Geophys. Res., 113*, A08110, doi:10.1029/2007JA012684.

Burlaga, L. F. (1969), Directional discontinuities in the interplanetary magnetic field, *Sol. Phys., 7*, 54-71, doi:10.1007/BF00148406.

Collier, M. R., J. A. Slavin, R. P. Lepping, A. Szabo and K. Ogilvie (1998), Timing accuracy for the simple planar propagation of magnetic field structures in the solar wind, *Geophys. Res. Lett., 25*, 2509-2512, doi:10.1029/98GL00735.

Fu, H. S., J. B. Cao, T. L. Zhang, H. Reme and E. Lucek (2009), Statistical study of the solar wind deceleration in the Earth's foreshock region, *Chin. J. Geophys., 52*, 361-368.

Greco, A., W. H. Matthaeus, S. Servidio, P. Dmitruk, M. Wan, S. Oughton and P. Chuychai (2008), Statistical properties of solar wind discontinuities, intermittent turbulence, and rapid emergence of non-Gaussian distributions, *Geophys. Res. Lett., 35*, L19111, doi:10.1029/2011JA016569.

Haaland, S., G. Paschmann and B. U. Ö. Sonnerup (2006), Comment on "A new interpretation of Weimer et al.'s solar wind propagation delay technique" by Bargatze et al., *J. Geophys. Res., 111*, A06102, doi:10.1029/2005JA011376.

Horbury, T. S., D. Burgess, and M. Franz (2001a), Three spacecraft observations of solar wind discontinuities, *Geophys. Res. Lett., 28*, 677-680, doi:10.1029/2000GL000121.

Horbury, T. S., D. Burgess, M. Franz and C. J. Owen (2001b), Prediction of Earth arrival times of interplanetary southward magnetic field turnings, *J. Geophys. Res., 106*, 30001-30010, doi:10.1029/2000JA002232.

Khrabrov, A. V. and B. U. Ö. Sonnerup (1998), DeHoffmann-Teller analysis, in *Analysis Methods for Multi-Spacecraft Data*, edited by G. Paschmann and P.W. Daly, pp. 221-248, ESA Publications Division, Noordwijk, The Netherlands.

Knetter, T. (2005), A new perspective of the solar wind micro-structure due to multi-point observations of discontinuities, PhD thesis, University of Cologne, Cologne, Germany.

Knetter, T., F. M. Neubauer, T. Horbury and A. Balogh (2004), Four-point discontinuity observations using Cluster magnetic field data: A statistical survey, *J. Geophys. Res.*, *109*, A06102, doi:10.1029/2003JA010099.

Kokubun, S., T. Yamamoto, M. H. Acuna, K. Hayashi, K. Shiyokawa and H. Kawano (1994), The GEOTAIL magnetic field experiment, *J. Geomag. Geoelectr.*, *46*, 7-21, doi:10.5636/jgg.46.669.

Lepping, R. P. and K. W. Behannon (1986), Magnetic field directional discontinuities: characteristics between 0.46 and 1.0 AU, *J. Geophys. Res.*, *91*(A8), 8725-8741, doi:10.1029/JA091iA08p08725.

Lepping, R. P., M. Acuna, L. Burlaga, W. Farrell, J. Slavin, K. Schatten, F. Mariani, N. Ness, F. Neubauer, Y. C. Whang, J. Byrnes, R. Kennon, P. Panetta, J. Scheifele and E. Worley (1995), The WIND magnetic field investigation, *Space Sci. Rev.*, *71*, 207-229, doi:10.1007/BF00751330.

Mailyan, B., C. Munteanu and S. Haaland (2008), What is the best method to calculate the solar wind propagation delay?, *Ann. Geophys.*, *26*, 2383-2394, doi:10.5194/angeo-26-2383-2008.

McComas, D. J., S. J. Bame, P. Barker, W. C. Feldman, and J. L. Phillips (1998), Solar wind electron proton alpha monitor (SWEPAM) for the Advanced Composition Explorer, *Space Sci. Rev.*, *86*, 563-612, doi:10.1023/A:1005040232597.

McGregor, S. L., W. J. Hughes, C. N. Arge, D. Odstrcil, and N. A. Schwadron (2011), The radial evolution of solar wind speeds, *J. Geophys. Res.*, *116*, A03106, doi:10.1029/2010JA016006.

Mish, W. H. and R. P. Lepping (1976), *Magnetic field experiment data processing system: Explorers 47 and 50*, NASA-GSFC, X-694-76-158, NASA Goddard Space Flight Center, Greenbelt, Maryland.

Neugebauer, M. (2006), Comment on the abundances of rotational and tangential discontinuities in the solar wind, *J. Geophys. Res.*, *111*, A04103, doi:10.1029/2005JA011497.

Neugebauer, M. and J. Giacalone (2010), Progress in the study of interplanetary discontinuities, *AIP Conf. Proc.*, *1216*, 194-197, doi:10.1063/1.3395834.

Neugebauer, M., D. R. Clay, B. E. Goldstein, B. T. Tsurutani and R. D. Zwickl (1984), A reexamination of rotational and tangential discontinuities in the solar wind, *J. Geophys. Res.*, *89*, 5395-5408, doi:10.1029/JA089iA07p05395.

Parker, E. N. (1958), Dynamics of the interplanetary gas and magnetic fields, *Astrophys. J.*, *128*, 664-676, doi:10.1086/146579.

Russell, C. T., G. L. Siscoe and E. J. Smith (1980), Comparison of ISEE-1 and -3 interplanetary magnetic field observations, *Geophys. Res. Lett.*, *7*, 381-384, doi:10.1029/GL007i005p00381.

Siscoe, G. L., L. Davis, P. J. Coleman, E. J. Smith and D. E. Jones (1968), Power spectra and discontinuities of the interplanetary magnetic field: Mariner 4, *J. Geophys. Res.*, *73*, 61-82, doi:10.1029/JA073i001p00061.

Smith, C. W., M. H. Acuna, L. F. Burlaga, J. L'Heureux, N. F. Ness, and J. Scheifele (1998), The ACE magnetic fields experiment, *Space Sci. Rev.*, *86*, 613-632, doi:10.1023/A:1005092216668.

Smith, E. J. (1973), Identification of interplanetary tangential and rotational discontinuities, *J. Geophys. Res.*, *78*, 2054-2063, doi:10.1029/JA078i013p02054.

Söding, A., F. M. Neubauer, B. T. Tsurutani, N. F. Ness, and R. P. Lepping (2001), Radial and latitudinal dependencies of discontinuities in the solar wind between 0.3 and 19 AU and -80° and +10°, *Ann. Geophys.*, *19*, 667-680, doi:10.5194/angeo-19-667-2001.

Sonnerup, B. U. Ö. and L. J. Cahill (1967), Magnetopause structure and attitude from Explorer 12 observations, *J. Geophys. Res.*, *72*, 171-183, doi:10.1029/JZ072i001p00171.

Sonnerup, B. U. Ö. and L. J. Cahill (1968), Explorer 12 observations of the magnetopause current layer, *J. Geophys. Res.*, *73*, 1757-1770, doi:10.1029/JA073i005p01757.

Sonnerup, B. U. Ö. and M. Scheible (1998), Minimum and maximum variance analysis, in *Analysis Methods for Multi-Spacecraft Data*, edited by G. Paschmann and P. W. Daly, pp. 185-220, ESA Publications Division, Noordwijk, The Netherlands.

Sonnerup, B. U. Ö., I. Papamastorakis, G. Paschmann and H. Lühr (1987), Magnetopause properties from AMPTE/IRM observations of the convection electric field: Method development, *J. Geophys. Res.*, *92*, 12137-12159, doi:10.1029/JA092iA11p12137.

Sonnerup, B. U. Ö., I. Papamastorakis, G. Paschmann and H. Lühr (1990), The magnetopause for large magnetic shear: Analysis of convection electric fields from AMPTE/IRM, *J. Geophys. Res.*, *95*, 10541-10557, doi:10.1029/JA095iA07p10541.

Weimer, D. R. (2004), Correction to "Predicting interplanetary magnetic field (IMF) propagation delay times using the minimum variance technique,", *J. Geophys. Res.*, *109*, A12104, doi:10.1029/2004JA010691.

Weimer, D. R. and J. H. King (2008), Improved calculations of interplanetary magnetic field phase front angles and propagation time delays, *J. Geophys. Res.*, *113*, A01105, doi:10.1029/2007JA012452.

Weimer, D. R., D. M. Ober, N. C. Maynard, W. J. Burke, M. R. Collier, D. J. McComas, N. F. Ness and C. W. Smith (2002), Variable time delays in the propagation of the interplanetary magnetic field, *J. Geophys. Res.*, *107*, 1210, doi:10.1029/2001JA009102.

Weimer, D. R., D. M. Ober, N. C. Maynard, M. R. Collier, D. J. McComas, N. F. Ness, C. W. Smith and J. Watermann (2003), Predicting interplanetary magnetic field (IMF) propagation delay times using the minimum variance technique, *J. Geophys. Res.*, *108*, 1026, doi:10.1029/2002JA009405.

Appendix A
DeHoffmann-Teller Analysis

By definition, a deHoffmann-Teller (HT) frame is one in which the electric field vanishes throughout the volume around the point considered. It then follows directly from Faraday's law that the magnetic field in a HT frame must be time-stationary:

$$\nabla \times \mathbf{E} = -\frac{\partial \mathbf{B}}{\partial t} = \mathbf{0} \tag{A.1}$$

For this project the objective is to use single satellite (ACE) measurements of the electric field $\mathbf{E} = -\mathbf{V} \times \mathbf{B}$ given in the GSE coordinate system to find a different frame in which $\mathbf{E} = \mathbf{0}$ around a given data point. To avoid complicating things unnecessarily, only frames moving with a constant velocity relative to the GSE frame are considered. Since solar wind structures move with non-relativistic speeds in the GSE frame we do not need to consider relativistic effects and can do a simple Galilean transformation to obtain the electric field in the new reference frame moving with velocity $\mathbf{V}_G$ relative to the GSE frame:

$$\mathbf{E}' = \mathbf{E} + \mathbf{V}_G \times \mathbf{B} \tag{A.2}$$

A prime denotes quantities in the transformed coordinate system, unprimed are in the GSE system. The electric field in the HT frame can be written:

$$\mathbf{E}' = \mathbf{E} + \mathbf{V}_{HT} \times \mathbf{B} = -\mathbf{V} \times \mathbf{B} + \mathbf{V}_{HT} \times \mathbf{B} = (\mathbf{V}_{HT} - \mathbf{V}) \times \mathbf{B} = \mathbf{0}$$

For a single set of measurements $\mathbf{V}$, $\mathbf{B}$ in the GSE frame, solving for $\mathbf{V}_{HT}$ results in a one-dimensional solution space:

$$\mathbf{V}_{HT} = \mathbf{V} + c\frac{\mathbf{B}}{|\mathbf{B}|} \tag{A.3}$$

Here c is an arbitrary constant. If two or more sets of measurements for $\mathbf{V}$, $\mathbf{B}$ are used a solution exists only in the case that the one-dimensional solution space for each set of

measurements have a common intersection in three-dimensional velocity space. The probability of this happening in practice is zero, so generally it is not possible to find a unique solution for $\mathbf{V}_{HT}$ from experimental data. Instead the goal is to find an approximation for $\mathbf{V}_{HT}$ minimizing the electric field, or more specifically, the mean square of the electric field, for the data points considered. For the sake of simplicity this solution will be referred to as a HT frame even though it is only an approximation and not a true HT frame. Given a set of measurements $\mathbf{V}_i$ and $\mathbf{B}_i$, i = 1,2,...,N, the mean square of the electric field, call it F, can be written as a function of the transformation velocity $\mathbf{V}_G$:

$$F(\mathbf{V}_G) = \frac{1}{N}\sum_{i=1}^{N}|\mathbf{E}_i'|^2 = \frac{1}{N}\sum_{i=1}^{N}|(\mathbf{V}_G - \mathbf{V}_i)\mathrm{x}\,\mathbf{B}_i|^2 \tag{A.4}$$

Since $F(\mathbf{v}_G)$ is a positive quadratic function of $\mathbf{V}_G$ it must have a unique minimum, which can be found by solving $\nabla F = \mathbf{0}$ where differentiation is with respect to the components of $\mathbf{V}_G$. Writing out the square of the electric field for the i^{th} measurement:

$$\begin{aligned}|(\mathbf{V}_G - \mathbf{V}_i)\mathrm{x}\,\mathbf{B}_i|^2 &= ((V_{G,y} - V_{i,y})B_{i,z} - (V_{G,z} - V_{i,z})B_{i,y})^2 + ((V_{G,z} - V_{i,z})B_{i,x} \\ &- (V_{G,x} - V_{i,x})B_{i,z})^2 + ((V_{G,x} - V_{i,x})B_{i,y} - (V_{G,y} - V_{i,y})B_{i,x})^2\end{aligned} \tag{A.5}$$

Differentiating with respect to one of the components of $\mathbf{V}_G$ yields (by use of chain rule):

$$\begin{aligned}&\frac{\partial}{\partial V_{G,x}}\left(|(\mathbf{V}_G - \mathbf{V}_i)\mathrm{x}\,\mathbf{B}_i|^2\right) \\ &= 2((V_{G,z} - V_{i,z})B_{i,x} - (V_{G,x} - V_{i,x})B_{i,z})(-B_{i,z}) + 2((V_{G,x} - V_{i,x})B_{i,y} \\ &- (V_{G,y} - V_{i,y})B_{i,x})(B_{i,y}) \\ &= 2\left((B_{i,y}{}^2 + B_{i,z}{}^2)(V_{G,x} - V_{i,x}) - B_{i,x}B_{i,y}(V_{G,y} - V_{i,y}) - B_{i,x}B_{i,z}(V_{G,z} - V_{i,z})\right)\end{aligned} \tag{A.6}$$

The result of differentiating with respect to the other components follows by permutation (x→y, y→z, z→x), and writing out ∇F gives:

(A.7)

$$\nabla F = \begin{bmatrix} \frac{\partial}{\partial V_{G,x}} \\ \frac{\partial}{\partial V_{G,y}} \\ \frac{\partial}{\partial V_{G,z}} \end{bmatrix} F = \frac{1}{N}\sum_{i=1}^{N} \begin{bmatrix} \frac{\partial}{\partial V_{G,x}} \\ \frac{\partial}{\partial V_{G,y}} \\ \frac{\partial}{\partial V_{G,z}} \end{bmatrix} \left|(\mathbf{V}_G - \mathbf{V}_i)x\,\mathbf{B}_i\right|^2$$

$$= \frac{1}{N}\sum_{i=1}^{N} \begin{bmatrix} 2\left((B_{i,y}{}^2 + B_{i,z}{}^2)(V_{G,x} - V_{i,x}) - B_{i,x}B_{i,y}(V_{G,y} - V_{i,y}) - B_{i,x}B_{i,z}(V_{G,z} - V_{i,z})\right) \\ 2\left(-B_{i,x}B_{i,y}(V_{G,x} - V_{i,x}) + (B_{i,x}{}^2 + B_{i,z}{}^2)(V_{G,y} - V_{i,y}) - B_{i,y}B_{i,z}(V_{G,z} - V_{i,z})\right) \\ 2\left(-B_{i,x}B_{i,z}(V_{G,x} - V_{i,x}) - B_{i,y}B_{i,z}(V_{G,y} - V_{i,y}) + (B_{i,x}{}^2 + B_{i,y}{}^2)(V_{G,z} - V_{i,z})\right) \end{bmatrix}$$

$$= 2\frac{1}{N}\sum_{i=1}^{N} \left(\begin{bmatrix} B_{i,y}{}^2 + B_{i,z}{}^2 & -B_{i,x}B_{i,y} & -B_{i,x}B_{i,z} \\ -B_{i,x}B_{i,y} & B_{i,x}{}^2 + B_{i,z}{}^2 & -B_{i,y}B_{i,z} \\ -B_{i,x}B_{i,z} & -B_{i,y}B_{i,z} & B_{i,x}{}^2 + B_{i,y}{}^2 \end{bmatrix} \begin{bmatrix} V_{G,x} - V_{i,x} \\ V_{G,y} - V_{i,y} \\ V_{G,z} - V_{i,z} \end{bmatrix} \right)$$

$$= 2\frac{1}{N}\sum_{i=1}^{N} \overline{\overline{\mathbf{K}}}_i (\mathbf{V}_G - \mathbf{V}_i)$$

As can be seen the expression was simplified by defining

$$\overline{\overline{\mathbf{K}}}_i = \begin{bmatrix} B_{i,y}{}^2 + B_{i,z}{}^2 & -B_{i,x}B_{i,y} & -B_{i,x}B_{i,z} \\ -B_{i,x}B_{i,y} & B_{i,x}{}^2 + B_{i,z}{}^2 & -B_{i,y}B_{i,z} \\ -B_{i,x}B_{i,z} & -B_{i,y}B_{i,z} & B_{i,x}{}^2 + B_{i,y}{}^2 \end{bmatrix} = \left|\mathbf{B}_i\right|^2 \overline{\overline{\mathbf{P}}}_i \qquad \text{(A.8)}$$

where $\overline{\overline{\mathbf{P}}}_i$ is a projection matrix into the plane perpendicular to $\mathbf{B}_i$, having elements

$$P_{i,mn} = \left(\delta_{mn} - \frac{B_{i,m}B_{i,n}}{\left|\mathbf{B}_i\right|^2}\right), \qquad \delta_{mn} = \begin{cases} 1, m = n \\ 0, m \neq n \end{cases} \text{ (Kronecker Delta)} \qquad \text{(A.9)}$$

The solution for $\mathbf{V}_G = \mathbf{V}_{HT}$ is found by setting $\nabla F = \mathbf{0}$. Let angle brackets denote an average over the N measurements, e.g. $\langle \mathbf{V} \rangle = \frac{1}{N}\sum_{i=1}^{N} \mathbf{V}_i$. The equation to solve for $\mathbf{V}_{HT}$ can then be written:

$$2\frac{1}{N}\sum_{i=1}^{N}\overline{\overline{\mathbf{K}}}_i(\mathbf{V}_{HT}-\mathbf{V}_i)=\mathbf{0}\Rightarrow\frac{1}{N}\sum_{i=1}^{N}\overline{\overline{\mathbf{K}}}_i\mathbf{V}_{HT}=\frac{1}{N}\sum_{i=1}^{N}\overline{\overline{\mathbf{K}}}_i\mathbf{V}_i$$
$$\Rightarrow\left\langle\overline{\overline{\mathbf{K}}}\right\rangle\mathbf{V}_{HT}=\left\langle\overline{\overline{\mathbf{K}}}\mathbf{V}\right\rangle \qquad \text{(A.10)}$$

Assuming the matrix $\left\langle\overline{\overline{\mathbf{K}}}\right\rangle$ to be non-singular, the approximated HT frame velocity can then be calculated as:

$$\mathbf{V}_{HT}=\left\langle\overline{\overline{\mathbf{K}}}\right\rangle^{-1}\left\langle\overline{\overline{\mathbf{K}}}\mathbf{V}\right\rangle \qquad \text{(A.11)}$$

An analytical error estimate for $\mathbf{V}_{HT}$ can be derived as outlined by *Khrabrov and Sonnerup* [1998]. Without delving into the somewhat lengthy details, the uncertainty can be characterized by a variance matrix:

$$\overline{\overline{\mathbf{S}}}=\frac{F(\mathbf{V}_{HT})}{2N-3}\left\langle\overline{\overline{\mathbf{K}}}\right\rangle^{-1} \qquad \text{(A.12)}$$

This defines a variance ellipsoid in velocity space with principal axes given by the eigenvectors $\mathbf{e}^K{}_j$ of the matrix $\left\langle\overline{\overline{\mathbf{K}}}\right\rangle$. The variance in any direction given by a unit vector $\mathbf{n}$ (that is, the uncertainty in the component $\mathbf{V}_{HT}\cdot\mathbf{n}$) is then given by

$$\sigma_n{}^2=\mathbf{n}\cdot\overline{\overline{\mathbf{S}}}\cdot\mathbf{n}=\frac{F(\mathbf{V}_{HT})}{2N-3}\mathbf{n}\cdot\left\langle\overline{\overline{\mathbf{K}}}\right\rangle^{-1}\cdot\mathbf{n}=\frac{F(\mathbf{V}_{HT})}{2N-3}\sum_{j=1}^{3}\frac{(\mathbf{n}\cdot\hat{\mathbf{e}}_j)^2}{\lambda^K{}_j} \qquad \text{(A.13)}$$

where $F(\mathbf{V}_{HT})$ is the mean square of the residual electric field left in our estimated HT frame, N is the number of data points used for the HT analysis, $\hat{\mathbf{e}}_j=\frac{\mathbf{e}^K{}_j}{|\mathbf{e}^K{}_j|}$ are the normalized eigenvectors of $\left\langle\overline{\overline{\mathbf{K}}}\right\rangle$ and $\lambda^K{}_j$ are the associated eigenvalues. In this study the HT frame is applied for two different purposes, which call for two different error estimates. First, the HT frame is used for propagation of solar wind data in which case the uncertainty along the direction of propagation is the quantity of interest. This can readily be calculated by substituting the PFN estimate for $\mathbf{n}$ in the above equation. Second, the

HT frame is used as a reference frame for calculating the electric field, which is then given by:

$$\mathbf{E} = -(\mathbf{V}_{BULK} - \mathbf{V}_{HT}) \times \mathbf{B} \tag{A.14}$$

It is then the maximum uncertainty in the plane perpendicular to **B** that is of interest. The matrix for projection onto the plane perpendicular to **B** is:

$$P_{mn} = \left(\delta_{mn} - \frac{B_m B_n}{|\mathbf{B}|^2} \right), \qquad \delta_{mn} = \begin{cases} 1, m = n \\ 0, m \neq n \end{cases} \text{ (Kronecker Delta)} \tag{A.15}$$

This projection matrix leaves vectors in the plane perpendicular to **B** unchanged, so for normal vectors within this plane we have:

$$\mathbf{n} \cdot \overline{\overline{\mathbf{P}}} \cdot \overline{\overline{\mathbf{S}}} \cdot \overline{\overline{\mathbf{P}}} \cdot \mathbf{n} = \mathbf{n} \cdot \overline{\overline{\mathbf{S}}} \cdot \mathbf{n} = \sigma_n^{\,2} \qquad (\mathbf{B} \cdot \mathbf{n} = 0) \tag{A.16}$$

This shows that the matrix $\overline{\overline{\mathbf{P}}} \cdot \overline{\overline{\mathbf{S}}} \cdot \overline{\overline{\mathbf{P}}}$ has two eigenvectors along the principal axes of the variance ellipse in the projection plane, the semi-axes lengths given by the square root of the associated eigenvalues (the third eigenvector is along **B** with eigenvalue zero). Hence, the maximum uncertainty in the plane perpendicular to **B** can be found as the square root of the maximum eigenvalue of $\overline{\overline{\mathbf{P}}} \cdot \overline{\overline{\mathbf{S}}} \cdot \overline{\overline{\mathbf{P}}}$.

Appendix B

Examples of Solar Wind Data

Interaction between the solar wind and Earth's magnetosphere is mainly governed by variability in three solar wind parameters: The IMF, velocity and density. This study works predominantly with the IMF because it is the most important of the three parameters, but the velocity also comes into play, both for propagation and for estimating electric fields. Density is the least important of the three and has not been considered in this study.

Figure B-1 shows the distribution of IMF vectors for two different years (2002 and 2007) in a spherical coordinate system converted from GSE coordinates.

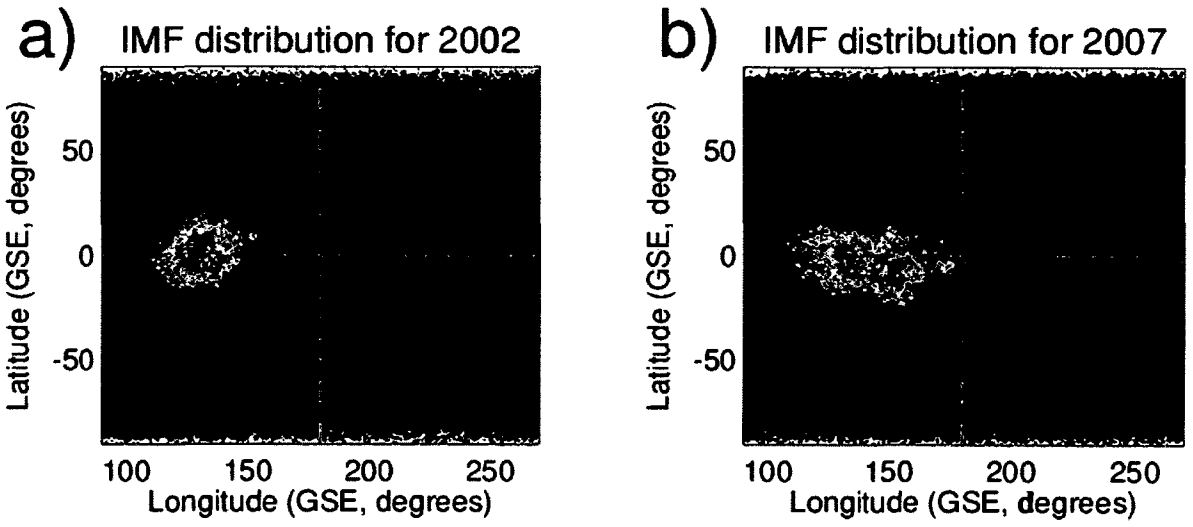

Figure B-1 Near-Earth IMF Distribution. Distribution of IMF vectors pointing towards Earth (vectors pointing towards the Sun have been turned 180°) for 2002 (a) and 2007(b) as measured by ACE.

The plot shows the half of the sphere pointing towards Earth. IMF vectors pointing towards the Sun have been turned 180° (it presumably doesn't matter for propagation whether the IMF inside a flux tube is pointing towards or away from the Sun). The IMF

is mainly pointing into the eastern quadrants (east is in the positive Y_{GSE} direction, the definition of east/west when looking at the Sun is opposite to what it is for Earth) centered about 45° from the $-X_{GSE}$-axis as would be expected from the Parker spiral pattern. For 1998-2006 from which this study uses data the distributions look similar to that of 2002 with yearly variations appearing more random than systematic. However, for 2007-2009 (during solar minimum) the distributions look somewhat different with a wider spread in the distribution, suggesting that significant solar cycle dependent variations are present.

Figure B-2 shows the distribution of bulk velocities for 2002.

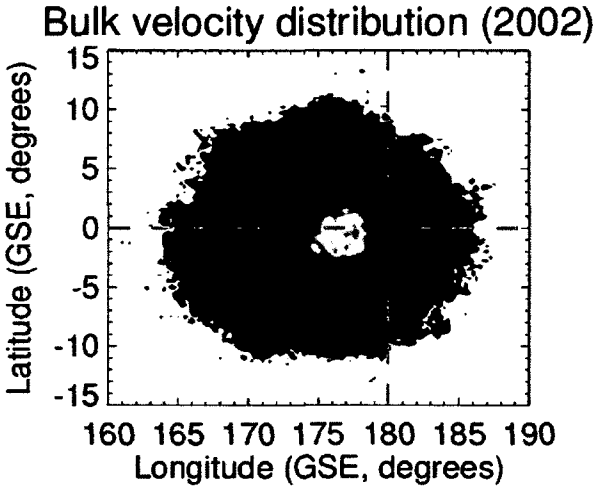

Figure B-2 Solar Wind Velocity Distribution. Distribution of solar wind bulk velocity vectors seen by ACE for 2002.

Distributions for other years look essentially the same, mostly centered a few degrees east of the $-X_{GSE}$-axis, an offset that is due to the corotational velocity of the GSE coordinate frame. About 53% of observations are within 5° and 95% within 10° of the $-X_{GSE}$-axis.

An important aspect of solar wind data is the relation between the velocity and magnetic field. This is relevant for the purpose of understanding the results obtained by the various PFN estimation methods and also for discussing the use of

deHoffmann-Teller frames. Figure B-3 shows a 24-hour interval of solar wind bulk velocities and IMF in the same plot.

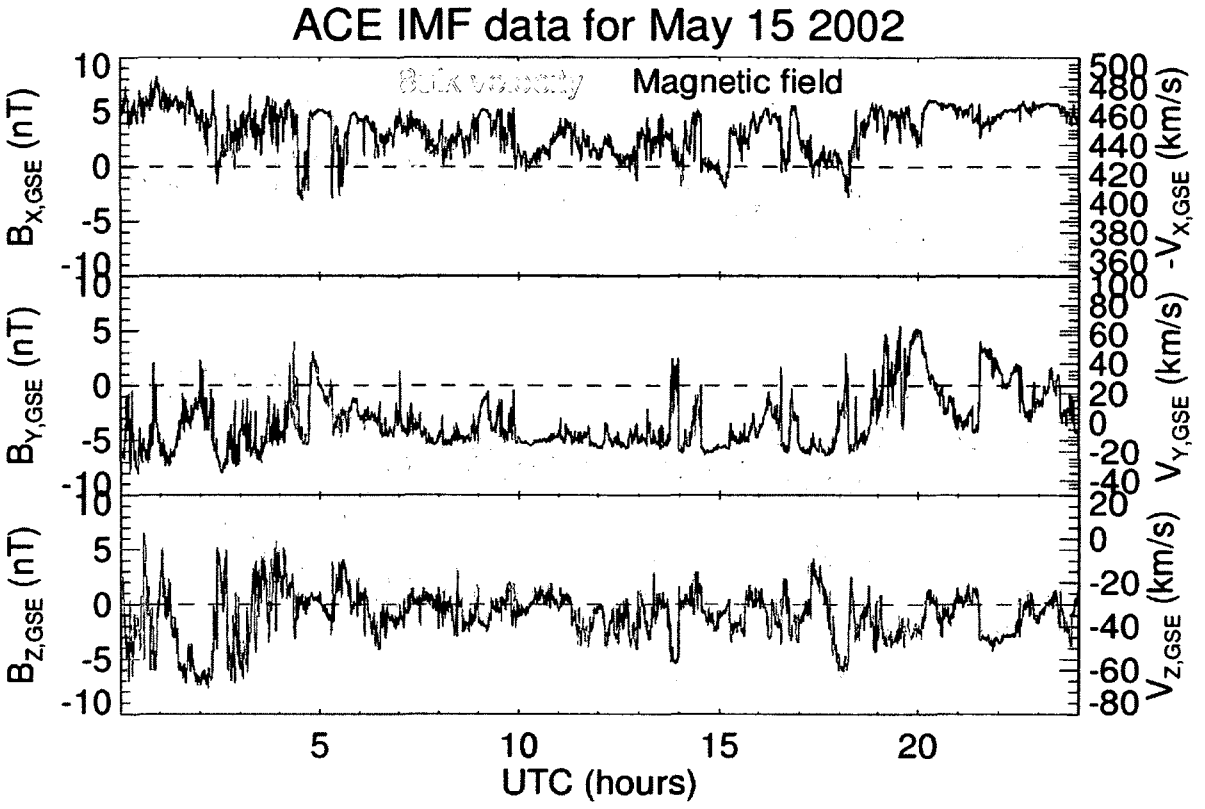

Figure B-3 Velocity and IMF Example. Solar wind bulk velocity and IMF for May 15 2002.

Velocities are highly correlated (or anticorrelated) with the IMF. This seems reasonable given that the magnetic field "guides" the plasma, which can move easily along the magnetic field but not across it. However, the correlation is stricter than this simple observation warrants, and the details reveal important information about the structure of the solar wind.

A fundamental relation in plasma physics is the definition of the Alfvén velocity in terms of the plasma density and magnetic field:

$$\mathbf{V}_A = \pm \frac{1}{\sqrt{\mu_0 \rho}} \mathbf{B} \tag{B.1}$$

This is the phase velocity of shear Alfvén waves, the simplest of wave solutions to the basic set of MHD equations. As Equation (B.1) shows, shear Alfvén waves propagate parallel or antiparallel to the magnetic field. The associated oscillating perturbations in velocity and magnetic field are perpendicular to **B** and similarly related by

$$\delta\mathbf{V} = \pm \frac{1}{\sqrt{\mu_0 \rho}} \delta\mathbf{B} \tag{B.2}$$

where $\delta B << \mathbf{B}$ and hence $\delta \mathbf{V} << \mathbf{V}_A$. Now consider the possibility that shear Alfvén waves are propagating along flux tubes in the solar wind. ACE would then observe small fluctuations in velocity and magnetic field satisfying the relation (B.2), superposed on relatively stable background quantities. HT analysis on ACE data should find a frame travelling with the Alfvén velocity given by (B.1) relative to the plasma rest frame. Another possible source of small-scale fluctuations is turbulence for which the velocity and magnetic field perturbations do not need to adhere to the relation (B.2).

For rotational discontinuities one of the jump conditions dictates that the change in velocity and magnetic field across the discontinuity obeys the same alfvenic relationship:

$$[\mathbf{V}_t] = \pm \frac{1}{\sqrt{\mu_0 \rho}} [\mathbf{B}_t] \tag{B.3}$$

Here brackets denote the jump value (that is, the difference between upstream and downstream quantities) and the subscript t indicates that only the tangential component may change. The normal component is required to be constant, nonzero and is given by:

$$V_n = \pm \frac{1}{\sqrt{\mu_0 \rho}} B_n \tag{B.4}$$

Equation (B.4) is known as the Walén relation and is often used as a validity check to see if HT analysis on a discontinuity yields a proper rest frame expected for a rotational discontinuity.

In contrast to above discussed alfvenic fluctuations, the flux tube model assumes flux tubes to be separated by tangential discontinuities, which have $V_n = B_n = 0$ and do not impose any requirements on how the tangential velocity on either side must be related. In other words, the plasma velocity inside a flux tube is independent of the plasma velocity in neighboring flux tubes. Observations show that the tangential velocity changes across solar wind discontinuities according to (B.3), except with a smaller than expected proportionality factor [*Neugebauer*, 2006, and references therein], and that B_n is small [*Knetter et al.*, 2004; *Knetter*, 2005], leaving it an open question whether they are rotational or tangential. This discussion is relevant to solar wind propagation because rotational discontinuities propagate in the plasma rest frame while tangential do not, but since B_n and hence V_n is small the impact on propagation times in the GSE frame is negligible relative to the uncertainty in propagation times associated with the uncertainty in PFN estimates derived from single satellite data.

Nevertheless, because the relative occurrence of tangential and rotational discontinuities has been a much debated topic the distribution found in this study is shown in Figure A-4 for completeness.

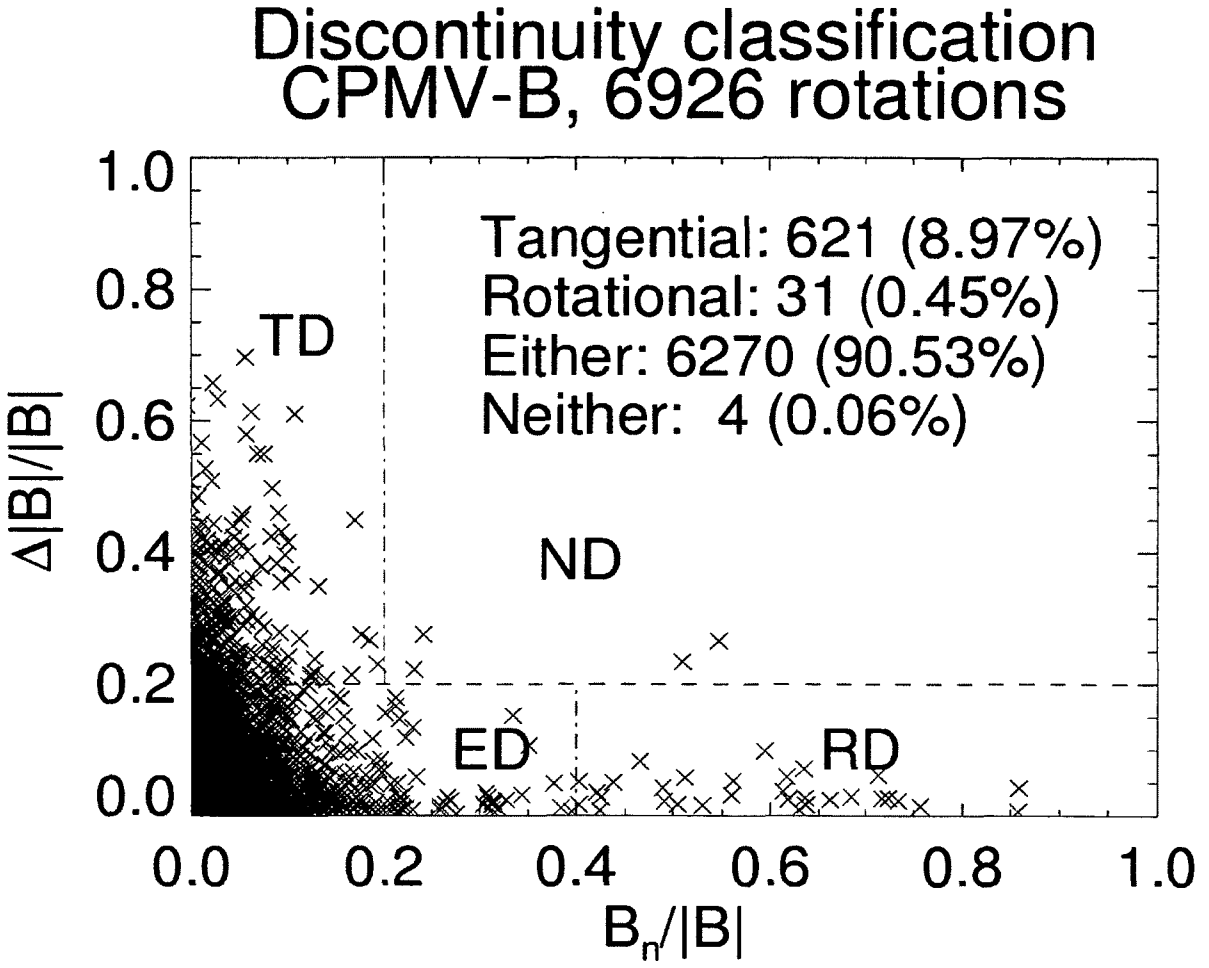

Figure B-4 Classification of Discontinuities. Classification of the set of IMF discontinuities used in this study (see Table 5-2). The CPMV-B method with parameter values that gave least error in propagation delays was used to derive PFN estimates required for calculation of B_n.

In line with previous studies [e.g., *Neugebauer and Giacalone*, 2010] the normal component $B_n/|B|$ and change in magnetic field magnitude $\Delta|B|/|B|$ have been used to classify discontinuities as tangential (TD), rotational (RD), possibly either (ED) or neither (ND).

A PFN estimate is required to determine B_n, and older studies using the MVAB method showed discontinuities to be predominantly rotational. This was turned around with studies using triangulation to find much more accurate PFN estimates. Using Cluster

data *Knetter* [2005] analyzed 353 discontinuities and found only a single (questionable) rotational discontinuity with the rest divided by 12% tangential and 88% "either". So most likely the rotational discontinuities identified here are most if not all due to inaccurate PFN estimates. However, in agreement with results presented by *Knetter* [2005] this would only serve to increase B_n and hence cause EDs to be misidentified as RDs while $\Delta|B|/|B|$ is unaffected. Hence the TD/ED ratio found in this study is valid. Previous studies have consistently found between 10% and 15% of discontinuities to be tangential (*Neugebauer* [2006]). However, these have also used different and stricter criteria for identifying discontinuities.

Figure B-5 and Figure B-6 show another data sample, now with a deHoffmann-Teller frame velocity added along with its associated uncertainty.

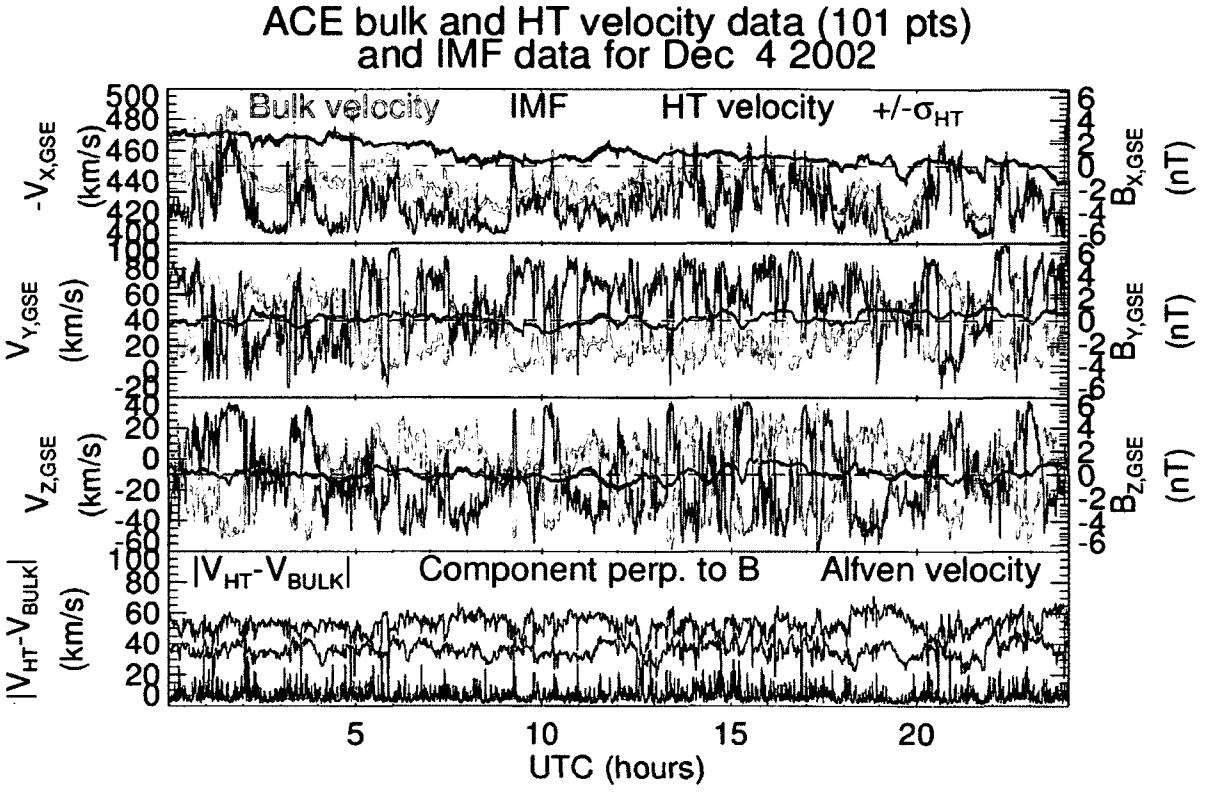

Figure B-5 HT Velocity Example (N_{HT}=101). HT velocity example using a high number of data points (101) to derive the HT frame estimates. Also plotted are the bulk velocities (yellow) and IMF (green) from which the HT velocities are derived. The grey curves surrounding the HT velocity indicate the associated error estimates σ_{HT}. The bottom plot shows the magnitude of the difference (V_{HT} - V_{BULK}), its component perpendicular to the magnetic field and the Alfvén velocity.

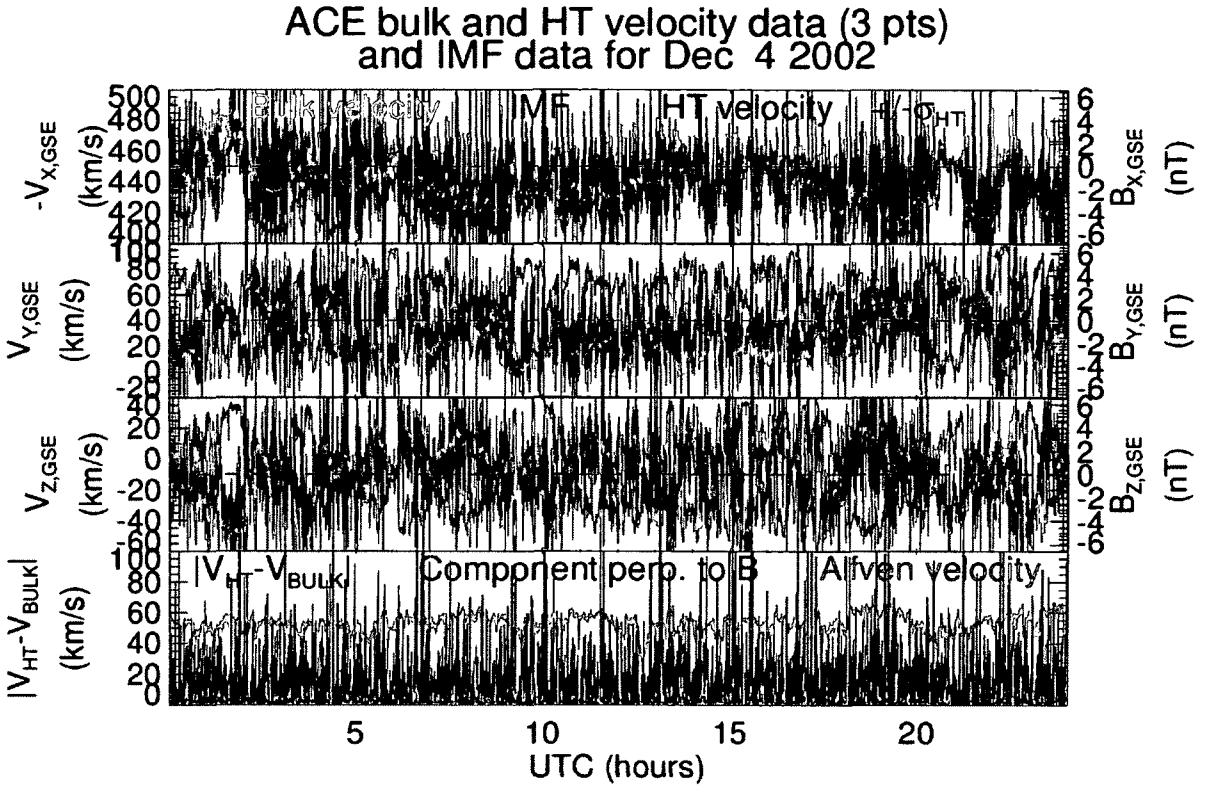

Figure B-6 HT Velocity Example (N_{HT}=3). Same HT velocity example and format as in Figure B-5 but using only 3 data points to derive HT frame estimates.

The bottom graph shows the magnitude of the HT frame velocity in the plasma rest frame, its component perpendicular to the magnetic field and the Alfvén speed. In Figure B-5 a high number of data points (101) were used to calculate HT frame estimates while in Figure B-6 the minimum of 3 points were used. For N_{HT} = 101 the HT frame velocity deviates significantly from the bulk velocity, much more than its associated uncertainty, suggesting that structures are propagating in the plasma rest frame. The small perpendicular component shows that the direction of propagation is consistently quite close to parallel to the magnetic field. For N_{HT} = 3 the HT velocities are dominated by high frequency, large amplitude fluctuations around an average that follows the bulk velocity. In the plasma rest frame HT velocity spikes exceed the Alfvén velocity significantly, but again the component perpendicular to the magnetic field consistently remains small. As N_{HT} is increased the fluctuations gradually smooth out but with an

average that starts deviating from the bulk velocity, the difference being parallel to the magnetic field.

Figure B-7 shows Walén scatter plots for each GSE-component using N_{HT} = 101 and data for a whole year (1999).

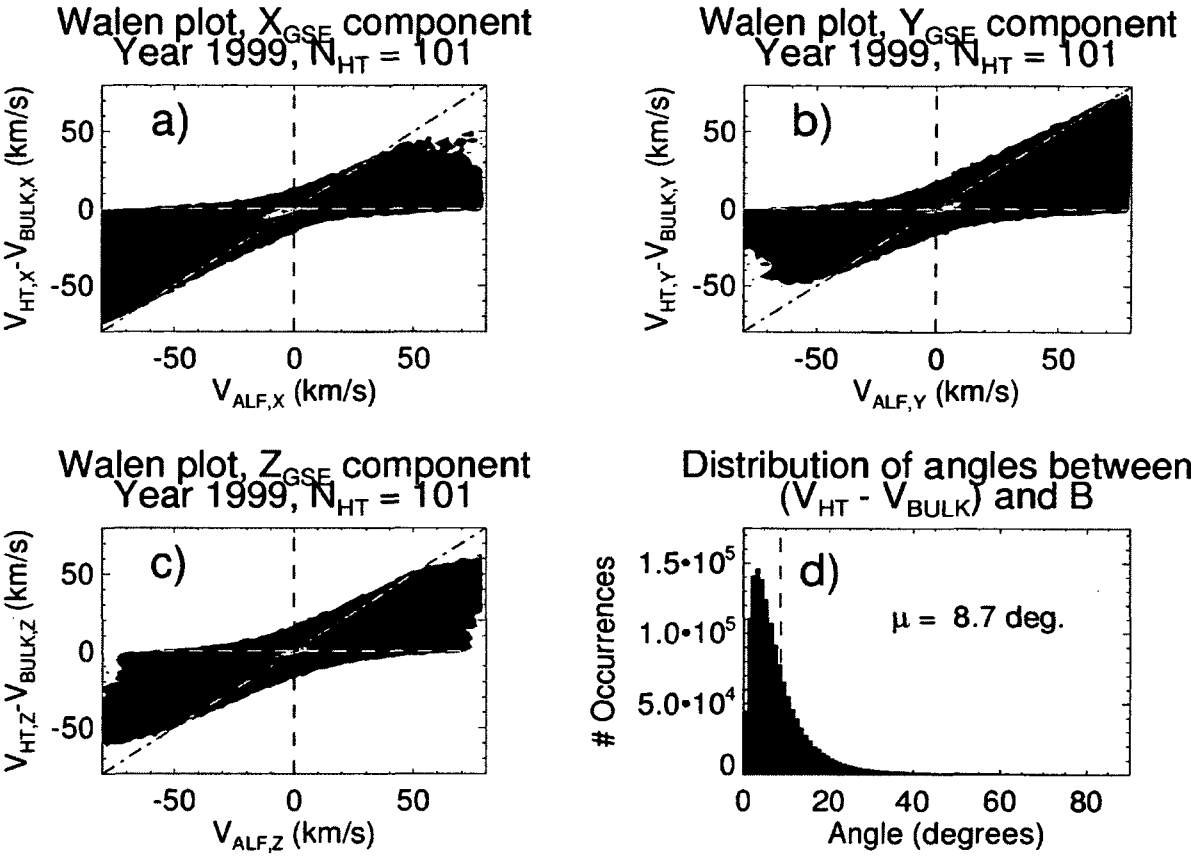

Figure B-7 Walén Scatter Plots. Walén scatter Plots (a-c) showing HT velocities (N_{HT} = 101) in the plasma rest frame (V_{HT} - V_{BULK}) as a function of Alfvén velocities. The red diagonal marks where HT frames move with the Alfvén velocity in the rest frame. Plot d) shows the distribution of angles between (V_{HT} - V_{BULK}) and the magnetic field.

The diagonal in the Walén plots is where the HT frame velocity in the plasma rest frame equals the Alfvén velocity, and according to Equation (B.1) data points should be close to this diagonal if the HT frame is tracking Alfvén waves. In practice, measurements tend to show alfvenic velocities to be smaller than given by Equations (B.1)-(B.4) [*Neugebauer,*

2006, and references therein]. Those basic relations assume the plasma to be isotropic, meaning that particle pressure/temperature is the same in all directions. In a collisionless plasma like the solar wind around 1 AU it is expected that anisotropy develops because particle motion parallel and perpendicular to the magnetic field are independent. Accounting for this introduces an anisotropy factor, which is multiplied on the right side of Equations (B.1)-(B.4) and may lower velocities (though, observed velocities are still lower than expected even with this adjustment, an unresolved problem in solar wind research). Hence, the Walén scatter plots in Figure B-7 suggest that HT frames are indeed tracking Alfvén waves propagating away from the Sun along the magnetic field most of the time.

While HT frames move close to parallel to the magnetic field in the plasma rest frame, phase front normals found by the various methods in this study are mostly close to perpendicular to the magnetic field. For this reason the difference between HT and bulk velocities generally only has a small impact on data propagation delays. In Figure B-8 the distribution of angles between ($\mathbf{V}_{HT}$ - $\mathbf{V}_{BULK}$) and PFN estimates found by the CPMV-B method (after filtering, the PFNs actually used for data propagation) is shown in Plot a).

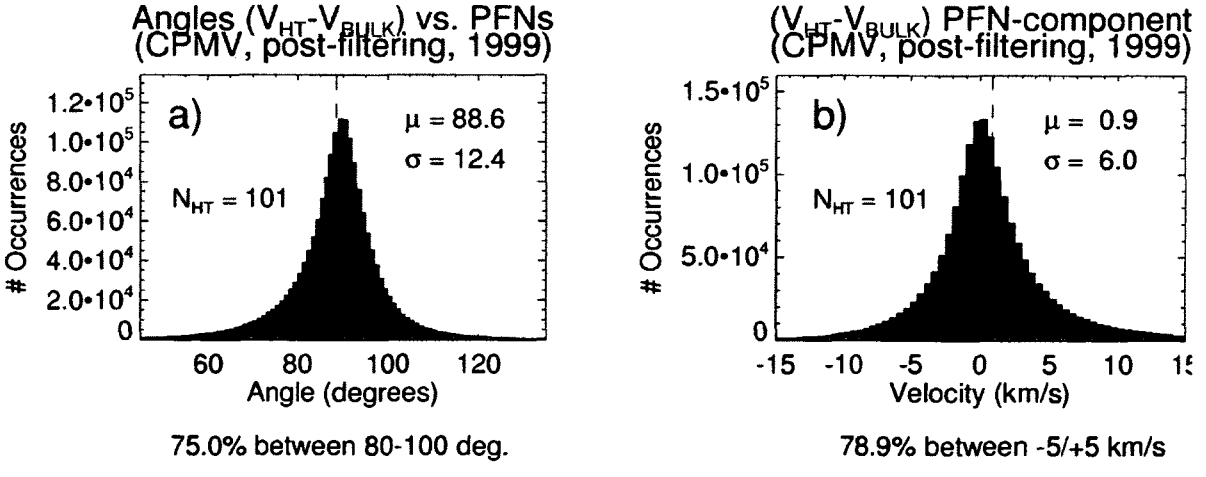

Figure B-8 Velocity Difference and PFNs. Angles between (V_{HT}-V_{BULK}) and PFNs used for data propagation (CPMV-B method) for all of 1999 (Plot a) and the component of (V_{HT}-V_{BULK}) along the PFNs (Plot b).

For 75% of observations the PFNs are less than 10 degrees from perpendicular to the difference ($\mathbf{V}_{HT}$ - $\mathbf{V}_{BULK}$), and accordingly Plot b) shows that the component of ($\mathbf{V}_{HT}$ - $\mathbf{V}_{BULK}$) along PFNs generally stays close to zero (79% within ±5 km/s).

Keep in mind that the above statistics cover all solar wind data and is therefore dominated by the long intervals of relatively quiet IMF. A subtle point in Figure B-8 is that while the peaks of the distributions are precisely centered on 90 degrees and 0 km/s, the means (indicated by dashed lines) are shifted because the wings are slightly asymmetrical with a longer tail below 90 degrees and above 0 km/s, respectively. Since PFNs were defined to point away from the Sun this agrees with Figure B-7 showing that HT frame velocities relative to the plasma rest frame are predominantly away from the Sun along the magnetic field.

As described in Appendix A the uncertainty in the HT frame velocity estimate $\mathbf{V}_{HT}$ can be defined in terms of a variance ellipsoid. Specifically, the uncertainty (standard deviation) in the component $\mathbf{V}_{HT} \cdot \mathbf{n}$ is given by the radius of the ellipsoid along $\mathbf{n}$. The orientation and shape of the variance ellipsoid are given by the eigenvectors and eigenvalues of a variance matrix, defining the direction and length of the semi-principal axes.

Figure B-9 shows some variance statistics when using 101 data points for HT analysis on all ACE velocity data from 2002.

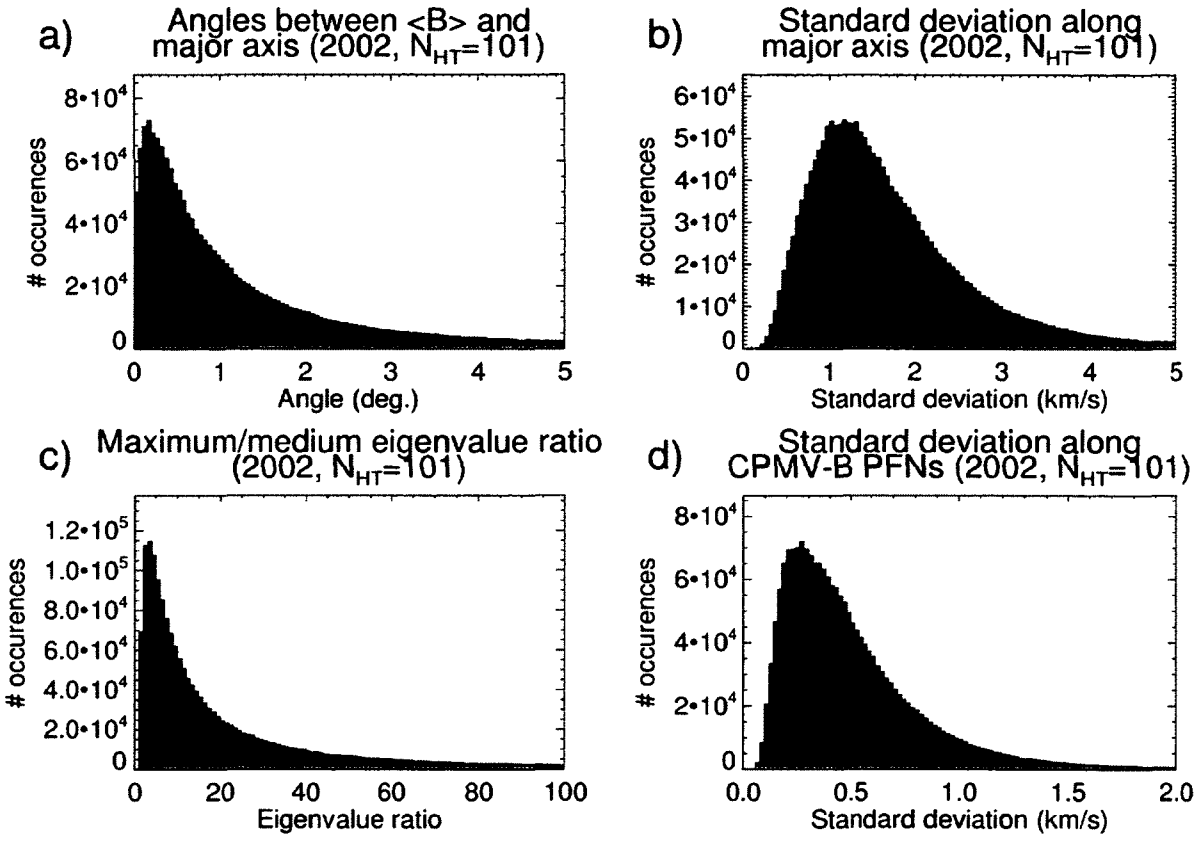

Figure B-9 HT Velocity Uncertainty Statistics. Plot a) shows the distribution of angles between B and the direction of maximum uncertainty, Plot b) the distribution of standard deviations in the maximum direction, Plot c) the distributions of ratios between maximum/medium eigenvalues and Plot d) the distribution of standard deviations along CPMV-B PFNs.

Plot a) shows that the direction of maximum variance is very close to $\langle \mathbf{B} \rangle$ (averaged over the interval used for HT analysis, here 101 points), and Plot b) shows that even in the direction of maximum variance the standard deviation is mostly below 5 km/s. Plot c) shows the distribution of ratios between maximum and medium eigenvalues of the variance matrix. Note that this is a ratio between variances and taking the square root gives the ratio between the corresponding standard deviations. Finally, Plot d) shows the distribution of standard deviations in the direction of PFN estimates calculated by the CPMV-B method, most of the distribution being below 1 km/s. The same plots for $N_{HT} = 3$ show a much higher maximum standard deviation almost exactly in the direction

of $\langle \mathbf{B} \rangle$ (distribution in Plot a) peaks below 0.05 degrees) and with much higher eigenvalue ratios. The component along PFNs remains low with the distribution peaking below 1 km/s though with a longer tail (91.5% below 5 km/s).

Appendix C
Data Mixing

It is necessary to make some grossly simplifying assumptions in order to estimate propagation delays from single satellite data. These assumptions often break down, and as a result propagated data points arrive at the target in a different sequence than they were measured at the source. Throughout this study the occurrence of out-of-sequence data is referred to as data mixing. Figure C-1 shows an example of ACE IMF data propagated to Geotail and plotted alongside measured Geotail data.

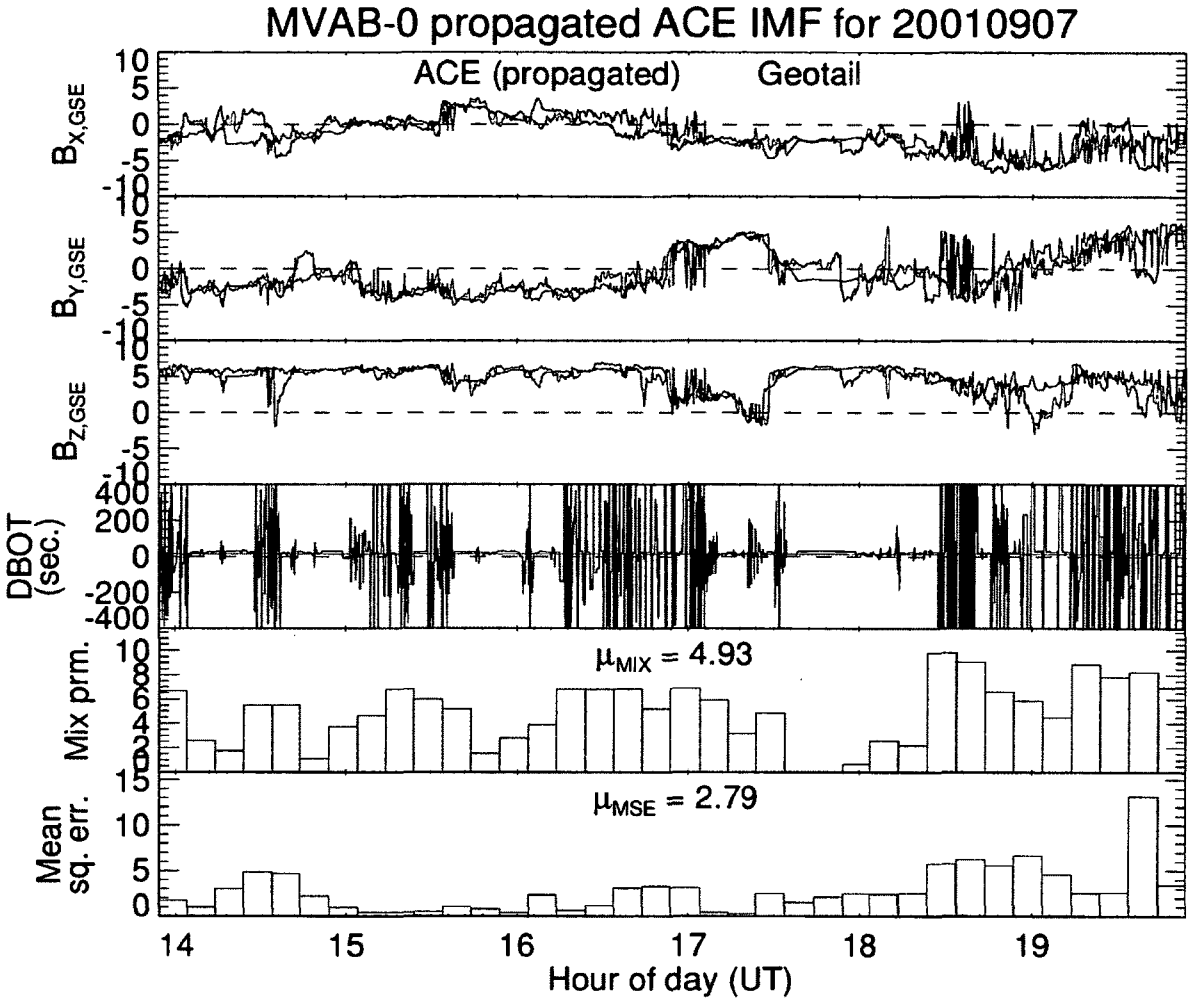

Figure C-1 Data Mixing Example. 6 hours of ACE data propagated to Geotail by MVAB-0 method with (N_{MVA}, r_{ev}, $N_{HT,P}$, θ_{lim}) = (31, 5, 3, 79°), plotted along with DBOT, mix parameter and mean square error. See text for description of DBOT and mix parameter.

Also plotted is "duration between observation times" (DBOT) showing the time difference in the original source data between neighboring points in the propagated series. Negative values indicate data mixing. The bottom plot shows a "mix parameter", which is an indicator for the amount of data mixing taking place in each 10-minute interval. The mix parameter has been defined as:

$$M_{10M} = \left(-\frac{N_{NEG.}}{N_{10M}} \sum_{NEG.} DBOT \right)^{\frac{1}{4}} \qquad (C.1)$$

Here N_{10M} is the number of points in the 10-minute interval, and the summation runs over the $N_{NEG.}$ negative DBOT values in the interval. The printed μ_{MIX} value is the mean of M_{10M} values in the bottom plot.

Figure C-1 illustrates 2 different types of data mixing. One is characterized by short duration and/or low to moderate absolute DBOT values and will be referred to as intermittent mixing. The other has large absolute DBOT values and is mostly of longer duration and will be referred to as extended mixing. There is not a clear distinction between the two types, but most of the time data mixing can be categorized as one or the other. In terms of the mix parameter intermittent mixing can be seen to typically have $M_{10M} < 5$ and extended mixing $M_{10M} \geq 5$.

Figure C-2 shows the distribution of mix parameter values when using MVAB-0 to propagate ACE data to Geotail for the entire Geotail solar wind data set.

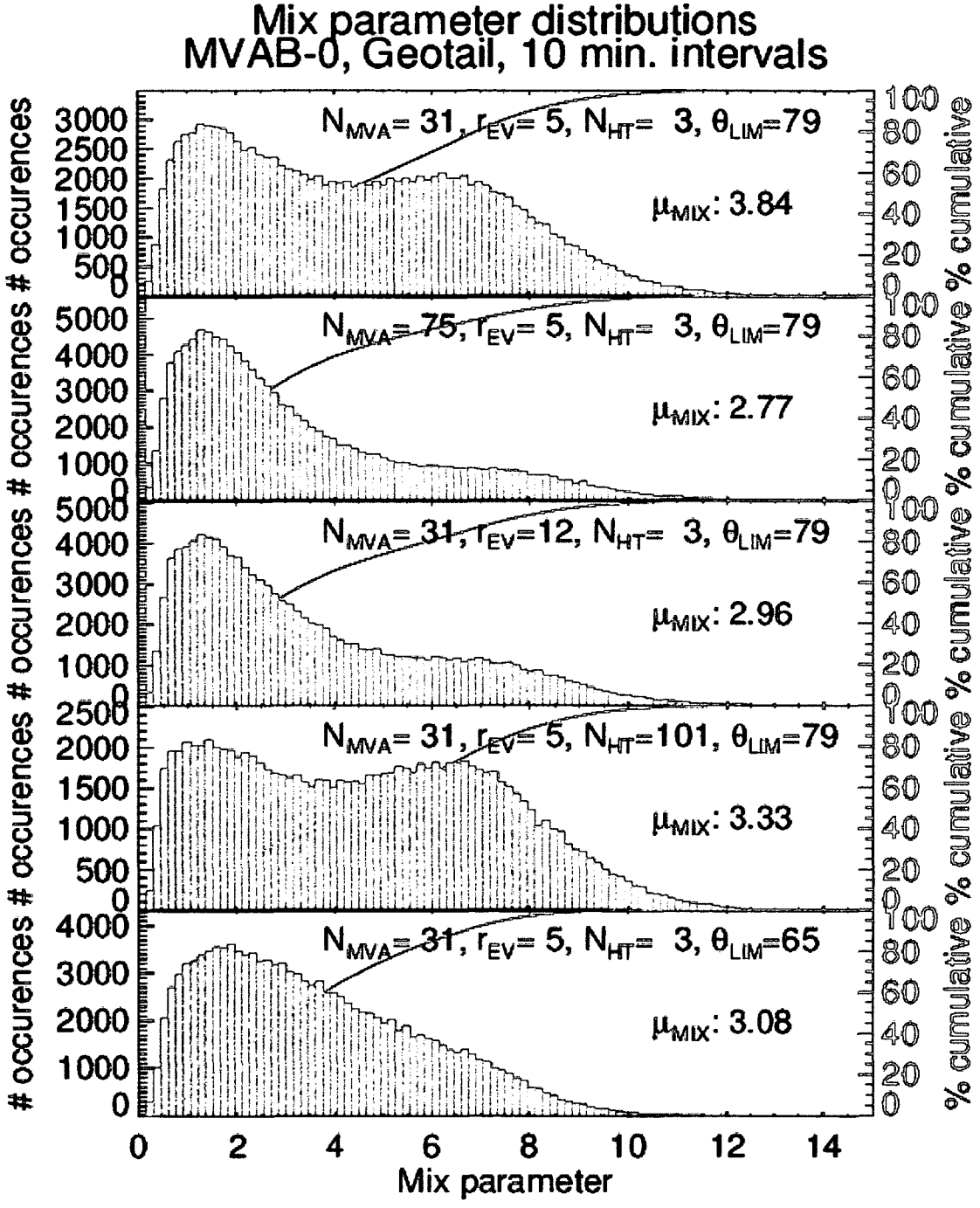

Figure C-2 Mix Parameter Distributions. Distributions of mix parameter values when using MVAB-0 to propagate ACE data to Geotail with 5 different parameter value combinations.

5 different sets of parameter values have been used. The top plot uses the parameter combination (N_{MVA}, r_{ev}, $N_{HT,P}$, θ_{lim}) = (31, 5, 3, 79°) found to give the lowest mean square error in Part 1 (and used in Figure C-1), and the four others have one of the parameter values changed so as to reduce data mixing, yet produce good test scores (see Figure 6-28 and Figure 6-29).

Each of the parameters N_{MVA}, r_{ev}, $N_{HT,P}$ and θ_{lim} affect data mixing as the value is changed, but in different ways. At first sight increasing N_{MVA} would appear to increase intermittent mixing. This is somewhat counterintuitive given that higher N_{MVA} generally means slower variations in PFN directions. Note also that eigenvalue ratios decrease with increasing N_{MVA}, causing a larger percentage of PFNs to be filtered out (given the same r_{ev}) and replaced by interpolation. Both of these effects are expected to decrease intermittent mixing. The explanation is that they are also effective in eliminating some extended mixing, which is then replaced by intermittent mixing. Most extended data mixing occurs due to intervals with high PFN-velocity angle, and interpolation of PFNs helps avoid some of these intervals (see notes for Algorithm C). Increasing $N_{HT,P}$ is expected to decrease data mixing by smoothing out sudden velocity fluctuations. This would generally lower mix parameter values slightly, but only noticeably during intervals with low M_{10M} where velocity fluctuations may be a dominant source of mixing. Decreasing the limit angle reduces extended mixing as expected, and again this produces a slight increase in the number of intervals with intermittent mixing because this becomes dominant where extended mixing was eliminated. Above observations help understand how parameters for other methods affect data mixing as well.

Data mixing affects each of the three different test scores used in this study. P_{MATCH} was designed to indicate a detrimental effect of data mixing: Distinct transitions being unidentifiable in propagated data. This in turn has an impact on $\sigma_{\Delta t}$, which relies on automated identifications of IMF discontinuities to compare predicted to actual arrival times, making it an issue to define $\sigma_{\Delta t}$ in a concise, meaningful way (see notes for Algorithm G). In contrast, the mean square error is a pleasingly simple quality measure. Examining how it is affected by data mixing is important given that its definition did not

require considering this carefully. Generally, data mixing causes propagated IMF data to take on "average" values during intervals where it is uncertain which source data is arriving at the target. There are three different mechanisms for averaging through data mixing to lower mean square errors.

The first applies around transitions when source data from two adjacent flux tubes overlap at the target and it is uncertain which flux tube the target is actually seeing during the overlap. Averaged data values will likely be off (it is one flux tube or the other), but only by about half of what they would be off when the wrong flux tube is predicted. Where the error is reduced by a factor of two, the square error is reduced by a factor of four. This suggests that a method for reducing data mixing must "pick" the right flux tube about ¾ of the time or more in order to improve mean square errors. Conversely, increased data mixing could produce worse results up to about ¾ of the time without increasing the mean square error. Even if the above explanation is oversimplified it does illustrate that the mean square error as a test score favors data mixing.

The second mechanism applies primarily in the interior of flux tubes, specifically by smoothing out small-scale structure in propagated data. In this study a ~60-second smoothing window was applied to both propagated and target data in order to eliminate foreshock waves with periods of ~30 seconds. This resulted in significantly improved test scores for μ_{MSE}. However, unlike foreshock waves, solar wind small-scale structure is not limited to short periods < 1 minute. Data mixing may then act to further reduce small-scale structure and in turn produce lower mean square errors.

The third mechanism applies when ACE and the target satellite are seeing different structures, typically during intervals with high PFN-velocity angle. Extended data mixing then lowers absolute data values and hence the average error for intervals with a large difference in propagated/measured IMF.

Figure C-3 shows the same data as in Figure C-1, but with a higher value of N_{MVA}=75 having been used for propagation (the parameter value set in the second plot in Figure C-2).

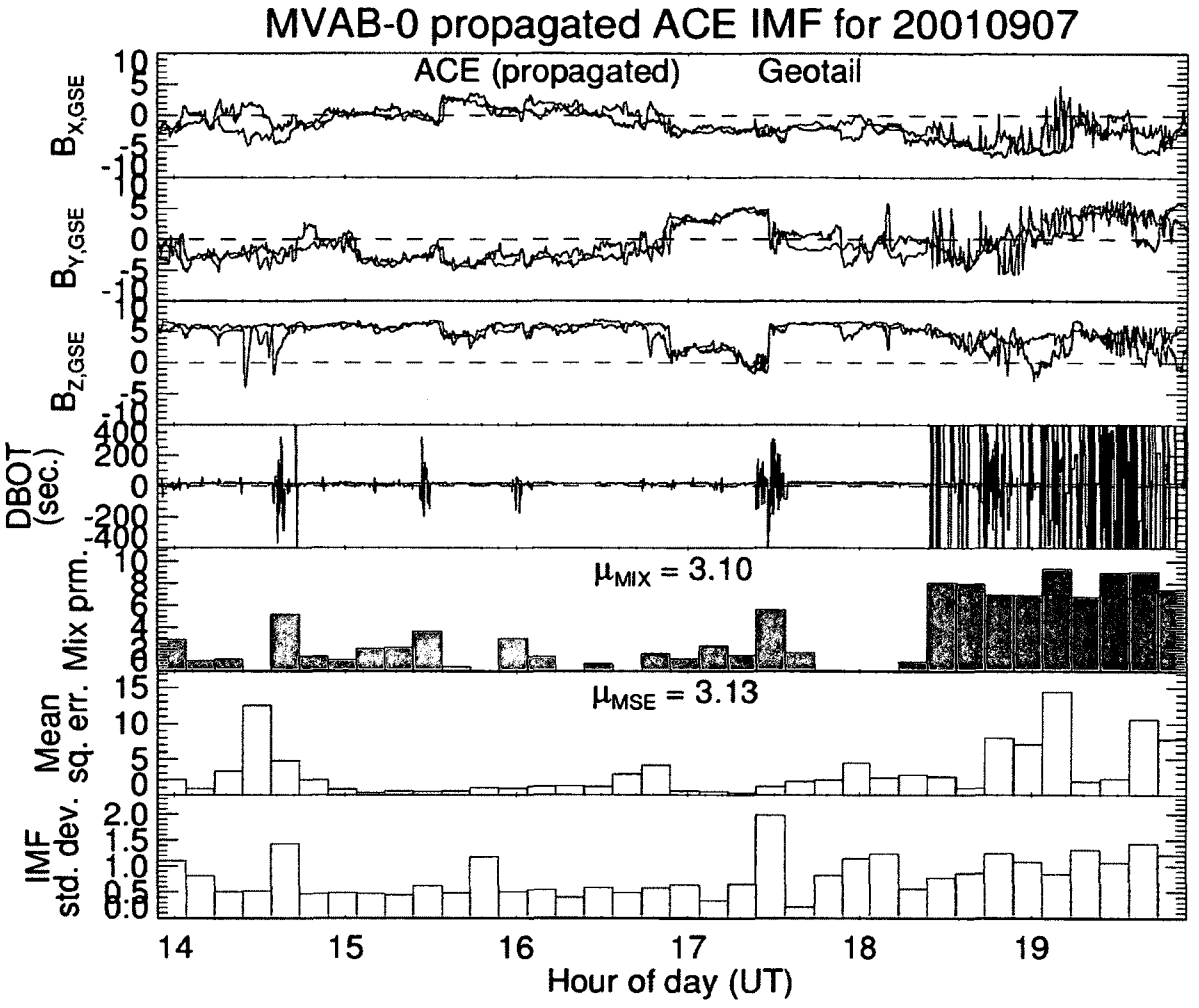

Figure C-3 Reduced Data Mixing Example. 6 hours of ACE data propagated to Geotail by MVAB-0 method, (N_{MVA}, r_{ev}, $N_{HT,P}$, θ_{lim}) = (75, 5, 3, 79°), plotted along with DBOT, mix parameter, mean square error and average standard deviation for x/y/z IMF components (Geotail data).

The average mix parameter drops from 4.93 to 3.10, mostly due to elimination of extended mixing. Notice how transitions around 15:30UT and 17:00UT that were somewhat ill-defined due to extended mixing with N_{MVA}=31 are now well defined and even accurately predicted. However, overall the mean square error was significantly lower with more extended mixing (2.79 nT^2 versus 3.13 nT^2). A small flux tube arriving around 14:40UT was inaccurately predicted with N_{MVA}=75 but mostly eliminated by data

mixing with N_{MVA}=31, and at the end of the interval extended mixing also serves to lower overall errors because the satellites are seeing different structures.

Figure C-4 and Figure C-5 show ACE IMF data before propagation along with calculated propagation delays. They cover the same interval and use the same two parameter value sets as in Figure C-1 and Figure C-3.

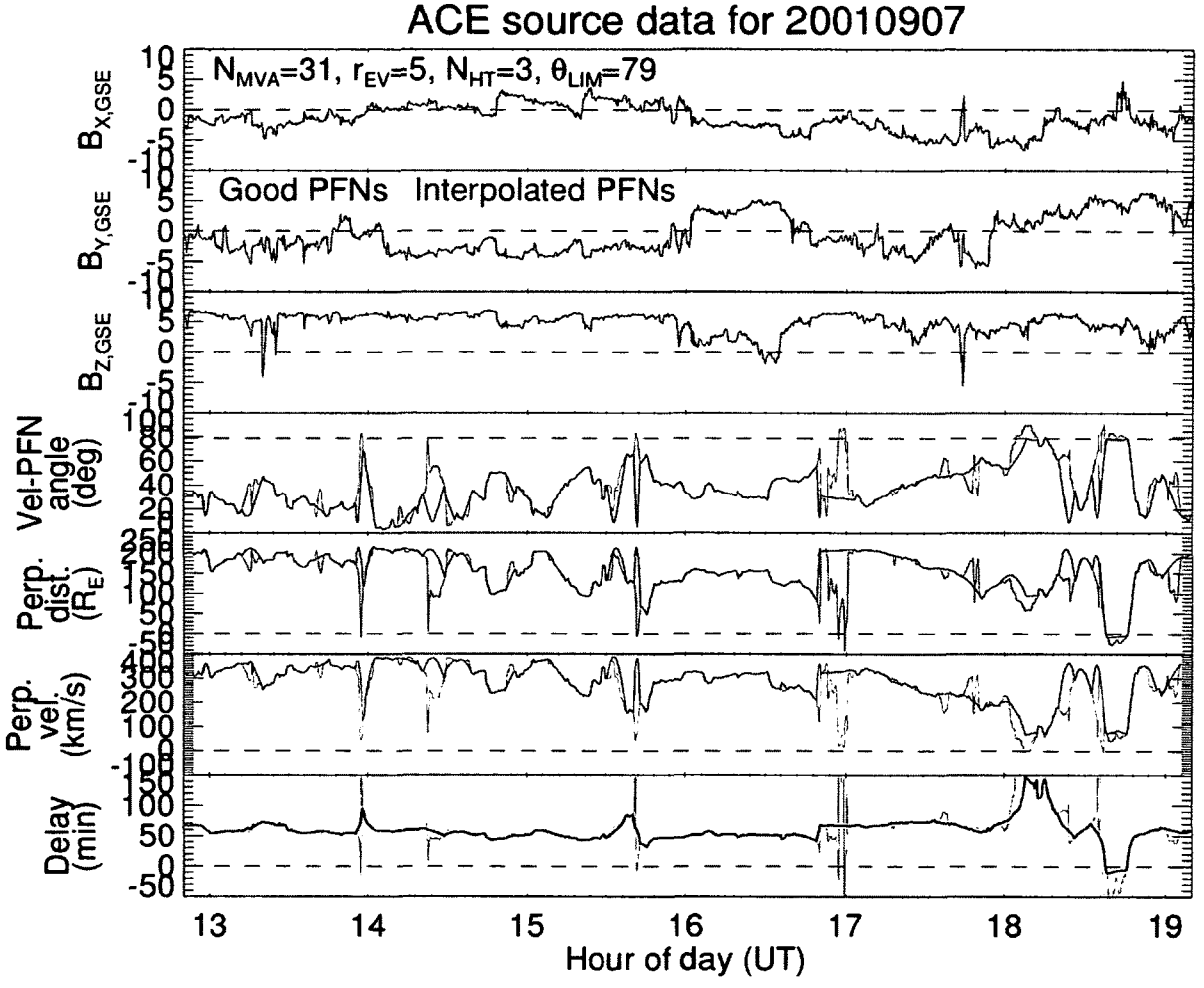

Figure C-4 Delay Calculation Example. ACE source IMF data before propagation and delay calculation results that gave the propagated data series shown in Figure C-1 (MVAB-0 method with (N_{MVA}, r_{ev}, $N_{HT,P}$, θ_{lim}) = (31, 5, 3, 79°)). In the bottom 4 plots light and dark colors indicate values before and after filtering/interpolation of PFNs.

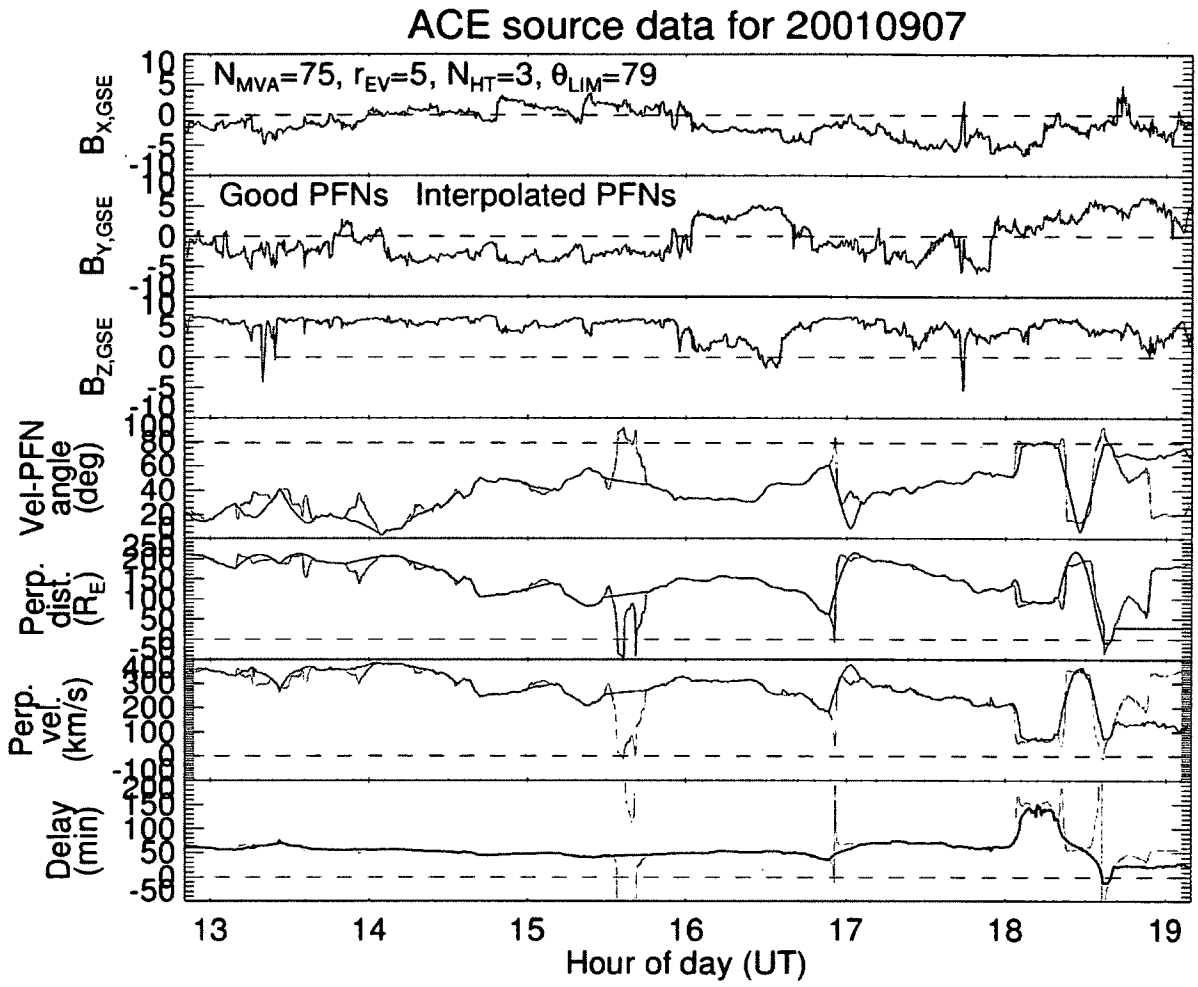

Figure C-5 Delay Calculations with Reduced Mixing. ACE source IMF data before propagation and delay calculation results that gave the propagated data series shown in Figure C-3 (MVAB-0 method with (N_{MVA}, r_{ev}, $N_{HT,P}$, θ_{lim}) = (75, 5, 3, 79°)). In the bottom 4 plots light and dark colors indicate values before and after filtering/interpolation of PFNs.

Also plotted are the PFN-velocity angles and, closely correlated, the source-target separation and propagation velocity along the PFN, the ratio of which gives the propagation delay. Light colors on the IMF plots indicate where PFNs where removed and interpolated because of too low eigenvalue ratio. The four bottom plots show with darker colors the values that were actually used for propagation and with lighter colors the values that were changed due to filtering. Whenever a sufficiently fast drop in the

propagation delay occurs in the bottom plot, data from before and after the drop will be mixed in the propagated series. Figure C-4 shows that most extended mixing in Figure C-1 occurred because of intervals with high PFN-velocity angles causing large changes in propagation delays. Figure C-5 shows how a higher value of N_{MVA} gives more gradual variations with PFN-velocity angles less frequently venturing into high territory. There are also longer intervals of PFN interpolation, and both of these factors contribute to eliminate extended data mixing as seen in Figure C-3.

A comparison of results for MVAB-0 propagated data with two properly chosen parameter values is useful for a closer examination of how data mixing affects mean square errors. One parameter value set is $(N_{MVA}, r_{ev}, N_{HT,P}, \theta_{lim})_1 = (31, 5, 3, 79°)$ and is close to optimal in terms of both μ_{MSE} and $\sigma_{\Delta t}$ ($\mu_{MSE} = 2.94\ nT^2$). The other is $(N_{MVA}, r_{ev}, N_{HT,P}, \theta_{lim})_2 = (75, 5, 101, 65°)$, which is also close to optimal for $\sigma_{\Delta t}$, but with significantly higher μ_{MSE} ($3.10\ nT^2$), which is likely due to decreased data mixing (see Figure 6-29). The average mix parameter value was 4.44 for set 1 and 2.66 for set 2. Again ACE data was propagated for the whole Geotail data set and split into 10-minute intervals (134,388 of them). For each of these the mix parameter, mean square error, IMF standard deviation and average limit angle of propagated points were calculated. The IMF standard deviation was calculated as an average of the standard deviations in the GSE X/Y/Z-components, same as in the bottom plot of Figure C-3. Results are plotted in Figure C-6.

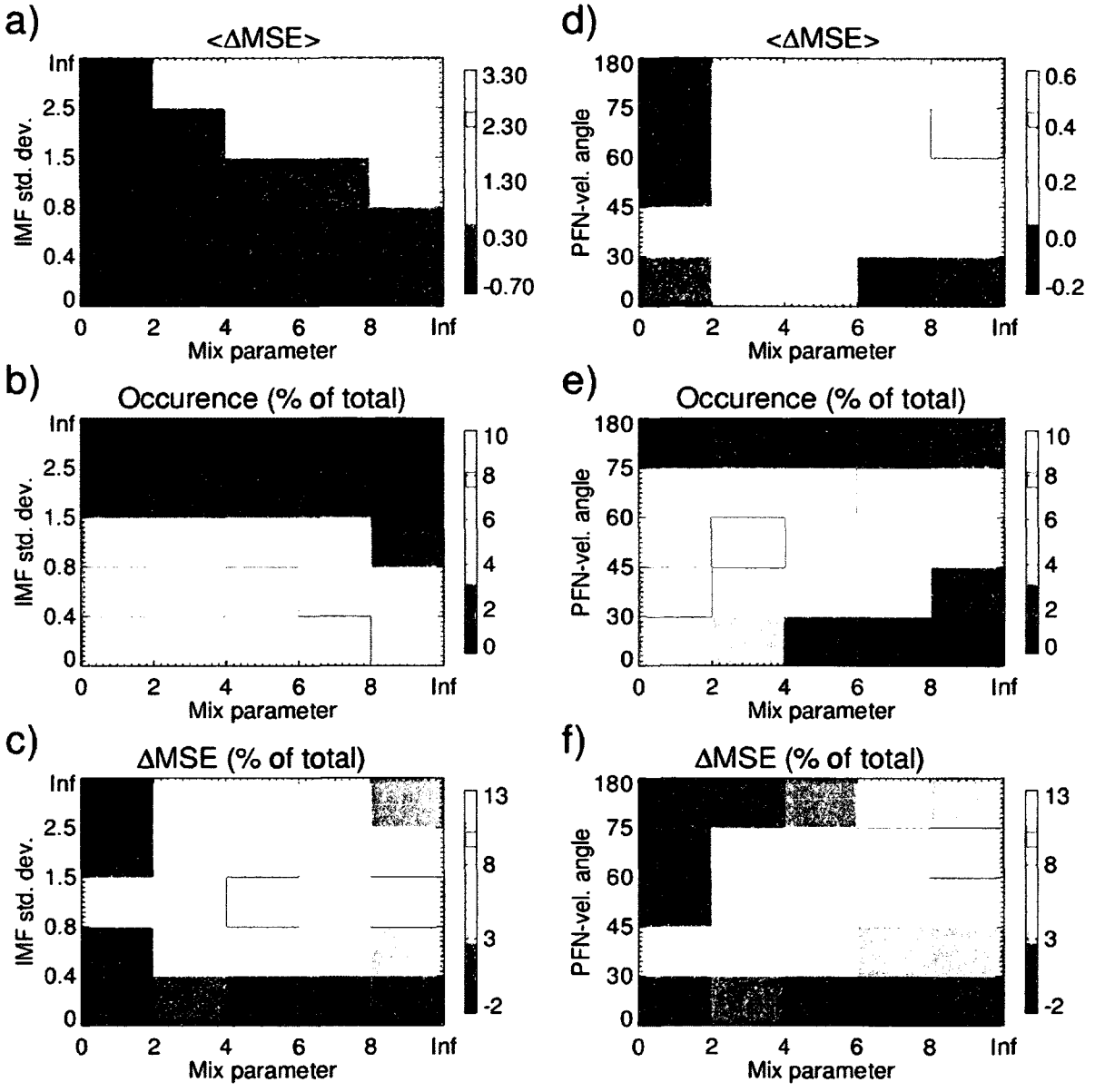

Figure C-6 Data Mixing and Mean Square Errors. Difference in mean square error between the two MVAB-0 parameter value sets (N_{MVA}, r_{ev}, $N_{HT,P}$, θ_{lim}) = (31, 5, 3, 79°) and (N_{MVA}, r_{ev}, $N_{HT,P}$, θ_{lim}) = (75, 5, 101, 65°) as a function of mix parameter, IMF standard deviation and PFN-velocity angle. ACE data was propagated for the Geotail data set and split into 134,388 10-minute intervals.

Plots a) and d) show the average difference in mean square error, set 2 minus set 1. Here the PFN-velocity angle and mix parameter refer to set 1 (occurrence distribution of mix

parameters was shown in Figure C-1, top plot), and the IMF standard deviation refers to the Geotail target data. Note that the occurrence of limit angles above 75° is artificially decreased due to employment of a limit angle of 79°.

The biggest reductions in mean square errors are seen to occur with extensive data mixing during intervals with high IMF variability and high PFN-velocity angles. However, as the occurrence distributions in Plots b) and e) show there are relatively few observations with these characteristics. The observation count has been weighted into Plots c) and f), showing the accumulative contribution to the total difference in mean square errors in percent. In summary, data mixing appears to contribute to lowering mean square errors almost regardless of mix parameter, IMF variability or PFN-velocity angle, though not evenly. 68% of the data had IMF standard deviation < 0.8 nT (characteristic of the interior of flux tubes) and made a 24% contribution to the reduction in mean square error evenly spread across intermittent and extensive data mixing. Data with IMF standard deviation > 0.8 nT, mix parameter > 4 and PFN-velocity angle > 45° make up 11% of the observations but contribute 48% of the total reduction in mean square error.

Appendix D
Permissions for Copyrighted Material

The following are excerpts of private email exchanges, showing permissions to use copyrighted figures included in this dissertation.

Figure 2-1 Comet Hale-Bopp Copyright Dan Schechter.

Hi Dan,
I am graduate student at University of Alaska Fairbanks working on finishing my dissertation on the solar wind. I would like to include an image showing the dust/gas tails on a comet and found the attached image of Hale-Bopp which I believe is yours. If correct, can I have your permission to include this image in the dissertation?
Thank you,
Poul Jensen

Hi Poul,
Thank you for giving me the courtesy of asking for my permission. Feel free to add my Hale-Bopp picture to your dissertation. Credit me if that is appropriate. Send me a copy if that is not too much trouble.
Cheers,
Dan

Figure 2-3 Parker Spiral Structure of Solar Wind Copyright Joe Borovsky.
Figure 2-4 Near-Earth Flux Tube Structure Copyright Joe Borovsky.

Hi Joe,
Attached are two of your figures:

1) Solar wind flux tube structure in ecliptic plane of inner solar system and
2) Close-up of the flux tube structure in the vicinity of L1 and Earth's magnetosphere.
With your permission I would like to use these figures with the introductory material in my dissertation to illustrate flux tube structure of the solar wind. Let me know if this is acceptable.
Thank you,
Poul

Hi Poul,
Sorry I forgot to reply earlier.
No problem, go ahead and use the figures. If you need better jpg files of the figures, let me know and I will send them.
Take care,
Joe

Figure 6-35 Comparison to Previous Study Copyright Dan Weimer.

Hi Dan,

I am planning to include the attached figure in my dissertation. It contains a copy of Figure 1 from your 2008 JGR paper for comparison to my results, and per requirements I have to get written permission (email is fine) from you in order to do so. Let me know if this is acceptable.

Thank you,

Poul

Dear Poul,

Yes, that is OK with me, to use this figure.

...

Good luck with your thesis!

Dan Weimer